High Precision Angle Calibration for Spherical Measurement Systems

By

David G. Martin

A thesis submitted in partial fulfilment of the requirements for the degree of Doctor of Philosophy in Engineering

University of Warwick, School of Engineering

February 2009

Table of Contents

List of Figures

List of Tables

Acknowledgements

I would like to acknowledge all those people who have helped me throughout this long process.

First I would like to thank Pierre Thiry and Bill Stirling for having given me the opportunity and encouragement to pursue this work at the ESRF.

I would like to thank my colleagues in the ESRF Alignment and Geodesy group; Daniel Schirr-Bonnans, Christophe Lefevre and Noel Levet. In particular, however, I would like to acknowledge the hard work of Bruno Perret, Laurent Maleval and Gilles Gatta without whom the realization this project would have been far more difficult than it was. Bruno‘s advice, Solid Works drawings and fabrication of all manner of mechanical bits and pieces, and Laurent’s breadth of knowledge in electronics and interfacing complex equipment have been invaluable. Gilles understanding of the art of uncertainty analysis, Labview programming and patient experiments leading to the arduous Type A evaluations has been tremendously appreciated.

I would like to thank my supervisor Professor Derek Chetwynd for his advice and the time he has taken in reading and proposing improvements and clarifications to this work. The long distance working arrangement between Coventry and Grenoble has been a pleasant challenge that has worked out very well indeed.

Finally I would like to thank my wife Marie-Christine, and three children, Thomas, Matthew and Rachel for their love and patience. It has not always been easy over the past years. Je vous aime.

To Marie-Christine, Thomas, Matthew and Rachel

Declaration

I declare that this thesis is my own work except for the following help with specific equipment and techniques:

- Several Type A repeatability tests on the horizontal angle comparator and vertical angle comparator shown in Figure 6.6 and Figure 6.23 were performed by Gilles Gatta (ESRF ALGE group).

Information derived from the published or unpublished work of others has been acknowledged in the text and a list of references is given.

This thesis has not been submitted in any form for another degree or diploma at any university or other institution of tertiary education.

…….. ……..

Signature Date

Abstract

The European Synchrotron Radiation Facility (ESRF) located in Grenoble, France is a joint facility supported and shared by 19 European countries. It operates the most powerful synchrotron radiation source in Europe. Synchrotron radiation sources address many important questions in modern science and technology. They can be compared to “super microscopes”, revealing invaluable information in numerous fields of diverse research such as physics, medicine, biology, geophysics and archaeology.

For the ESRF accelerators and beam lines to work correctly, alignment is of critical importance. Alignment tolerances are typically much less than one millimetre and often in the order of several micrometers over the 844 m ESRF storage ring circumference. To help maintain these tolerances, the ESRF has, and continues to develop calibration techniques for high precision spherical measurement system (SMS) instruments. SMSs are a family of instruments comprising automated total stations (theodolites equipped with distance meters), referred to here as robotic total stations (RTSs); and laser trackers (LTs).

The ESRF has a modern distance meter calibration bench (DCB) used for the calibration of SMS electronic distance meters. At the limit of distance meter precision, the only way to improve positional uncertainty in the ESRF alignment is to improve the angle measuring capacity of these instruments. To this end, the horizontal circle comparator (HCC) and the vertical circle comparator (VCC) have been developed. Specifically, the HCC and VCC are used to calibrate the horizontal and vertical circle readings of SMS instruments under their natural working conditions. Combined with the DCB, the HCC and VCC provide a full calibration suite for SMS instruments. This thesis presents their development, functionality and in depth uncertainty evaluation.

Several unique challenges are addressed in this work. The first is the development and characterization of the linked encoders configuration (LEC). This system, based on two continuously rotating angle encoders, is designed improve performance by eliminating residual encoder errors. The LEC can measure angle displacements with an estimated uncertainty of at least 0.044 arc seconds. Its uncertainty is presently limited by the instrumentation used to evaluate it. Secondly, in depth investigation has lead to the discovery of previously undocumented error-motion effects in ultra-precision angle calibration. Finally, methods for rigorous characterisation and extraction of rotary table error motions and their uncertainty evaluation using techniques not previously discussed in the literature have been developed.

Acronyms and Abbreviations

There are many acronyms and abbreviations. Generally the abbreviation is defined the first time it is met in the text.

Abbreviation	***Term***
ADM	Absolute Distance Meter
ATR	Automatic Target Recognition
ALGE	ESRF ALignment and GEodesy group
BIPM	Bureau International des Poids et Mesures
CAT	Computer Aided Theodolite systems
CGPM	Conférence Générale des Poids et Mesures
CIPM	Comité International des Poids et Mesures
CMM	Coordinate Measuring Machine
COFRAC	COmité FRançais pour l'ACcréditation
DCM	Distance meter Calibration Bench
EDM	Electronic Distance Meter/Measurement
ESRF	European Synchrotron Radiation Facility
FDA	Functional Data Analysis
FESM	Form Error – Spindle Motion error separation
GUM	Guide to the expression of Uncertainty in Measurement
GUM1	Supplement number 1 to the GUM
HCC	Horizontal Circle Comparator
HTM	Homogeneous Transformation Matri(x)(ces)
HLS	Hydrostatic Levelling System
IFM	Interferometric Distance Meter
ISO	International Organization for Standardization
JCGM	Joint Committee for Guides in Metrology
LEC	Linked Encoders Configuration
LNE	Laboratoire National d'Essais
LT	Laser Tracker
MTBF	Mean Time Between Failure
NIST	National Institute of Standards and Technology
NMI	National Metrology Institute
NPL	National Physical Laboratory
PDF	Probability Density Function
PTB	Physikalisch-Technische Bundesanstalt
RMSE	Root Mean Squared Error
RTS	Robotic Total Station
SI	International System of Units/ Le Système International d'Unités
SMR	Spherically Mounted Retro-Reflector
SMS	Spherical Measurement Systems

Abbreviation	*Term*
SR	Storage Ring
UKAS	United Kingdom Accreditation Service
UPR	Undulation Per Revolution
VCC	Vertical Circle Comparator
VIM	ISO/CEI GUIDE 99:2007: International Vocabulary of Metrology
3D	Three Dimension(s)(al)

1 Introduction: challenges in super-precise large scale metrology

1.1 Introduction

This thesis addresses the problem of the calibration of spherical measurement systems (SMSs). By SMSs we are referring to laser trackers (LT) and robotic total stations (RTS). These instruments are used extensively in large scale (volume) metrology. They are able to determine three dimensional coordinates of a point by measuring two orthogonal angles (horizontal and vertical) and a distance to a reflector.

Large scale metrology includes fields that require very high precision alignment over relatively large areas and volumes such as particle accelerator alignment, aircraft and vehicle manufacture. The field of particle accelerator alignment for example is unique in that it overlaps both the fields of metrology and traditional surveying and geodesy. Standard measurement precision is typically sub-millimetric over distances ranging between several hundred metres and nearly 30 km! New and planned machines go beyond even this, requiring micro-metre alignment precision on the same scales. The use of extremely specialised techniques and instruments are needed to guarantee that these requirements can be met.

A review of some instruments used in, and examples of large scale metrology objects can be found in [1]. A repository of papers presented during the regular International Workshop on Accelerator Alignment (IWAA) can be found at [2]. This repository covers most fields related to large scale metrology in accelerators.

In particular, a prerequisite to the attainment of these high degrees of precision is that there confidence in the instruments employed and measurements made. One very important way in which to assure this confidence is instrument calibration. Calibration is distinct from instrument testing in so far as it establishes a relation between the measurand[1] (e.g. distance or angle) with its measurement uncertainties provided by a measurement standard and the

[1] Measurand – quantity to be measured (VIM)

corresponding indications with associated measurement uncertainties given by a measuring instrument or system. Calibration is built upon the concept of traceability[2].

The problem of the calibration of the electronic distance meters (EDM) integrated into SMS instruments has been studied extensively. However, at present there is neither a standard nor even an instrument capable of calibrating the angles issued from these instruments under their typical operating conditions and over their full measurement range (i.e. 360 degrees for the horizontal vertical circles/encoders). This thesis proposes two instruments designed specifically to investigate the angle measuring capacity of laser trackers (LTs) and robotic total stations (RTSs). It then goes on to rigorously analyse their behaviour and provide a detailed statement of their uncertainty.

This chapter will set the stage with a discussion of the background context to the development of these instruments and a brief outline of the thesis.

1.2 Context summary

1.2.1 The European Synchrotron Radiation Facility

Many important questions in modern science and technology cannot be answered without a profound knowledge of the intimate details of the structure of matter. To help in this quest, scientists have developed ever more powerful instruments capable of resolving the structure of matter down to the level of atoms and molecules. Synchrotron radiation sources, which can be compared to "super microscopes", reveal invaluable information in numerous fields of research including physics, medicine, biology, meteorology, geophysics and archaeology to mention just a few. There are about 50 large research synchrotrons in the world, not to mention smaller rings used in hospitals etc…, being used by an ever-growing number of scientists and engineers.

The European Synchrotron Radiation Facility (ESRF) located in Grenoble, France is a joint facility supported and shared by 18 European countries. It operates the most powerful synchrotron radiation source in Europe. The annual budget for the operating costs of the ESRF is of the order of 80 million Euros. Approximately 600 people work at the ESRF and

[2] Property of a measurement result whereby the result can be related to a reference through a documented unbroken chain of calibrations, each contributing to the measurement uncertainty (VIM)

more than 6000 researchers come each year to the ESRF to carry out experiments. More than 1900 applications are received each year for beam time and about 1500 papers are published annually on work carried out at the ESRF[3].

For the ESRF accelerators and beam lines to work correctly, alignment is of critical importance. Alignment tolerances are typically less than one millimetre and often in the order of several micrometers over the 844m Storage Ring (SR) circumference.

The ALignment and GEodesy (ALGE) group is responsible for the installation, control and periodic realignment of the ESRF accelerators and experiments[3]. The uncertainty in distance and angle observations issued for the SR survey network calculations are in the order of 0.1 mm and 0.5 arc-seconds respectively. The uncertainty in the point determinations, as expressed by their absolute error ellipses, is less than 0.15 mm (semi-major axis) at the 95% confidence level.

To help ensure these results, the ESRF has a 50 m long distance meter calibration bench (DCB). This bench is used to calibrate the distance meters integrated into the robotic total stations (RTSs) and laser trackers (LTs) used for all of the high precision metrological work at the ESRF. Since February 2001, this bench has been accredited by Comité Français pour l'Accréditation COFRAC (accreditation number 2-1508), under the ISO/CEI 17025 standard. [4] COFRAC is the official French accreditation body. It is equivalent to and recognized by the United Kingdom Accreditation Service (UKAS) in the UK.

At present, the limit to which calibration can be used to improve the distance measuring capability of the instruments used to determine the ESRF survey network has been reached. The only way to further better results is to improve the angle measuring capacity of these instruments. The SMS angle calibration standards were developed to address this problem in the context of alignment of the ESRF. Nevertheless, as with the ESRF DCB, the angle standards can be applied to almost all types of LTs and RTSs available on the market.

[3] Experiments are installed on beamlines. Typically there are several alignment critical components on a beamline.

1.2.2 Planimetric alignment at the ESRF

At the ESRF the main survey networks are measured with high precision RTSs equipped with automatic target recognition (ATR). The instrument of choice (at the time of writing) is the Leica TDA5005. This instrument measures both distance and angles. However, because of the nature of the ESRF survey networks, angle measurements are of greatest importance.

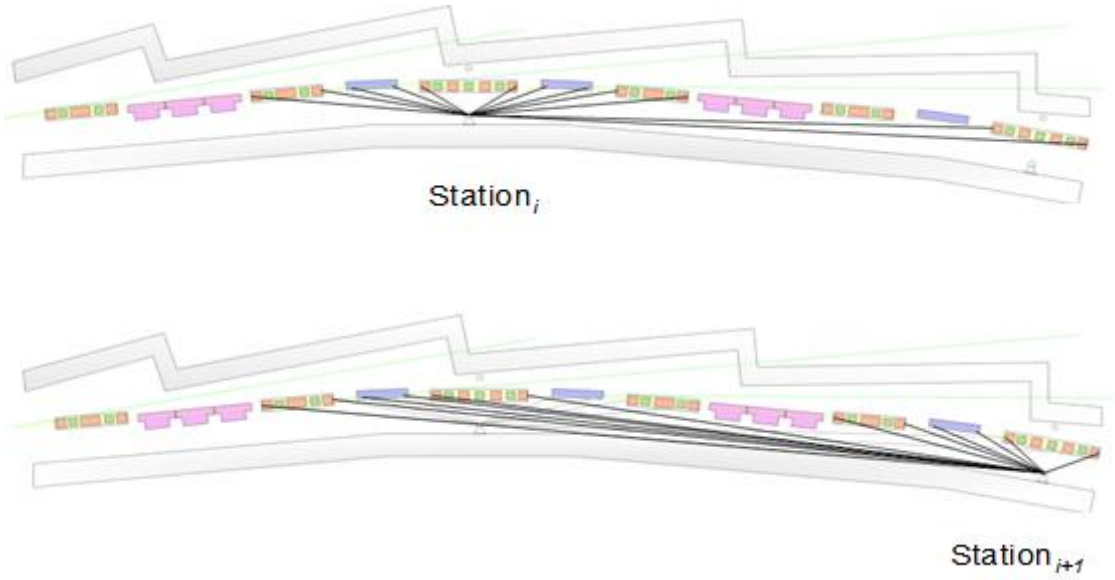

Figure 1.1 The ESRF Storage Ring (SR) planimetric survey network.

The ESRF planimetric survey is based on a very regular network composed of 32 cells. In each cell there are 3 instrument stations of which two are symmetric. Each instrument station makes the same observations in each cell: stations 1 and 2 have 14 distance/angle observations each and station 3 has 28 distance/angle observations. We remark that this is a long narrow network (Figure 1.1) which is typical of most particle accelerators.

At the ESRF the direction most sensitive to alignment errors is orthogonal to the travel of the beam. Because of the confines of the tunnel this direction is also the most sensitive to angle measurements. This is illustrated in Figure 1.2. At present we are at the limit of distance precision of the TDA5005. To improve the survey results, we must improve the angle measuring capacity of the TDA5005. This can be accomplished by calibration.

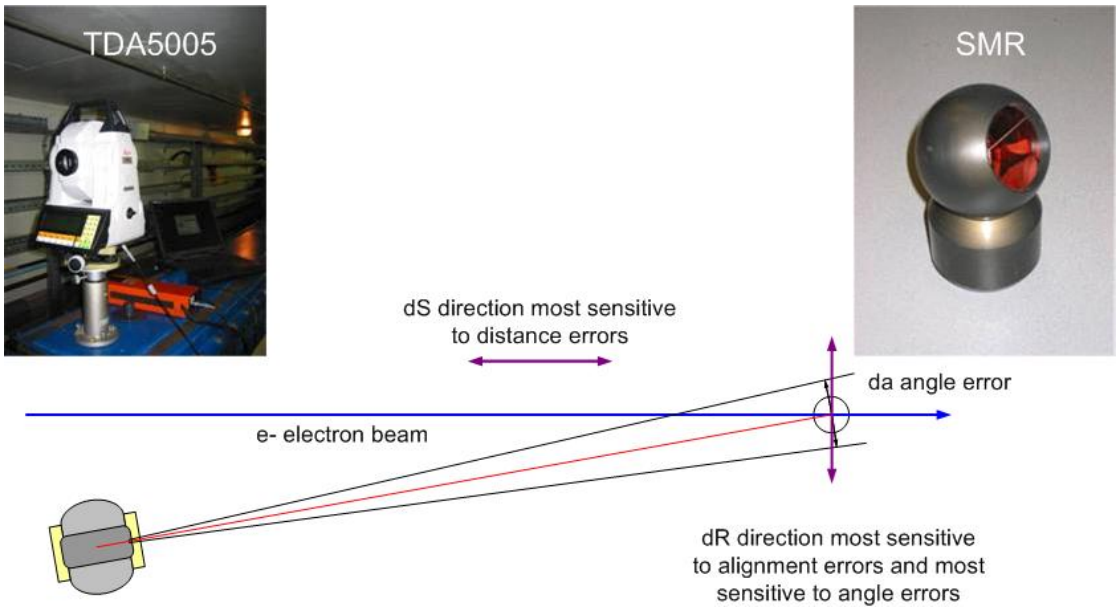

Figure 1.2 At the ESRF, as with most accelerators, the directions most sensitive to alignment errors are those orthogonal to the direction of travel of the electron beam. Due to the constraints of the tunnel, the survey network is typically long and narrow. Under these conditions, the direction most sensitive to alignment errors is also the most sensitive to angle measurements.

To better understand the problem of the bias in angle error residuals, we will look at a study made at the ESRF which helps to illustrate the influence of angle errors on the survey network calculation (Figure 1.3). [5]

Consider that the centre of the horizontal angle reading system and the centre of rotation of the instrument are not coincident but offset by a value δ. Choosing an angle α one can correct all of the observed angles for an eccentricity with respect to the observation axis. One can then minimise the standard deviation of the angle residuals issued from the least squares calculation by iteratively varying the values of δ and α for each instrument used in the survey and re-running the calculation to find the minimum of the angle residuals.

The angle residuals are given for STAT, and ROTATION. The STAT denomination represents the classical least squares calculation without the δ and α corrections. The ROTATION heading is used for the δ and α modified results. The results of this study (Figure 1.3) shows convincingly in the right hand box plot labelled ROTATION, that even though we cannot state their origin, we can affirm that with the classical least squares case the angle residuals are not minimum. This result could imply that there are systematic angle errors present in the measurements.

One of the principal aims of this project is to develop an angle calibration curve that can be reliably used to help improve the results of the survey network calculations.

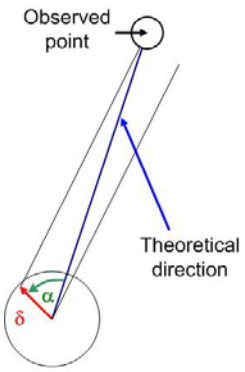

	STAT SD (arc-sec)	Rotation SD (arc-sec)
syxyjul99_before	0.40	0.37
syxyjul99_after	0.43	0.41
syxydec99	0.52	0.50
syxyjul00_before	0.63	0.44
syxyjul00_after	0.64	0.48
syxydec00	0.58	0.37
syxymar01	0.52	0.40
syxymar01_after	0.48	0.44
syxyjul01	0.53	0.45
syxydec01	0.52	0.50
syxyaug02	0.70	0.65
syxyjan03	0.53	0.46
syxyjan03_after	0.56	0.49
syxyaug03	0.54	0.49
syxyjan04	0.50	0.39
syxymay04	1.08	0.72
syxyaug04	0.99	0.72
syxydec04	0.67	0.57
syxyjan05	0.53	0.50
syxyaug05	0.66	0.64
syxydec05	0.57	0.44
syxymar06	0.64	0.49
syxyjun06	0.53	0.39
Mean	**0.60**	**0.49**

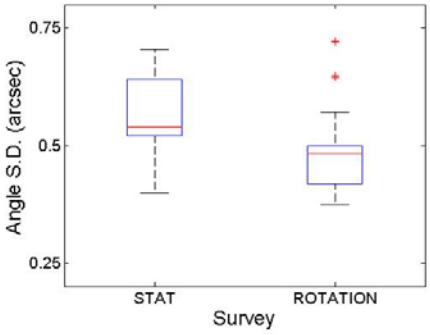

Figure 1.3 Angle residuals issued from 23 ESRF Booster Synchrotron (SY) network least squares adjustment calculations. The angle residuals are given for STAT, and ROTATION. STAT represents the classical least squares calculation without the correction discussed in this section. With the ROTATION results, the δ and α correction described above is applied to the angle observations to optimise the angle residuals issued from the least squares calculation.

1.3 The spherical measurement systems calibration program

The SMS calibration program is a suite of three instrument standards dedicated to the calibration of the distance meters, and the horizontal and vertical circles of LTs and RTSs. Traceability requirements, financial considerations and instrument constraints impose that these three component parts be calibrated separately at the ESRF.

Electronic distance meters (EDMs), absolute distance meters (ADMs) and interferometric distance meters (IFMs) are calibrated using the dedicated distance meter calibration bench (DCB) that we have already introduced. The horizontal circles of RTSs and LTs are calibrated using the horizontal circle comparator (HCC). The vertical circles are calibrated using the vertical circle comparator (VCC). The majority of the present work is dedicated to the design, calibration and error compensation of the HCC and to a lesser extent, the VCC.

The HCC is an instrument designed to provide an angle standard over the full 360 degree horizontal circle. Calibration is made by direct comparison of the spherical measurement system (SMS) horizontal circle reading to the HCC. The VCC is a structural rail installed on a

heavy duty adjustable height stand. The SMS is calibrated by comparing its measured vertical circle reading to the spherically mounted retro-reflector (SMR) installed on the VCC with the SMR vertical displacements measured by an interferometer. The required distance between the SMS instrument being calibrated and its SMR is measured directly by the instrument itself. The measurand, the vertical angle, is derived by simple trigonometry.

1.4 Aims and objectives

The principal objective of this thesis is to establish a suite of traceable calibration standards applicable to SMS instruments. In particular, two angle standards, the HCC and VCC are developed in the context of traceability and calibration as laid down by ISO/CEI 17025 and the Guide to the expression of Uncertainty in Measurement. This publication is commonly referred to as the GUM. The HCC, VCC and ESRF DCB in this larger context of traceability, calibration, and testing are shown in Figure 1.4.

It is particularly noteworthy that calibration is considered to be distinct from instrument testing. Typically instrument testing uses it own measurements to control its performance. T These tests, even if they are prescribed by a standard, do not however provide a means of establishing traceability. Traceability refers to an unbroken chain of comparisons relating an instrument's measurements to a known standard. Calibration to a traceable standard is used to determine an instrument's uncertainty and systematic errors. If there are systematic errors and they can be modelled, then one can improve the overall instrument performance. In the context of the ESRF, this instrument error modelling is used to improve the uncertainty in the survey networks. The improvement in the uncertainty of the ESRF survey networks is another main objective of this work.

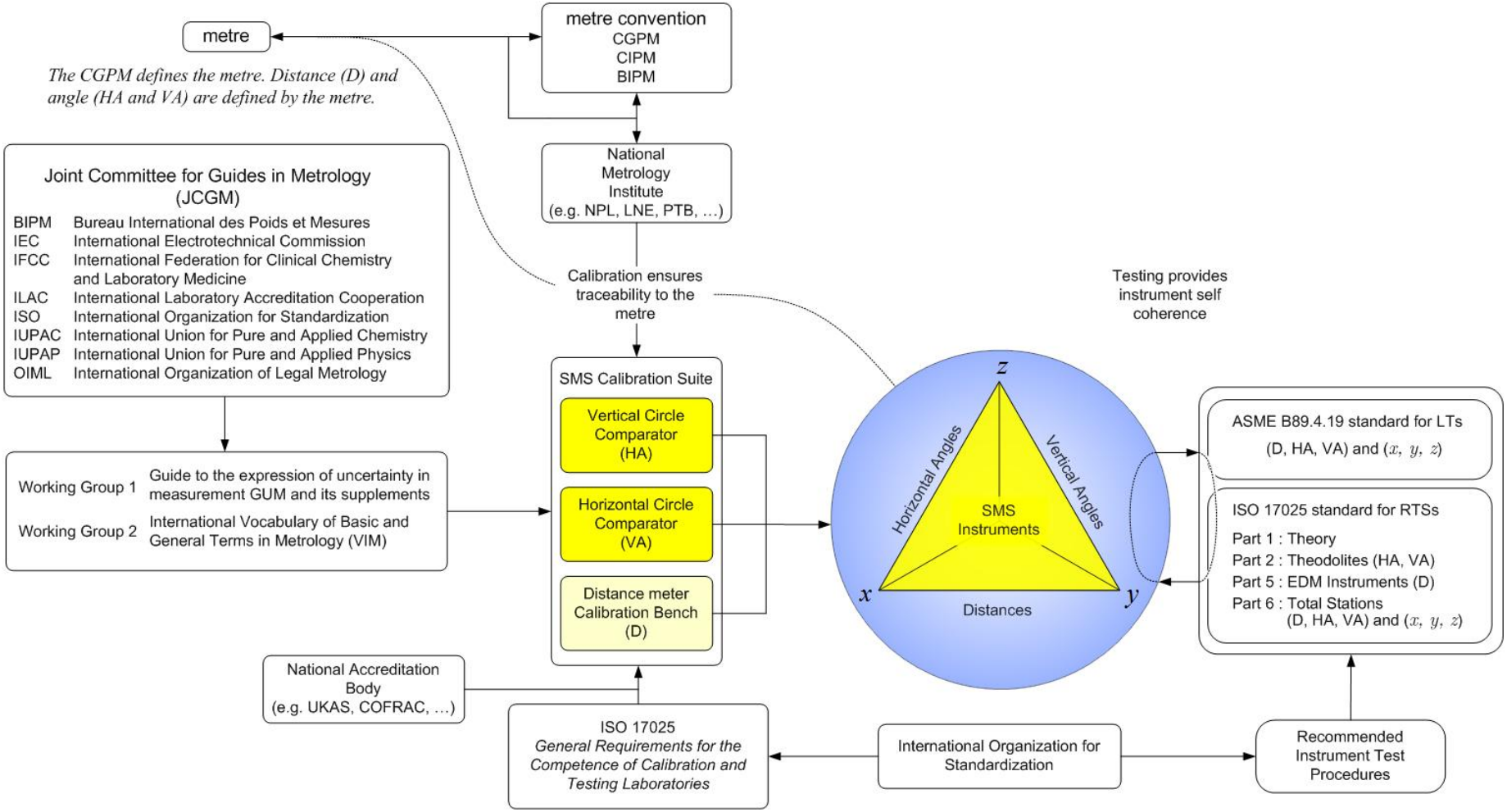

Figure 1.4 The main objective of this thesis is to establish two traceable standards that can be used to calibrate angles issued from RTSs and LTs. It is principally concerned with the HCC, the VCC and SMS instruments. This figure places these standards in the larger context of calibration and testing in general.

1.5 Thesis outline

This thesis introduces and studies in depth novel solutions to the problem of calibrating SMS angle measuring systems by examining their horizontal and vertical circles in their natural operating environment. The best of these instruments have remarkable angular discrimination and precision ($k = 1$) in the order of 0.5 arc seconds. The aim is to calibrate them in the ISO/CEI 17025 sense of calibration with the best possible expanded uncertainty (i.e. $k = 2$).

The thesis is divided into seven chapters including this one. Chapter two provides a general introduction to the thesis. It discusses in several subsections background information and important topics to be addressed in the subsequent chapters. First different definitions of angle measurement are given ending with the official international system of units (SI) derived unit, the radian. It discusses uncertainty in angle measurement. Different types of angle measurement (i.e. discrete systems –autocollimators and polygon mirrors, and continuous systems – angle encoders) and orders of precision in different environments are considered. Calibration versus testing and the interest in establishing and using a traceable angle standard is discussed. The chapter finishes with a review of literature, previous work and standards relevant to this field of study.

Chapter three introduces the HCC and the VCC - the two angle calibration instrument standards. First there is a discussion of what the HCC and VCC are designed to do. This is followed with a review of common errors associated with SMSs. Selection criteria for the HCC and VCC and an in depth discussion concerning concepts related to the different components of these instruments follows. The chapter concludes with remarks concerning the laboratory environment in which they are placed.

Chapter four discusses instruments and techniques that are used to calibrate and evaluate the HCC and VCC performance. There are three subsections in this chapter each addressing important subtopics. The first section reviews the different instruments; their intrinsic uncertainty and applicability, for the evaluation of the angle calibration standards. The second section discusses form error- spindle motion separation techniques (FESM) that will be used

to provide in part the HCC uncertainty. The third section introduces homogeneous transformation matrices that will be used to develop an HCC calibration model.

Chapter five follows naturally with the experimental work made to evaluate the uncertainty of the HCC. The chapter opens with some general remarks concerning modelling used in this experimental work. The HCC is composed of two parts; the angle acquisition system (LEC); and the reference plateau, and the laboratory environment. Discussions concerning the evaluation of these two parts using several different techniques and instruments are made. This chapter closes with a summary of the different results and their applicability to the compensation of the different errors associated with the HCC.

Chapter six reviews the different factors contributing to the uncertainty of the HCC and the VCC. It builds on the previous two chapters providing a clear statement of the uncertainty in the calibration of RTS and LT angles. This chapter provides detailed uncertainty calculations for the HCC and the VCC following the classical GUM framework, and for the HCC, the GUM supplement number 1 approach.

Chapter seven concludes the thesis and closes with some remarks aimed at further work and improvements SMS calibration project.

2 Angle measurement

This chapter is a general introduction to the thesis. It provides background information on important topics relevant to the subsequent chapters. First definitions of angle measurement are made ending with the official SI ('Système International d'Unités') derived unit. It then discusses uncertainty in angle measurement; addressing different types of measurement (i.e. discrete systems –autocollimators and polygon mirrors, and continuous systems – angle encoders) and orders of precision in different environments – industrial and laboratory. It discusses the ideas of calibration versus testing and the interest in establishing and using a traceable angle standard. The chapter closes with a literature review and discussion of previous work and international standards relevant to the calibration of robotic total stations and laser trackers.

2.1 Origin of angle measurement

Because of its importance, it is appropriate to ask what an angle is. In most dictionaries plane angle (as distinct from solid angle which is not considered in this thesis) tends to be defined as the space formed between two intersecting lines or planes. For example the Oxford English Dictionary gives the following definition: "The indefinite space between two lines or surfaces that meet, at or close to their meeting point; the shape formed by lines that meet. Also: the degree of divergence of two lines from one another, or of one line from a horizontal or vertical reference line or axis; an analogous property of a plane or planes … The magnitude of an angle between two lines is measured in terms of the amount of rotation about the point of intersection required to bring one line into correspondence with the other, and is generally expressed either in degrees (a full circle being 360 degrees) or in radians (a full circle being 2π radians)."[6][4]. A variety of other examples taken from different dictionaries are given in [7].

Legend has it that ancient Babylonian astronomers needed a way to express differences between directions to stars observed from the earth. They invented the angle, and a unit, the 'degree', to express these direction differences. They made a degree one 360^{th} of a full turn of

[4] angle, n.2 (OED)

the earth through the sky. The obvious question is why did they choose to make the degree one 360th of a turn around the sky? The answer is not clear and perhaps lost in antiquity.

One commonly accepted view is that: "This division of the circle is very ancient, and appears to have been originally applied to the circle of the Zodiac, a degree being the stage or distance travelled by the sun each day according to ancient Babylonian and Egyptian computation, just as a sign (as in e.g. Aries or Leo) represented the space passed through in a month".[6][5] This approach is supported by the fact that the Babylonians used the sexagesimal or base-sixty system for counting.[8] Another clue to the origin of this unit is an inscription translated from a clay tablet found at Shush (350 km from the ancient city of Babylon) in 1934 that (correctly) relates the ratio of the perimeter of a regular hexagon to the radius of its circumscribed circle by the factor six. This factor (6) multiplied by the base of their sexagesimal system (60) gives 360 [9].

Regardless of the origin of this system, it has persisted for millennia and is still used very extensively today in measuring angles, geographic coordinates, and time.

2.1.1 Units of angle measurement

There are three angle units in common use today; the sexagesimal (base-sixty), the centesimal (base-one hundred), and the radian (base π) systems. The sexagesimal (base-sixty) originated with the ancient Sumerians (circa 2000 BC), and was adopted by the Babylonians. Its popularity among the Babylonians could be derived from the fact that the number 60 has a large number of conveniently sized divisors, 1, 2, 3, 4, 5, 6, 10, 12, 15, 20, 30, 60. For example, an hour can be divided evenly into segments of any of twelve lengths: 60 minutes, 30 minutes, 20 minutes, etc…. With so many factors, many simple fractions can be used and it is known that the Babylonians were fond of using common (vulgar) fractions in their mathematical operations.[8] Its unit is the degree and symbol is $^\circ$. The degree is defined as one 360th part of a full circle. The right angle (the angle between two straight lines which intersect such that adjacent angles are equal) has 90 degrees. One degree is divided into 60 minutes (symbol ') which its self is divided into 60 seconds (symbol "). Fractions of a second

[5] degree, n. (OED)

are expressed in decimal notation. This is the most extensively used unit for representing angle in engineering. [10] Seconds will be denominated by arc-second(s) in this thesis.

The centesimal system was introduced by the famous French mathematician Lagrange at the end of the eighteenth century. It was part of the drive by Napoleon to modernize measurement with the introduction of the metric system.[11] Its basic unit is the grad. The international symbol for this unit today is the gon (Annex B ISO 31-1). The grad is defined as one 400^{th} part of a full circle. The right angle has 100 gon. Although, the grad is divided into minutes (one 100^{th} of a gon) and seconds (one 100^{th} of a minute), in practice, only decimal fractions of the gon are used. Being based on the decimal system, its main advantage is its ease of use. Angles are easy to add and subtract in mental arithmetic. A disadvantage is that the common angles such as 30° used in geometry must be expressed in fractions (i.e. $30° = 100/3$ gon). It is the unit primarily used by surveyors (géomètres) in France. The ESRF ALGE group is heavily influenced by French surveying culture and has traditionally used the centesimal system in all of its angle measurement.

The third angle unit is the radian. Its symbol is rad. It is used in many branches of mathematics, science and engineering and is the official SI unit.[12] One radian is the angle subtended at the centre of a circle by an arc of circumference that is equal in length to the radius of the circle. There is 2π rad in a full circle. It is a so-called derived unit. “Derived units are products of powers of base units. Coherent derived units are products of powers of base units that include no numerical factor other than 1. The base and coherent derived units of the SI form a coherent set, designated the set of coherent SI units.” [12] (p. 116) The radian is expressed in terms of the SI base unit the metre and is defined as $m \cdot m^{-1} = 1$ (i.e. it is a dimensionless unit).

That the official unit of angle is a derived dimensionless unit is of little practical importance. Pragmatically, engineers continue to measure angle as a physical quantity regardless of its official definition. However, as a point of principal, as well as a purist question of traceability, one may argue that angle has a historically well defined magnitude. Emerson[7] points out that all lexicographers are agreed that angles can be considered as

quantities in so far as implicitly or explicitly an angle has magnitude. In [13] angle is described as essentially a phenomenon at a point. It has no linear dimension and has traditionally been regarded as a difference of direction viewed from a point.

Angle magnitude has been measured for millennia by surveyors, astronomers and engineers. The metre was originally defined so that the land distance between Earth's poles and Equator would be exactly 10,000,000 metres. It has only been since 1983 that it has been defined in terms of the speed of light in vacuum[6]. [12] Indeed the original physical length of the metre was defined by angle measurement with Delambre's and Mechain's meridian expedition of 1792-1799. [11] Finally, one may point out that it is physically impossible to measure the length of an arc of a circle thus rendering it, at least theoretically, impossible to make a direct estimate of the true value of the measurand under the current SI definition of angle. Because of this definition, there is no defined standard artefact for the measure of angle.[14]

Angle will be considered to be a physical quantity with magnitude in this work. For the most part, the unit of angle used in this thesis will be the degree, or more often the arc-second. This is also the most commonly used angle unit and the one quoted by the National Metrology Institutes (NMIs). Nevertheless, given the SI definition of angle, we will make every effort to provide traceability to the metre.

2.2 Angle measurement and orders of precision

2.2.1 Angle measurement

The determination of angle is one of the oldest human measurement activities. For example, without modern equipment, it is far easier and more accurate to measure the angle between two distant points than to measure distances between them. At its origin, it is believed that the Egyptians faced with the regular flooding of the Nile and consequent obliteration of any established boundaries required regular surveys to re-establish the local cadastre. They also used crude instruments, by today's standards, to survey and construct their temples and pyramids. This is known because the accuracy of orientations of their constructions is

[6] The metre is the length of the path travelled by light in vacuum during a time interval of $1/299\,792\,458$ second.

apparent even today – taking into account the polar declination over the past several thousand years.

Mankind has developed over its history a rich variety of angle measuring instruments ranging from the most simplistic Groma consisting of four stones hung by cords from sticks set at right angles where measurements were taken by the visual alignment of two of suspended cords to modern high precision electronic theodolites. In fact, until the 1970s angle measurement was ubiquitous. It was only accurate way in which to measure position on the earth's surface, for example.

More recently of course, GNSS has rendered angle measurement obsolete for the most part in geodesy and many exterior engineering applications. Nevertheless, angle measurement remains of primary importance in industrial, typically indoor, environments.

2.2.2 Modern industrial angle measuring instruments

There are essentially two instrumental approaches to angle measurement. The first is the sub-division of the circle. This results in a discrete measure. The second approach is to use an encoder and measure continuously over the full 360 degree circle. Clearly the distinction between discrete and continuous is somewhat arbitrary. The context should generally clear any ambiguity. One may also consider a third category of instruments designed to measure continuously over relatively small angles, but with a very high precision. A selection of typical instruments and their claimed uncertainties is given in Table 2.1. Finally, one can distinguish between industrial and laboratory environments.

Examples of instruments using the circle dividing approach in industry are angle gauges, indexing tables and polygon mirrors coupled with autocollimators.

Angle gauges are widely used in industry. They are made from high quality hardened steel or tungsten lapped with a near optical, wringable finish. When calibrated in an accredited laboratory, angle gauges have a typical uncertainty in the order of ±1 arc-second. With a set of 12 angle gauge blocks, one may establish in additive or subtractive combinations any required angle to within 1½ arc-second.

The indexing table is based upon accurate meshing of two face gears of identical shape and pitch; one on the top which rotates and one on the bottom that is fixed. During operation, the table is displaced axially to disengage the teeth, and radially to the desired angle. The Moore 1440 Precision Index is an example of this type of instrument. It is guaranteed to be accurate to within ±0.1 second of arc at any of the 1440 indexed positions. Indexing tables are also widely used in manufacture and industry. The use of angle gauges and indexing tables is reviewed in [10].

Continuous measurement over the full 360 degree circle employs an encoder. Examples of instruments that employ angle encoders are laser trackers LTs, robotic total stations RTSs and theodolites. The theodolite is an instrument used widely in surveying and engineering. It consists of a telescope mounted within two orthogonal axes; the horizontal, and the vertical axis. In most applications, the theodolite works in the gravity frame. When the telescope is pointed at a desired object, the angle of each of these axes can be measured with great precision; typically on the scale of the arc-second. For a complete discussion of theodolites and classical surveying instruments in general refer to [15].

The so-called total station and RTS incorporates an EDM into the body of the theodolite. With a RTS, one can measure both angles and a distance to a corner cube reflector or spherically mounted retro-reflector (SMR). Angles are read from their encoders electronically. RTSs and LTs use reflected light and a detector (charged coupled device CCD or complementary metal-oxide-semiconductor CMOS) to determine the angular position of the distant point. Computing the shift indicated by the imaging sensor permits accurate measurement even when the prism is not in line with the optical axis of the instrument. Modern surveying instruments are discussed in [16] and electronic distance meters are reviewed in [17, 18].

A third category of instruments designed to measure or set angles continuously over relatively small angles, but with high precision; includes the sine bar, and the autocollimator combined with an optically flat mirror. Another instrument capable of measuring relatively small angles (±10 degree) very precisely and similar in principle to the sine bar is the angle

interferometer. Other commonly used angle measuring instruments are the inclinometer and the level.

Table 2.1 Example industrial angle measuring instruments and manufacturers claimed or generally accepted best uncertainties.

	Instrument	*Manufacturer/Instrument*	*Manufacturers Claimed Uncertainty (arc-sec)*
Discrete	Angle gauges		1 [a]
	Indexing tables	Moore 1440 Precision Index	0.1 [b]
	Polygon mirror/autocollimator	MOLLER WEDEL ELCOMAT 3000	0.1 [c]
Continuous	Angle encoder	HEIDENHAIN RON 905	0.4 [d]
	Laser tracker	LEICA LTD 500	2 [e]
	Total station	LEICA TDA5005	0.5 [f]
Small angle	Sine bar		2 [a]
	Angle interferometer	AGILENT 10770A/10771A	0.1 [g]
	Electronic/optical level	TRIMBLE DiNi 12	0.2 [h]
	Inclinometer	WYLER BlueLevel	0.2 [i]

a) [10] Angle gauges pp 7-9, sine bar pp 30-31
b) http://mooretool.thomasnet.com
c) http://www.moeller-wedel-optical.com (accessed 12 March 2008)
d) http://www.heidenhain.com (accessed 12 March 2008)
e) http://www.leica-geosystems.com 'PCMM System Specifications Leica Absolute Tracker'
f) http://www.leica-geosystems.com 'Industrial Theodolites & Total Stations data sheet'
g) http://www.home.agilent.com
h) http://www.trimble.com 'Datasheet - DiNi Digital Level – English'
i) http://www.wylerag.com

Note that all internet cited instrument specifications were accessed on 12 March 2008.

The sine bar is typically used in manufacturing to set angles. When a sine bar is placed on a flat surface its top edge is designed to be parallel to it. If one side is raised by a known distance, using gauge blocks for example, then the top edge of the bar will be tilted forming an angle that may be calculated by the application of the sine rule. Other variants of this principle are also used.

An autocollimator is an optical instrument for used for non-contact measurement of angles. In industry they are used to align components and measure deflections in optical or mechanical systems. The autocollimator works by projecting an image onto a target mirror, and measuring the deflection of the returned image against a scale, either visually or in

modern instruments by means of an electronic detector. Modern high precision autocollimators can measure a few one hundredths of an arc-second. Minimum uncertainties attained in industry are in the order of a few tenths of arc-second. The use of sine bar and autocollimator are reviewed in [10].

The angle interferometer is an instrument often used to control straightness and flatness. One such system is the Agilent 10770A angular interferometer and the Agilent 10771A angular reflector. This system can measure angles with a quoted precision of ±0.2% of calculated value ±0.05 arc-second per meter of distance travelled by the moving optic. Thus for pitch and roll angle displacements of less than 50 arc-seconds, one can measure to the 0.1 arc-second level of uncertainty.[19]

Levels and inclinometers use the gravity field as a reference to determine small angle displacements. Modern instruments can resolve down to 0.2 arc-second. Inclinometers in modern survey instruments and levels are discussed in [15] and [16].

2.2.3 Angle measurement in national metrology institute (NMI) environments

National metrology institutes (NMIs) maintain their country's primary measurement standards. These standards underpin an infrastructure of traceability within the country and throughout the world that ensures accuracy and consistency of measurement. One of the primary missions of these laboratories is to establish standards and techniques to calibrate instruments used in industry and manufacture. Typically these laboratories maintain the most precise standards available. Typical NMI uncertainties for a selection of calibration services are given in Table 2.2.

Most NMIs offer calibration services for angle gauges, indexing tables, polygon mirrors, and autocollimators. For the most part, calibration techniques are similar from one country/NMI laboratory to the next. Typically the calibration of indexing tables and polygon mirrors, the most demanding instruments in terms of calibration; both employ a rotary or an indexing table, and a high precision autocollimator.

Techniques for the calibration of polygon mirrors and indexing tables from four example NMI laboratories are considered here; the National Physical Laboratory (NPL) in the UK, the

National Institute of Standards and Technology (NIST) in the United States, the Laboratoire National d'Essais (LNE) in France, and the Physikalisch-Technische Bundesanstalt (PTB) in Germany. The NPL and NIST [20] use indexing tables while the LNE [14] and PTB [21] use rotary tables. All four laboratories use high precision autocollimators.

Table 2.2 Expanded uncertainties ($k = 2$)[7] taken from the NMI laboratory web sites at the time of writing (March 2008). All values represent the best possible uncertainties expressed in arc-seconds.

	Laboratory			
	NIST [a)]	*NPL* [b)]	*LNE* [c)]	*PTB* [d)]
Polygon mirror	0.14	0.11	0.06	0.05
Indexing tables	0.14	0.04	0.06	0.05
Autocollimators		0.03	0.06	0.05

a) http://www.nist.gov/
b) http://www.npl.co.uk
c) http://www.lne.eu/
d) http://www.ptb.de

For indexing tables, the calibration procedure consists of mounting and centring the indexing table to be calibrated on the NMI reference table. A precision mirror is installed on the top of the indexing table being calibrated. The calibration proceeds by rotating one table through a nominal angle (e.g. 30°), rotating the other table back through the negative nominal angle and measuring the difference with a high precision autocollimator. This measured difference on the autocollimator represents the combined errors of the two angular movements involved. The reference index or rotary table angle reading must be added into the calculation. With an indexing table such as the one used at the NPL, each angle, for both the reference table and the table being calibrated is measured at each of the nominal angles. In the case of the 30° example there are a total of 144 measurements in the calibration (i.e. $360°/30° = 12$ $\Rightarrow 12 \times 12 = 144$).

[7] Uncertainty is discussed in chapter 6.2. Typically an expanded uncertainty where $k = 2$ has a coverage interval of 95%.

The calibration of polygon mirrors proceeds in exactly the same way with the indexing table and mirror replaced by the polygon mirror. The nominal angle is the mirror separation angle. Generally measurements are only made once at each mirror separation angle. The LNE and PTB use their rotary tables to calibrate autocollimators. They are both capable of setting and reading very small angle differences. At the NPL calibration of autocollimators is made using the NPL-designed small angle generator. This instrument is a sine bar using interferometry to measure the vertical displacements.

2.2.4 Ultimate limits to precision

The problem is not so much designing an instrument capable of resolving angles to extreme precisions; rather it is validating and in particular ensuring the traceability (see chapter 2.3 below) of those angles. For example the LNE and PTB rotation tables cited earlier can resolve down to below one thousandth of an arc second. [14, 22] Similarly, the NPL small angle generator has much higher resolution than the expanded uncertainty listed in Table 2.2 above. There are several other techniques such as X-ray interferometry[23] and ring lasers [24] that also permit nano-radian (i.e. a few 10-4 arc-second) or even better sensitivity. Even high precision RTSs and LTs, whose manufacturers quoted precision is in the order of 0.5 arc-seconds and 2 arc-seconds respectively, have encoder resolution much higher than this; typically a few hundredths of an arc-second.

The internationally agreed method of ensuring angle traceability , or more strictly inter-comparison, by the NMIs is the polygon mirror coupled with a high precision autocollimator. A large scale inter-laboratory comparison EUROMET 371 organized by the PTB and involving many of the European NMIs was made at the end of the 1990s. Inter-laboratory comparisons are the only way of assigning a global uncertainty to a measurand. One of the main conclusions of this study was that although the intrinsic quality of the angle measurement systems was better, the uncertainty in the use of polygon mirrors cannot achieve better than 0.02 arc-seconds.[14]

The highest precision inter-laboratory comparison result found in the literature concerns one made between the instrumentation and methodology of the primary standards used at the

National Metrology Institute of Japan (NMIJ)[25] and PTB (section 2.2.3). These methods "have been compared by calibrations of high resolution angle encoders and gave a coincidence in the full scale within an uncertainty of 0.002 arc seconds ($k = 2$)." The author states however that: "Both methods are based on elaborate measuring set-ups and are restricted to the special application in metrology."[26].

2.3 Instrument calibration and testing

One of the stated aims of this thesis is to provide an ISO 17025 prepared standard to calibrate angles issued from LTs and RTSs. In this section we will refine what exactly we mean by calibration in this sense. The ISO 17025 standard states that a calibration certificate must include, among other things, the calibration result or value and where appropriate the units of measurement. It must also include the uncertainty of the measurement and a statement of the coverage factor of this uncertainty.

2.3.1 Calibration

What is calibration? The Oxford English Dictionary definition for the verb calibrate is; "To determine the calibre of; spec. to try the bore of a thermometer tube or similar instrument, so as to allow in graduating it for any irregularities: to graduate a gauge of any kind with allowance for its irregularities. b. To determine the correct position, value, capacity, etc., of; to set an instrument so that readings taken from it are absolute rather than relative; spec. to mark (a radio) with indications of the position of various wavelengths or stations." [6] Here we find the notions of; graduation for irregularities, the determination of the correct value, and the assignation of absolute as opposed to relative. When engineers and scientists think calibration, they are generally thinking in these terms.

There is another (similar) definition for the act of calibration given by the ISO/CEI GUIDE 99:2007: International vocabulary of metrology — Basic and general concepts and associated terms (VIM). [27]

> "
>
> 2.39 (6.11)
> calibration

operation that, under specified conditions, in a first step, establishes a relation between the **quantity values** with **measurement uncertainties** provided by **measurement standards** and corresponding indications with associated measurement uncertainties and, in a second step, uses this information to establish a relation for obtaining a **measurement result** from an indication

NOTE 1 A calibration may be expressed by a statement, calibration function, calibration diagram, calibration curve, or calibration table. In some cases, it may consist of an additive or multiplicative correction of the indication with associated measurement uncertainty.

NOTE 2 Calibration should not be confused with adjustment of a measuring system, often mistakenly called "self-calibration", nor with verification of calibration.

NOTE 3 Often, the first step alone in the above definition is perceived as being calibration.

"

This official definition represents the international consensus reached through ISO (the International Organization for Standardization). ISO is a worldwide federation of national standards bodies (ISO member bodies). The main difference between this and the previous definition are the dual concepts of measurement uncertainties and measurement standards. Implicit in this definition and indeed defined further in this same VIM chapter (i.e. Chapter 2 Measurement) are the concepts of:

metrological traceability:	property of a measurement result whereby the result can be related to a reference through a documented unbroken chain of calibrations, each contributing to the measurement uncertainty.
metrological traceability chain:	sequence of measurement standards and calibrations that is used to relate a measurement result to a reference.
metrological traceability to a measurement unit:	metrological traceability where the reference is the definition of a measurement unit through its practical realization (i.e. traceability to a measurement unit of the International System of Units). For example, in the case of angle calibration, the metrological traceability is to the metre (see chapter 2.1.1)

In the present work, the VIM definition of calibration will be adopted.

2.3.2 Testing

Instrument testing is quite distinct from calibration. The principle difference between the two is the notion of traceability. Traceability is at the root of all legal metrology and measurement. Traceability ensures the measurand is an accurate representation of what it is trying to measure. With traceability, it is possible to demonstrate an unbroken chain of comparisons that ends at a NMI. Calibration ensures traceability whereas instrument testing does not.

A calibration is performed in an accredited laboratory. Laboratory accreditation is awarded from an internationally recognized organization such as the United Kingdom's UKAS, France's COFRAC or Germany's DAR, Italy's SINAL or Switzerland's SAS to mention a few of the European national accreditation bodies. An accredited laboratory is required to follow the ISO/CEI 17025 standard. [28]

Instrument testing does not necessarily follow the same rigor as calibration does (i.e. ISO 17025). This is not to say that testing does not follow rules. There are many standards, not to mention generally accepted ad-hoc agreements for instrument testing. For example, this thesis presents a method to calibrate angles issued from high precision RTSs and LTs. However, there are two internationally accepted standards that deal with the testing of these instruments. [29, 30] Another fundamental difference between testing and calibration is that testing relies upon the instrument itself and some type of statistical test to validate its correct functioning. Calibration relies upon an standard traceable to an NMI.

2.3.3 Interest in instrument calibration

There are two main reasons to calibrate an instrument. The first is to respect obligations to standards one adheres to. For example, if one subscribes to the ISO 9001:2000 standard, Chapter 7.6 'Control of monitoring and measuring devices', requires that 'whenever necessary to ensure valid results, measuring equipment shall be calibrated or verified at specified intervals, or prior to use, against measurement standards traceable to international or national measurement standards; where no such standards exist, the basis used for calibration or verification shall be recorded'.[31] Thus traceable calibration provides the assurance that the

instrument is operating within some set of desired uncertainty limits. These limits may be imposed by legislation, some approach to risk management or simply the manufacturers stated instrument uncertainty.

Another reason one may be interested in calibration is to improve on instrument measuring capacities. This epitomises the notion of calibration as generally understood by scientists and engineers and given in the Oxford English Dictionary.

One approach to modern precision measurement is to assume the instrument is perfect and has no residual error. Of course this is untrue but given the manufacturer's confidence in the instrument, and its stated uncertainty, the residual errors form the baseline measurement limit. At the opposite end of the spectrum is the model approach where one relies extensively on some form of mathematical model or correction to improve the uncertainty in a (low quality) instrument. Inevitably, most modern instrumentation lies somewhere between these two extremes employing a combination the two approaches. Thus calibration can also provide a means whereby instrument precision may be significantly improved. A calibration curve, provided that the underlying error is systematic and stable, can be modelled to ameliorate overall performance.

2.3.4 Whole instrument versus component calibration

Finally, one can differentiate between whole instrument versus component calibration. Naturally one would like to link as closely as possible the instrument performance in the field to its performance and error map in the calibration laboratory. For example RTSs and LTs have a large number of important composite parts. Among these elements are; a telescope (RTS) and optics, two orthogonal reading axes with angle encoders, an inclinometer (RTS and sometimes LT) to ensure the gravity reference, an imaging system, servo motors to follow the retro-reflector, one or more electronic distance meter(s) and/or an interferometer (LT), and a retro-reflector (SMR). [32] All of these component parts act together to determine the three dimensional coordinate of the position of the SMR.

There is a real danger that calibrating these component parts independently will not represent correctly the overall error map of the instrument. Thus, it is important to strive to

calibrate the instrument in as representative manner as possible. Having said this, it is not always practical or even possible to calibrate the different parts of an instrument together.

2.4 Literature review and previous work

2.4.1 Background and previous work

In the 1970s and 1980s, there was pressure from industry to develop easy to employ three dimensional measuring systems. This pressure was from aircraft manufacturing, ship and car building and particle accelerators to name a few. At this time reliable high precision electronic theodolites were (becoming) available on the market. Instruments such as the Kern E2 were capable of measuring angles to sub-arc-second accuracy. In parallel high precision distance meters with resolutions in the order of 10 µm such as the Kern Mekometer and the Comrad Geomensor were also becoming commercially available. These instruments along with industrial photogrammetric systems and larger and lager three dimensional gantry type Coordinate Measuring Machines (CMMs) were opening new horizons in industrial large scale metrology.

High precision theodolites were particularly attractive and systems were developed employing theodolite intersections using what was referred to as Computer Aided Theodolite (CAT) software. These systems with their extensive analysis software coupled with just emerging personal computer (PC) technology helped pave the way for the more inclusive SMSs studied here. Wendt and Zumbrunn [32] studied these systems extensively identifying, or at least cataloguing, and quantifying many of their error sources. Their stated objective was to provide a series of draft guidelines that would enable the user to quickly and reliably determine and/or verify measurement uncertainty of these systems. These CAT systems have since become largely obsolete but these guidelines and error analysis remain valid for the qualification of angle measurement.

In the 1990s a number of comparative tests between the different systems available on the market (CAT, photogrammetric, CMMs, early LTs etc…) were made. These tests were a type of precursor to the whole instrument calibration (section 2.3.4) aimed at in this work. They typically used an artefact such as a tetrahedron. One example made by more than 30

participants is described in [33]. The results of the tests were based on the agreement between the coordinate determinations made by the different instruments used in the test. These comparisons were very similar in spirit to the inter-laboratory comparisons made between ISO 17025 accredited laboratories. One perceived drawback of these artefact comparisons was the fact that their limited size, typically a few m3, studied localized regions of the instrument used, such as their angle encoders, and so did not properly characterise the true instrument performance.

Several theodolite/total station calibration and testing techniques have been proposed in the past. They can be divided into two broad groups. These groups are the so-called 'conventional' and 'new' test methods; terms coined by Ingensand [34] in 1990. Conventional methods use multiple targets and require the circle position to be changed. One example of this approach was the artefact comparison discussed above. Another performed at Boeing is discussed below in more detail. New methods aim to automate the test procedure as much as possible. Ingensand sets out a series of specifications for the new test method:

- High accuracy – better than 0.3 arc-seconds,
- Fully automatic test sequence,
- Testing the angle encoder in the instrument's operational position,
- Testing the full measuring range,
- Analysis of systematic errors found during the tests,
- Automatic determination of a correcting function and transfer to the theodolite of the correction parameters,
- Ease of use,
- Suitability for various theodolite models,
- Qualification of both vertical and horizontal angle reading systems.

Palmateer [35] describes an example of the conventional type test developed in a collaboration between NIST and Boeing. First a reference network of points is measured several times from different vantage points by a 'certified measurement system', a system of superior quality to the instrument to be tested. These data sets are then used in a least squares calculation to determine the three dimensional coordinates of the measured points $(x, y, z)_{ref}$. The second stage of this technique involves measuring the network with the instrument to be

tested. Coordinates are determined using the same techniques of multiple data sets and least squares adjustment. Test results are compared with the reference network and analysed as a function of range.

This technique is not easy to implement. However is does have the merit of employing a whole instrument test technique providing uncertainty and bias information. The technique could be conceivably be used to provide a type of thee dimensional (3D) network standard. However this would require considerable time and effort and one could justifiably question the stability of this system given the time it would take to complete the measures.

The first of the new test methods was developed by Maurer in 1982 [36] to test the horizontal circles of electronic theodolites. The test instrument was intended to investigate possible short periodic errors in the readings of electronic theodolites. Maurer used an HP 5526A interferometer to measure differences to two prisms installed on a bar with a prism separation of 636.6 mm. A sector of ±8.5 gon (±7.65º) could be calibrated in one go. In practice, the theodolites were tested with the measuring intervals starting at 0, 5, 10, 15, 20 … 390, 395 gon (0, 4.5, 9, 13.5, 18, … 351, 355.5 degrees). The overall measuring uncertainty (k=1) was 0.13 arc-seconds. [34]

Of the new test methods, the most comprehensive instrument example is the Theodolitprüfmaschine (Theodolite-Testing-Machine or TPM) developed by Ingensand while at Wild Leitz (later Leica).[34] He describes this instrument as a theodolite (the one being tested) inside another theodolite (the standard).

The TPM standard is composed of three parts; an electronic autocollimator, and two high precision angle encoders mounted orthogonally to one another (d, e and f respectively in Figure 2.1). Not shown in this figure are the servo motors which rotate the different elements about he vertical (horizontal circle calibration) and trunnion (vertical circle calibration) axes.

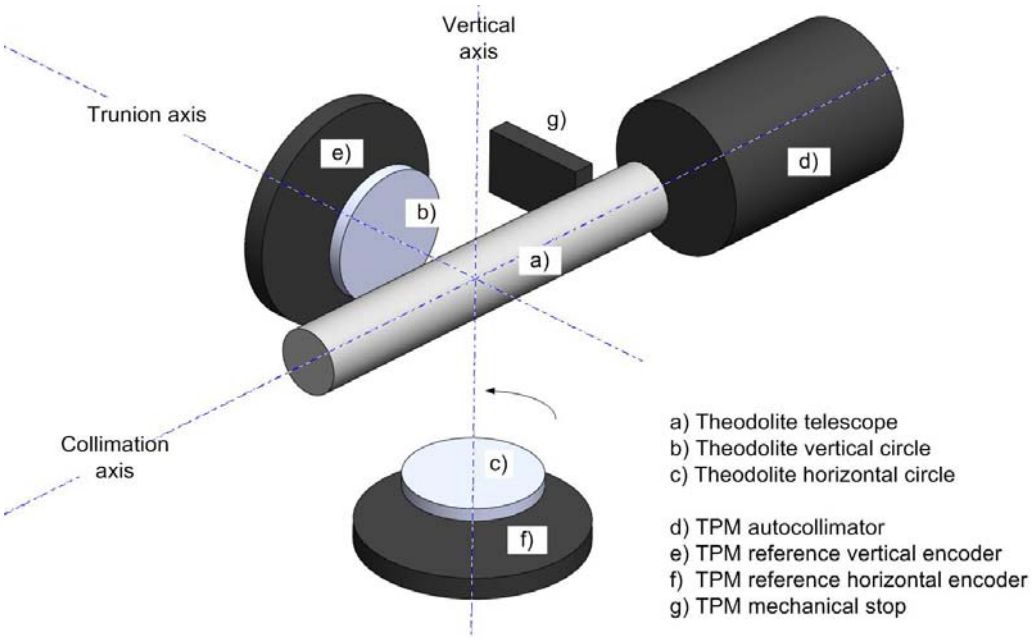

Figure 2.1 Set up used by the TPM for the calibration of theodolite horizontal circles.

For the horizontal circle test, a mirror is installed on the theodolite telescope (a in Figure 2.1) and the telescope and autocollimator are placed in the horizontal position. To start, the motorized test system rotates the theodolite counter-clockwise against a mechanical stop (g). The base of the theodolite and its horizontal circle (c), as well as the reference horizontal encoder (f), are then turned counter-clockwise through an angle. The theodolite telescope (a) resting against the stop (g) is not moved. The measurement terminates with the theodolite telescope (a), horizontal circle (c) and the reference horizontal encoder (f) being turned slightly clockwise to be brought into co-linearity with the autocollimator (d). The theodolite angle error is determined by subtracting the reference circle and autocollimator readings from the theodolite horizontal circle reading. This is repeated for the desired number of angles.

The theodolite vertical circle (b in Figure 2.1) is tested by rotating the autocollimator (d) in a plane about the trunnion axis. A fork shaped driver (not shown in the figure) turns the theodolite's telescope through a predetermined vertical angle α .The measurement is made after the autocollimator (d) is brought into co-linearity with the theodolite telescope (a). The error is determined by subtracting the reference vertical encoder and autocollimator readings from the theodolite vertical circle reading.

The uncertainty given for this technique ($k = 1$) is 0.1 arc-second. There are several of these instruments currently being used by Leica and a certificate issued from measurements made

on them is delivered to the client when a theodolite is purchased. Although it remains the reference in the field for this type of test, its drawback is that it tests the angle encoders and not the full instrument in its normal operating environment. This test procedure cannot be used with LTs specifically because of this.

Professor Ingensand wrote in an e-mail to the author that it is unlikely any encoder errors remain in instruments tested with the TPM. However, he went on to say that "the encoder is just one component of the accuracy of direction measurements. There are additional effects:

- Thermal and mechanical drifts of the encoder and the tacheometer respectively.
- Horizontal and vertical eccentricity of the telescope which will be compensated by dual face observations.
- The focus function which is caused by the non-colinearity of the optical axis of the focusing lens, and,
- Thermal effects of the telescope."[37]

Other possible error sources not mentioned here are linked to the drive assemblies and motorization of the RTS and LT. These additional effects can only be observed when the instrument is working in its natural operating conditions and observing real targets. In other words we must use a whole instrument calibration to determine them.

A method was proposed by a French team using a Moore 1440 indexing table to test horizontal theodolite circles. Measurements are made by manually pointing and reading the theodolite. The uncertainty in the test method given as 5.8 arc-seconds (0.0018 grad). [38] More recently a team at the Vilnius Gediminas Technical University developed a test bench designed to test theodolite horizontal angles. The test bench is composed of a precision rotary encoder, and a 12 sided polygon mirror coupled with an electronic autocollimator. The instrument to be tested is installed on the rotary table. Its base rotates together with the table. However, the body of the total station is loosely constrained so that it does not move with the rotary table. The test procedure consists of rotating the table through an angle controlled by the rotary encoder and manually sighting the instrument being tested to a reference mark. The rotary table angle displacement is read and the autocollimator makes a measure to one of the 12 polygon mirrors.[39] This test method is still under development at the time of writing and no uncertainty is given. However, the manual pointing of the instrument being tested is

considered non-optimal and time consuming. Furthermore measuring just 12 positions on the horizontal circle is very limited. As with the previous methods, there is no testing of the vertical circle.

A team at the Stanford Linear Accelerator Complex (SLAC) located at Stanford University in the United States has developed a system for testing horizontal angles of LTs.[40] This system uses a high precision rotary table. The rotary table standard is calibrated using a system involving two autocollimators and two mirrors installed on a fixture on the rotary table. The technique is very similar to the classical cross calibration system used to calibrate polygon mirrors. [10, 41] The uncertainty ($k = 1$) given for this test is 0.2 arc-seconds.

The LT test consists of mounting the instrument on the rotary table and turning the table through a set of test angles. The LT automatically follows the rotary table movement. A calibration curve is established by direct comparison between the rotary table and LT horizontal angle readings. The test results show that this calibration curve could be employed to considerably improve measurement results. This is the first test method that successfully approaches the whole instrument calibration discussed in section 2.3.4 above. The vertical angles are not tested at present.

2.4.2 Standards

Two standards exist for the testing of these instruments. The first which concerns the theodolite and total station systems is the ISO 17123 series of international standards concerning Field procedures for testing geodetic and surveying instruments. [42] . The LT test procedure is outlined in: the American standard ASME B89.4.19 – 2006 [30]; the German standard VDI 2617 part 10; and presently under the ISO 10360 standard.

All of these standards promote test procedures. Recall the instrument testing does not ensure the fundamental concept of traceability (refer to section 2.3). Typically the instrument being tested is used in the verification procedure. Results are given by statistical tests. The advantage of these standards is that they are widely accepted in industry by both users and manufacturers. It would be helpful therefore if the test procedures outlined in the standards could be emulated by a calibration procedure. This is the case of distance meter calibration

methods employed at the ESRF DCM which resemble closely those outlined in both the ISO 17123 [42] and ASME B89.4.19 – 2006 [30] standards. Similarly the VCC follows closely the tests outlined in [30]. However, this emulation is not always practical or even possible.

2.4.3 National Metrology Institutes (NMIs)

No techniques (to the author's knowledge) have been developed by the NMIs specifically for the calibration of RTSs and LTs. However, two institutes, the PTB in Germany and the LNE have developed etalons that could possibly be used for the calibration of the horizontal circle of RTSs at least. [14, 21, 43] Indeed, one standard, the LNE 'Plateau de Référence Angulaire' angle acquisition system has served to a certain extent as a model for the HCC LEC discussed below. The instruments bear mention because they are in principle able to ensure with a very small uncertainty, traceable horizontal angle measure over the full 360 degree circle.

3 The SMS calibration instruments

This chapter introduces spherical measurement systems (SMSs), their errors and calibration. The main focus is the horizontal circle comparator (HCC) and the vertical circle comparator (VCC). The chapter starts with a discussion of common laser tracker (LT) and robotic total station (RTS) errors, followed by an outline of what the HCC and the VCC are designed to do to characterise them. This is followed by the selection criteria for the HCC and VCC, and an in depth discussion of their component parts. The chapter concludes with remarks concerning the laboratory environment in which the HCC and VCC are located.

3.1 Spherical measurement system (SMS) errors

3.1.1 General remarks

Before discussing the general requirements for a calibration standard, it is worthwhile reviewing generic errors associated with these instruments. There are two principal error source groups. The first are the environmental factors influencing the performance of these systems, and the second are the instrumental errors.

These sources of error can be grouped into those associated with the user, the instrumentation and the work piece. These three factors exist in the measurement environment which can itself have a significant effect on errors. The links between the different error sources are illustrated in Figure 3.1.

Errors can arise in the interaction between each of these factors. For example the user may set false parameters in the instrumentation, measure wrong positions on the work piece or use a target of an incorrect dimension. The work piece might move accidentally and unknowingly. The temperature of the environment may evolve over time influencing both the work piece size and the index of refraction. [43]

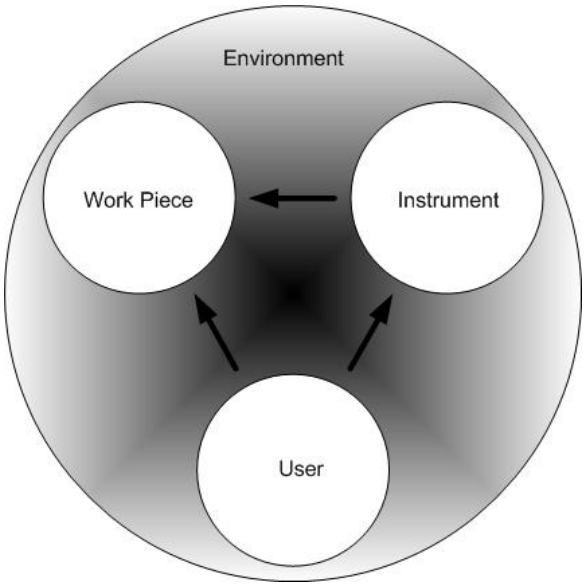

Figure 3.1 Interaction between the user, the instrumentation, the work piece being measured and the measurement environment. [43]

In this thesis we are specifically interested in errors in instrumentation. Environmental errors such as refraction effects will be discussed in more detail at the end of this chapter. User influences are not discussed.

Although they are conceptually different, laser trackers (LTs) and robotic total stations (RTSs) share many errors in common. There are three main instrumental error sources associated with SMSs; distance meter errors, angle errors and instrument construction errors.[4, 15, 32, 43-45] A schematic of these instruments and a catalogue of their principal errors are shown in Figure 3.2. The remainder of this section will be dedicated to a listing and discussion of the different errors associated with LTs and RTSs.

Distance meter errors are generally treated apart from angle errors. It is commonly thought, that angle errors are independent of distance. This is only partly true. At the ESRF, an angle dependence on distance for both RTSs and LTs has been observed. [4] This is discussed briefly in section 3.6. However, it is unlikely, but not proven here, that the observed angle dependence on distance varies as a function of horizontal or vertical circle reading. It is assumed that this error is a function of the instrument optical system and not related to the direction of observation. Therefore, in principle, there is no information loss treating these errors separately.

Although it would be desirable to treat all error sources together to give a true three dimensional error map, in practice, this is, at least at present, impractical. Construction errors are by their nature inseparable from both angle and distance meter errors and thus are treated as an integral part of each calibration.

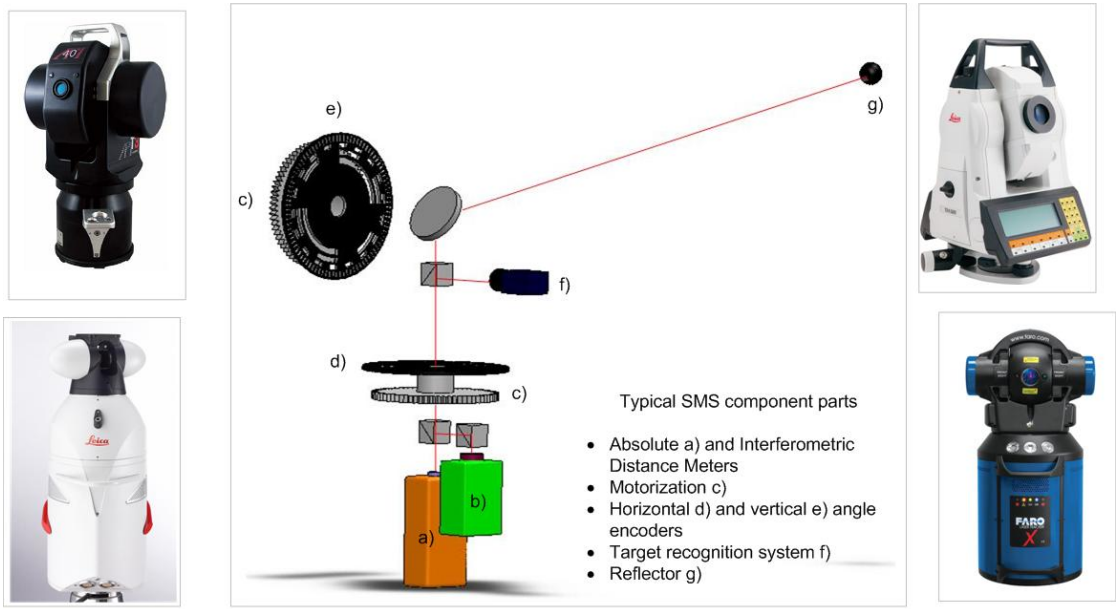

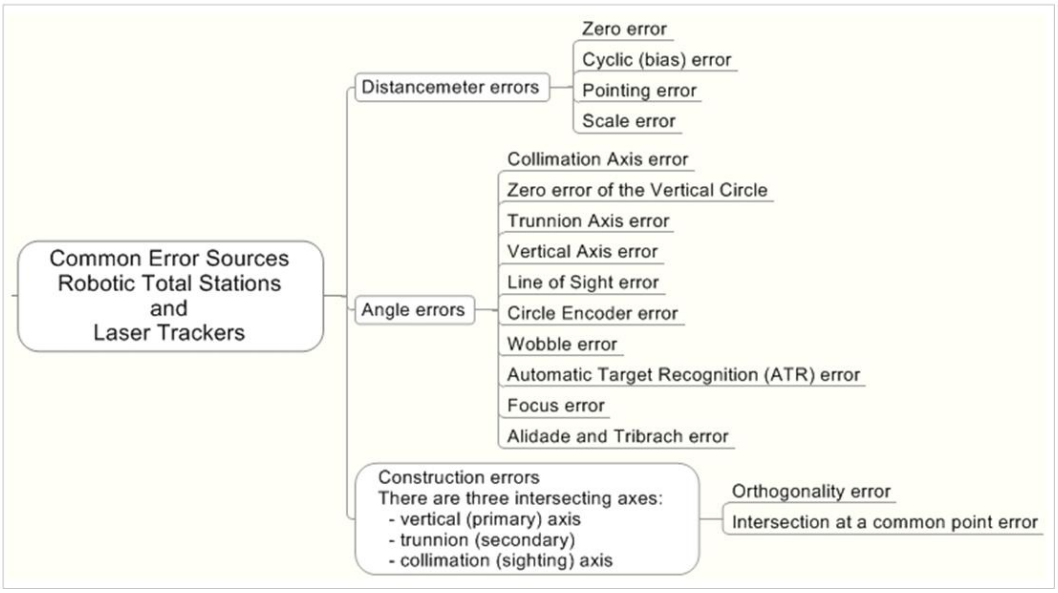

Figure 3.2 Schematic drawing showing the principal components in RTSs and LTs as well as a catalogue of the main errors associated with these instruments.

3.1.2 Construction errors

Spherical measurement systems are composed of a package of sub-assemblies that must be properly aligned and oriented in order for the instrument produce correct measurement results.

Most analytical models assume that horizontal and vertical angles as well as distances are measured with respect to a single, fixed, reference centre point somewhere within the instrument. Furthermore, the three axes (trunnion-X, collimation-Y, and vertical-Z) defining the instrument coordinate system must be orthogonal and meet at this point. In practice it is impossible to engineer such a solution and most instruments employ an internal mathematical model that renders raw observed data into horizontal and vertical angles and distance measurements based upon a set of calibration parameters that account small misalignments resulting from the instrument's design or construction. Common effects of such design or manufacture artefacts include collimation errors that affect angle measurements and index errors that affect distance measurements.

3.1.3 Distance meter errors

Electronic distance meters (EDMs) errors incorporated into LTs and RTSs are not the focus in this work. They are included here for two reasons; the first for completeness distance being a fundamental element of these instruments; and the second because their calibration gives a very good example of one of the main objectives of this work, namely, a calibration curve. There are three nominal types of EDMs used in these instruments. Laser trackers use interferometric (IFM) and absolute distance meters (ADM). Note that the terms IFM and ADM are industry denominations. RTS distance meters are simply referred to as EDMs. The principle differences between these instruments are in their mode of operation, the carrier wavelength of the light (electromagnetic radiation) used, and in their precision.

With EDMs integrated into RTSs, the distance is deduced by determining the phase difference between the transmitted and reflected (i.e. returned) beam of radiation. A carrier wave, typically in the near infra-red is, amplitude modulated by an oscillator. [17, 18] The laser tracker ADM measurement technique is also based on a systematic modulation of a light beam. There are different modulation methods which superimpose a periodic structure on the measurement beam. The ADM modulates the linear polarization of the laser light. Interferometers integrated into laser trackers are based on the heterodyne interferometer

principle whereby a polarized beam is split into two parts which travel different paths and are re-combined to create interference. Heterodyne interferometry is discussed in section 4.1.1.

Table 3.1 Principle of measurement, uncertainty and operating ranges of EDMs, ADMs and IFMs integrated into LTs and RTSs.

Electronic distance meter type	*Measurement principle*	*Typical maximum operating range (mm)*	*Representative uncertainties from different instrument manufacturers not including environmental effects*
EDM	Phase difference	6000000	0.5 mm + 2ppm
ADM	Modulation of polarization	30000	0.015 mm
IFM	Heterodyne interferometry	50000	0.001 mm

The advantage of interferometers is that they provide very precise distance measurements in a continuous stream. The disadvantage is of course that they can only measure relative distances. Laser tracker ADM distances meters, like EDMs measure absolute distances. They are typically used to re-initialize the interferometer (i.e. set the IFM distance datum) when interferometer laser beam has been lost and must be re-established. However, because of steadily improved precisions, and simplicity of use, ADMs are used more and more, and often in preference to the IFM.

There are four main distance meter errors: the zero error; the cyclic error (bias); the scale error and the pointing error. The zero error is the datum error for the zero value of the measurand (i.e. the difference between zero and the instrument reading at zero). The cyclic error is a systematic error characteristic of EDM instruments based on the phase measuring principle. They are periodic with wavelength typically equivalent to the fine measuring length of the modulation frequency of the carrier wave being used. Scale errors are caused primarily by the oscillator and by the emitting and receiving diodes. [17] Pointing error is due to the misalignment or non-coaxiality of the EDM signal and the collimation axis.

Of these four errors, it is common to calibrate the zero and cyclic errors. Note that these errors and their calibration apply to the distance meter and reflector pair. Pointing errors

should be adjusted for optimal instrument performance. Similarly scale errors due to modulation frequency variations should be generally calibrated and/or adjusted using a calibrated frequency meter.

All distance meters are calibrated in the same way. A good example of distance meter calibration is performed at the ESRF. [4] This will be discussed in more detail in section 3.3 below.

3.1.4 Angle errors

There are a large number of errors having an influence on the directions observed from RTSs and LTs. Most systematic angle errors can be reduced to negligible levels after theoretically eliminating first order effects. This is done by employing what is generally referred to as two face measurements. Two face (face left and face right) or forward and reverse instrument position measurements are a pair of observations to the same fixed point made in the two possible instrument positions. First a face left observation is made and then the instrument is rotated by 180º about both the trunnion-X and vertical-Z axes and a face right observation is made. Similarly, the errors associated with the automatic target recognition (ATR) or laser tracking instrumentation are corrected by observing the laser spot in different positions on the CCD or PSD image sensor. These errors are typically corrected automatically by onboard software using parameters derived from a series of manufacturers recommended test measurements made outside of the normal operation. Finally other errors linked to the servo motion of the instrument about its axes (e.g. wobble error) are corrected in real time with onboard inclinometers and compensators.

All errors with parameters that can be derived from self testing and onboard software are corrected for. Some residual errors do remain. These errors have three sources. The first are simply random errors; the second are due to drifts in the parameter values during normal instrument operation and between self testing operations; and the third are uncorrected systematic errors such as those shown in the distance meter calibration curves of Figure 3.4 below. It is the characterisation of these latter type errors that is of interest.

3.1.4.1 Collimation Axis Error

The line of collimation must be perpendicular to the trunnion axis. The axis has to move in a plane at right angles to the trunnion axis while tilting the RTS telescope or LT mirror. If this condition is not fulfilled, a collimation axis error exists. The collimation axis error is composed of two parts, the horizontal collimation and vertical collimation axes errors. The effect of a vertical deviation of the collimation axis is constant. It is impossible to determine separately a vertical collimation axis error and a zero error of the vertical circle. Thus, the term collimation error refers only to the horizontal deviation of the collimation axis, while the vertical deviation is a component of the zero error of the vertical circle. Averaging face left and face right readings and/or software reduces this error to negligible or second order levels.

3.1.4.2 Zero Error of the Vertical Circle

A zero error of the vertical circle occurs if the reference direction of the theodolite vertical circle (corresponding to the zero point) is not parallel to the vertical axis. This error will cause all vertical (zenithal) angles to be measured too small or too large according to the sign of the error. Averaging face left and face right readings and/or software reduces this error to negligible or second order levels.

3.1.4.3 Trunnion Axis Error

The deviation of the trunnion axis from a plane perpendicular to the vertical axis is known as the trunnion axis error. The vertical circle will no longer be in a vertical plane and angles will be measured with respect to a false zenith. Averaging face left and face right readings and/or software reduces this error to negligible or second order levels.

3.1.4.4 Vertical Axis Error

The vertical axis error is not an instrumental error, but indicates an incorrect set-up. This occurs, when the vertical axis is not precisely vertical. Modern instruments with built-in compensators reduce the influence of a vertical axis error to negligible or second order levels.

3.1.4.5 Line of Sight Error

The collimation line of sight of axis has to intersect the trunnion axis. If this condition is not fulfilled, an error is present. Averaging face left and face right readings and/or software reduces this error to negligible or second order levels.

3.1.4.6 Circle Encoder Error

Both the horizontal and the vertical encoders must be in a plane at right angles to the vertical axis and the trunnion axis. Furthermore the centre of the horizontal encoder must be aligned with the vertical axis. Similarly, the centre of the vertical circle must be aligned with the trunnion axis. If these conditions are not met, an error is introduced. Averaging the readings at the forward and reverse positions and/or software eliminates this error. Furthermore modern instruments make a complete scan of the encoder circle reducing the effect of the non-perpendicularity of the two circles to negligible or second order levels.

3.1.4.7 Wobble Error

The rotation of the theodolite around the vertical axis causes a wobble error. In relation to the measured object, the inclination of the vertical (Z) axis changes for each observation. For precise angular measures, the wobble error has to be measured simultaneously with the direction measurement, and of course eliminated by its addition to circle reading. In modern instruments, the compensator reduces the wobble error to negligible or second order levels.

3.1.4.8 Automatic Target Recognition (ATR) Error

The ATR system transmits a laser beam that is reflected by a SMR and received by a built-in CCD camera. The position of the received light spot is computed and results in two computed offsets that are used to correct the horizontal and vertical angles. Automatic target recognition errors are reduced to negligible or second order levels by internal software.

3.1.4.9 Focus Error

RTSs are equipped with pan-focal telescopes with a continuous range of lens settings to obtain sharp images of close and distant targets. Due to the movement of the internal focusing lens, the geometrical and optical characteristics of the telescope change with respect to the

focus setting. For instance, when the focusing lens is moved, different components are changed notably the image scale, the optical distortion, and the collimation axis.

3.1.4.10 Alidade and Tribrach Error

When the theodolite vertical axis is not aligned with the centre of the tribrach axis, a default exists. It is an assembly error and cannot be compensated. It is only important if a forced centring system is being used.

3.2 DCB, HCC and VCC selection criteria

Instruments designed to calibrate horizontal RTSs and LTs must fulfil a certain number of criteria. Foremost among these criteria is traceability. Although not formally a prerequisite, it is highly desirable that the instrument have a smaller uncertainty than the instrument being calibrated. Available LTs and RTSs have manufacturers stated angle uncertainties ($k = 1$) in the order of 2 arc-seconds and 0.5 arc-seconds respectively. Therefore, ideally the expanded ($k = 2$) uncertainty should be (considerably) less than 0.5 arc-seconds. Precise (e.g. 1 arc-second) positioning is not essential, but the angle standards must be capable of setting its position and measuring over the full 360º circle. Finally, the specifications set out by Ingensand [34] in section 2.4.1 remain valid; in particular, the possibility of an automatic test sequence, calibration of the instrument over its full measuring range, suitability for various RTS and LT models, and the qualification of both vertical and horizontal angle reading systems are essential attributes to fulfil.

Recall there are three main components in these instruments; the distance meter (EDM, ADM, and/or IFM), the horizontal circle and the vertical circle. Other parts such as the compensator are calibrated with these components. Ideally we might want a standard that could measure these three components simultaneously to produce a 3D error map. Practically this is difficult, if not impossible. To physically investigate all possible angles and distances that could be measured naturally (i.e. horizontal angles over ±180 degrees; vertical angles over ±45 degrees; and distances up to 50m), one would require a type of igloo shaped laboratory 100 m in diameter and 70 in height. Everything involved with this laboratory

would certainly be colossal; not least the structural, the air conditioning and the cost considerations. Clearly some compromise must be made.

In the present work, the decision has been made to separate their calibration. The EDMs, ADMs, and/or IFMs are calibrated on the 50 m long ESRF DCB. The horizontal circles are calibrated with the HCC and the vertical circles are calibrated using the VCC. All three of these standards are traceable to the SI unit, the metre. Apart from this, the selection of the standards and techniques described in the following are dictated mainly by instrument constraints (e.g. minimum measurement distance), available resources (e.g. laboratory space, instrumentation etc…) and financial constraints.

3.3 EDM, ADM and IFM distance meter calibration

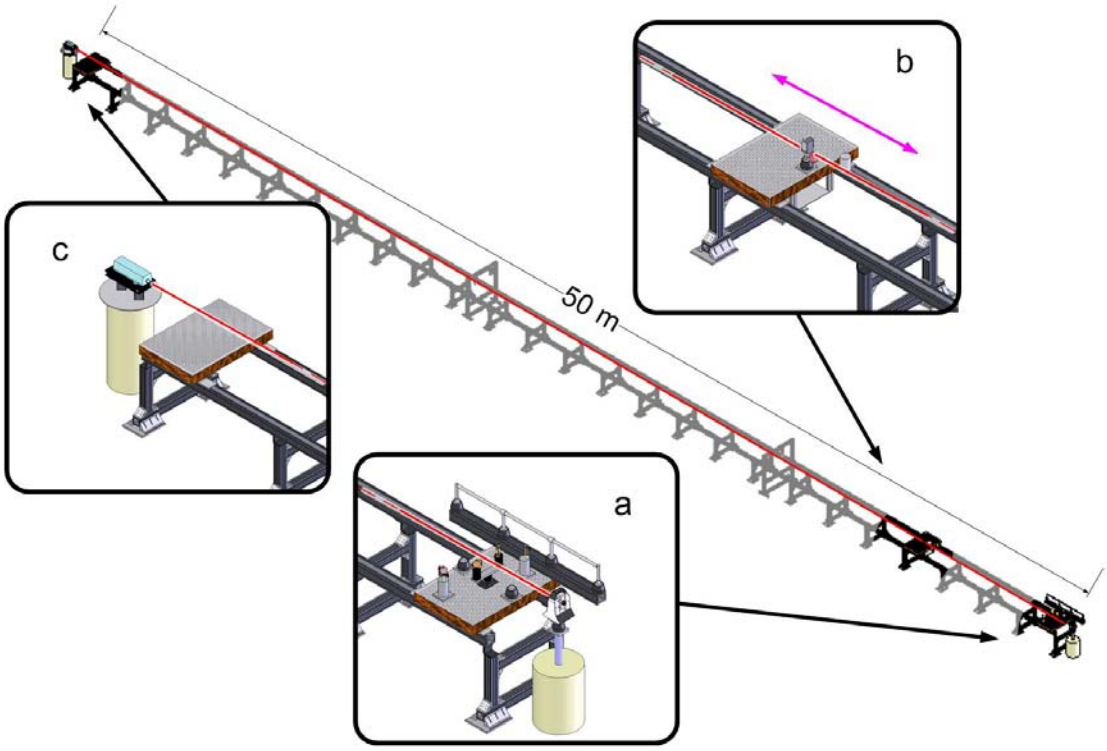

Figure 3.3 Schematic of the ESRF calibration bench. Zoom a) is the instrument station; zoom b) the servo carriage with the instrument and interferometer reflectors and zoom c) the interferometer station. After the zero error has been determined the servo carriage is moved in 10 cm intervals from 2 m to 50 m to determine the instrument cyclic (bias) error. (Drawing prepared from Solid Works design drawings made by B. Perret)

The ESRF has a 50 m long calibration bench (refer to Figure 3.3). An interferometer is installed on a fixed pillar at one end of the bench and the instrument to be measured (RTS or LT) is installed on a fixed pillar or heavy tripod at the other end. The interferometer and

instrument reflector are installed on a servo-controlled carriage. The bench is equipped with an accredited meteorological station which measures temperature, pressure and humidity. Additional temperature sensors are installed at regular intervals along the length of the bench to improve corrections for the variations in refraction along the line of sight.

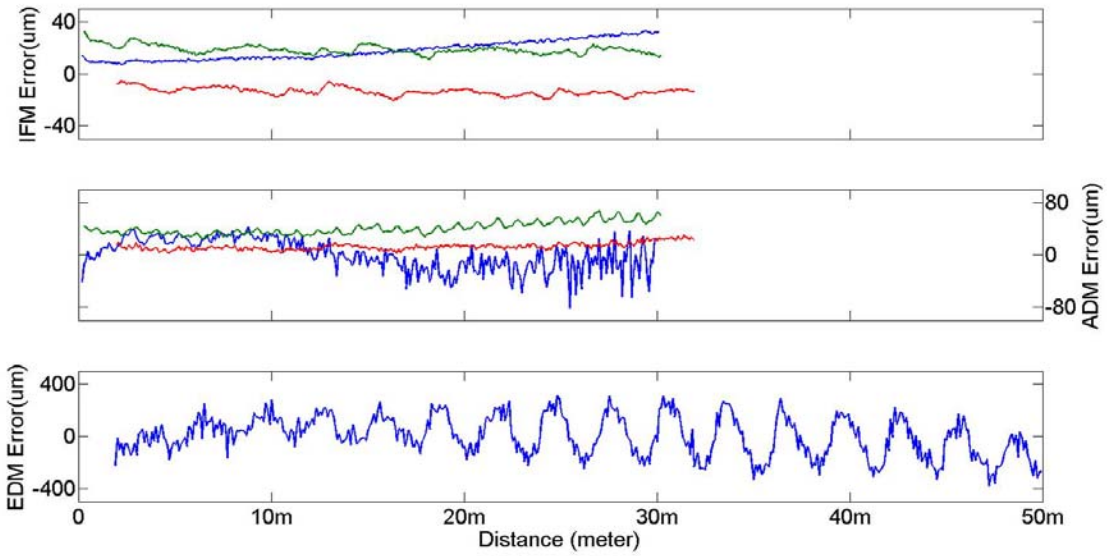

Figure 3.4 Typical Interferometer (IFM), Absolute Distance Meter (ADM) and EDM distance error curves. Different curves are from different instruments. The IFM and ADM curves are from three different instrument manufacturers. The EDM curves are three instruments of the same manufacturer and type. The expanded uncertainties ($k = 2$) in these calibration curves are 0.050 mm for the IFM and ADM curves and 0.165 mm for the EDM curves.

A typical calibration comprises the determination of the zero (index) error, followed by the determination of the cyclic (bias) error by comparison of measured distance displacements with the accredited laser interferometer. Distances are measured by moving the servo-carriage at regular 10cm intervals along the bench. This results in a calibration curve - an example of which is shown in Figure 3.4. This curve can be modelled and applied to considerably improve field measurements. At the ESRF, the enlarged uncertainty for these calibrations is 0.17 mm for a 2m to 50m EDM calibration with an instrument resolution of 0.1 mm; and 0.05 mm for a 0.3 to 50 m LT ADM or IFM calibration.[4, 44]

3.4 Horizontal angle calibration

Horizontal angles are calibrated against the horizontal circle comparator or HCC. The HCC is composed of a reference plateau, a rotation table, and an angle acquisition system (refer to

Figure 3.5). The conception and choice of composite parts of the HCC was made by the author, although several colleagues contributed to design detailing.

The reference plateau is fixed on the rotation table and rotates with it. The heart of the HCC is the angle standard. This standard, the angle acquisition system, or linked encoders system (LEC) is incorporated into the rotation stage. Each of these systems will now be discussed in turn.

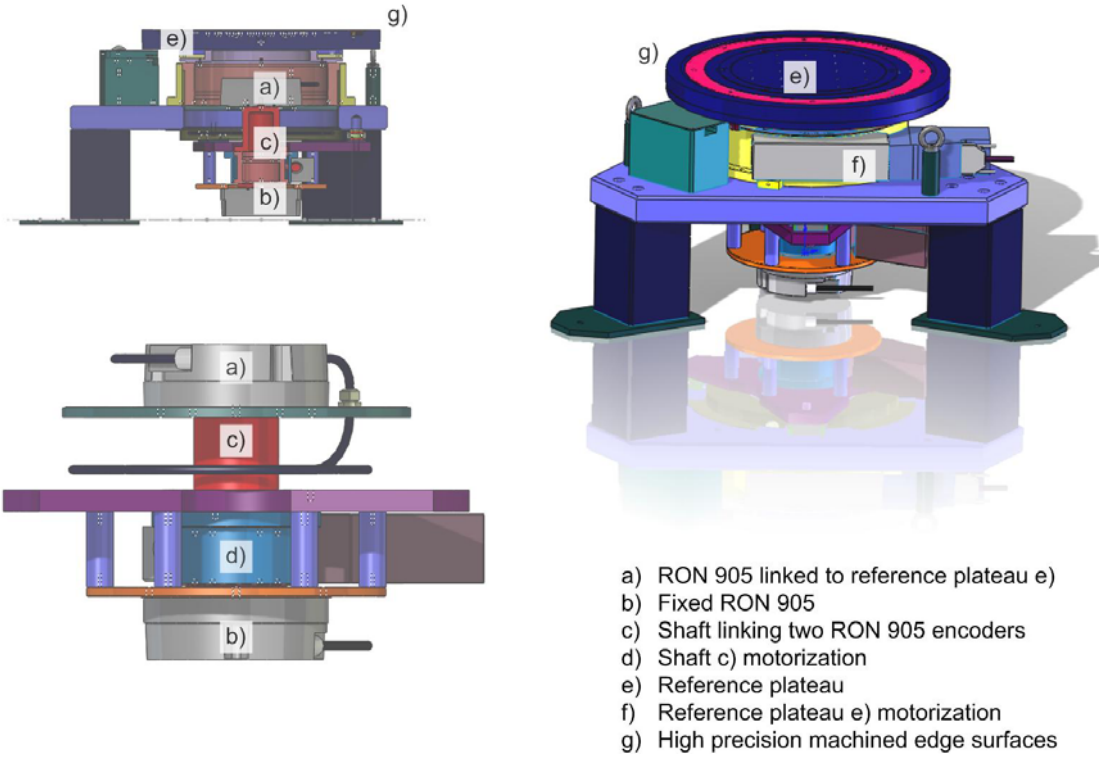

Figure 3.5 Schematic of the HCC assembly showing reference plateau e), the rotation table f) and the LEC system a), b), c), and d).

3.4.1 The Reference plateau

The reference plateau e) in Figure 3.5 is a stainless steel 500 mm diameter 40 mm thick plate. It has a regular grid of M6 threaded holes for fixation. There is a 20 mm bore in its centre. This bore is used for the forced centring of instruments installed on the plateau. Finally there is a high precision machined surface 20 mm wide around the circumference; both on the side and on the top edges. These surfaces, shown as g) in Figure 3.5 above act as targets for the capacitive probes used in the determination of the plateau wobble, or inclination, and eccentricity movements.

At the origin, the primary reason a 500 mm diameter was chosen was to permit the installation of a hydrostatic levelling system (HLS)[8][45, 46]. Although provision was made for the system, it has as yet, not been used. The idea was to be able to measure both the inclination of the plateau and its movement with respect to an exterior reference point. This would provide a high precision standard fully referenced to the gravity system. The 500 mm diameter base line provided is sufficiently large this type of work. It is the author's intention to ultimately activate this system.

3.4.2 Rotation stage

The plateau and angle acquisition system are installed on a Micro-Controle RV350CC high-performance precision rotation stage (f in Figure 3.5). The stage has the following manufacturer's quoted performances: minimum incremental motion 0.001º; absolute positional accuracy 0.005º; wobble 16 μrad; eccentricity error 4 μm; maximum rotation speed 80º per second. An important choice in the employment of this particular rotation stage is its normal centred load capacity of 6500 N. This ensures that any LT or RTS instrument commercially available on the market can easily be accommodated.

3.4.3 Angle Acquisition System - Linked Encoders Configuration (LEC)

Although commercially available encoders can provide uncertainties in the order of 0.5 arc seconds ($k = 1$)[9], the target of the LEC system is to provide a standard with an expanded uncertainty (i.e. $k = 2$) in the order of 0.1 arc seconds or better. In principle, the LEC is capable of reducing residual error in the already excellent commercially available angle encoders to negligible levels.

The LEC uses two Heidenhain RON 905 angle encoders mounted in juxtaposition. One RON 905 is fixed to the main support assembly and does not move. The second RON 905 body is fixed to the main plateau and rotates with it. The two RON 905 encoders are linked

[8] The author has written several papers on the HLS installation at the European Synchrotron Radiation Facility. The first reference provides an overview of the ESRF systems and references to earlier works concerning them. The second reference provides a thorough theoretical and practical review of HLSs.
[9] See for example the Renishaw RESR angle encoder system with a manufacturers stated uncertainty of 0.5 arc seconds (http://www.renishaw.com/); or the Heidenhain RON 905, actually used in this work, with a manufacturers stated uncertainty of 0.4 arc seconds (http://www.heidenhain.com); both accessed November 2008.

through a precision alignment shaft assembly. The shaft and encoders are rotated continuously by Micro-Controle RV120CC high-performance precision rotation stage (c in Figure 3.5). Although the maximum speed of the RV120CC is 80 degrees per second, it is typically operated at 20 degrees per second, thus taking 18 seconds to rotate through 360 degrees. The two RON 905 encoder positions are read out simultaneously and continuously. This assembly, referred to as the LEC for the linked encoders configuration can reduce considerably, or even theoretically eliminate altogether, the residual RON 905 encoder errors. [47, 48]

3.4.3.1 System Encoder Errors

For the encoder system output to reflect the actual rotary motion of the HCC plateau, each of the following points must be respected [49]:

- Each part of the system must rotate in its bearings without radial run out (i.e. lateral motion) of its axis of rotation.
- The shaft system connecting the main plateau (e in Figure 4) to the encoders (a and b in Figure 4) should be rigid in torsion.
- The coupling should be designed such that the angular motion of the encoder rotating in its bearing is the same as that of the plateau rotating in its own bearing system.
- The spacing of the lines around the edge of the encoder scale should be uniform and the read-head should interpolate between them in a linear manner.
- The encoder scale should be truly circular with the axis of rotation passing perpendicularly through its centre.
- The read-head should read the scale without parallax or other geometric error and be rigidly mounted to the non-rotating frame of reference.

If any of the above is not true there will be an error between the angular position of the plateau and that reported by the encoder system. Most of these errors, including bearing wander, coupling errors and the effect of scale eccentricity and distortion, are reduced considerably using multiple read-heads. Heidenhain, the manufacturer of the RON 905, gives its angle uncertainty as 0.4 arc-seconds. The remaining errors below this threshold can be reduced again using the LEC.

3.4.3.2 The RON 905 Incremental Angle Encoder and the Photoelectric Scanning Principle

The RON 905 Angle encoder incorporates measuring standards made of periodic structures known as graduations. These graduations are applied to a glass substrate. The precision graduations are manufactured from a photolithographic process referred to as DIADUR™ which is characterized by a high definition and homogeneity of the line edges. This process produces gratings with a period of 10 μm. Together with the photoelectric scanning process described below, this high edge definition is a precondition for the high quality of the output signals.

The photoelectric or image scanning principle is based on two scale gratings with equal grating periods; the circular scale is moved relative to the fixed scanning reticule. Parallel light is passed through the gratings, projecting light and dark surfaces onto a photoelectric detector. When the two gratings move relative to each other, the incident light is modulated. If the gaps are aligned, light passes through. On the other hand, if the lines of one grating coincide with the gaps of the other, no light passes through. Photocells convert these variations in light intensity into nearly sinusoidal electrical signals. ([50], refer also to Figure 3.6)

The RON 905 circular scale has 36000 gratings. One signal period corresponds to 0.01 degree or 36 arc-seconds. Interpolation of the varying intensity sinusoidal signals over the 0.01 degree grating period permits the extremely high angle resolution of the RON 905. Heidenhain guarantees a signal quality of ± 1%. This corresponds to maximum position deviations within one signal period of approximately 0.0001 degree or 0.36 arc seconds.

The RON 905 encoder is equipped with 4 read-heads located at 90 degree intervals around the circular scale. Each of the read-head outputs a signal that has a 90 degree phase difference with respect to its neighbour. Read signals at opposite sides of the encoder circle are 180 degree out of phase (i.e. when one of the read signals is null; the other is maximum and vice versa).

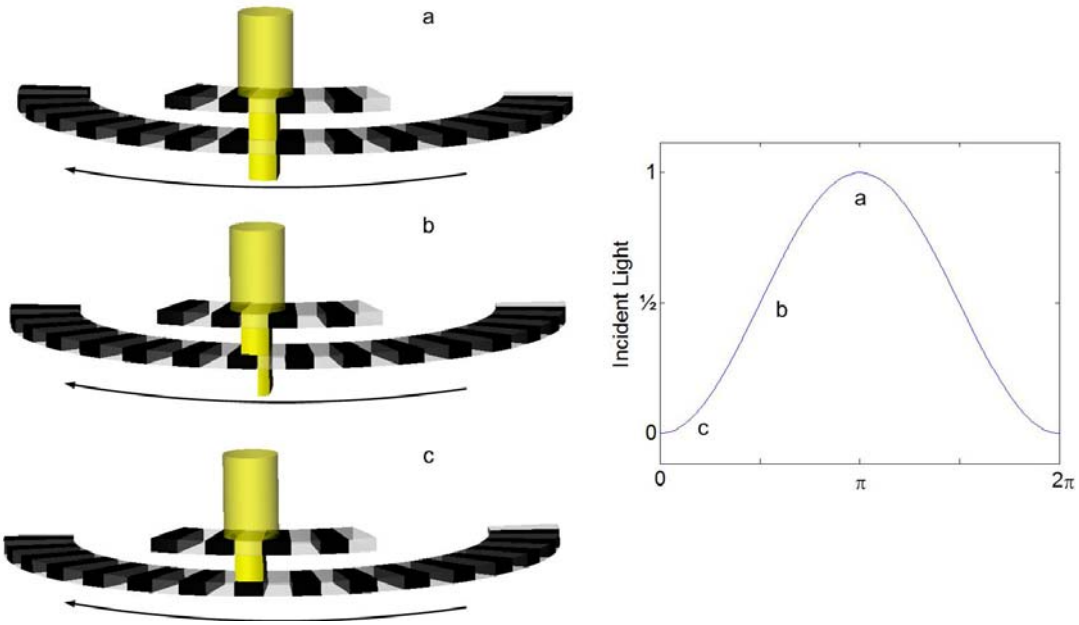

Figure 3.6 The photoelectric or image scanning principle used with the RON 905 angle encoders is based on two scale gratings with equal grating periods; the circular scale is moved relative to the fixed scanning reticule. Parallel light is passed through the gratings, projecting light and dark surfaces onto a photoelectric detector. When the two gratings move relative to each other, the incident light is modulated. If the gaps are aligned, light passes through, while, if the lines of one grating coincide with the gaps of the other, no light passes through. Photocells convert these variations in light intensity into nearly sinusoidal electrical signals.

It should be noted that strictly speaking, just two detectors 90 degrees out of phase can give the quadrature signals for the Lissajous figure. Two read heads are also sufficient to eliminate the important first harmonic error. It is not entirely clear why the RON 905 employs four read heads. Other reputable high precision angle encoder manufacturers use only two read heads citing "Use of two read heads will remove errors due to eccentricity and all other odd harmonics. Four read heads have been employed in some installations to good effect, but more give progressively lower return on investment; careful selection of the ring cross-section offers a more powerful way of limiting the higher distortion harmonics."[49, 51] [52] states that the use of four scanning units with the Heidenhain ERO 7001 system permits the elimination of up to harmonic order two distortion errors. Finally, the PTB angle standard manufactured by Heidenhain, as is the RON 905, uses 16 read heads. This is mainly for auto-calibration but eight read heads are disposed in such a way as to eliminate higher harmonic errors.[21, 22]

The two output signals are generated by subtracting one of the two 180 degree out of phase signals from the other (i.e. . $I_1 = I_{0°} - I_{180°}$ and $I_2 = I_{90°} - I_{270°}$). Thus when the grating disk

is rotated, two nearly sinusoidal signals are issued from the RON 905 encoder. These signals (I_1 and I_2) are themselves 90 degree out of phase. They form the parametric equations/ quadrature signals ($x = \cos\gamma$ and $y = \sin\gamma$) describing a lissajous or circle. The interpolated angle function α_{RONi} given by $\alpha_{RONi} = \tan^{-1}(x/y)$ is proportional to the position within one grating (i.e. $\alpha/2\pi \times 36$ arc-seconds) of the RON 905 encoder disk. [53] Figure 3.7 shows the generation of the four read head signals during a movement of the encoder disk. Note for clarity, the following symbols will be used for the following angles:

- γ will be used for the RON 905 quadrature signals,
- α_{RONi} will be used to designate the interpolated RON 905 angle function associated with one of the two RON 905 angle encoders (i.e. $i = 1$ or 2),
- θ is used to represent the rotation of the HCC plateau and Micro Controle RV350 rotation table,
- φ will be used in the next and subsequent chapters to designate the angles separating adjacent probes in the form error – spindle motion error (FESM) separation technique.

A third signal for the reference mark defining the encoder disk zero is also simultaneously output from the RON 905. However, this reference is not used in this work for technical reasons associated with the NI-PCI-6115 A/D card used in data acquisition. This card only has four input channels which is just sufficient for the four RON 905 quadrature input signals (i.e. two for each RON 905) used in the LEC configuration discussed in section 3.4.3.3 below. To determine the absolute position on the disk with respect to the position at start up in this application, either one must count the number of $\cos\gamma$ and/or $\sin\gamma$ periods traversed, or use the RV350 rotation stage absolute encoder. This is discussed in more detail in section 3.4.3.4 .

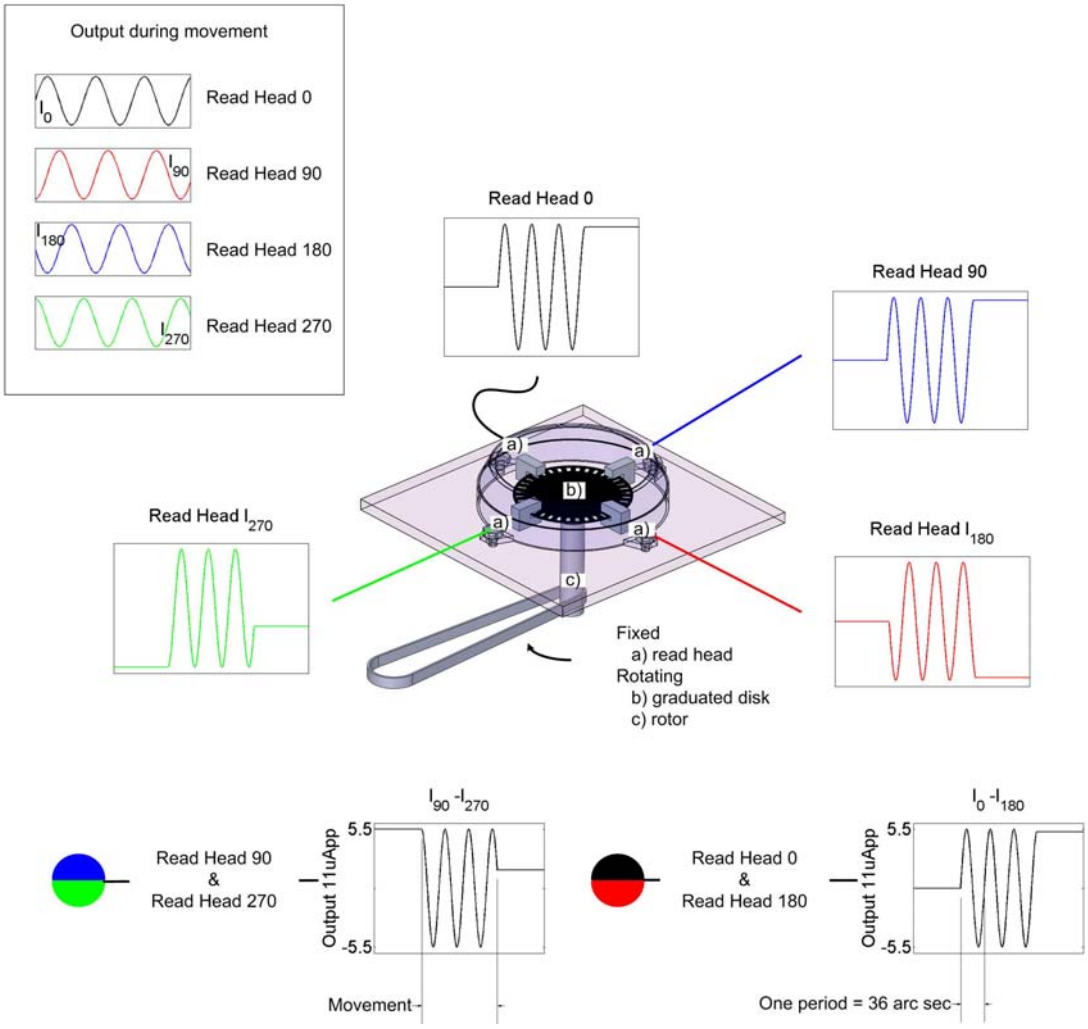

Figure 3.7 Four signals from the four read heads located at 90 degrees intervals around the encoder grating disk are generated by the RON 905. When the rotor shaft, linked to the graduated disk is rotated, these read heads 'see' four sinusoidal signals 90 degrees out of phase. This is illustrated in the upper left hand box. The two signals on opposite sides of the circle (I_0, I_{180} and I_{90}, I_{270}) are subtracted from each other giving the two signals 90 degrees out of phase shown at the bottom of the figure. These two quadrature signals are used to determine the interpolated angle function α_{RONi} .

3.4.3.3 The LEC output signals

The aim of the LEC is to reduce residual error in the already excellent commercially available angle encoders to negligible levels. To this end, the LEC uses two Heidenhain RON 905 angle encoders mounted in juxtaposition; one fixed to and motionless with the main support assembly; and the second rotating with the main plateau. The two RON 905 encoders are linked through a precision alignment shaft assembly. The shaft and encoder grating disks are rotated continuously by a Micro-Controle RV120CC precision rotation stage. Thus the output from the LEC is composed of two continuously oscillating sets of quadrature signals

(i.e. $(\cos\gamma,\sin\gamma)_{\text{RON1}}$ and $(\cos\gamma,\sin\gamma)_{\text{RON2}}$). This is illustrated in Figure 3.9 showing the RON signals input from the plateau RON 905 (RON1) and the fixed RON (RON2).

Under normal operation, the plateau RON 905 (RON1 Figure 3.9 at top) and fixed RON 905 (RON2 at bottom) output one set of quadrature ($v_1 = \cos\gamma$ and $v_2 = \sin\gamma$) signals each. These signals are combined to determine the interpolated angle functions α_{RON1} and α_{RON2} using the arctangent (i.e. $\alpha_{RONi} = \tan^{-1}(v_1/v_2)$); which produces the classical saw tooth function graph. This saw tooth function is re-dressed by so-called unwrapping the phase[10] which produces a continually increasing (or decreasing) straight line function of α_{RONi} associated with the rotating RON 905 encoder disk. Because the two RON 905 encoder grating disks are rigidly connected, the slopes of lines associated with these increasing linear angle functions α_{RON1} and α_{RON2} are parallel. In the ideal case, subtracting α_{RON2} from α_{RON1} leaves a straight horizontal line with value (i.e. the y intercept) equal to the difference between α_{RON1} and α_{RON2}.

In reality, there are small departures from the ideal straight lines and the subtraction leaves residual angle errors associated with the LEC configuration and its two RON 905 encoders. In principle averaging $\alpha_{RON1} - \alpha_{RON2}$ over a full rotation of the encoder grating disks will eliminate or reduce to an insignificant level the effect of these residual angles. This will be discussed in more detail in 3.4.3.4 below. Note that typically $\alpha_{RON1} - \alpha_{RON2}$ is referenced to some zero. For example we can subtract the difference at some time t from the difference at start up (i.e. $(\alpha_{RON1} - \alpha_{RON2})_t - (\alpha_{RON1} - \alpha_{RON2})_{startup}$). This is illustrated in Figure 3.8 below.

[10] Unwrapping the phase in this sense consists of correcting or redressing the phase angles by adding multiples of $\pm 2\pi$ when absolute jumps between consecutive elements are greater than or equal to a default jump tolerance – typically π radians

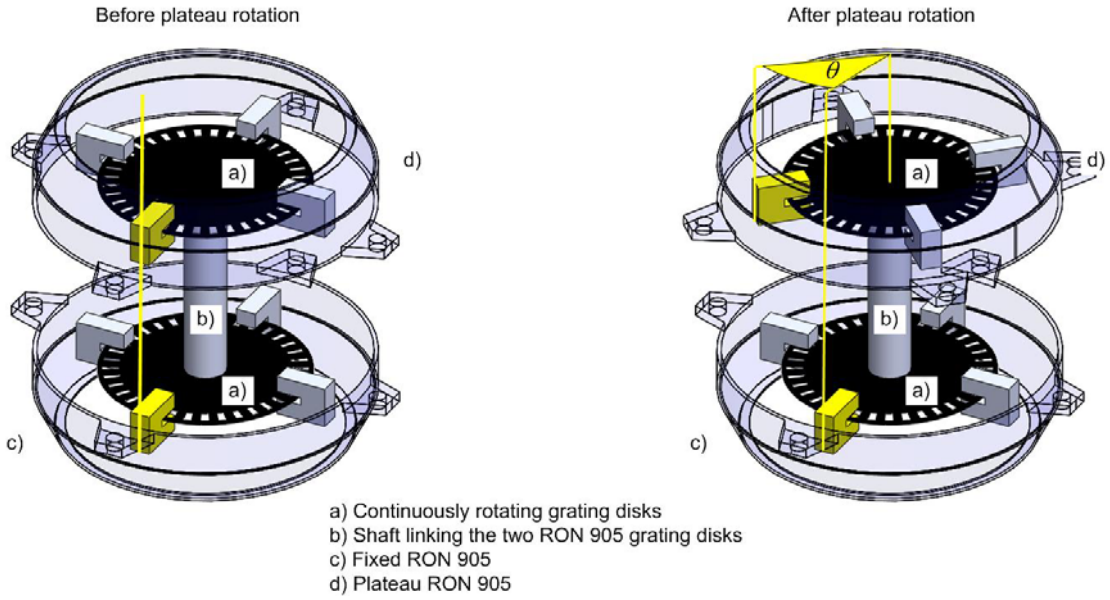

Figure 3.8 When the plateau is moved through an angle θ, its RON 905 encoder (d), and four read heads, move with it through the same angle (right hand image). Recall that the encoder gratings (a) are in continuous rotation.

For the following discussion please refer to Figure 3.8, Figure 3.9 and Figure 3.10. When the plateau is rotated through a given angle θ [11], its RON 905 and associated read heads are also moved with it through the same angle (see Figure 3.8). This will induce a change in velocity of the RON1 read heads with respect to the 'constant' velocity (e.g. 20 degrees/second) static situation shown in Figure 3.9; and with respect to the still static fixed RON2 read heads. During the movement, there will be a compression, or elongation (i.e. frequency modulation); depending on the plateau rotation direction relative to the rotation direction of the encoder grating disks, of the plateau RON 905 quadrature signals. This frequency modulation shown in the quadrature signals of Figure 3.10, will in turn impose a change in slope of α_{RON1}. When the movement stops, the situation will return to the static state shown in Figure 3.9. However, there will be a net change in the separation distance between the slopes of α_{RON1} and α_{RON2} corresponding to the angle moved. Because each period of the quadrature signals corresponds to one graduation or 36 arc-seconds, each change of 2π in the $\alpha_{RON1} - \alpha_{RON2}$ will correspond to an angle movement of 36 arc-seconds. For

[11] It is important to avoid confusion in the difference between the plateau rotation angle θ, and the LEC angle α. The plateau rotation angle θ is a classic rotation with 360 degrees representing a full circle closing upon itself. The LEC signal output represents the arctangent function of the quadrature signals over one encoder grating. It also has an output of 0 to 360 degrees. However in this case 360 degrees represents 36 arc seconds of the plateau rotation θ.

example an angle difference on the right hand graph of Figure 3.10 of -7.81-(-1.47) radians or -6.35 will correspond to a plateau rotation $(-6.35/2\pi)\times 36$ or -36.38 arc seconds. One final point, although not visible (at right of Figure 3.10), the residual angle errors associated with the LEC and its two RON 905 encoders will still be present.

3.4.3.4 LEC residual errors

If we consider that: firstly the two RON 905 encoder circles are rigidly connected to one another and thereby rotate synchronously, secondly, the rotation is at a constant velocity, and thirdly the two encoder disks are perfect; then their unwrapped angle functions α_{RON1} and α_{RON2}, in Figure 3.9 will increase or decrease in parallel. This is not generally the case so there will be deviations around this ideal straight line.

In so far as the rigidity of the link between the two encoders is concerned; instantaneous movements of the gratings with respect to one another are expected to be negligibly small. However, experience has shown there are longer term drift movements, particularly after a start-up or after a period of several hours of inactivity. The Micro-Controle RV120CC rotation stage is not perfect and so there are small speed variations. However, because the two encoders are rigidly linked, at least in the short term sense, these variations will not affect the parallelism of the α_{RON1} and α_{RON2} ; rather their instantaneous slopes will vary, and so the theoretical straight line conditions will not apply. Finally, the RON905 encoder gratings are not perfect. They have manufacturer's quoted maximum position deviations within one signal period of approximately 0.0001 degree or 0.36 arc seconds. It is these grating errors, at least over the short term, that will in principle dominate the magnitude of the residual errors shown in the far right graph of Figure 3.9. Real errors with the LEC are considered in section 5.2. However we first we will discuss how to quantify these errors.

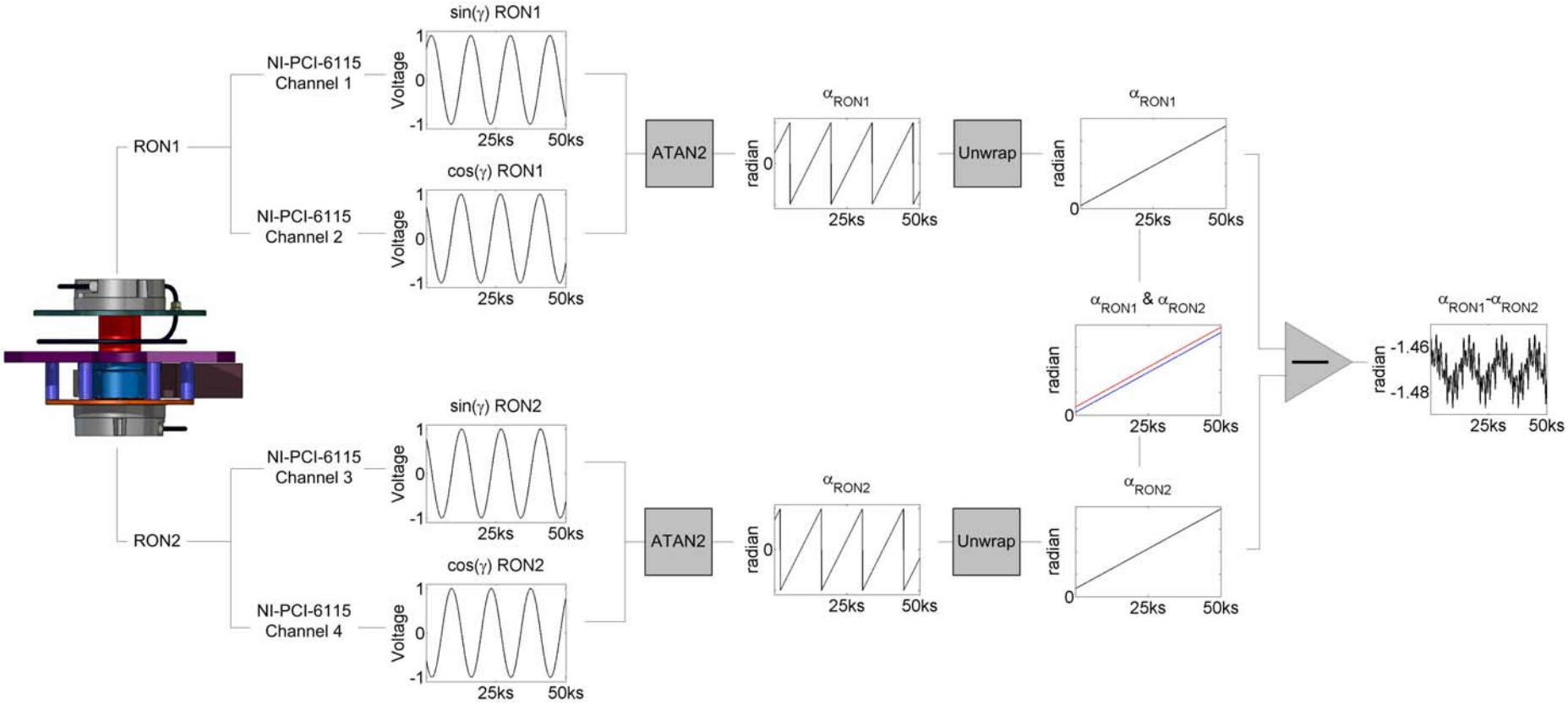

Figure 3.9 Under normal operation (i.e. continual rotation of the encoder gratings), the plateau RON 905 (RON1 at top) and fixed RON 905 (RON2 at bottom) output one quadrature ($v_1 = \cos\gamma$ and $v_2 = \sin\gamma$) signal each. Each period of these signals corresponds to the passage of one RON 905 encoder grating which is equivalent to 36 arc-seconds of rotation. These signals are combined (ATAN2) to give an angle $\alpha_{RONi} = \tan^{-1}\left(v_1/v_2\right)$ producing the classical saw tooth arctangent (i.e. $-\pi$ to π) function α_{RON1} and α_{RON2}. These signals are redressed by unwrapping the phase (Unwrap) which gives a line whose slope is a function of the speed of rotation of the gratings. Because the two encoder grating disks are rigidly connected, the slopes of the two lines are parallel. Subtracting one line from the other leaves residual angle errors associated with the LEC and its two RON 905 encoders (at far right).

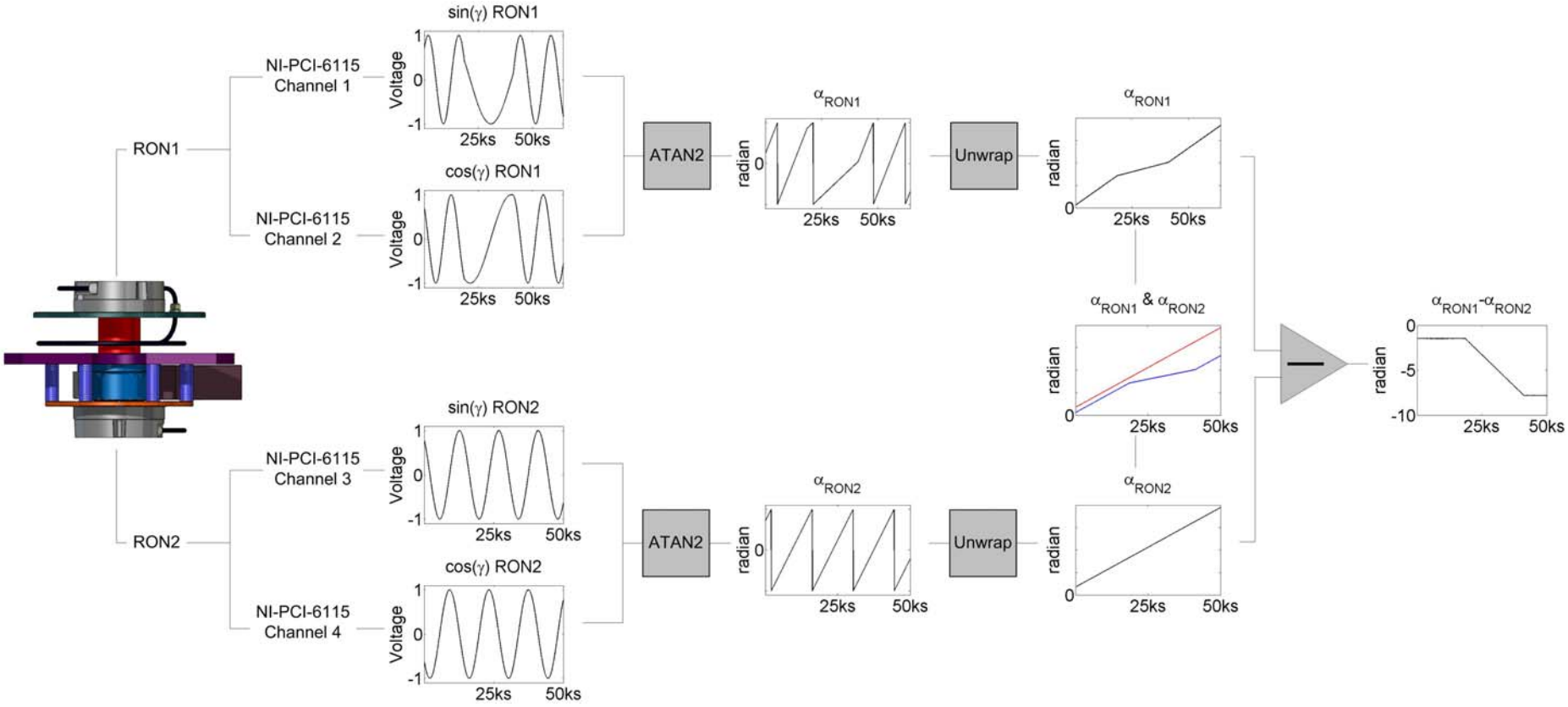

Figure 3.10 When the plateau is moved, the attached RON 905 (RON1), as well as its read heads, also move with it (refer to Figure 3.8). This will induce a change in velocity of the RON1 read heads with respect to the static situation (Figure 3.9) 'constant' velocity (i.e. 20 degrees/second), and with respect to the still static RON2 read heads. This will lead to a frequency modulation of the RON1 quadrature signals and to a change in slope of α_{RON1} while the plateau is in motion. When the movement stops, the situation will return to normal shown in Figure 3.9. However, there will be a net change in the separation distance between the two lines associated with α_{RON1} and α_{RON2} corresponding to the displacement angle. Although not visible (at right), the residual angle errors associated with the LEC and its two RON 905 encoders will still be present.

First, we consider the LEC residual errors are smooth and continuous. Secondly, we will consider that even if the function $\alpha_{RON1} - \alpha_{RON2}$ does not repeat itself after one full rotation, the error at zero will be the same after every revolution. This is to say:

$$\left(\alpha_{RON1} - \alpha_{RON2}\right)_0 - \left(\alpha_{RON1} - \alpha_{RON2}\right)_{i\times 2\pi} \cong 0 \text{ for all } i \text{ under consideration}$$

These assumptions will be investigated in detail in section 5.2 and shown to be essentially true. Given these assumptions we may represent the residual error function $\Delta\alpha_{RON}$ over one rotation of 2π radians by a Fourier series as in (3.1).

$$\begin{aligned} \Delta\alpha_{RON} &= \alpha_{RON1} - \alpha_{RON2} \\ &= \frac{a_0}{2} + \sum_{n=1}^{\infty}\left(a_n \cos\left(nt\right) + a_n \sin\left(nt\right)\right) \end{aligned} \tag{3.1}$$

The advantage of using this representation is that the sum of the cosine and sine terms, which represent the residual errors, is 0; and so the angle moved is given by the DC part $a_0/2$ of the Fourier series. The DC part of a Fourier series is simply the mean value of the constituent parts. As one final note, we will want to reference this value to some arbitrary zero value. Thus the angle movement registered by the LEC is given by (3.2) where $i\times 2\pi$ represents some 2π rotation indexed by i with respect to the $zero$ rotation.

$$\begin{aligned} \Delta\alpha_{RON} &= \left(\frac{a_0}{2}\right)_{i\times 2\pi} - \left(\frac{a_0}{2}\right)_{zero} \\ &= \left(\frac{\sum_{m=1}^{p}\left(x_{RON1} - x_{RON2}\right)_m}{p}\right)_{i\times 2\pi} - \left(\frac{\sum_{n=1}^{q}\left(x_{RON1} - x_{RON2}\right)_n}{q}\right)_{zero} \end{aligned} \tag{3.2}$$

Typically the number of samples p and q are (very nearly) equal. The simplicity of (3.2) is satisfying. Another advantage to this approach is that we may decrease the uncertainty in the angle displacement $\Delta\alpha_{RON}$ by averaging both over a larger number of samples p and q, and/or averaging over a number of consecutive turns (e.g. $i = t\cdots t+u$) where t and u are rotation numbers. Nevertheless, both of these approaches have limitations and ultimately there is a compromise. When one increases the number of samples in turn, the processing becomes more and more demanding. When one increases the number of turns that are averaged, the total time over which a measurement takes place increases. At present, the RON 905 data is

sampled using a National Instruments NI-PCI-6115 A/D at a typical frequency of 500 kilo-samples /second. With a standard revolution speed of 20 degrees per second a full revolution takes 18 seconds. Thus equation $\Delta\alpha_{RON}$ in (3.2) is evaluated with $m = n = 9$ Mega-samples.

We implicitly assume in (3.2) that the integer number of 36 arc second gratings passed during a plateau rotation can be resolved. This is conceptually similar to counting fringes in a conventional interferometer, and is accomplished by counting the number of full sine periods (i.e. $\sin\gamma$ RON1 and $\sin\gamma$ RON2) in Figure 3.9 and Figure 3.10, and subtracting one from the other.

This is done with the HCC. However, there is a real danger of loosing a count from time to time. However, there is another piece of information available. The RV350 which drives the plateau has an inbuilt encoder. Its accuracy is in the order of 3.6 to 7.2 arc seconds. This is more than sufficient to keep track of the integer number of 36 arc second gratings that have been moved. Thus, the RV350 encoder can be used to determine the absolute position of the plateau as well as the integer number of gratings, or multiples of 36 arc seconds, of an angle displacement. The phase difference between the $\Delta\alpha_{RON}$ before and after the movement, which will be between -π and π, can be used to refine the angle. With this approach, there is no need to count the sine periods issued from $\sin\gamma$ RON1 and $\sin\gamma$ RON2 in Figure 3.9 and Figure 3.10. The value of an HCC angle movement θ_{LEC} with respect to some zero position using the RV350 and the phase difference issued from the LEC will be given by (3.3).

$$\theta_{LEC} = \left(\alpha_{LEC-RV350}\right)_i - \left(\alpha_{LEC-RV350}\right)_{zero}$$

where: (3.3)

$$\alpha_{LEC-RV350} = \frac{\text{integer}\left(\text{RV350 reading} \times 100\right)}{100} + \left(\frac{\Delta\alpha_{RON} + \pi}{2\pi}\right) \times 0.01$$

As a final word on the LEC, [54] offers an alternative discussion of this aspect, which, although expressed in a more mathematical manner, is no more rigorous than that given here.

3.4.4 Horizontal angle calibration procedure

To calibrate the robotic total station RTS or laser tracker LT horizontal circle, the instrument is installed on the reference plateau; its SMR is positioned in a fixed socket located

at nominal distance from the instrument and a horizontal angle is observed; the HCC angle is taken; the HCC is turned through an angle θ_{HCC} ; the instrument being calibrated is rotated back through the same nominal angle, $-\theta_{RTS}$; the SMR is observed by the RTS or LT; the HCC angle is read; and the differences between the HCC angle readings and RTS or LT horizontal circle observations are compared. This procedure, illustrated in Figure 3.11, is repeated the desired number of times.

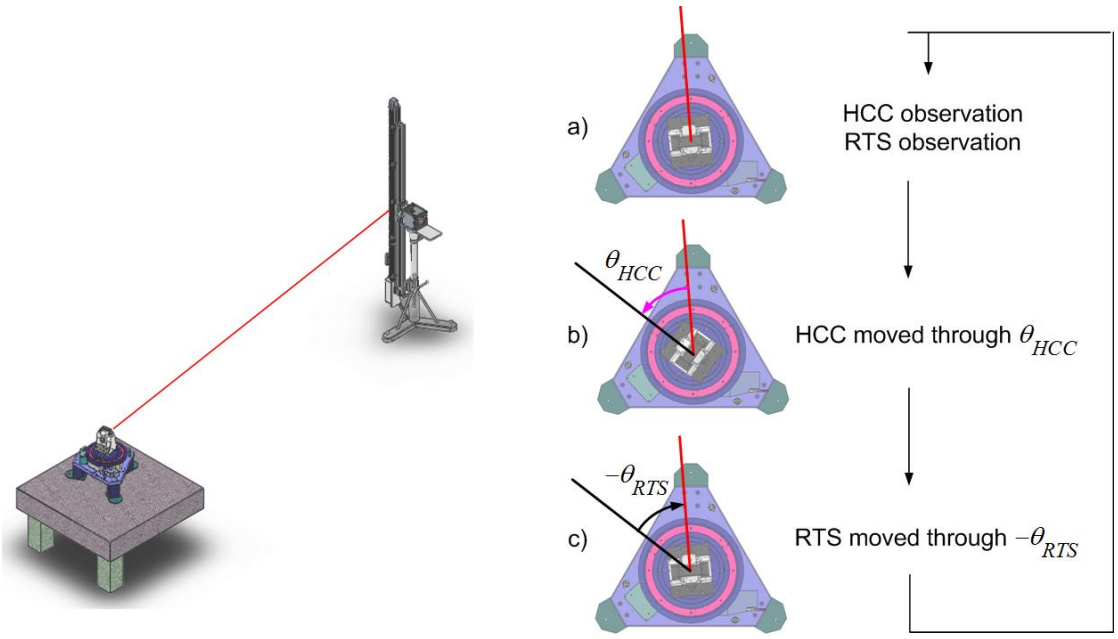

Figure 3.11 RTS and LT horizontal angle calibration procedure: a) Observe the target and record the RTS angle reading θ'_{RTSi} . Record HCC LEC angle issued θ'_{HCCi} ; b) rotate the HCC through the angle θ_{HCC} without moving the RTS; c) Rotate the RTS through the nominal angle $-\theta_{RTS}$ without moving the HCC; and repeat the RTS and HCC observations and record the RTS angle reading $\theta'_{RTS(i+1)}$, record HCC LEC angle $\theta'_{HCC(i+1)}$ and compare the angle differences. This procedure is repeated the desired number of times.

One of the main advantages of this method is that any angle displacement over 360 degrees can be investigated. The nominal target spherically mounted retro reflector (SMR) distance is dictated by the instrument. For example, the calibration of the Leica TDA5005, (one of) the most precise RTS instruments available on the market, has a manufacturers minimum target distance of 6m because of its automatic target recognition (ATR) system. (In practice this restraint can be relaxed somewhat.) The TDA5005 is of particular interest because it is the instrument used at the ESRF. [55] This procedure is fully automatic. The RTS finds the SMR

target and automatically points to it by means of its ATR system. The LT continuously points at the SMR.

3.4.5 Strengths and weaknesses

The specifications and design of the HCC were made by the author. Its fabrication was awarded to the French company Micro-Controle. One of the key issues with the HCC was cost. The industrial solution adopted using commercially available parts (Micro-Controle rotation stages and the Heidenhain rotary encoders) permitted a considerable economy as well as flexibility and robustness. For example the RV350 and RV120 rotation stages have 10000 hours mean time between failure (MTBF) specifications. The drawback of this 'off the shelf' approach is the potential for larger overall uncertainty because of less attention to detail. For example no particular attention was taken to optimise the HCC with regard to temperature induced errors. Similarly, the manufacturers' positional, wobble and eccentricity uncertainties were accepted at face value. Nevertheless, the flexibility of the HCC permits different tasks including the calibration of polygon mirrors and autocollimators, albeit with a larger uncertainty than those of the NMI laboratories.

The HCC can be compared to similar instruments at the LNE in Paris and the PTB in Braunschweig in Germany [21, 48]. These angle comparators have smaller uncertainty. However, they are designed for very task specific purpose, namely the calibration of high precision polygon mirrors and autocollimators. Considerable care was taken in their design to reduce different error sources. For example, the instruments' design largely avoids or compensates for heat sources and heat sinks. A special angle encoder was developed in collaboration with the company Heidenhain for the PTB angle comparator. It improves performance by increasing the diameter of the encoder disk and the number of gratings ($2^{18} = 262\ 144$ signal periods), and by using 16 read heads of which 8 are installed for the purpose of instrument self calibration. With both the PTB and the LNE angle comparators, considerable efforts were made in the mechanical design to minimize positioning errors and mechanical errors such as wobble and eccentricity. The downside of this is of course is their highly focused application area. For example both of these instruments have stringent mass

restrictions for objects placed on them which are very much less than the HCC 6500 N load capacity restriction.

The heart and most important part of the HCC is the angle acquisition system, the LEC. Using the LEC permits a considerable improvement on the Heidenhain RON905 encoder. Indeed given the manufacturer's uncertainty of the RON905 of 0.4 arc-seconds ($k=1$), and 90 Mega-samples over one rotation of the LEC, the LEC resolution is given by (3.4). However, instrument resolution is not uncertainty. This will be investigated in detail in chapter 5

$$\begin{aligned} \sigma_{LEC} &= \sqrt{2} \times \sigma_{RON905} \Big/ \sqrt{n} \\ \sigma_{LEC} &= \sqrt{2} \times 0.4 \Big/ \sqrt{9\left(10^7\right)} = 60 \times 10^{-6} \text{ arc-seconds} \end{aligned} \tag{3.4}$$

In summary, the HCC meets all of the criteria outlined by Ingensand in section 2.4.1 and in particular: low uncertainty (this will be investigated in detail in chapter 5 below); a fully automatic test sequence; the calibration of the horizontal circle in the instrument's operational position; calibration over the full measuring range; ease of use; and suitability for various RTS and LT models. Its principal drawback, namely the use of off the shelf parts results in bias errors. This requires that HCC be calibrated. This calibration is discussed in chapters 4 through 6.

3.5 Vertical angle calibration

Vertical angles are generally referred to as zenithal angles in the industry. LTs and RTSs have their zero zenithal angle reading in the vertical direction; the direction of the normal to the gravity field. The direction towards the centre of the earth is at 180°. This orientation is generally only approximate for the LTs.

Whereas it is important to examine the horizontal circle over the full 360°, this constraint is generally relaxed with vertical circles. First, no instrument available on the market is capable of observing a target directly over the full 360° vertical circle. For example its base prevents it from reading angles between approximately 150° and 210°. Often taking vertical readings near the zenith (i.e. 0º) is difficult as well. Generally theodolite systems can be equipped with pentagonal prisms; and both RTSs and LTs can use mirrors and other accessories to observe

very high or low zenithal angles thereby keeping the vertical circle readings to within ±45° of the horizontal. These systems are not considered in this work. However, one can say that the typical working range of the vertical circle of LTs and RTSs is within ±45° of the horizontal (i.e. vertical circle readings of 90°±45° and 270°±45°).

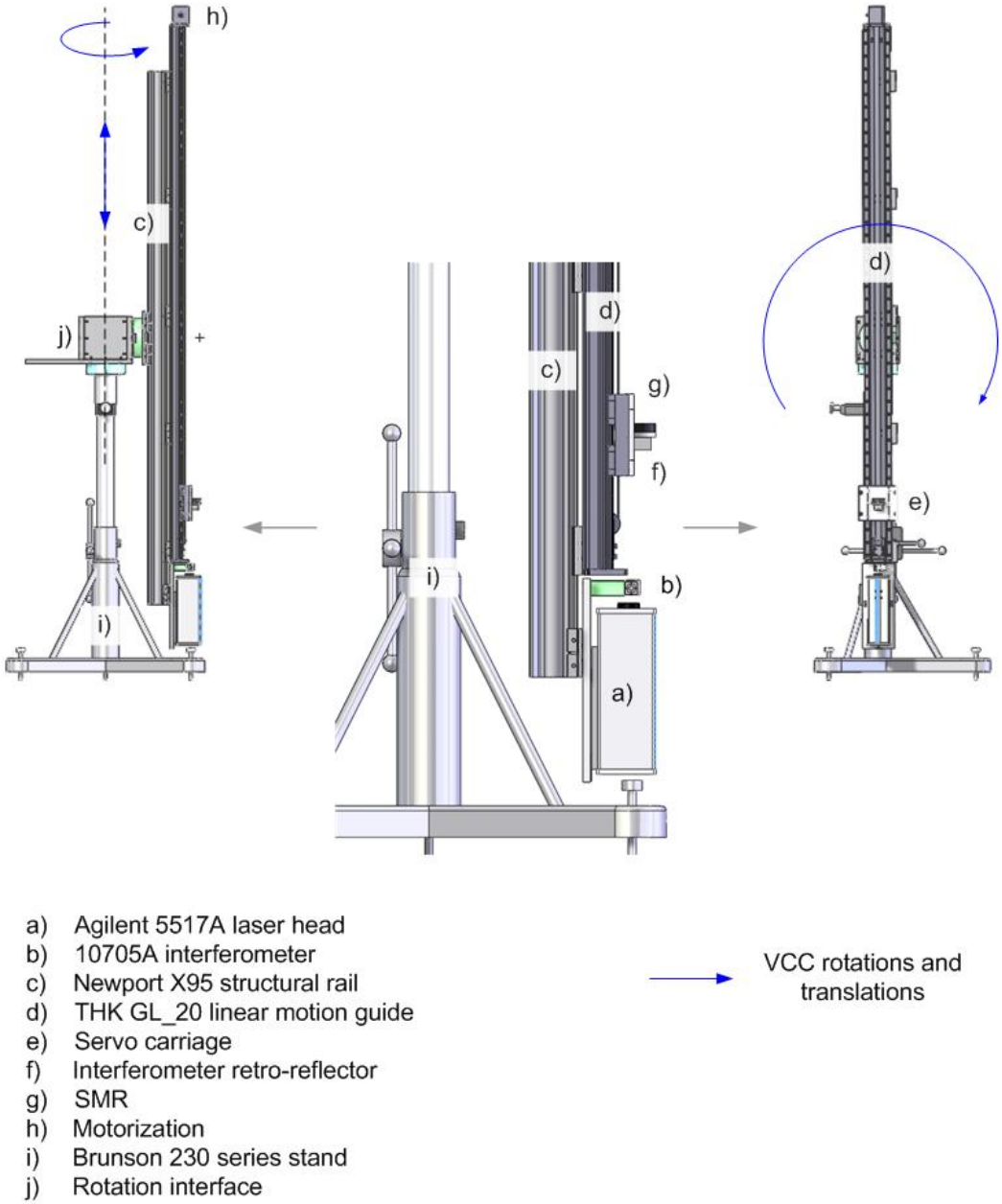

Figure 3.12 Schematic of the VCC assembly.

The VCC is composed of a 3m long extruded aluminium Newport (Micro-Controle) X95 structural rail; a motorized 2.5m long THK GL_20 linear motion guide with carriage; a Leica Level 20 inclinometer mounted on the THK carriage; and an Agilent 5517A laser head, 10705A single beam interferometer and 10780 receiver system. The THK linear motion guide

is fixed on the Newport rail. The Agilent interferometer system is positioned at one end of the rail while the motorisation driving the carriage is at the opposite end. Its reflector, a Leica 1½ inch SMR, is placed on the THK carriage. The full system is placed on a Brunson 230 series heavy duty adjustable height stand. The VCC system is interfaced to the stand with a system which permits it to be rotated in any orientation. Thus when the VCC, a multipurpose tool, is oriented vertically it can be used to calibrate the vertical circles of RTSs and LTs. The VCC system is shown schematically in Figure 3.12. It was entirely designed and assembled in house by the ESRF ALGE group.

3.5.1 Vertical angle calibration procedure

The calibration procedure compares the SMS vertical circle readings with the vertical displacements of the SMR which are controlled by the interferometer system. Naturally this requires the distance between the instrument being calibrated and the VCC to be known. These distances are measured automatically with the RTS and LT and given that the instrument distance meter is calibrated on the ESRF DCB (see section 3.3); the distances are traceable with an assigned uncertainty and coverage factor. The general measurement scheme is shown in Figure 6.2 on page 184 (section 6.3) where a full discussion of the VCC uncertainty is made.

3.5.2 VCC vertical angle calculation

3.5.3 Strengths and weaknesses

It is immediately clear that there are two drawbacks to this system. The first is its limited range of application, and the second is its relatively large uncertainty. For example using the VCC at the minimum recommended operating distance of the Leica TDA5005 of 6m, the operational range is ±10.4º (i.e. for a vertical displacement range of ±1.1 m at a distance of 6 m). In practice, this range can be decreased to approximately 2.5 m before the ATR no longer works. However, even at this distance the operational range is only ±23.75º. As it turns out this is of little consequence at the ESRF where vertical angle observations are always less than ±10º. However for a wider range of RTS applications it is a limiting factor. For LT

applications, the minimum distance is not a problem. The LT can be placed as close as desired to the VCC. For example angles up to ±65º can be investigated at a distance of 0.5m.

The second problem is the uncertainty. The VCC uncertainty is discussed in detail in section 6.3. The main results are presented here. The uncertainty in the vertical angle determination of the VCC is non-linear and principally dependent upon the magnitude of d_0, and the uncertainty with which it can be measured. d_0 is the first distance measured by the instrument being calibrated to the VCC. It is shown in Figure 6.2 on page 184. Figure 3.13 shows the interplay between d_0 and VCC uncertainty. Shorter d_0 results in a larger vertical angle range. However this is at the cost of a larger uncertainty. It is relatively easy to obtain a reasonable VCC uncertainty and a large measurement range with the LT. This is not true with the RTS where the best manufacturer's uncertainty is barely attainable over the range of ±10º. This can be considerably improved by measuring the distance between the RTS and the SMR at the start with a LT. However this improvement is not considered here.

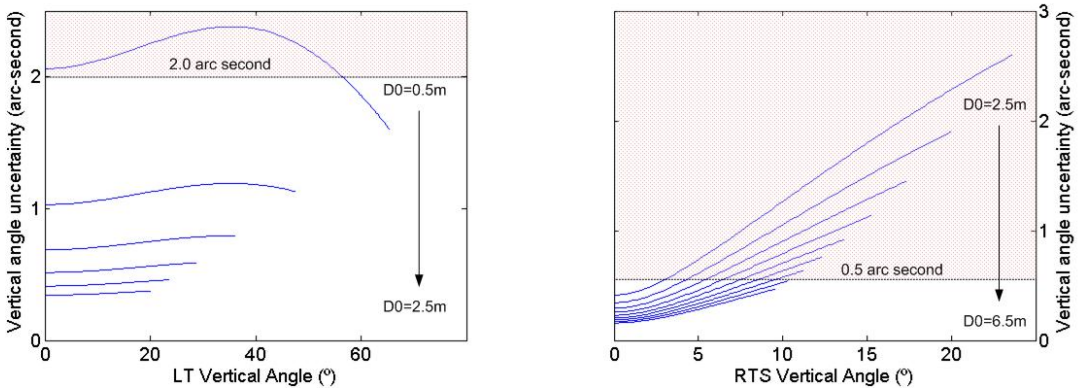

Figure 3.13 Graphs showing the dependence of the vertical angle uncertainty $U(\alpha')$ for the LT (left) and RTS (right) as a function of d_0. Shorter d_0 results in a larger vertical angle range at the cost of a larger uncertainty. Recall the best manufacturer's measurement uncertainties are 2.0 and 0.5 arc-seconds for the LT and the RTS respectively.

In summary, the VCC does not perform as well as the HCC; for the RTS in any event. Its original purpose was to perform the LT tests outlined in [30]. The original VCC design was similar to the HCC. This is to say the instrument would be rotated about its trunnion axis (Figure 3.2) and angles compared to a vertically mounted LEC. This was abandoned for two reasons; first the complexity of the system and secondly its cost. However, the advantage

between a direct comparison instrument such as the HCC and one based upon an indirect comparison such as the final version of the VCC is obvious.

3.6 Angle as a function of distance

It is worth noting that a number of studies at the ESRF have shown that there appears to be an effect of distance on angle measurements. [56] This is to say that if one observes a point that advances away from the RTS instrument in a perfectly straight line, there are small but highly systematic angle variations about a constant angle. Curiously, this effect has also been observed with LT instruments. Two different experimental approaches have been made and both give confirmatory results. They are discussed in [56] and [4]. However, any conclusions are at a qualitative rather than quantitative level at the time of writing. This effect will be investigated in greater detail in the future.

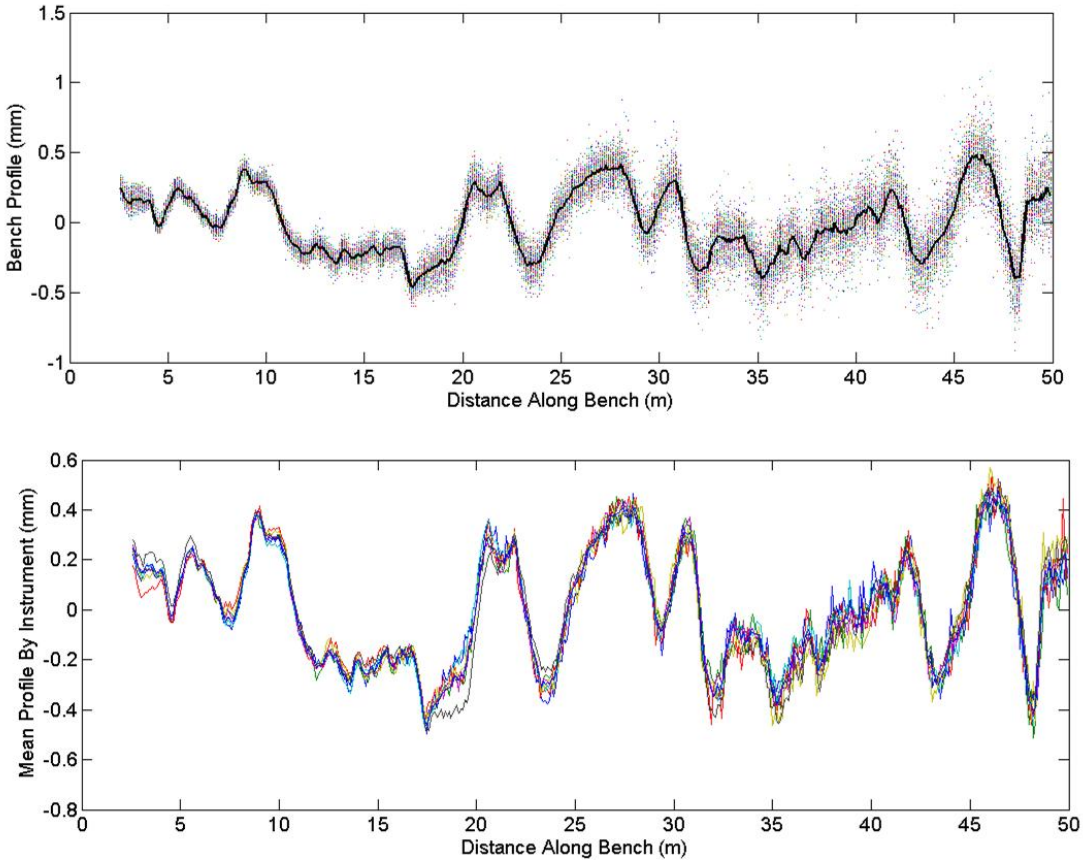

Figure 3.14 The top graph shows the ESRF DCB profile as a function of distance. It shows the results of 75 independent determinations of this profile with 7 different RTS and LT instruments. The bottom graph shows the mean profile of between 5 and 15 determinations each of the 7 instruments. One observes small variations of these mean values with respect to one another.

The experimental approach discussed here is the one that uses the mean DCB profile as a reference standard. Another method, not discussed here, uses a capacitive probe instrument referred to as the wire position sensor or WPS and a stretched carbon wire.

The method involves first determining the mean DCB profile with a large number of independent observations with a number of different instruments. This mean profile is then considered to be the reference standard. It is shown in the top graph of Figure 3.14. Then the mean values of the DCB profiles are determined for each instrument (see the bottom graph in Figure 3.14). Finally the mean DCB profile is removed from each of the instrument profiles to give an apparent instrument error as a function of distance shown in Figure 3.15. The top graph of this figure shows the apparent error for all 7 instruments used in the study (6 RTSs and one LT). The bottom graph shows the results for the LT.

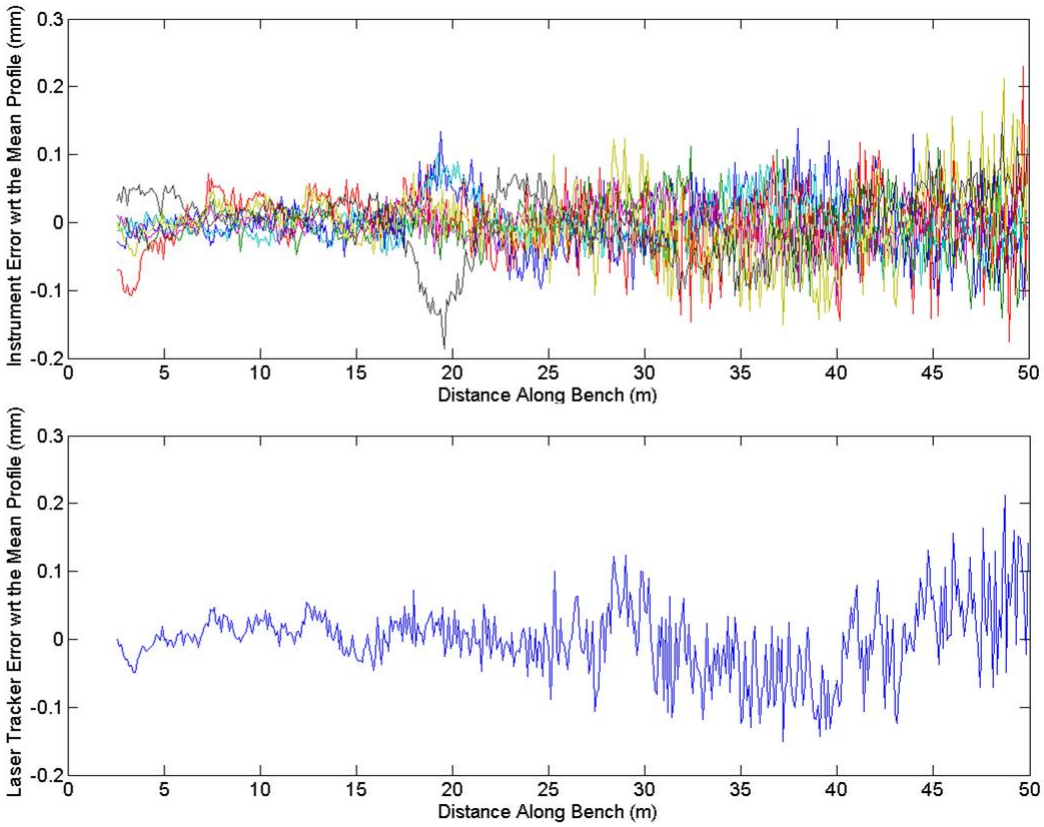

Figure 3.15 These graphs show the apparent error in the angle reading reduced to an offset distance as a function of distance along the ESRF DCB. Each of these curves represents the mean value of between 5 and 15 determinations of 474 points along the DCB with respect to the mean profile shown in the top graph of Figure 3.14. The bottom graph shows the results of this apparent error using a LT instrument.

Although this issue is an important subject in its own right, it will not be studied further in this thesis. Nevertheless, it is an important issue and is the subject of ongoing studies at the ESRF. It has been presented here for completeness with respect to the potential errors encountered with SMS instruments. These errors do not influence results issued from the HCC because it works with near-enough to fixed distances.

3.7 Laboratory

The laboratory environment is important because it has an influence on both the vertical and horizontal calibration results. There are two main influences that must be considered; the first is temperature; the second is refraction. Temperature can impinge on every physical element in the laboratory while refraction affects both electronic distance and angle observations.

3.7.1 Layout

The laboratory layout is shown in Figure 3.16. It is 9.05 m long by 4.45 m wide. Its height is 3 m. The maximum useable length is approximately 6.5 m. It is equipped with an air conditioning system.

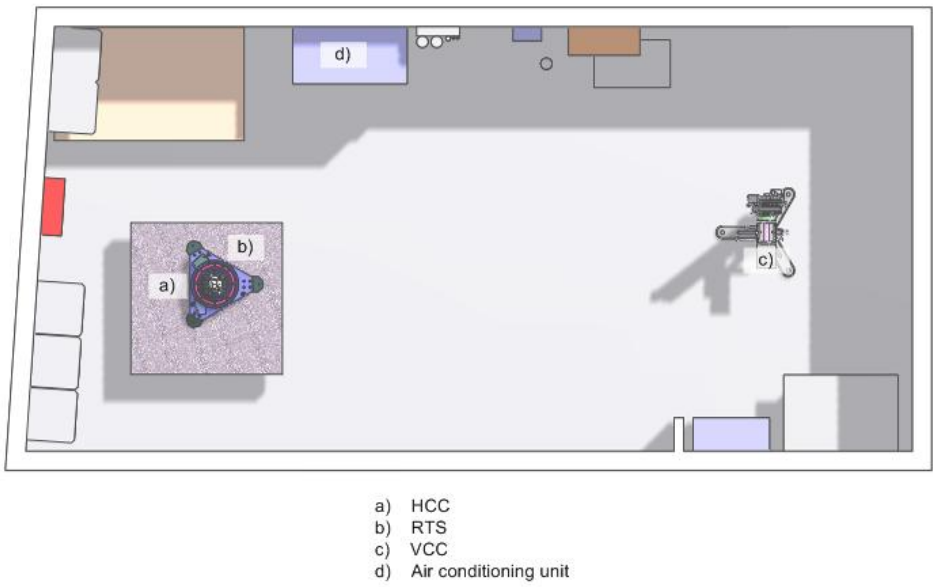

Figure 3.16 Schematic diagram of the laboratory where horizontal and vertical angle calibration is performed with the HCC and VCC.

3.7.2 Temperature

The effect of temperature on the different elements in the laboratory is complex. It can for example cause positional drifts of the different laboratory components (e.g. HCC, VCC, LEC, marble etc …) over time. For certain tests where sub-micro-meter uncertainty is investigated the temporal evolution in temperature gradients is clearly seen in the measurements. A host of thermocouples are used with the different experiments discussed in chapter 5. Their effects will be discussed when appropriate. As a general rule, temperature is maintained within ±0.1 Celsius at any point over a 24 hour period within the laboratory. However there are spatial variations in the order of ±0.9 Celsius. This is due mainly to the air conditioning system (see Figure 3.17 and Figure 6.18).

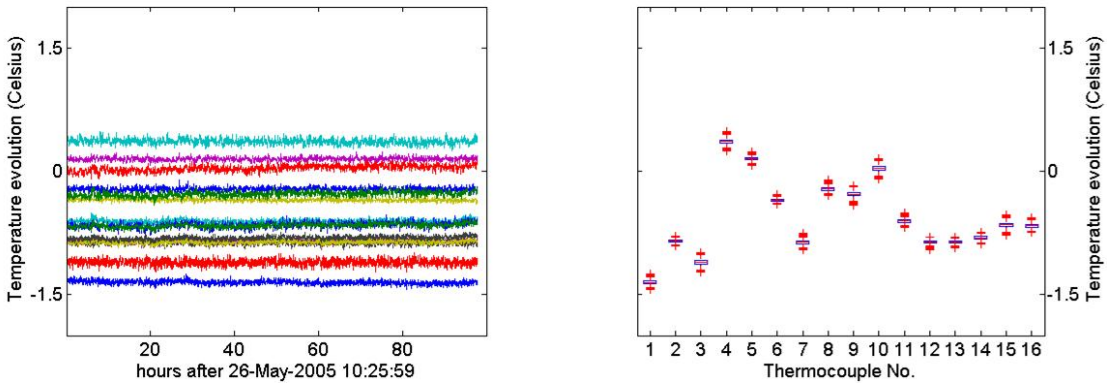

Figure 3.17 Temperature evolution over 100 hours at 16 different positions on a grid at 2.2m height in the laboratory. The left hand graph shows the temperatures with respect to the thermocouple located above the RTS position. The right hand graph shows box plots for the 16 thermocouples temperature over the 100 hour period. There is considerable spatial variation but small temporal variation.

3.7.3 Refraction

Refraction effects must be considered in all precision optical measurements. Because we are forced to work in ambient conditions, refraction is considered a very real problem with both angle and distance in survey measurements. The effect of refraction on survey distance and angle measurements is expressed as (3.5) and (3.6) respectively. [57-59] Note that the classical corrections made in geodesy such as the reduction to sea level, and the spheroidal correction due to curvature of the earth, are not considered here (see for example [17]).

$$C_d = \int_{r=0}^{R} N dr \tag{3.5}$$

$$C_\alpha = \frac{1}{R}\int_{r=0}^{R} r\frac{\delta N}{\delta z} dr \tag{3.6}$$

In (3.5) C_d is the correction to a measured distance due to refraction, and N is the refractivity ($N = n - 1 ; n = c/v_p$). n is the refractive index (index of refraction) and is defined as the ratio of the phase velocity c of light (in this case) in a reference medium (i.e. vacuum) to the phase velocity v_p, in the medium itself (i.e. the air along the line of sight). In (3.6) C_α is the correction to a measured angle due to refraction, $\frac{\delta N}{\delta z}$ is the refractivity gradient of the air perpendicular to line of sight, and R is the line of sight path length. Note that despite

the parameter z, equation (3.6) is applicable, in an industrial environment[12], to both horizontal and vertical angles.

The integral in equation (3.6) is taken along the line of sight from the source point (light source) to the detector (RTS) (Figure 3.18). It is important to note that C_α, unlike the distance correction which is linearly dependent on the length of the line of sight, is weighted proportionally to the proximity to the point where the angle is being measured (RTS or LT station or detector as shown in Figure 3.18), with r being the distance from the source point (i.e. $r/R \to 1$ as we approach to the point where the angle is being measured). Thus the refractive gradient over the 10% of the line closest to the instrument position counts 10 times more in the integral than the refractive gradient over the 10% of the line closest to the source or reflected point (light source in Figure 3.18).

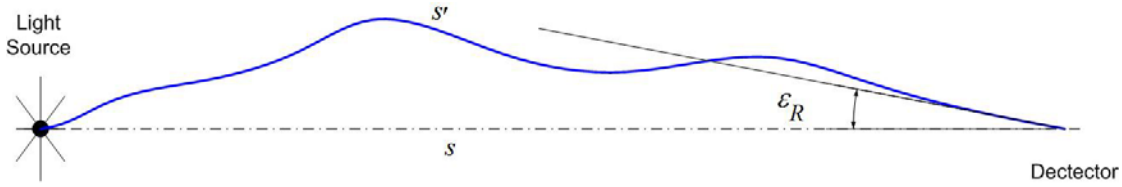

Figure 3.18 The influence of refraction on light travelling through the atmosphere. The actual distance travelled s' will be longer than the true distance s between points. Similarly there will be an angle error ε_R due to the angle of arrival of the light.

Refractive effects are present in the laboratory calibration measurements as well as in the ESRF survey networks. In the laboratory context, refractive effects must be considered on LT and RTS angles, and EDM and IFM distances made in the range of 1 to 8 m.

Recall that atmospheric refractive effects arise from density variations in the propagation medium (i.e. air) due to spatial and temporal variations in the atmospheric state. This state which is dependent upon a number of atmospheric parameters (e.g. temperature, pressure, humidity, CO_2 content…) is highly non-uniform in our normal measuring environment. There exist several possibilities to measure the effect of refraction on distance and angle measurements. For example, one method to measure the effect of refraction on angle and distance is to use the dispersometer principle and measure the differential effect on two

[12] In the surveying and geodesy community elaborate models for vertical refraction in outdoor environments have been developed. Neither these exterior environments nor the refraction models developed for them are considered in this thesis.

different colours of light. A second is to model it using easily measured parameters temperature, pressure and humidity.

Serious effort was devoted to the direct measurement of refraction effects on terrestrial (vertical) angle and distance measurements by the geodetic community before the advent of GPS. Today, efforts in this domain are restricted mostly to large scale metrology. The main effort in this field was the development of dispersometer type instruments. The impetus behind this development was to measure elevation differences using vertical angle observations over long lines of sight. This was done to reduce the time and uncertainty attributed to classical optical levelling runs. Although never commercialised, viable systems have been prototyped [59, 60] and work. Similarly very promising techniques employing ultrasound have been employed to correct for the effects of refraction on distances. [61]

A commonly used method of evaluating the effect of refraction is to model it using the easily measured environmental parameters temperature, pressure and humidity. Equations for the refractive index of air n were derived originally by Barrel and Sears [62] , then later by Edlen [63]. Today, the International Association of Geodesy [64] recommends using the equations developed by Ciddor [65] and Ciddor and Hill [66].

The group refractivity N_g for visible and near infrared waves at standard conditions is given by (3.7) [64].

$$N_g = \left(n_g - 1\right)10^6 = 287.6155 + \frac{4.8864}{\lambda^2} + \frac{0.06800}{\lambda^4} \tag{3.7}$$

Here λ is the carrier wavelength in micrometers and n_g is the group refractive index in standard air at temperature=0 °C or 273.15 K, pressure = 1013.25 hPa, partial water vapour pressure= 0.0 hPa and CO_2 content of 375 ppm. The group refractivity of visible and near infrared waves in ambient moist air is given by (3.8) [64]

$$N_L = \left(n_L - 1\right)10^6 = \left(\frac{273.15}{1013.25} \times \frac{N_g \times p}{273.15 + t}\right) - \left(\frac{11.27e}{273.15 + t}\right) \tag{3.8}$$

Here N_g is the group refractivity as defined in (3.7), t the temperature in degree Celsius, p the total pressure in hectopascal hPa, and e the partial water vapour pressure in hPa. The partial water vapour pressure is more conveniently written in terms percentage humidity [67]:

$$e = \frac{1}{100} 6.1078 \times \exp\left(\frac{17.269t}{t + 237.29} \right) \tag{3.9}$$

The classical distance correction used in surveying and geodesy distance measurements is given by (3.10).

$$D_{corrected} = D_{raw} \left(N_{L_{ref}} - N_{L_{meas}} \right) \tag{3.10}$$

Assuming laboratory reference conditions of $t = 20$ Celsius; $P = 1013.25$ hPa; $h = 60\,\%$ humidity; and the interferometer wavelength of 633 nm the correction to measured distances is given by (3.11).

$$D_{corrected} = D_{raw} \left(279.2 - \frac{80.96}{273.15 + t} + \frac{0.6884h \exp\left(\frac{17.27t}{237.3 + t} \right)}{273.15 + t} \right) \tag{3.11}$$

For the refraction influence on measured angles, the refractivity gradient $\frac{\delta N}{\delta z}$ is derived in (3.12).

$$\frac{\delta N}{\delta z} = \frac{\delta N}{\delta t} \frac{\delta t}{\delta z} + \frac{\delta N}{\delta P} \frac{\delta P}{\delta z} + \frac{\delta N}{\delta h} \frac{\delta h}{\delta z} \tag{3.12}$$

This leads to the rather involved expression of the refractivity gradient as a function of common meteorological parameters (3.13). Note that the factor 80.96 applies to the LT wavelength of 633 nm. If one considers the RTS with a wavelength of 850 nm, replace 80.96 by 79.43.

$$\frac{\delta N}{\delta z} = C_1 \frac{\delta t}{\delta z} + C_2 \frac{\delta p}{\delta z} + C_3 \frac{\delta h}{\delta z}$$

$$C_1 = -\left[\frac{80.96}{{k_2}^2} - \frac{0.6884h\left(\frac{17.27}{k_2} - \frac{17.27t}{{k_2}^2} \right)k_1}{k_2} + \frac{0.6884hk_1}{{k_2}^2} \right]$$

$$C_2 = \frac{80.96}{k_2} \qquad (3.13)$$

$$C_3 = -\frac{0.6884k_1}{k_2}$$

$$k_1 = \exp\left(\frac{17.27t}{237.3 + t} \right); k_2 = 273.15 + t$$

Refraction effects in the HCC, VCC laboratory are quantified in section 6.7.

4 Metrology used in the calibration of the HCC and VCC: instrumentation, techniques and theoretical capabilities

This chapter discusses instruments and techniques that are used to evaluate the performance, uncertainty and aptness for the task at hand of the horizontal circle comparator (HCC) and the vertical circle comparator (VCC). The first section reviews the different instruments; their accuracy, precision and applicability. The second section introduces the form error spindle motion separation technique which is essential in the evaluation of the HCC. The linked encoders configuration (LEC) provides the angle standard for the evaluation of spherical measuring system (SMS) horizontal circle readings. It measures the rotation about the primary (vertical) axis. However, there are five additional degrees of freedom, namely the tilts about the x and y axes and the translation movements along the x, y and z axes, which influence measurements made on the HCC. Capacitive probe measurements and the form error - spindle motion error separation (FESM) technique provides the means whereby these movements can be evaluated and corrected. The chapter finishes with a short section concerning homogeneous transformation matrices which are used in full circle evaluation (i.e. over 360 degrees) of the HCC.

4.1 Instruments

The HCC and VCC must be calibrated in order to have confidence in their results, establish their uncertainty, and provide traceability to fulfil the requirements outlined in section 2.3. The actual calibration problem is discussed in the next chapter; however, beforehand we must look at instruments and techniques that can be used to perform it. Recall that traceability is the property of a measurement result whereby the result can be related to a reference through a documented unbroken chain of calibrations, each contributing to the measurement uncertainty. Thus the instruments used in the calibration of the HCC and VCC must themselves have a clearly established traceability. Recall also that given the SI definition of angle and its lack of a clearly defined standard or artefact, it is preferable to establish traceability of the HCC and VCC to the metre (see section 2.1.1).

There are four instruments used extensively in the calibration, or at least the qualification and identification of errors, of the HCC and VCC. Three, the interferometer, the laser tracker (LT), and the capacitive probe are traceable to the metre and hence are can be considered standards in their own right, provided they have properly a established traceability, uncertainty and coverage factor. The fourth, the autocollimator and polygon mirror, is used by the national metrology institutes (NMIs) as the instrument and artefact of choice for inter-laboratory comparisons ensuring commonality in measurement results. [14] The NPL provides a calibration for autocollimators directly traceable to the metre.

4.1.1 Interferometry

Interferometry is the workhorse in all high precision metrology. It is the standard of choice for distance measurement at the ESRF.

All interferometry used in this thesis is based on the frequency based heterodyne principle. The laser emits light that contains two frequencies, f_1 and f_2, both in the red light range but orthogonally polarized ($f_1 \approx f_2 \approx 4.73\times10^{14}$ Hz), and differ by approximately $f_1 - f_2 \approx 2.5\times10^{6}$ Hz. A polarizing beam splitter separates two beams into reference and measuring paths. They are then reflected and recombined whereupon they interfere at a receiver and produce an output proportional to the irradiance of their interference. Displacement in a heterodyne system is derived from the change in phase (Δf_1) that occurs with a change in optical path of the measurement leg with respect to the reference leg of an interferometer. This Doppler-shifted signal $f_2 - \left(f_1 \pm \Delta f_1\right)$ is compared with the reference signal and converted into precise time-based velocity and position-displacement information. Although the irradiance contains frequency components for $2f_1$, $2f_2$, $f_2 - f_1$ and $f_1 + f_2$, the receiver bandwidth is restricted to the relatively low and stable $f_2 - f_1$ frequency range.

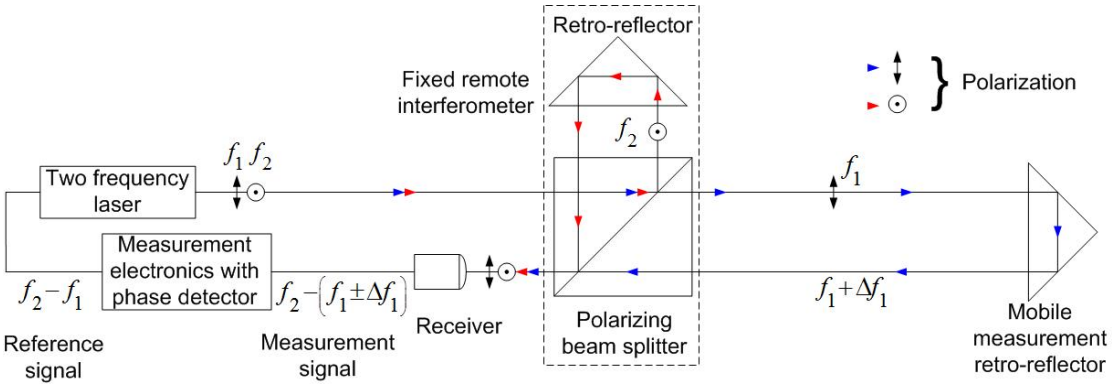

Figure 4.1 Heterodyne dual frequency laser interferometer.

In this work, interferometry is used for the calibration of distance meters and capacitive probes. It is also used for vertical angle calibration in the VCC. Each of these applications has its own intrinsic uncertainty which will be discussed later when appropriate.

Interferometry is a mature measurement science. Instrument uncertainties are typically less than 1 µm. The main error sources are Abbe and cosine errors, and refraction effects. These errors are illustrated in Figure 4.2. Recall, Abbe error results from a combination of a beam offset from the centre of the reflector translation and an angular error. Note that one could also have the case of probe perpendicular but tracks not parallel, which essentially leads to Abbe error expressed as $\varepsilon = y\sin\alpha$ rather than $\varepsilon = y\tan\alpha$ shown in the figure. Cosine error results when the measurement axis is not parallel to the axis of travel. Refraction effects were discussed in section 3.7.3.

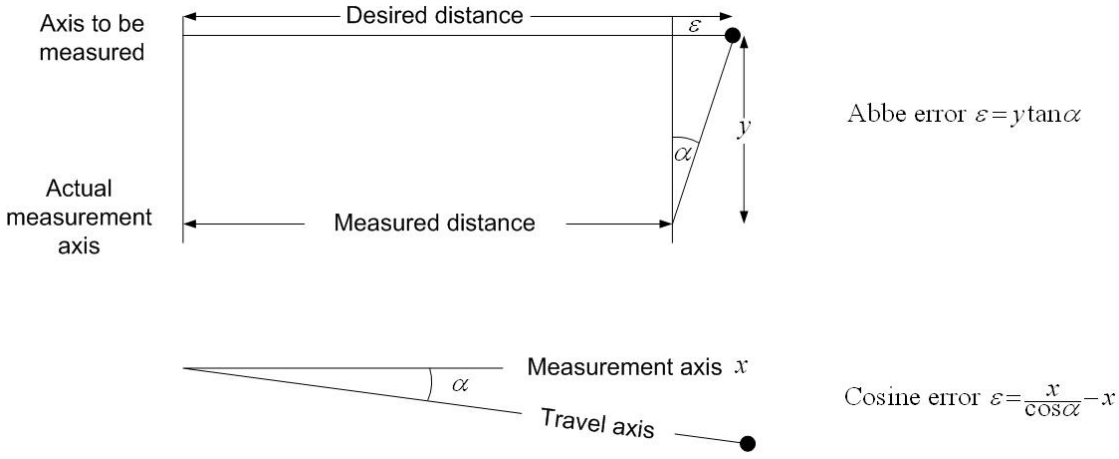

Figure 4.2 Abbe and cosine errors in interferometry.

Distance meter calibration is done on the ESRF distance meter calibration bench (DCB) (see section 3.3). The standard is an Agilent 5519A laser source coupled with an Agilent

10766A linear interferometer. Data is processed using the Agilent 10885A PC axis board. This electronic provides a resolution of 4.9 nm. Capacitive probes are calibrated on a dedicated bench using an Agilent 5519A laser source, 10716A high resolution interferometer, 10724A Plane Mirror Reflector, and electronics board 10887B calibrator electronics housed in a 55292A USB Expansion Module. This system has a nominal resolution of 2.5 nm. The VCC uses an Agilent 5517B laser source, a 10705A single beam interferometer, 10780F remote receiver, a Leica 1½ inch SMR and the 10887B calibrator electronics housed in a 55292A USB Expansion Module. Like the DCM this system has a resolution of 4.9 nm. The laser sources have a calibration uncertainty of less than 10 fm (accredited calibration certificates issued by the Laboratoire National d'Essais LNE) for 633000000 fm or roughly 0.016 µm per m.

4.1.2 Laser tracker

Because an interferometer measures a relative displacement, one must not lose signal during the measurement process. With a classical linear interferometer this imposes the difficult constraint that the reflector remains perfectly 'in line' with the laser beam. With a laser tracker (LT), although one still measures an 'in line' distance, the manner in which one moves from one point to the other is not constrained to follow a straight line. Thus the LT is extremely useful when one considers it to be a servo-controlled laser interferometer. However to benefit from the interferometric distance, one must one must minimize the influence of the horizontal and vertical angles issued from the LT. In practice, angle influence is small if one remains nearly 'in line'; this is to say the LT is aligned with the two targets one wants to measure the distance between. The magnitude of the error depends upon the configuration.

The different laser tracker manufacturers give the following uncertainties ($k = 1$) for a measured coordinate[13]:

- Leica AT901-B, AT901-MR, AT901-LR, 10µm + 5ppm;
- API (Automated Precision Inc) Tracker3, ±5ppm;

[13] Specifications are derived from manufacturers brochures downloaded from their respective internet sites (http://www.leica-geosystems.com, http://www.faro.com, http://www.apisensor.com) in October 2008.

- FARO Laser Tracker Xi 31 µm, 46 µm, 68 µm at 2m, 5m and 10m respectively

These manufacturers' specifications translate to the following uncertainties for a coordinate at distance of 5m[14] from the tracker:

- Leica AT901-B, AT901-MR, AT901-LR 35µm;
- API (Automated Precision Inc) Tracker3 25 µm;
- FARO Laser Tracker Xi 46 µm.

Manufacturers also give for the specifications interferometer incorporated into these instruments: Leica AT901-xx, 0.5 µm; API Tracker 3, ±0.5 ppm; and the FARO Tracker Xi, 0.5 µm+0.4 ppm. Calibration curves for these instruments made on the ESRF distance meter calibration bench (DCM) are shown in the top graph of Figure 3.4. The COFRAC accredited DCB expanded ($k = 2$) uncertainty for this calibration is 50µm for these calibrations.

4.1.3 Möller Wedel Elcomat 3000 autocollimator with 12 sided polygon mirror

Recall that when a collimated beam of light is projected onto a plane reflector which is square to the beam, the beam will be reflected back along the same path. When the reflector is tilted at an angle α with respect to the incident beam, the reflection of the beam is 2α . The relationship between the deviation d and the angle α is shown in Figure 4.3.

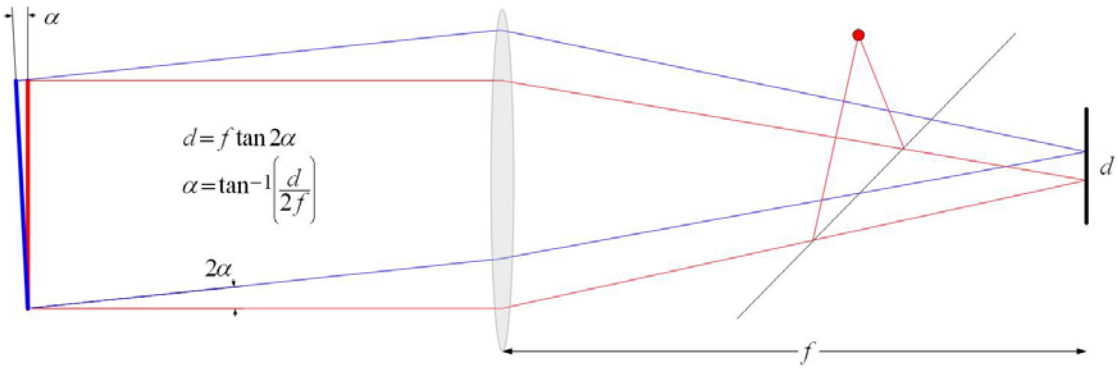

Figure 4.3 Autocollimation principle used in electronic autocollimators such as the ELCOMAT 3000.

A review of errors associated with autocollimator systems is given in [68]. Their conclusions suggest that the principal sources of error are related to the difficulties to quantify

[14] Results from tests made at the ESRF in the cadre of a call for tender during the summer of 2008 are in agreement with the specifications given by Leica. These tests also found that the specifications for the FARO tracker appear pessimistic while those of the API tracker appear optimistic.

errors associated with the measurement of imperfect, non-flat faces of the artefact, which cause the instrument to misinterpret the average orientation of the surface. They draw particular attention to the definition of the angle of the surface. They demonstrate the pyramid, eccentricity and other related errors are generally very small.

This system is used regularly in the control of the HCC. However it is not used in its formal calibration. The manufacturers stated uncertainty for the Elcomat 3000 is ± 0.1 arc-second over any 20 arc-second range and ± 0.25 arc-second over the total instrument range. Its reproducibility is given as 0.05 arc-second. In this thesis, the autocollimator measures angle displacements with a 12 sided polygon mirror. Möller Wedel provides a (non-accredited) calibration certificate with an uncertainty of 0.3 arc-seconds for the separation angles of this polygon mirror.

4.1.4 Capacitive probes

4.1.4.1 General remarks

Capacitive probes are used extensively in this thesis. They are particularly solicited in the calibration of the HCC. One of their main advantages is that they can be calibrated 'in-house' to provide a traceable standard with a well defined uncertainty and coverage factor. This uncertainty will be developed in chapter 6. Here we will develop some background and discuss how they are calibrated.

Capacitance describes how the space between two conductors affects the electric field between them. It is given by (4.1) where ε_0 is the permittivity of vacuum, ε_r is the relative dielectric constant of the material between the two plates, A the area in m^2 of the capacitor plate and D the gap distance or spacing in m. For ordinary capacitance measures in air, A and the product $\varepsilon_0\varepsilon_r$ - the dielectric are constant. Thus the capacitance is inversely proportional to the gap distance.

$$C = \frac{\varepsilon_0 \varepsilon_r A}{D} = \left(8.854 \times 10^{-12}\right)\left(1.000264\right)\frac{A}{D} = \frac{8.856 \times 10^{-12} A}{D} \tag{4.1}$$

There are several different ways to exploit the relation given in(4.1). A general review is given in [69]. Important contributions and references to the field of capacitive displacement

measurement technology are found in [70] and [71]. For other reference material see for example [72, 73]. High precision techniques used for capacitance displacement measurement are usually based on the AC bridge methods [70].

4.1.4.2 Capacitive probes and control electronics employed at the ESRF

The capacitive probe has detection and guard electrodes. It employs the so-called active guarding technique outlined in [71]. For an accurate measure of capacitance only the electric field between the detection electrode and the target should be measured. To remove fringe field effects, another conductor surrounds the detector electrode and is kept at the same voltage. The configuration used at the ESRF is a cylinder (the detector electrode) within a cylinder (the guard electrode) separated by an insulating film. When an excitation voltage is applied to the detector electrode, a separate circuit applies the exact same voltage to the guard. Because there is no difference in voltage between the detector electrode and the guard, there is no electric field between them. Any other conductors in the vicinity of the capacitive probe will form an electric field with the guard and only the detector electrode forms an electric field to the target.

The capacitive probes and control electronic used in this thesis come from the French company Fogale Nanotech. They are based on a French patent no. 2640373 A1, European Patent EP0378017 [74]. This is a variant of the AC bridge method. The schema on the last page of this patent is given in Figure 4.4.

The English abstract of EP0378017 gives the following explanation. Note that all references in this paragraph are to Figure 4.4 below. 'The capacitive dimensional measuring chain with linear output consists mainly of a capacitive sensor ($1a$) formed by a detection electrode and a guard electrode surrounding the detection electrode supplied respectively by two sources of bias voltage (V_p and V_p'), a reference capacitor ($6a$) supplied by a reference voltage source ($7a$), and a circuit (9) which measures the distance (e) between the detection electrode and a conducting component (P) placed opposite this electrode. The sources of bias voltage are variable and are controlled in amplitude by a distance-measuring signal (V_e) delivered by the measuring circuit. The measuring circuit contains means (90 to 93) for amplifying and

demodulating an input error signal which represents a difference between a charge on the capacitance of the sensor (C_{cpt}) formed between the detection electrode (10) and the component (P) separated by the distance (e) to be measured and a charge on the reference capacitor. The distance-measuring signal supplied by the measuring circuit represents linearly the distance to be measured (e) and, because of the control of the amplitude, stabilizes the sources of bias voltage in temperature and time.'

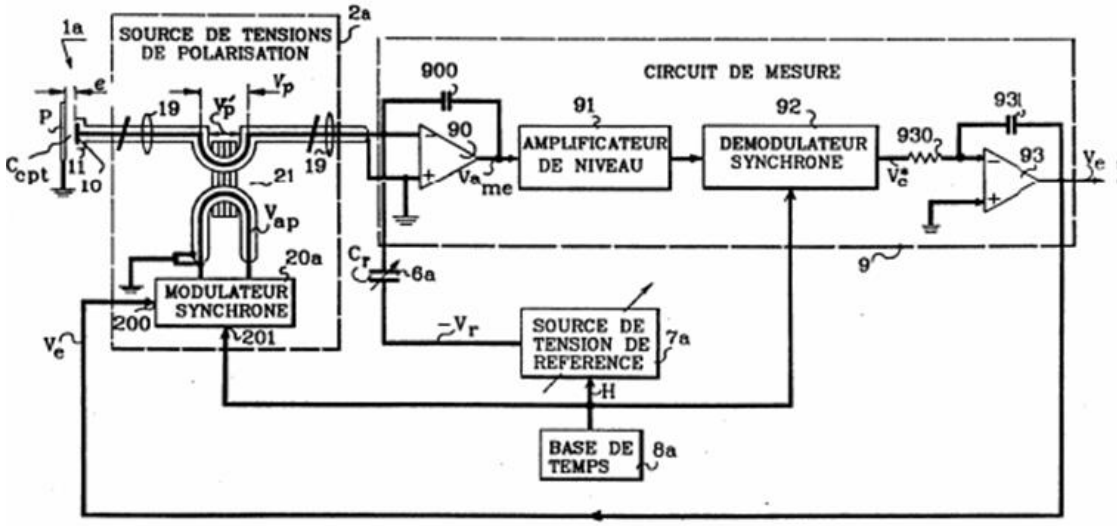

Figure 4.4 Capacitive probe circuit used at the ESRF.

The objective of the circuit assembly in Figure 4.4 is to produce an output DC voltage V_e which is linearly dependent on the gap distance e between the detection electrode and the conducting target P . The capacitance is measured by providing an oscillating voltage across the capacitor and ensuring through a closed loop that the charge on the detector electrode is matched with the charge on the reference capacitor. Effectively, the circuit matches capacitances through the device of frequency matching.

When the electrode bias voltage V_p is applied to the secondary winding of the transformer, a bias voltage V_p' is produced in the detector electrode (Figure 4.4). This in turn generates a current in the coaxial cable connected to the inverting input (–) of the operational amplifier (90). A second current is applied to this same amplifier entry via the reference capacitor C_r which is powered by the variable reference voltage ($7a$).The operational amplifier (90) produces a voltage Va_{me} which is a function of the difference between the first and second

currents. This voltage is amplified and the resulting signal demodulated by a synchronous demodulator (lock-in amplifier) (92). This demodulator is controlled by a precision time base (8*a*)[75].

A key component, the synchronous demodulator, or lock-in amplifier, has the advantage that it is not affected by noise in the input signal. The noise at the input to a lock-in amplifier appears at the output as an AC oscillation. This means that the desired DC signal response can be separated from the noise accompanying it in the output by means of a simple low-pass filter.[76] Integrating the output signal over a relatively long period of say 1 second permits the reduction of noise in the frequency domain to 1 Hz band around the reference signal.

The detector must be 'programmed' to recognize the signal of interest. This is achieved by supplying it with a reference voltage of the same frequency and with a fixed phase relationship to it. The lock-in amplifier demodulator operates by multiplying the input and reference signals together to yield the 'Demodulator Output' signal shown in Figure 4.5. Since there is no relative phase-shift between the signal and reference phases, the demodulator output is a sinusoid at twice the reference frequency but with a positive mean value. The mean level is the DC component of the demodulator output, so it can be easily isolated. The filtered output (V_e in Figure 4.4) is then output to an analog-to-digital converter (ADC) card.

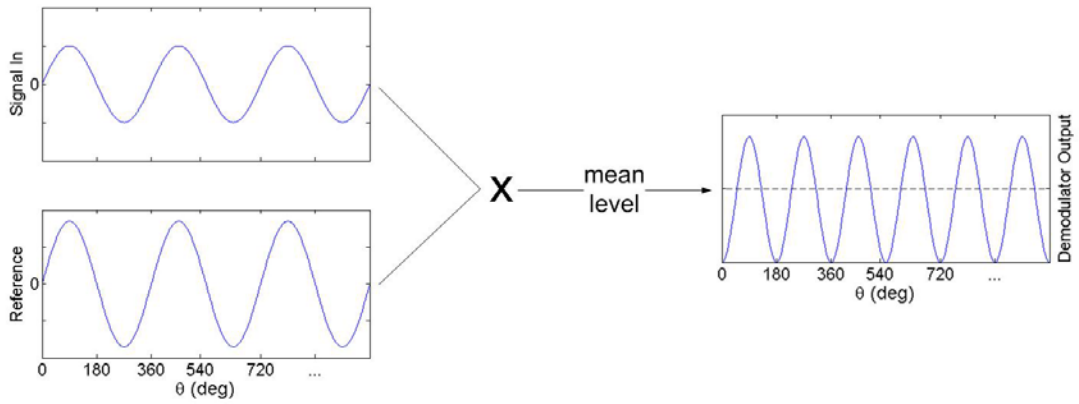

Figure 4.5 Lock in amplifier

The output signal V_e is also used for the negative 'high gain' feedback loop control of the electrode bias voltage V_p so as to satisfy the relation $Q_{cpt} = Q_r$ where Q_{cpt} is the charge formed between the detector electrode and the target P and Q_r is the charge on the reference

capacitor C_r. The equality of these two charges comes from the fact that current I_{err} through the operational amplifier (90) tends to zero so the two currents I_r and I_{cpt} input to this amplifier tend to equality. From this we can formulate the following relations:

$$\begin{aligned} &I_{err} = I_r - I_{cpt}; \quad I_{err} \to 0; \quad I_r = I_{cpt} \\ &\frac{V_r}{Z_r} = I_r; \quad \frac{V_p}{Z_{cpt}} = I_{cpt}; \quad \frac{V_r}{Z_r} = \frac{V_p}{Z_{cpt}} \\ &Q_r = Q_{cpt}; \quad V_r C_r = Q_r; \quad V_p C_{cpt} = Q_{cpt}; \quad V_r C_r = V_p C_{cpt} \end{aligned}$$

The circuit output voltage V_e controls the bias voltages V_p and V_p' through the relation

$$\begin{aligned} &V_p = V_p' = K_p V_e; \; V_r C_r = V_p C_{cpt} = K_p V_e C_{cpt} \\ &V_e = \frac{V_r}{K_p}\frac{C_r}{C_{cpt}} \\ &V_e = K_2 e \end{aligned} \tag{4.2}$$

where K_p and K_2 are constants and the capacitance between the detector electrode and target C_{cpt} is inversely proportional to the output voltage V_e and hence the distance e as required with equation (4.1) [75].

4.1.4.3 Capacitive probe calibration

The slightly non-linear proportionality constant K_2 requires in (4.2) calibration against a known distance. Capacitive probes and their electronics are calibrated on a dedicated bench against an Agilent 5519A laser interferometer. The interferometer (Agilent 10716A High Resolution Interferometer with an Agilent 10724A Plane Mirror Reflector) and electronics board (Agilent 10887B Calibrator Electronics housed in an Agilent 55292A USB Expansion Module) have a nominal resolution of 2.5 nm.

The calibration consists of aligning the target and probe at a minimum probe reading, which also corresponds to the minimum probe target distance, and then moving the target in appropriate steps to the maximum probe reading. The calibration bench is shown in Figure 4.6.

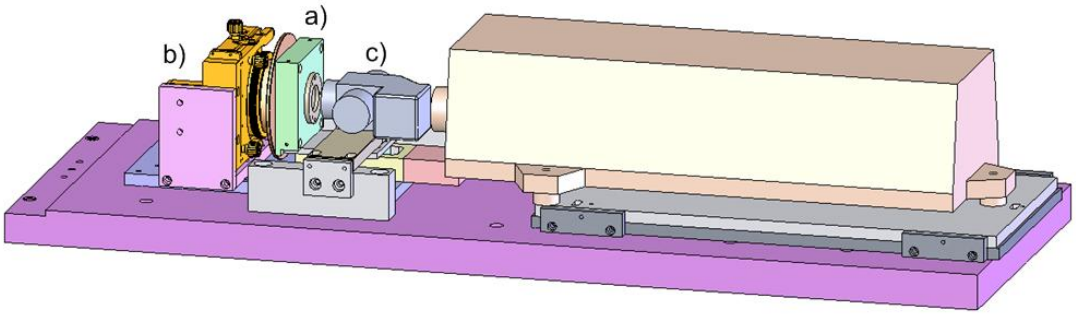

Figure 4.6 Capacitive probe calibration bench showing: a) the servo-controlled target; b) the probe support and c) the high precision interferometer.

A calibration curve can be constructed from the probe versus interferometer readings. An example of this type of calibration curve is given in Figure 4.7. In the top left graph, the probe output is plotted against the interferometer displacement. The top right graph shows the non-linearity of the probe output. The bottom graph shows the residuals with respect to a polynomial model.

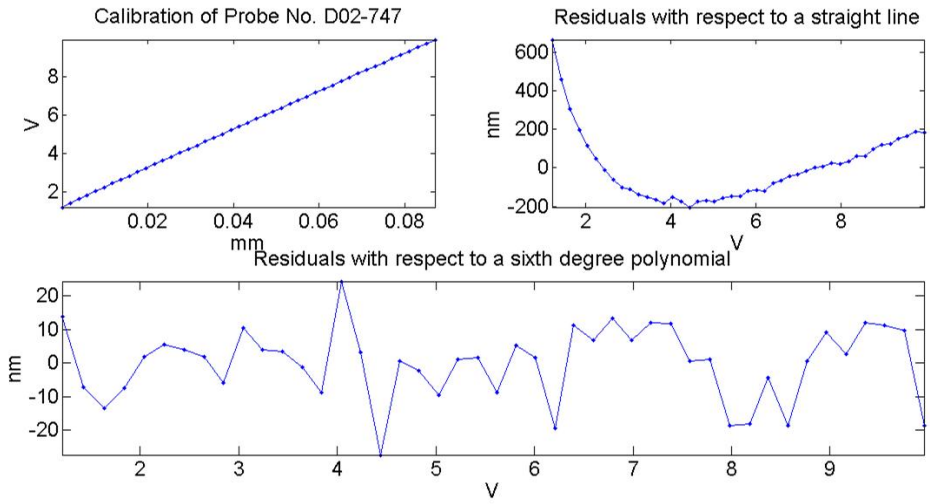

Figure 4.7 Example of a capacitive probe calibration curve.

At the nominal working distance of 20 mm between the interferometer and the mirror, capacitive probe measurement range of 250 μm, and a maximum tolerated alignment angle deviation of 30 arc minutes; interferometer Abbe errors will be less than 10 nm. The interferometer readings are corrected for refractive effects with uncertainty of $0.4\times10^{-6}L$ where L is the distance measured (i.e. 20 mm). Meteorological parameters do not vary over the five minutes required to make the calibration which typically consists of 40 points or

more. The expected uncertainty ($k = 1$) for one point in the calibration curve of a probe with a measurement range of 250µm is 13 nm.

4.1.4.4 Precautions using capacitive probes

Several precautions must be observed when using capacitive probes. Because the detector's electric field is focused by guarding, it creates a field that is a projection of its size and shape. A cylindrically shaped sensor such as the type used in this work projects a cylindrical electric field. However, the projected field spreads over the gap distance. This spreading can be up to 30%. Therefore the target surface area must be at least 30% larger than the sensor area. Secondly, the range of the sensor is a function of its area - the greater the area, the larger the range. In general, the maximum useful gap is approximately 40% of the sensor diameter. However in practice, the gap distance is typically considerably less than this. Circular probe sensors with radius of 3 mm were used for all of the measures in this work. Target shape can also influence the probe output. For example spherical or cylindrical shaped targets can considerably alter probe output with respect to a flat reference surface. These effects have been studied in [77]. The main work here involves measuring to a flat and to a cylindrical surface with a radius of 500 mm. In the case of the cylindrical surface, the arc to chord separation is just 5 nm for a 3 mm radius probe. This is below the sensitivity of one part in 10000 of the range given by the manufacturer Fogale Nanotech for the capacitive probes and electronics (i.e. 25 nm for a 250 µm range probe).

Another problem is ensuring the parallelism between the probe and target surfaces. Clearly if the probe is tilted the shape of the spot where the field hits the target elongates and changes the interaction between the probe and target. Typically probe misalignment is such that the minimum reading is in the order of 10 to 20 µm. This is an indication of the misalignment of the parallelism of the probe with respect to the target. The 250 µm range Fogale Nanotech probes measure from zero to an offset of 250 µm. Thus with 6 mm overall diameter probes (3 mm radius) and measurement range of 250 µm this represents a modest elongation of 20 µm for 6000 µm if the probe is maximally misaligned (i.e. ~11 arc minutes). Probe alignment is investigated in more detail in section 6.6.

4.2 Form error - spindle motion error separation (FESM)

4.2.1 Introduction to FESM with the HCC

The horizontal circle calibration method employed with the HCC consists of sighting a target with SMS to be calibrated, turning the HCC through an angle, bringing the instrument back through the same angle; re-sighting the target and comparing the results (refer to section 3.4.4). For this to work correctly, the primary (vertical or z) SMS instrument and HCC axes must be coincident and all of their rotations must be identical in magnitude and opposite in sign. In practice, this is not the case.

For a rotation about the principal axis of the HCC, there will be coupled unwanted movements associated with its other five other degrees of freedom. These movements are due to spindle motion errors. Spindle motion errors are combinations of movement or run out along the x, y, and z axes ($sx(\theta)$, $sy(\theta)$, $sz(\theta)$) and angular movements ($wx(\theta)$ and $wy(\theta)$) due to wobble (i.e. inclination) about the x and y axes as the rotation stage turns through an angle θ about its primary z axis. The notion of spindle motion error is inherently complex and virtually always expressed in terms how it manifests in the context of a particular application. For example, it is what causes a perfectly set tool to cut a non-circular part. As will be shown in the next chapter (section 5.5.8), uncorrected spindle motion error is the chief contributing factor to the uncertainty in the HCC.

One way to measure spindle motion errors is with capacitive probes (section 4.1.4). Probe measurements are made to an artefact fixed to, or actually part of the object being moved. The probe(s) must be independent of the object in motion. Regardless of its nominal shape, the artefact will not be geometrically perfect. The deviations from artefact nominal shape are referred to as form errors. When a probe is employed to measure spindle motion error, it also unavoidably measures the form error of the artefact. For a reliable measure of movement, this artefact form error must be separated from the spindle motions.

Several techniques have been developed for the accurate measure of part features and in particular the separation of form errors from the part feature of interest. A review of many of these techniques is given in [78]. For technical reasons that will be discussed below, there is

only one technique, multi-probe form error - spindle motion error separation (FESM), that can be used on the HCC. Other related techniques are the classical reversal and multi-orientation or multi-step error separation methods. A review of these three methods is found in [79]. They are also discussed extensively in [80-86]. Additionally, an ISO standard [87] provides methods of specifying and testing the geometric accuracy of the axes of rotation used in machine tools. The scope of this standard can, in principle, can be applied to spindle motion generally.

Classical reversal techniques require a mechanical manipulation of the measurement system which results in a change in the sign of one component of the spindle motion and form errors. Simple arithmetic manipulation of the measurement signal then permits the separation of the errors into their component parts. The multi-probe FESM, with the multi-step method, comprises the family of so-called model based methods. Model based methods make assumptions about the form of the underlying errors. They work by manipulating the measurement system in such a way as to change the phase of one component of the combined error. The particularity of the model based methods is that although they can come very close, they are not theoretically capable of fully separating the form error from spindle motion error. In other words, the solution to the model is always mathematically incomplete. In practice this is not generally a problem.

4.2.2 Classical reversal FESM techniques

4.2.2.1 Radial error separation

The Donaldson Reversal is used to separate spindle radial motion and artefact form error. The principle of the technique is illustrated in Figure 4.8. The separation is made in two steps. At the start, the artefact and displacement probe are in the forward position (a in Figure 4.8). The artefact is rotated about the z axis while displacement measures $m_F(\theta)$ are made by the probe. The artefact and displacement probe are mechanically reversed (positioned at 180 º with respect to the forward position) and displacement measures $m_R(\theta)$ are made with the probe while the artefact is rotated about the z axis (b in Figure 4.8).

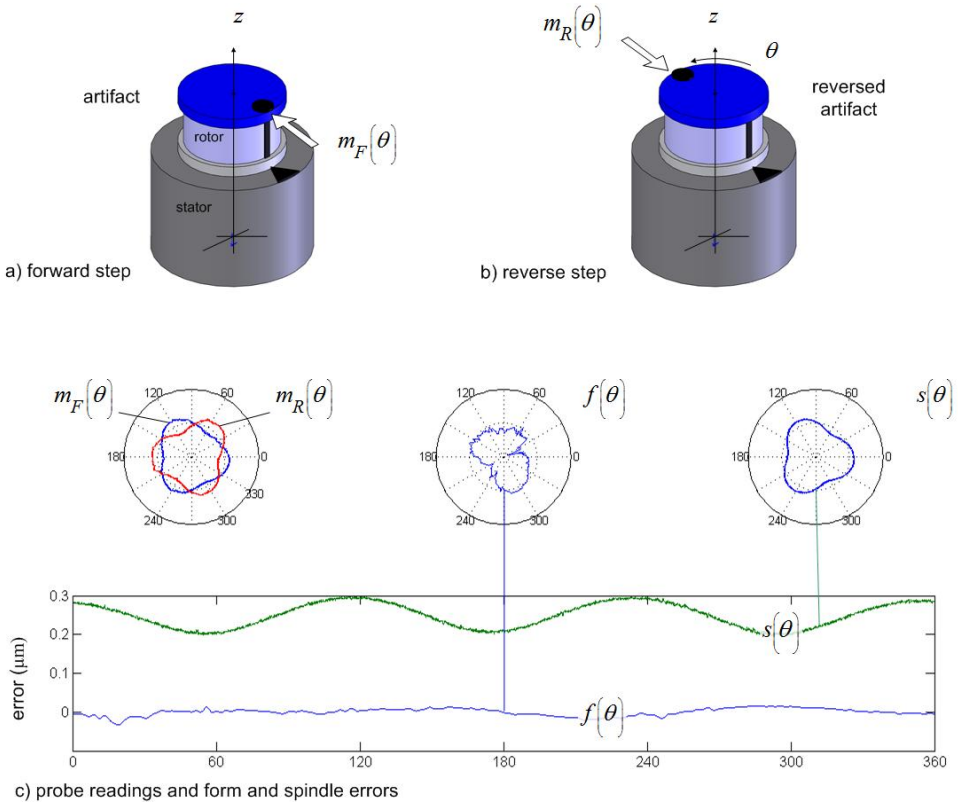

Figure 4.8 Donaldson Reversal method is shown showing example probe readings $m_F(\theta)$ and $m_R(\theta)$; the artefact form error $fe(\theta)$; the spindle motion $s(\theta)$; and the form and spindle error developed over 360 degrees.

The probe readings can be expressed as a function of the form and spindle motion errors:

$$\begin{aligned} m_F(\theta) &= fe(\theta) + s(\theta) \\ m_R(\theta) &= fe(\theta) + s(\theta + \pi) \\ &= fe(\theta) - s(\theta) \end{aligned} \tag{4.3}$$

Simple arithmetic manipulation of these equations gives the artefact form and the spindle motion errors directly:

$$\begin{aligned} fe(\theta) &= \frac{m_F(\theta) + m_R(\theta)}{2} \\ s(\theta) &= \frac{m_F(\theta) - m_R(\theta)}{2} \end{aligned} \tag{4.4}$$

4.2.2.2 Face error separation

In an exactly analogous manner, the form $fe(\theta)$, tilt $t(\theta)$ and axial $sz(\theta)$ error motions can be separated from the artefact form error using the so called Estler Face motion reversal (Figure 4.9). The artefact is rotated about the z axis while displacement measures $m_1(\theta)$ and

$m_3(\theta)$ are made by probes 1 and 2. The artefact and displacement probe 1 are mechanically reversed (positioned at 180 º with respect to the forward position) and displacement measures $m_2(\theta)$ and $m_4(\theta)$ are made with the probes while the artefact is rotated about the z axis. Note that probe 2 nominally located in the centre of the artefact face is not moved.

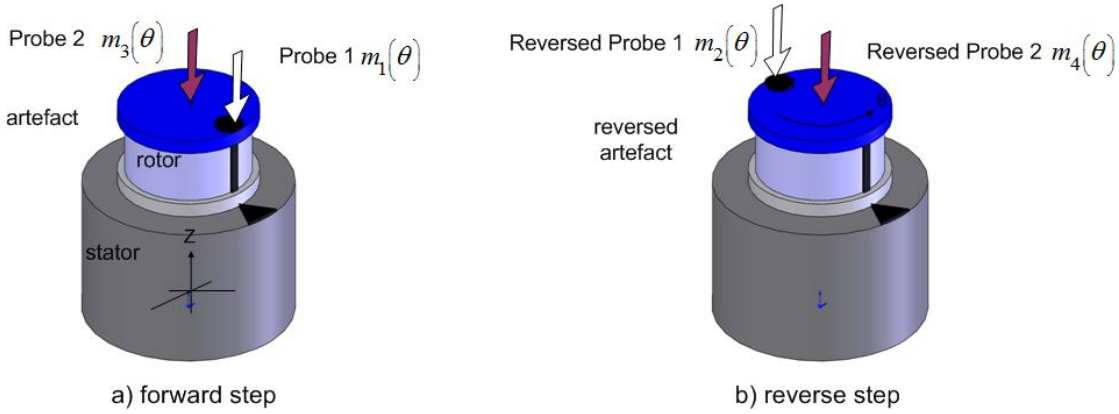

Figure 4.9 Estler face reversal.

The probe readings can be expressed as the summation of the artefact form error, and the tilt and axial motions:

$$\begin{aligned} m_1(\theta) &= fe(\theta) + t(\theta)r + sz(\theta) \\ m_2(\theta) &= fe(\theta) + t(\theta+\pi)r + sz(\theta) \\ &= fe(\theta) - t(\theta)r + sz(\theta) \end{aligned} \tag{4.5}$$

Since probe 2 only measures axial motion, the capacitive probe reading outputs $m_3(\theta)$ and $m_4(\theta)$ can be averaged to give $sz(\theta)$. Here r is the distance between probe 1 and probe 2 in Figure 4.9.

$$sz(\theta) = \frac{m_3(\theta) + m_4(\theta)}{2} \tag{4.6}$$

The tilt error $t(\theta)$ can then be derived by subtracting $m_2(\theta)$ from $m_{1(\theta)}$ in (4.5) to give:

$$t(\theta) = \frac{m_1(\theta) - m_2(\theta)}{2r} \tag{4.7}$$

Knowing $t(\theta)$ and $sz(\theta)$ gives $fe(\theta)$ from either one of the equations for $m_1(\theta)$ or $m_2(\theta)$ in (4.5). One can also add $m_1(\theta)$ and $m_2(\theta)$ and knowing $sz(\theta)$ solve (4.8)

$$fe(\theta) = \frac{m_1(\theta) + m_2(\theta) - 2sz(\theta)}{2} \tag{4.8}$$

4.2.2.3 Remarks concerning reversal FESM techniques

These two reversal techniques (Donaldson and Estler) can be extended to the general error motion case in 3D with probes oriented in arbitrary directions when the appropriate measurement geometry applies (e.g. with a spherical artefact). [79]

It is implicitly assumed in the classical reversal technique that the form of the readings $m_1(\theta), m_2(\theta), m_3(\theta), m_4(\theta)$ remain constant. This is to say that after manipulation, the reverse signals $m_2(\theta)$ and $m_4(\theta)$ are identical, apart from asynchronous movements, to $m_1(\theta)$ and $m_2(\theta)$ respectively. This presupposes there are no errors in angular reversal such as shifts in the radial and axial location on moving the part and probe. Similarly, the pieces and indeed the probe must not evolve (e.g. due to thermal effects) between the reversal manipulations. Finally, this technique, as with the multi-probe discussed next, can only compensate for the effects of repeatable error motions. Random fluctuations and measurement noise need to be small enough for this to be sensible. In classical roundness systems, random effects are averaged out by taking data over several revolutions. In principle, this is valid, but would need to be confirmed with the HCC which has fixed arc rotation of 370 degrees.

Unfortunately, despite their superior theoretical performance in FESM (i.e. total separation), the reversal techniques cannot be used because they require the physical manipulation of the probe which is not (presently) possible with the HCC. Another point to bear in mind is that reversal techniques require two separate manipulations to extract the form error and spindle motion error. This is not compatible with a real time determination of this information that we require in chapter 5.

4.2.3 Multi-probe FESM techniques

4.2.3.1 Radial error separation

Much of the initial work concerning multi-probe (FESM) separation technique is outlined in [81]. This is a model based method [88] that assumes the underlying error can be represented by a Fourier series.

A minimum of three probes are required for this technique to work. Following the argument of [81], we assume the probe signal is a combination of the form and spindle errors $m(\theta) = fe(\theta) + s(\theta)$. If two probes are used, to detect $fe(\theta)$, the spindle error contribution $s(\theta)$ must be undetectable or zero. If the part has an instantaneous movement of s at an angle δ with respect to the datum, and the two probes are placed at angles φ_1 and φ_2, they will see movements of $s\cos(\delta - \varphi_1)$ and $s\cos(\delta - \varphi_2)$. For the probes to not see s equation (4.9) must be satisfied.

$$s\cos(\delta - \varphi_1) + s\cos(\delta - \varphi_2) = 0 \tag{4.9}$$

This condition can only be satisfied if $\varphi_1 = \varphi_2$ (the probes occupy the same place) or when $\varphi_1 = \pi + \varphi_2$ (the probes are diametrically opposed). When probes are diametrically opposed, the odd harmonics of the underlying Fourier series model representation of $fe(\theta)$ are zero. Therefore two probes will not give sufficient information to determine $fe(\theta)$. It turns out that using three or more probes under controlled conditions will provide sufficient information to separate the form error from the spindle motion. The multi-probe FESM technique is the subject of the rest of this section.

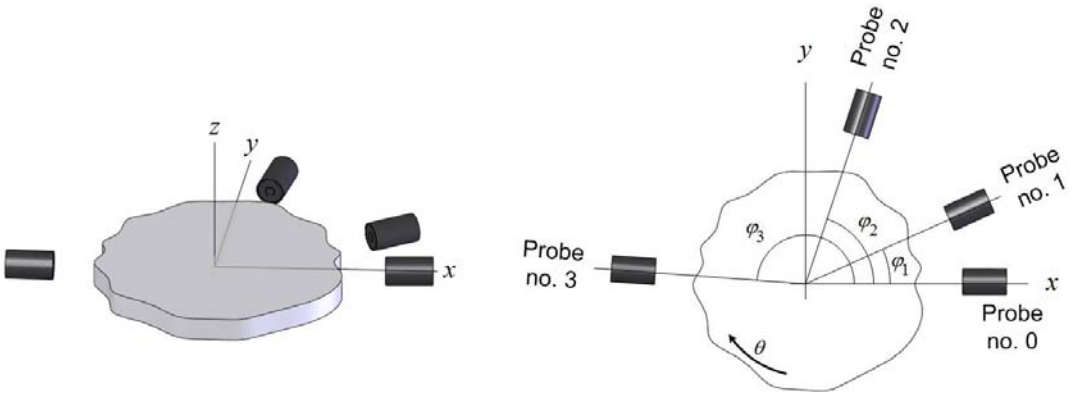

Figure 4.10 Setup for the multi-probe method of motion/form error separation. Several probes are arranged around the artefact at angles $\varphi_1, \varphi_2, \varphi_3 \cdots$. Probe no. 0 is aligned along the x axis. The probes are stationary and make readings $m_1(\theta), m_2(\theta), m_3(\theta) \cdots$ while the artefact rotates about its z axis.

The general setup for the multi-probe technique is shown in Figure 4.10. The probes themselves are positioned at angles φ_1, φ_2, $\varphi_3 \cdots$ with respect to probe no. 0 which is aligned

along the x axis and always equal to zero. Measurements from the different probes $m_0(\theta),\ m_1(\theta),\ m_2(\theta)\cdots$ are made simultaneously.

The multi-probe technique [81, 89-91] will first be derived and then simplified to the commonly used three point technique. The underlying principle of this method is the elimination of spindle motion from the observations $m_0(\theta),\ m_1(\theta),\ m_2(\theta)\cdots$ and the subsequent recombination of the form error $fe(\theta)$ by means of a Fourier series.

The observations or probe readings can be represented by equation (4.10). Here $sx(\theta)$ and $sy(\theta)$ are spindle error motions in the x and y directions. There are $n+1$ probes in the setup.

$$\begin{aligned} m_0(\theta) &= fe(\theta) + sx(\theta) \\ m_1(\theta) &= fe(\theta-\varphi_1) + sx(\theta)\cos(\varphi_1) + sy(\theta)\sin(\varphi_1) \\ &\vdots \\ m_n(\theta) &= fe(\theta-\varphi_n) + sx(\theta)\cos(\varphi_n) + sy(\theta)\sin(\varphi_n) \end{aligned} \tag{4.10}$$

Multiplying the measurement equations $m_i \to i = 0\cdots n$ in (4.10) by weighting coefficients 1, $a_1\cdots a_n$ and summing the results eliminates the spindle error contributions $sx(\theta)$ and $sy(\theta)$ by forcing them to be zero.

$$\begin{aligned} 1\{m_0(\theta)\} &= 1\{fe(\theta) + sx(\theta)\} \\ a_1\{m_1(\theta)\} &= a_1\{fe(\theta-\varphi_1) + sx(\theta)\cos(\varphi_1) + sy(\theta)\sin(\varphi_1)\} \\ &\vdots \\ a_n\{m_n(\theta)\} &= a_n\{fe(\theta-\varphi_n) + sx(\theta)\cos(\varphi_n) + sy(\theta)\sin(\varphi_n)\} \end{aligned} \tag{4.11}$$

The constants $a_i \to i = 2\cdots n$ are found by solving the simultaneous set of equations

$$\begin{aligned} a_1\cos(\varphi_1) + a_2\cos(\varphi_2) + \cdots + a_n\cos(\varphi_n) + 1 = 0 \\ a_1\sin(\varphi_1) + a_2\sin(\varphi_2) + \cdots + a_n\sin(\varphi_n) + 0 = 0 \end{aligned} \tag{4.12}$$

In (4.12), there are two equations for n unknown constants. Therefore a minimum of two coefficients a_1 and a_2 are required to satisfy (4.12) (i.e. n=2 and there are three probes in total). These coefficients are pre-determined by the orientation angles φ_1 and φ_2 of the probes and are given by $a_1 = \sin\varphi_2 / \sin(\varphi_1 - \varphi_2)$ and $a_2 = -\sin\varphi_1 / \sin(\varphi_1 - \varphi_2)$. More probes give

$n-2$ degrees of freedom in selecting $(a_3 \cdots a_n)$ and theoretically avoid harmonic suppression and improve measurement accuracy. Other problems, most notably their alignment, can reduce the advantages of more than 3 probes. Furthermore, even with three probes, the problem of harmonic suppression can be largely avoided (see section 4.2.4). Nevertheless, there remains the problem of determining the coefficients $(a_3 \cdots a_n)$ if more that three probes are used. Several propositions for the selection of these coefficients are discussed in [84].

It is assumed that the form error $fe(\theta)$ can be represented by a Fourier series where A_k and B_k are the Fourier coefficients

$$fe(\theta) = \sum_{k=1}^{\infty} \left(A_k \cos k\theta + B_k \sin k\theta \right) \tag{4.13}$$

Substituting (4.13) into the summed result of equation (4.11) gives:

$$\begin{aligned} m_0(\theta) + a_1 m_1(\theta) + \cdots + a_n m_n(\theta) \quad = \quad & \sum_{k=1}^{\infty} \left(A_k \cos k\theta + B_k \sin k\theta \right) \quad \cdots \\ & + a_1 \sum_{k=1}^{\infty} \left(A_k \cos k(\theta - \varphi_1) + B_k \sin k(\theta - \varphi_2) \right) \quad \cdots \\ & \vdots \\ & + a_n \sum_{k=1}^{\infty} \left(A_k \cos k(\theta - \varphi_n) + B_k \sin k(\theta - \varphi_n) \right) \end{aligned} \tag{4.14}$$

Expanding (4.14) using angle addition identities and collecting common terms of $A_k \cos k\theta$, $A_k \sin k\theta$, $B_k \cos k\theta$ and $B_k \sin k\theta$; and equating the left hand term of equation (4.14) to $M(\theta)$ gives (4.15).

$$\begin{aligned} M(\theta) \quad = \quad & \sum_{k=1}^{\infty} A_k \cos k\theta \left(1 + a_1 \cos k\varphi_1 + \cdots a_n \cos k\varphi_n \right) \quad \cdots \\ & + \sum_{k=1}^{\infty} A_k \sin k\theta \left(a_1 \sin k\varphi_1 + \cdots a_n \sin k\varphi_n \right) \quad \cdots \\ & + \sum_{k=1}^{\infty} B_k \sin k\theta \left(1 + a_1 \cos k\varphi_1 + \cdots a_n \cos k\varphi_n \right) \quad \cdots \\ & + \sum_{k=1}^{\infty} B_k \cos k\theta \left(a_1 \sin k\varphi_1 + \cdots a_n \sin k\varphi_n \right) \end{aligned} \tag{4.15}$$

Finally defining the terms $\alpha_k = 1 + a_1 \cos k\varphi_1 + \cdots a_n \cos k\varphi_n$ and $\beta_k = a_1 \sin k\varphi_1 + \cdots a_n \sin k\varphi_n$; and remarking from equation (4.12) that when $k = 1$, both $\alpha_1 = 0$ and $\beta_1 = 0$ we get equation (4.16).

$$M(\theta)=\sum_{k=2}^{\infty}\left(A_k\alpha_k-B_k\beta_k\right)\cos k\theta+\sum_{k=2}^{\infty}\left(A_k\beta_k+B_k\alpha_k\right)\sin k\theta \tag{4.16}$$

Calculating the discrete Fourier series of the summed probe readings $M(\theta)$ provides the coefficients F_k and G_k found by in (4.17) The coefficients A_k and B_k of equation (4.13) are then found by solving the matrix equation (4.18).

$$M(\theta)=\sum_{k=2}^{m}\left(F_k\cos k\theta+G_k\sin k\theta\right) \tag{4.17}$$

$$\begin{pmatrix}\alpha_k & -\beta_k\\ \beta_k & \alpha_k\end{pmatrix}\begin{pmatrix}A_k\\ B_k\end{pmatrix}=\begin{pmatrix}F_k\\ G_k\end{pmatrix}$$
$$A_k=\frac{F_k\alpha_k+G_k\beta_k}{\alpha_k^2+\beta_k^2} \tag{4.18}$$
$$B_k=\frac{F_k\beta_k-G_k\alpha_k}{\alpha_k^2+\beta_k^2}$$

In equations (4.17) and (4.18) $k=2\cdots m$, where m is the number of discrete harmonics used in the Fourier series. The $k=1$ harmonic represents the eccentricity or centring error of the principal axis of the artefact and the rotation stage. This once around error is generally removed from radial motion error measurements [79]. It contains no $fe(\theta)$, $sx(\theta)$ or $sy(\theta)$ information.

With A_k and B_k determined, $fe(\theta)$ is calculated from (4.13), and finally $sx(\theta)$ and $sy(\theta)$ are derived from (4.10) as shown below in (4.19).

$$\begin{aligned}sx(\theta)&=m_1(\theta)-fe(\theta)\\ sy(\theta)&=\left[m_2(\theta)-fe(\theta-\varphi_1)-sx(\theta)\cos\varphi_1\right]/\sin\varphi_1\end{aligned} \tag{4.19}$$

Before $sy(\theta)$ can be calculated, the term $fe(\theta-\varphi_1)$ must be determined using $fe(\theta)$, the form error determined using equation (4.13) for capacitive probe number 0 (Figure 4.10) lying on the x axis; to the form error seen by probe number 1 (Figure 4.10) lying at some arbitrary angle φ_1 with respect to the x axis. This requires shifting the form error $fe(\theta)$ by the angle φ_1. This manner in which this shift is accomplished is discussed in section 5.3.5.

4.2.3.2 Face error separation

The multi-probe error separation can also be used to determine the axial $sz(\theta)$ and wobble $wx(\theta)$ and $wy(\theta)$ error motions by separating them from the artefact vertical face form error $fe(\theta)$. The equations for the $n+1$ probe readings are given by equation (4.20).

$$\begin{aligned} m_0(\theta) &= fe(\theta) + sz(\theta) + wx(\theta) \\ m_1(\theta) &= fe(\theta - \varphi_1) + sz(\theta) + wx(\theta)\cos(\varphi_1) + wy(\theta)\sin(\varphi_1) \\ &\vdots \\ m_n(\theta) &= fe(\theta - \varphi_n) + sz(\theta) + wy(\theta)\cos(\varphi_n) + wy(\theta)\sin(\varphi_n) \end{aligned} \tag{4.20}$$

With four unknowns in (4.20), a minimum of four probes are required. As with the multi-probe radial separation technique the measurement equations $m_i \to i = 0 \cdots n$ in (4.20) are multiplied by weighting coefficients 1, $a_1, \cdots, a_n$ and the results summed eliminating axial $sz(\theta)$ and wobble $wx(\theta)$ and $wy(\theta)$ error motion contributions.

$$\begin{aligned} 1\{m_0(\theta)\} &= 1\{fe(\theta) + sz(\theta) + wx(\theta)\} \\ a_1\{m_1(\theta)\} &= a_1\{fe(\theta - \varphi_1) + sz(\theta) + wx(\theta)\cos(\varphi_1) + wy(\theta)\sin(\varphi_1)\} \\ &\vdots \\ a_n\{m_n(\theta)\} &= a_n\{fe(\theta - \varphi_n) + sz(\theta) + wx(\theta)\cos(\varphi_n) + wy(\theta)\sin(\varphi_n)\} \end{aligned} \tag{4.21}$$

The coefficients $a_1 \cdots a_3$ are found in the same way as (4.12) by solving the set of simultaneous equations (4.22). With four probes the coefficients $a_1 \cdots a_3$ are fixed. More probes give $n-3$ degrees of freedom in selecting $(a_4 \cdots a_n)$ and can theoretically avoid harmonic suppression and improve measurement accuracy [83, 84]. (Refer to section 4.2.4 Harmonic suppression in multi-probe FESM techniques for a further discussion of this subject.) Once again this improvement is strongly dependent upon probe alignment.

$$\begin{aligned} a_1 &+ a_2 &+\cdots+ a_n &+ 1 &= 0 \\ a_1\cos(\varphi_1) &+ a_2\cos(\varphi_2) &+\cdots+ a_n\cos(\varphi_n) &+ 1 &= 0 \\ a_1\sin(\varphi_1) &+ a_2\sin(\varphi_2) &+\cdots+ a_n\sin(\varphi_n) &+ 0 &= 0 \end{aligned} \tag{4.22}$$

From here, the solution to the form error follows analogously the radial error separation technique described in equations (4.13) to (4.18). With the $fe(\theta)$ known, $sz(\theta)$, $wx(\theta)$ and $wy(\theta)$ can be determined by solving (4.23) by least squares.

$$\begin{pmatrix} 1 & \cos(0) & \sin(0) \\ 1 & \cos(\varphi_1) & \sin(\varphi_1) \\ & \vdots & \\ 1 & \cos(\varphi_n) & \sin(\varphi_n) \end{pmatrix} \begin{pmatrix} sz(\theta) \\ wx(\theta) \\ wy(\theta) \end{pmatrix} = \begin{pmatrix} m(\theta)_0 - fe(\theta) \\ m(\theta)_1 - fe(\theta - \varphi_1) \\ \vdots \\ m(\theta)_n - fe(\theta - \varphi_n) \end{pmatrix} \tag{4.23}$$

However, as with the radial error separation, before doing so, $fe(\theta)$ must be shifted by $\varphi_1 \cdots \varphi_n$ to $fe(\theta - \varphi_1) \cdots fe(\theta - \varphi_n)$. This is discussed in the section 5.3.5.

4.2.4 Harmonic suppression in multi-probe FESM techniques

4.2.4.1 The problem statement

Harmonic suppression is well known phenomena with form error – spindle motion separation techniques and of particular interest in the multi-probe error separation. However, the interest in the harmonic behaviour of this technique goes beyond this classical problem. In particular it is a determinant factor in the HCC uncertainty calculation. Because of the importance of the multi-probe FESM technique in the SMS horizontal angle calibration using the HCC, the harmonic behaviour of this technique is fully investigated in this section. It will provide the necessary background and groundwork for the uncertainty calculation in chapter 6.

The determination of the form error requires the solution of equation (4.18) (repeated here for convenience).

$$\begin{pmatrix} \alpha_k & -\beta_k \\ \beta_k & \alpha_k \end{pmatrix} \begin{pmatrix} A_k \\ B_k \end{pmatrix} = \begin{pmatrix} F_k \\ G_k \end{pmatrix}$$

$$A_k = \frac{F_k \alpha_k + G_k \beta_k}{\alpha_k^2 + \beta_k^2} \tag{4.18}$$

$$B_k = \frac{F_k \beta_k - G_k \alpha_k}{\alpha_k^2 + \beta_k^2}$$

This equation is not defined when $\alpha_k^2 + \beta_k^2 = 0$. When this occurs, [83, 84] states that harmonics can be distorted or suppressed. In fact, harmonics are not suppressed unless they are explicitly removed from the calculation by eliminating all values associated with the harmonic k in equation (4.18) when $\alpha_k^2 + \beta_k^2 = 0$ or specifically when $\alpha_k = \beta_k = 0$. Recall, the probe signal does not contain spindle or form error but rather somewhat scrambled out-of-roundness information.[81] If harmonics k are included when $\alpha_k = \beta_k = 0$ the form error is

at minimum perturbed for the purely mathematical case and unusable for the normal case when noisy probe readings are used. The notion of a noisy signal, or a signal polluted with random error is essential. Many of the results discussed in this section related to harmonic errors are contingent upon a noisy signal.

The obvious response to this is to remove the incriminating harmonic. Doing this however also removes the information associated with it. This is not necessarily problematic; particularly if the contribution of the harmonic is small. Typically this is the case of higher order harmonics. However, it can be unacceptable if the eliminated information is essential. One important question is; under what circumstances can harmonic suppression be problematic? This section aims to answer, or at least shed light on this question by examining the nature of this phenomenon.

Recall by definition (section 4.2.3.1) that α_k and β_k are given by equation (4.24).

$$\begin{aligned} \alpha_k &= 1 + a_1 \cos k\varphi_1 + \cdots a_n \cos k\varphi_n \\ \beta_k &= a_1 \sin k\varphi_1 + \cdots a_n \sin k\varphi_n \end{aligned} \tag{4.24}$$

One reason to use more than the minimum number of probes is to try and avoid the harmonic suppression problem. Thus if we consider the worst case scenario for the time being as involving the minimum three probe configuration, we can get a clearer idea of its nature. The multi-probe configuration will be examined in detail in chapters 5 and 6.

Recall that the solution for a_1 and a_2 in equation (4.12) for the minimum of three probes is given by (4.25).

$$\begin{aligned} \alpha_k &= 1 + a_1 \cos k\varphi_1 + a_2 \cos k\varphi_2 \\ \beta_k &= a_1 \sin k\varphi_1 + a_2 \sin k\varphi_2 \\ \text{where} & \\ a_1 &= \sin\varphi_2 / \sin(\varphi_1 - \varphi_2) \\ a_2 &= -\sin\varphi_1 / \sin(\varphi_1 - \varphi_2) \end{aligned} \tag{4.25}$$

Substituting a_1 and a_2 into α_k and β_k, equating to zero, rearranging, and using angle identities gives the relationships in (4.26) .

$$
\begin{aligned}
\alpha_k = 0 &= 1 + \frac{\sin\varphi_2 \cos k\varphi_1 - \sin\varphi_1 \cos k\varphi_2}{\sin(\varphi_1 - \varphi_2)} \\
-\sin(\varphi_1 - \varphi_2) &= \sin\varphi_2 \cos k\varphi_1 - \sin\varphi_1 \cos k\varphi_2 \\
\sin\varphi_2 \cos\varphi_1 - \sin\varphi_1 \cos\varphi_2 &= \sin\varphi_2 \cos k\varphi_1 - \sin\varphi_1 \cos k\varphi_2
\end{aligned}
\qquad (4.26)
$$

$$
\begin{aligned}
\beta_k = 0 &= \frac{\sin\varphi_2 \sin k\varphi_1 - \sin\varphi_1 \sin k\varphi_2}{\sin(\varphi_1 - \varphi_2)} \\
\sin\varphi_2 \sin k\varphi_1 &= \sin k\varphi_2 \sin\varphi_1
\end{aligned}
$$

It is clear from these relations that when $\alpha_k = \beta_k = 0$, $\sin\varphi_1 = \sin k\varphi_1$ and $\sin\varphi_2 = \sin k\varphi_2$; and $\cos\varphi_1 = \cos k\varphi_1$ and $\cos\varphi_2 = \cos k\varphi_2$. This is because $\sin\varphi_1$ cannot be equal to $\sin\varphi_2$ and $\cos\varphi_1$ cannot be equal to $\cos\varphi_2$ for all cases, or the two probes would be in the same place. Recall also that the first probe in the configuration is by definition at $\varphi_0 = 0$ so we cannot have $\varphi_1 = 0$ and $\varphi_2 = \pi$ or vice versa either.

An analytic solution for k in the equations in (4.26) is not obvious [82], however, (4.25) can be investigated numerically to find k when $\alpha_k = \beta_k = 0$. Therefore (4.25) has been investigated[15] and shows that this condition occurs at values for harmonics j where $j = k \pm 1$ when $\mathrm{mod}(k\varphi_1, 360) = \mathrm{mod}(k\varphi_2, 360) = 0$. Here, mod refers to $k\varphi_i$ modulus 360 (or 2π)[16,17,18,19] [6, 92, 93]. This also implies that when $\alpha_k = \beta_k = 0$, $\sin k\varphi_1 = \sin k\varphi_2 = 0$.[20]

For example, for $\varphi_1 = 22.5°$ and $\varphi_2 = 60°$ we find the first occurrence $\mathrm{mod}(k \times 22.5, 360) = \mathrm{mod}(k \times 60.0, 360) = 0$ when $k = 48$. Therefore, $\alpha_{47} = \beta_{47} = 0$ and $\alpha_{49} = \beta_{49} = 0$. This degenerate condition will also occur at integer multiples of k (i.e. $q \times k$ for $q = 1 \cdots p$ and $p < m$) where m is the number of discrete harmonics used in the

[15] Numerical investigation of rational number (e.g. $(3/7)\pi\,(9/12)\pi\cdots$) pairs for denominators from 1 to 30 was made.
[16] In Matlab Modulus after division is given by M=mod(x,y).
[17] In computing, the modulo operation finds the remainder of division of one number by another. Given two numbers, a (the dividend) and n (the divisor), a modulo n (abbreviated as $a \mod n$) is the remainder, on division of a by n. For instance, the expression "7 mod 3" would evaluate to 1, while "9 mod 3" would evaluate to 0.
[18] A remainder left when a given number is divided into some integer; also, a number congruent to a given number modulo a third number;
[19] For each positive integer n, the relation of congruence between integers is defined as follows: a is congruent to b modulo n if $a - b$ is a multiple of n.
[20] This relationship is not formally proved. It has been shown to be true for all rational number numerator denominator pairs for integers from 1 to 30.

Fourier series in equation (4.17). Thus for our example, $\alpha_k = \beta_k = 0$ occurs at harmonics $k = 47,\ 49,\ 95,\ 97,\ 143,\ 145$ below the cut off $m = 180$. The behaviour of α and β and $1/\left(\alpha^2 + \beta^2\right)$ for the above example is shown in Figure 4.11.

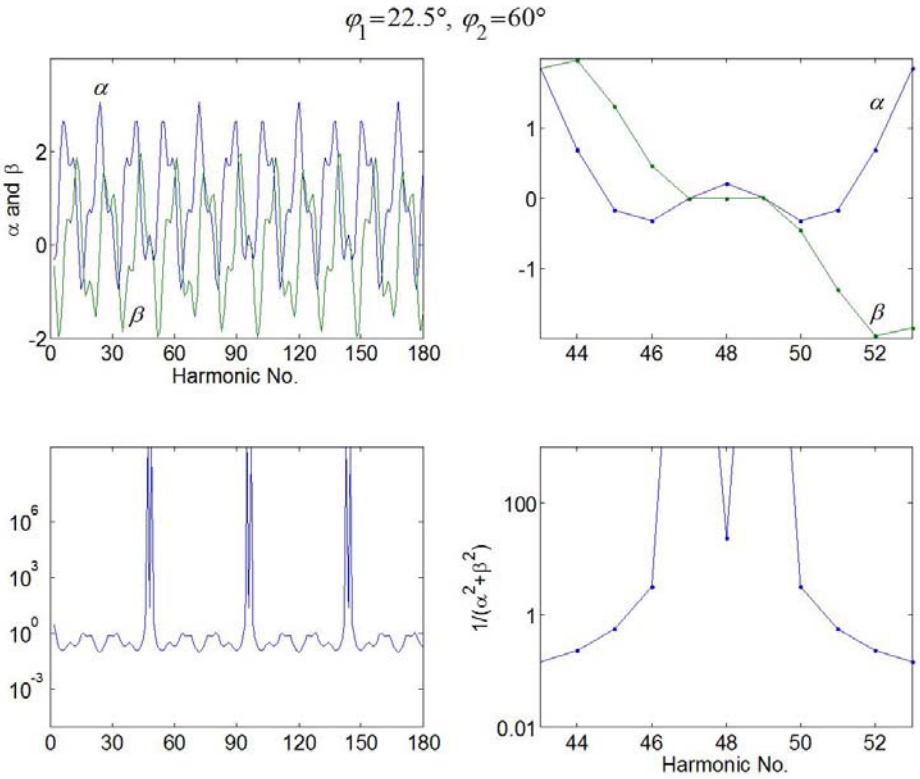

Figure 4.11 The transfer functions for A_k and B_k in equation (4.18) become undefined when $\alpha_j = \beta_j = 0$. This occurs at values for harmonics j where $j = k \pm 1$. In this example the upper graphs shows α and β and the lower graphs show $1/\left(\alpha^2 + \beta^2\right)$ for $\varphi_1 = 22.5°$ and $\varphi_2 = 60°$. The left hand graphs show the response over the full 180 harmonics while right hand graphs zoom in on the first occurrence where $k = 48$.

An algorithmic flow chart for the determination of k is given in Figure 4.12. If for example we have $\varphi_1 = n_1/d_1\,\pi = 4/27\,\pi$ and $\varphi_2 = n_2/d_2\,\pi = 5/12\,\pi$; the greatest common divisor of 12 and 27 is 3 (i.e. $g = 3$); then $f_1 = 12/3 = 4$ and $f_2 = 27/3 = 9$ and finally $k = 2 \times 4 \times 27 = 2 \times 9 \times 12 = 216$. If $k \le m$ in equations (4.17) and (4.18) then the form and spindle error cannot be recovered using the multi-probe error separation technique. Theoretically, these equations may become undefined for any combination angles φ_1 and φ_2 if m is large enough. For example when $\varphi_1 = 16.45°$ and $\varphi_2 = 61.106°$ the first occurrence of the condition $\alpha_{k\pm1} = \beta_{k\pm1} = 0$ is at $k = 180000$. It is important to note in flowchart Figure 4.12

that if $d_1 = d_2$, the value of k is generally relatively small. For example even if $d_1 = d_2 = 68$, (e.g. $\varphi_1 = 7/68\pi$ and $\varphi_2 = 49/68\pi$), $k = 136$.

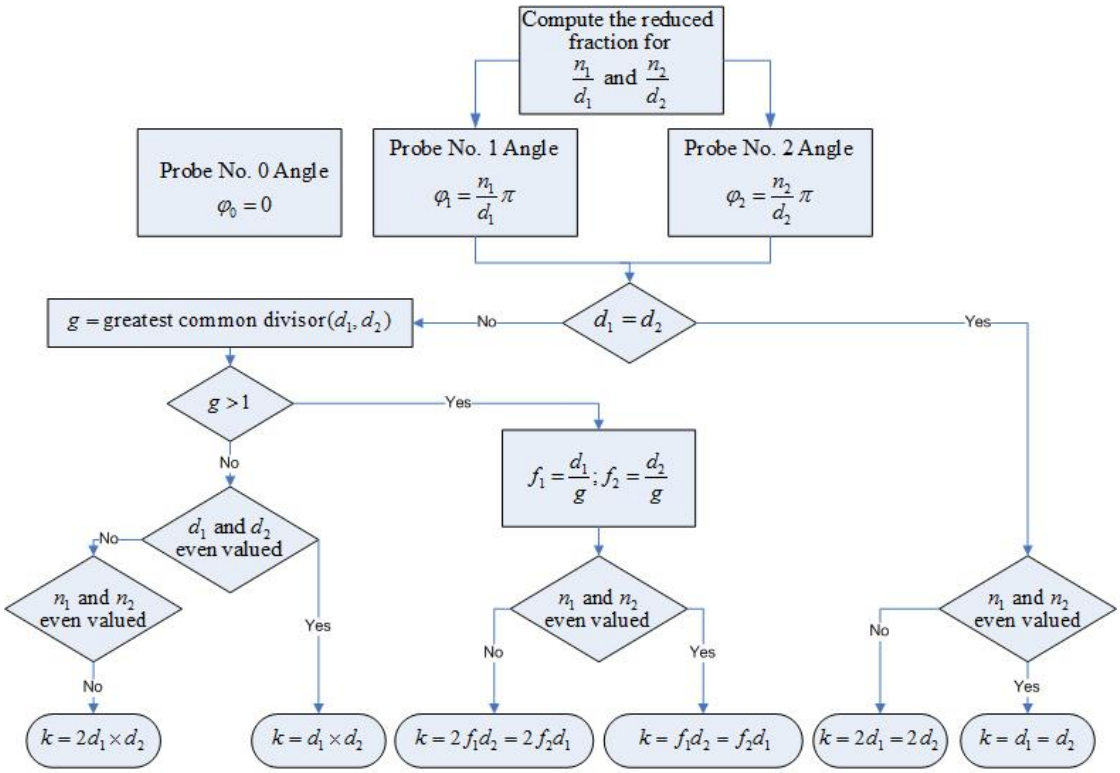

Matlab Code:

```
d1=11;d2=25;n1=1;n2=1;
p1=n1*pi/d1; p2=n2*pi/d2;
k2=1;
while ~(((mod(k2*p1,2*pi)<1E-5)|(2*pi-mod(k2*p1,2*pi)<1E-5))&
        ((mod(k2*p2,2*pi)<1E-5)|(2*pi-mod(k2*p2,2*pi)<1E-5))|
        (k2>1E5))
            k2=k2+1;
end;
```

Figure 4.12 Flow chart algorithm for the determination of the value of k for rational fraction values of φ_1 and φ_2. The Matlab code used to establish this flow chart is given.

4.2.4.2 Simulations

To continue our evaluations of the multi-probe separation technique, we must use a test signal. An arbitrary test signal comprising the form error and x and y spindle motions can be constructed for three hypothetical probes at probe angles 0, φ_1 and φ_2 using equations (4.10). The characteristics of the test signal used for the remainder of this and the next two sections are shown in Figure 4.13. Simulations in sections 4.2.4.3 and 4.2.4.4 use the same form error and spindle motions shown in the top and second from top graphs in this figure. The third graph shows example simulated probe readings for angles $\varphi_1 = 17\pi/121$ and $\varphi_2 = 15\pi/27$. The frequency content of the form error and spindle motions is given for reference in the

bottom two left hand graphs. Finally an example of the Gaussian random errors with a standard deviation of one part in one thousand of the probe reading range added to the simulated probe readings is shown in the bottom left hand graph of this figure. The mean value of the standard deviations of the probe reading errors used here was 0.0041 μm.

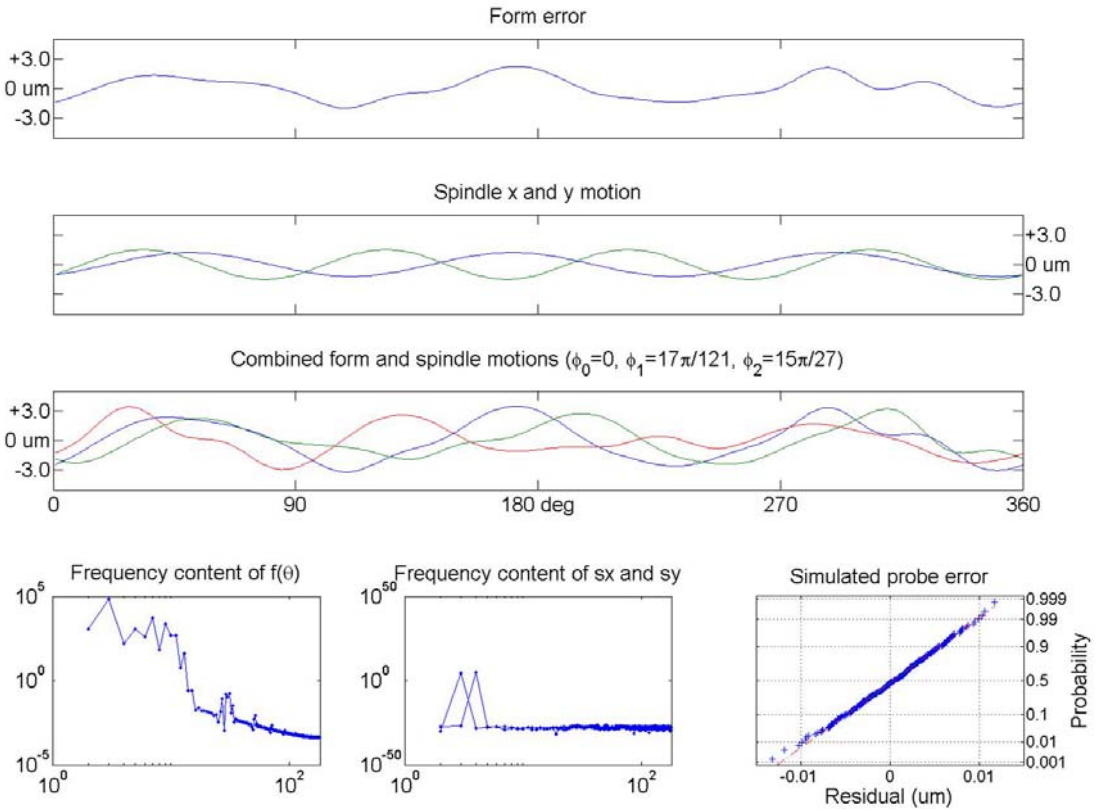

Figure 4.13 Characteristics of the simulated signal for the form error – spindle motion separation harmonic studies used in later sections of this chapter. This specific example has probe angles $\varphi_0 = 0$, $\varphi_1 = 17\pi/121$ and $\varphi_2 = 15\pi/27$.

All results given are the standard deviation of the residuals determined by subtracting the simulated form error from the separated form error for the 360 data points (i.e. the 360 simulated and separated form errors at 1 degree steps between 1 degree and 360 degrees). The separated form error is determined using the steps and equations outlined in section 4.2.3.1. This standard deviation will be referenced by $SD\left(fe_{sep} - fe_{sim}\right)$ for the remainder of this chapter. The harmonic cut off for all simulations is $m = 180$.

Finally, rational number angles (e.g. $3/7\,\pi, 9/12\,\pi \cdots$) numerator (denoted n) denominator (denoted d) pairs for integers ($n < d$) for n and d between 1 and 30 were used for the

angles of φ_1 and φ_2 in FESM simulations. The generality of this approach is addressed in section 4.2.4.5.

4.2.4.3 The resonance diagram

A resonance diagram[21] is a tool that can be used to visualise angles φ_1 and φ_2 for which values of k occur where $\alpha_{k\pm1} = \beta_{k\pm1} = 0$. The resonance diagram (Figure 4.14) is constructed by drawing lines between rational fractions of 2π radians on the x and y axes. Intersections of these lines give angles φ_1 and φ_2 for which the form error and spindle motion cannot be separated using the multi-probe technique above a given harmonic $j = k - 2$.

For example, the line $\varphi_1 - 2\varphi_2 = 0$ which runs on the resonance diagram from $(0,0)$ to $(2\pi,\pi)$ intersects the line $\varphi_1 + 8\varphi_2 = \pi$ which runs from $(0,\pi/8)$ to $(\pi,0)$ at $\varphi_1 = \pi/5$ and $\varphi_2 = \pi/10$ (graph a of Figure 4.14). The link between the resonance diagram and value of k discussed above is established by solving for the intersection point of the two lines and using the values of n_1, n_2 and d_1 and d_2 (a in Figure 4.14) in (4.27) as input into the algorithm of Figure 4.12 .

$$\begin{gathered} \varphi_1 + 8\varphi_2 = \pi \text{ and } \varphi_1 - 2\varphi_2 = 0 \\ \varphi_1 = \frac{1}{5}\pi = \frac{n_1}{d_1}\pi \text{ and } \varphi_2 = \frac{1}{10}\pi = \frac{n_2}{d_2}\pi \end{gathered} \tag{4.27}$$

Using the flow chart of Figure 4.12 we determine that $g = 5$, and $f_1 = 1$, so $k = 2 \times 1 \times 10 = 20$ for this combination of angles. Thus we can say that the form error cannot be separated from the spindle motion for harmonics greater than harmonic 18 for these probe angles. Alternatively, one may recuperate up to $j = (k-1) - 1 = 18$ harmonics for this combination of probe separation angles, which in many cases this may be adequate.

[21] The resonance diagram is related to a concept borrowed by the author from the accelerator physics community. In accelerator physics, what the author calls the resonance diagram is commonly referred to as the tune diagram. Lines and intersections of the tune diagram represent coupled resonances to be avoided because the beam closed orbit is unstable. Generally only low order resonances are considered by accelerator physicists. As with the tune diagram, the resonance diagram is a useful visualization tool.

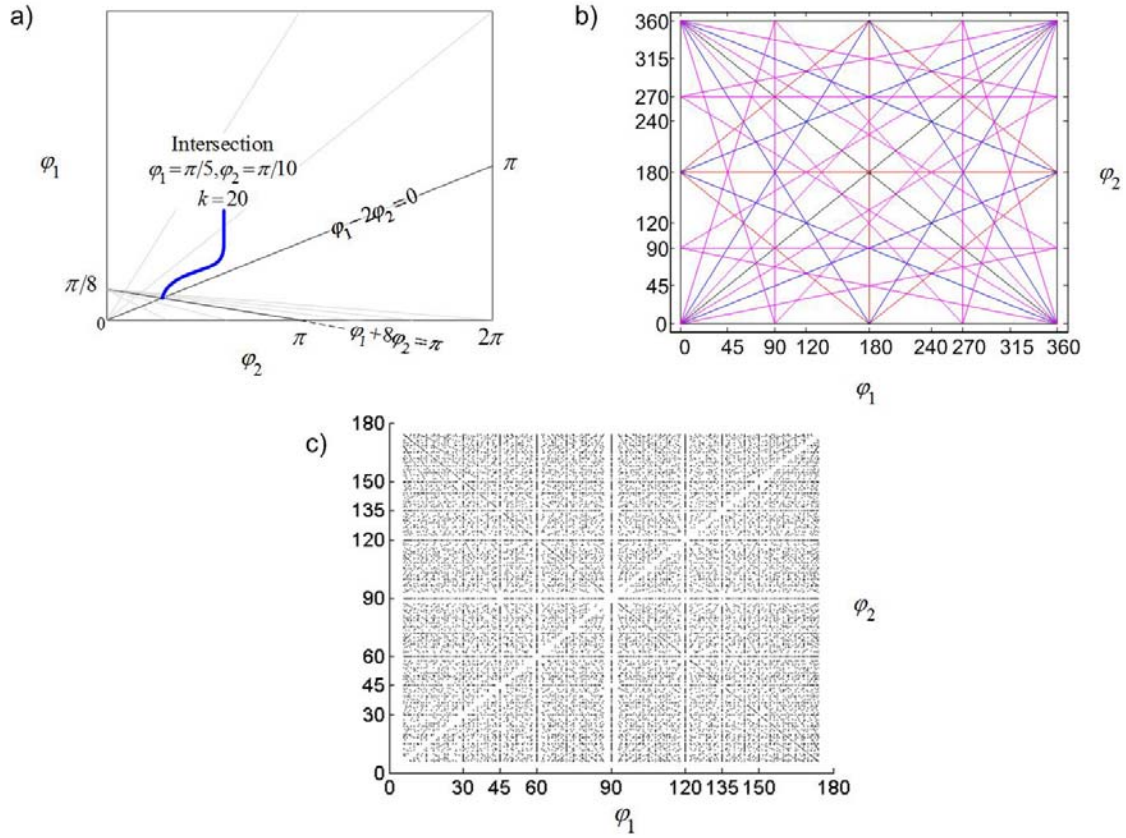

Figure 4.14 A resonance diagram permits the localisation and visualisation of combinations of angles $(0,\varphi_1,\varphi_2)$ where $\alpha_{k\pm1}=\beta_{k\pm1}=0$. The top left hand graph, shows the intersection of the two lines gives angles φ_1 and φ_2 for which $k=20$. The top right hand graph shows a partial resonance diagram. One remarks the symmetry between the 4 quadrants. The bottom graph shows the combinations of angles φ_1 and φ_2 for which $k<m$ and it is not possible to separate the form error from the spindle motion using the multi-probe technique.

The top right hand graph shows a proto resonance diagram with lines up to order 4. The order of a line is sum of the integer multiplicative constants for φ_1 and φ_2 describing the line. In our example, $\varphi_1+8\varphi_2=\pi$ is an order 9 line (i.e. $1+8$), while $\varphi_1+2\varphi_2=0$ is an order 3 line. Generally speaking the smaller the order of the line, the lower the harmonic k for which the form error cannot be separated from the spindle motion. The bottom graph c) of Figure 4.14 shows the combinations of angles φ_1 and φ_2, as black dots, for which it is not possible to separate the form error from the spindle motion. Note the case $\varphi_1=\varphi_2$ is not considered in this graph explaining the blank 'line' running form its lower left hand to upper right hand corners.

There is a clear symmetry between quadrants in the graphs of Figure 4.14. Therefore the simulations in the next section are conducted over the range $0\cdots\pi$ without loss of generality.

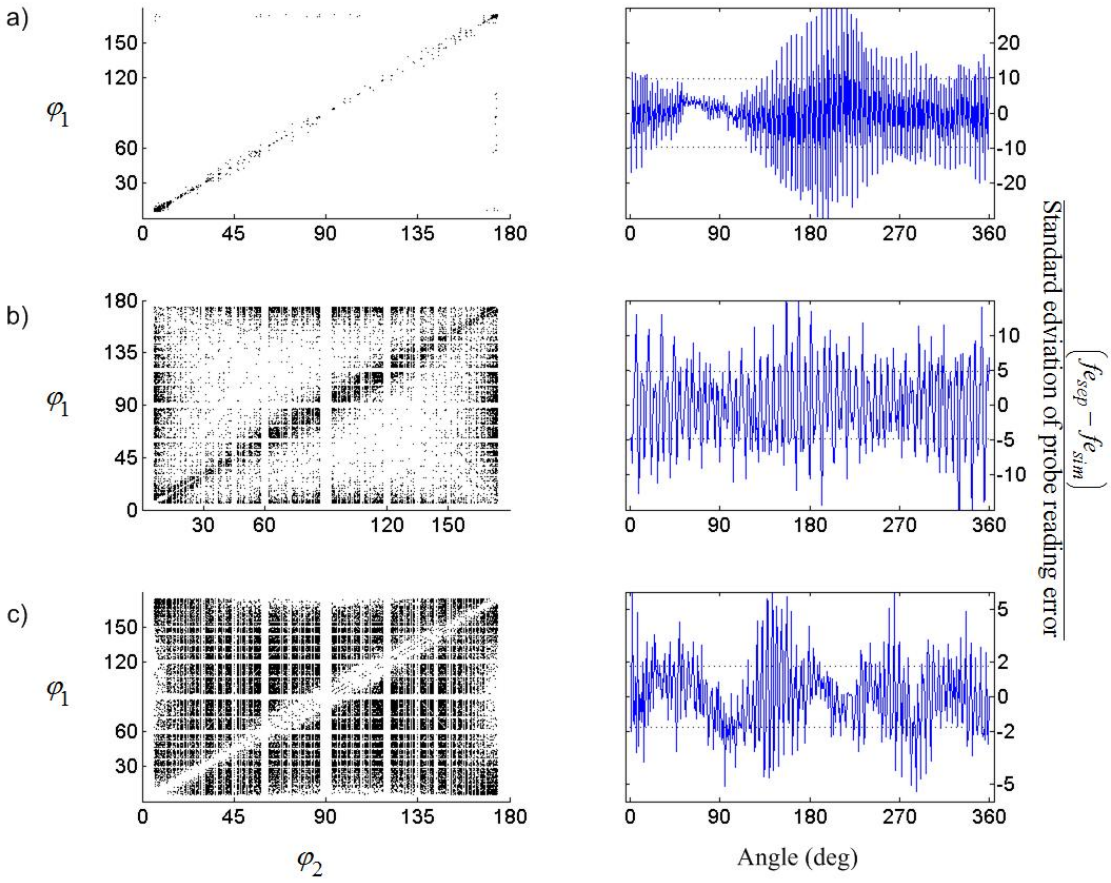

Figure 4.15 In all of these graphs $k > m$. The top left graph show probe separation angles φ_1 and φ_2 for which the standard deviation of the separated form error is between 12.5 and 250 times that of simulated input error. The top right hand graph shows and example of the difference between the simulated form error and the separated form error. Graph b) shows the same for angles where the separated form error is between 3 and 12.5 times that of simulated input error. Graph c) gives the same as a) for angles where the separated form error is below 3 times that of simulated input error.

The resonance diagram can be used to show what the residuals look like for different probe separation angles. Figure 4.15 gives examples where the simulated separation results are moderately to severely perturbed as a function of the probe separation angle.

4.2.4.4 Detailed harmonic analysis of the multi-probe error FESM technique

The harmonic behaviour of the multi-probe error separation technique is quite complex. Figure 4.16 shows a plot of the distribution of k values (i.e. $k < m$; $k > m$; and $k < m$ and $k > m$) as a function of d in the relation $\varphi = n\pi/d$. Recall that for each value of d , several values of n are possible and hence several values of k are also possible (see flow chart of Figure 4.12). This accounts for a certain number of points on this graph shown by green

circles where $k < m$ and $k > m$. Although it is entirely arbitrary; for illustration, the value of m in this example was taken to be 180. There are two interesting patterns in this graph. The first is the larger the value d, the more likely $k > m$. The second point is the relationship when $d_1 = d_2$ where k is always less than m; at least for this selection of data. This means that seemingly unrelated combinations of angles for φ_1 and φ_2 (e.g. $7\pi/29$ and $19\pi/29$) result in relatively low values of k; 58 in this case (see Figure 4.12).

There is an infinite number of angle combinations where the harmonic k is very large, and indeed very much larger that any practical cut off harmonic m. However, as we shall see next, the influence of a particular line in the resonance diagram spreads over into an adjacent region and can potentially perturb apparently a priori probe angle combinations for which there should be no influence. We get an inkling of this in the right hand graph of Figure 4.16, where under many circumstances when $k > m$ (i.e. the form error can be separated from the spindle motion error) there can be considerable variation in the magnitude of the error of the separated form error $SD\left(fe_{sep} - fe_{sim}\right)$. This graph represents only the 'black' squares shown in the left hand graph of this figure with combinations of n and d for which $k > m$ and the form error can in principle be separated from the spindle motion.

One thing is quite clear from the right hand plot of Figure 4.16, $SD\left(fe_{sep} - fe_{sim}\right)$ is always greater than the error input into the simulation (the straight line referenced as 'Standard deviation of errors introduced into the simulated probe readings' in the figure). This suggests that there is always an added cost due merely to the process of the separation. Recall once again that these results are conditional upon a noisy probe reading signal. If there is no error in the probe reading signals, there is no error in the separated form error.[22]

[22] This is not strictly true and will be examined in detail in section 4.2.4.5.

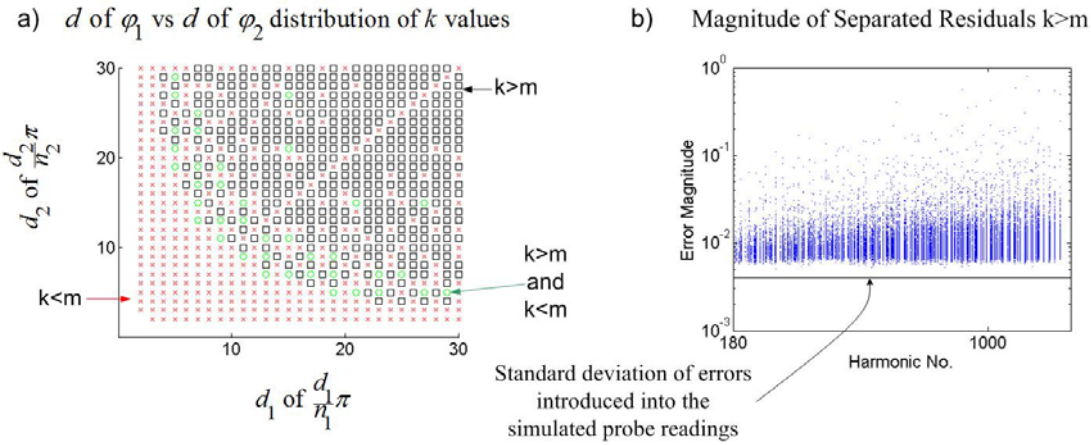

Figure 4.16 The left hand graph shows distributions of k values as a function of d in the relation $\varphi = n\pi/d$ with respect to an arbitrary cut off harmonic $m = 180$. The right hand graph shows that even for values of k for which the error separation is possible, there remains considerable variation and unexpectedly high errors in $SD\left(fe_{sep} - fe_{sim}\right)$.

Figure 4.17 shows a selection of residual plots determined by subtracting the theoretical form error from the separated form error (i.e. $\left(fe_{sep} - fe_{sim}\right)$) for 1 degree intervals between 0 and 359 degrees. The standard deviation of the probe reading error into the simulation was 0.0041 µm. The top graph (a) of this figure shows the separated error with the residuals shown in graph b). The first thing that is clear from residual plots of graphs b), c) and d) is that the separated form error, and hence the derived spindle motions is subject to systematic error. The second thing we remark is that there is no apparent link between the value of k and the magnitude of the residuals. This we have already surmised from the right hand graph of Figure 4.16.

To understand the nature of this phenomenon we must look more carefully at the behaviour of φ_1 and φ_2 as a function of one another. To get a feeling for this we will start by looking at three very different cases for $\varphi_0 = 0$, φ_1 constant, and variable φ_2; notably

$(0, \pi, \varphi_2)$, $(0, \pi/21, \varphi_2)$ and $\left(0, \frac{2778023}{8147317}\pi, \varphi_2\right)$.

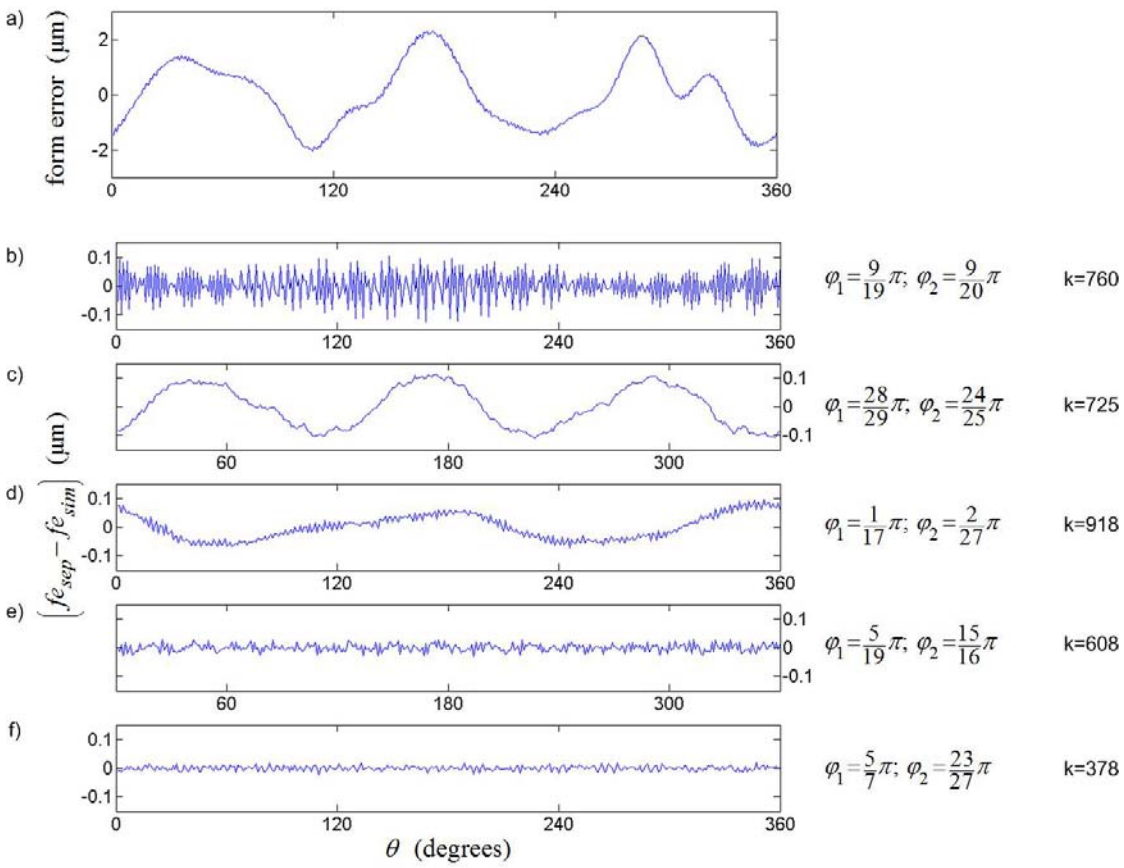

Figure 4.17 Selection of residual plots for which values of $k > (m = 180)$. The top graph shows the separated form error with the residuals (i.e. $\left(fe_{sep} - fe_{sim}\right)$) shown in graph b).

The value of $SD\left(fe_{sep} - fe_{sim}\right)$ is evaluated for $\varphi_2 = 1° \cdots 179°$. Figure 4.18 shows the results $SD\left(fe_{sep} - fe_{sim}\right)$ for these simulations. We can conceptualise the construction of this graph as moving across the resonance diagram (e.g. graph c in Figure 4.14) either in the horizontal of vertical sense. Moving horizontally φ_1 is variable and φ_2 fixed; vertically φ_2 is variable while φ_1 is fixed. Thus we are moving in the vertical sense for Figure 4.18.

In Figure 4.18 we remark that when $\varphi_2 = \varphi_1$ there is a blow-up or resonance in the residual standard deviation $SD\left(fe_{sep} - fe_{sim}\right)$. Physically, φ_2 cannot equal φ_1, because the probes would be superposed one on the other. However, separation angles of less than 2 degrees are possible with the 6 mm diameter capacitive probes used in this thesis and the HCC plateau target diameter of 500 mm. Thus, φ_2 can be very high on the shoulder of the (i.e. very close to) peak at $\varphi_2 = \varphi_1$ shown in these graphs. The effect of this resonance extends over several

degrees. One tentative conclusion of this is that all things being equal, small separation angles (i.e. $\varphi_2 \approx \varphi_1$) are inherently less stable. Finally, these graphs show error plots between 1 and 179 degrees. However, as mentioned earlier, these plots are self symmetric and the peak found at $\varphi_2 = \varphi_1$ will also be found at $\varphi_2 = \varphi_1 \pm \pi$.

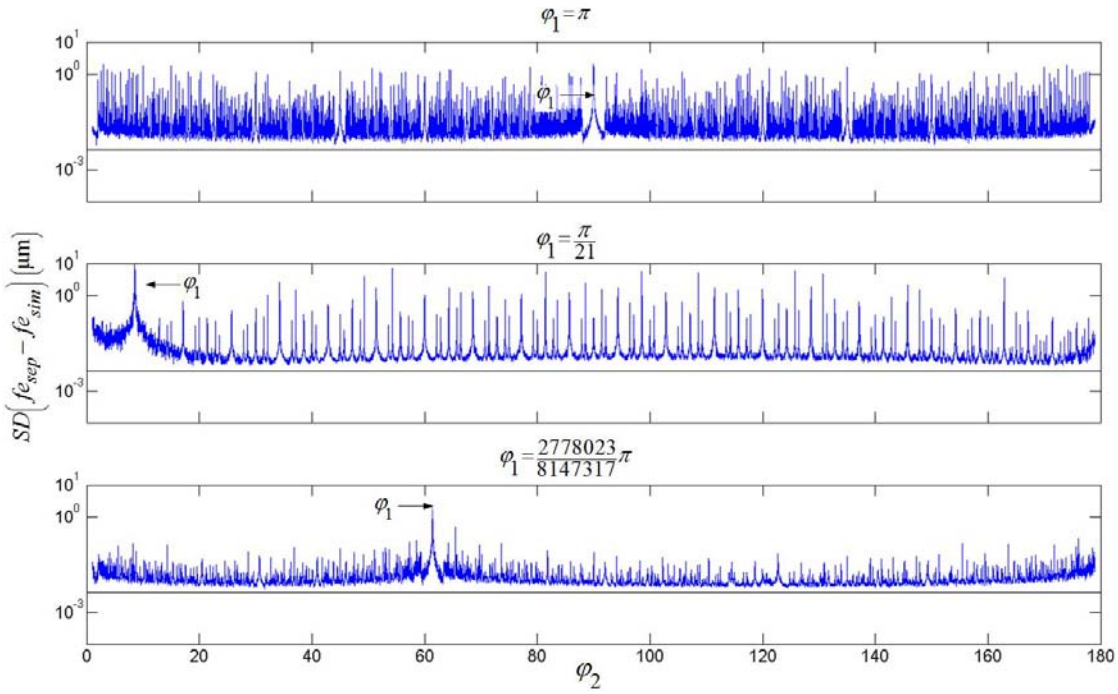

Figure 4.18 Plots of the standard deviation of the simulated theoretical form error subtracted from the actual separated error $SD\left(fe_{sep} - fe_{sim}\right)$ for three constant angles of φ_1, and φ_2 varied by 1 degree steps between 1 and 179 degrees.

For the case of $\varphi_1 = \pi$ there are a very large number of resonances. For the case of $\varphi_1 = \pi/21$ there are considerably fewer resonances but the shoulder of primary resonance where $\varphi_1 = \varphi_2$ is broader. The final example shows far fewer resonances overall. However even with this example whose value k is very large (i.e. $k \gg 2f_1 \times d_2$), there are perturbing resonances.

Appreciating a little of the behaviour of the separation error associated with φ_1 and φ_2, we are now in a position to investigate what happens in the vicinity of the φ angles for the $SD\left(fe_{sep} - fe_{sim}\right)$ plots shown in Figure 4.17. Figure 4.19 shows graphs similar to those of Figure 4.18 with a reduced scan range of ± 2.5 degrees on either side of the nominal φ value.

On these graphs, φ_2 is variable and φ_1 fixed on the left hand graphs; while φ_1 is variable and φ_2 fixed on the right hand graphs.

For example, on the left hand graph of a) in Figure 4.19, φ_1 is fixed at its nominal value of $9\pi/19$ or 85.26316 degrees and φ_2 is varied over a range of ±2.5 degrees from its nominal value of $9\pi/20$ or 81 degrees. Therefore φ_2 varies between 78.5 degrees and 83.5 degrees. On the right hand graph of a), the situation is inversed with φ_2 fixed and φ_1 variable over the range of approximately 82.76316 degrees to 87.76316 degrees.

The vertical line in the centre each graph is the angle for which the variable angle is nominally fixed. Thus we are scanning vertically in the resonance diagram on the left hand graphs and horizontally for the right hand graphs to ascertain the variability $SD\left(fe_{sep} - fe_{sim}\right)$ in the direct vicinity the angles φ_1 and φ_2.

Recall, the value on the ordinate axes represents the standard deviation of the residuals of the separated form error, derived from simulated probe readings with Gaussian random error of 0.0041 μm, minus the simulated form error (i.e. $SD\left(fe_{sep} - fe_{sim}\right)$). Each point in the graphs of Figure 4.19 is in fact the average of the standard deviations issued from 15 simulations. There are 501 points representing a total of 7515 simulations in each graph.

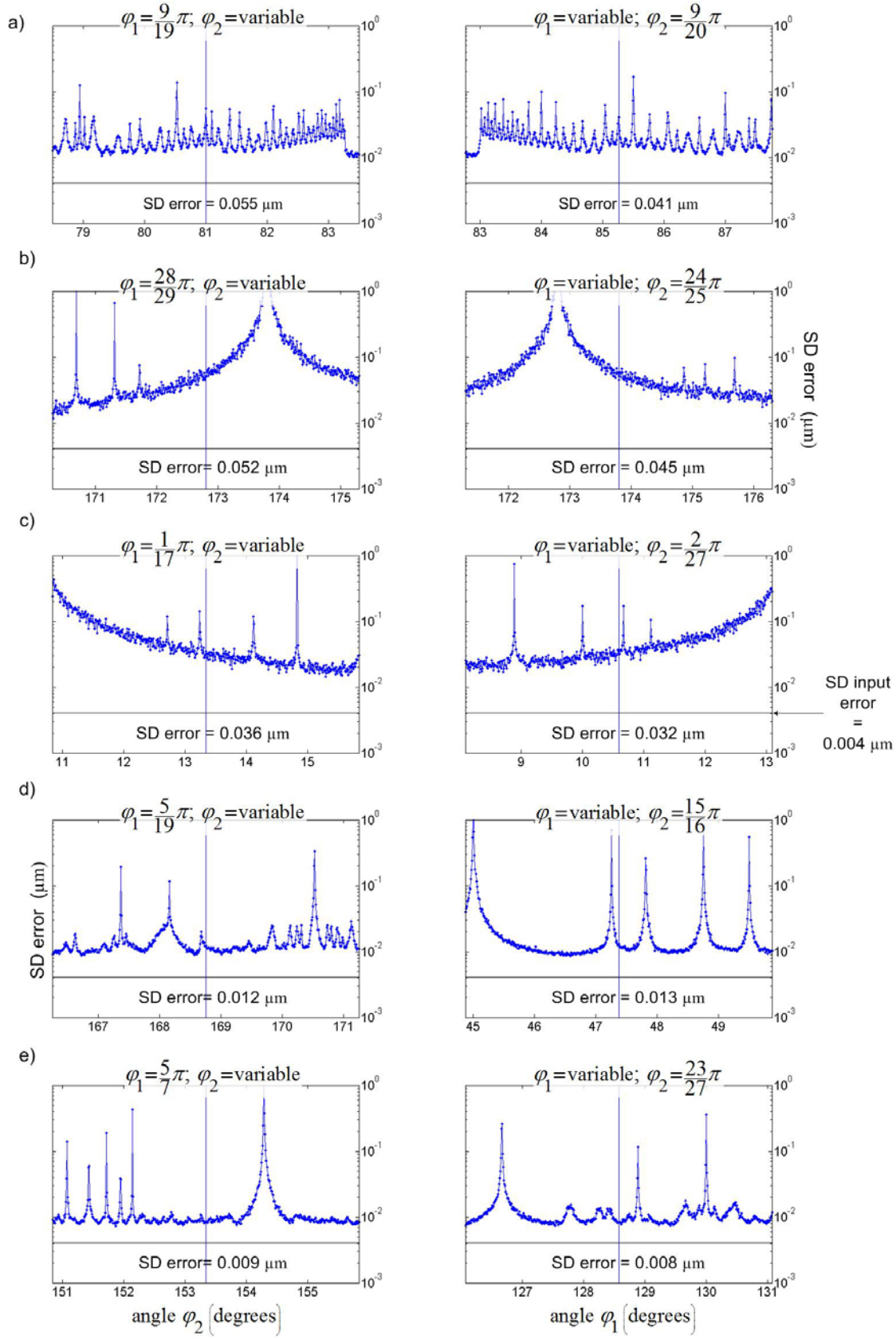

Figure 4.19 Behaviour of the separation error in the vicinity of φ_1 and φ_2. These graphs should be viewed in light of the residual error plots shown in Figure 4.17.

In graph a) we see that both φ_1 and φ_2 fall directly on peaks whose magnitudes are 0.055 μm and 0.041μm respectively. Does this account for the high frequency nature of the

systematic error shown in Figure 4.17? In graph b) both φ_1 and φ_2 fall quite high on the shoulder of a very large peak corresponding with error magnitudes are 0.052 µm and 0.042µm. Note that the peaks in graphs b) are the resonance where $\varphi_2 = \varphi_1$. In this example φ_1 and φ_2 are relatively close to one another. Could the fact that φ_1 and φ_2 fall on the shoulder instead of the peak be responsible for the low frequency harmonic content of the systematic error? This hypothesis is supported by similar error characteristics found in graphs c) of Figure 4.17 and Figure 4.19. Graphs d) and e) have low bias error. Figure 4.19 shows that they are away from any major peaks and have small error magnitude (0.009 µm and 0.008µm in the case of graph d).

These graphs underline the complexity and nature of the uncertainty we can expect using the multi-probe FESM technique. These results must be kept in mind when considering used in the determination of the HCC collimation error using real data in chapters 5 and 6.

4.2.4.5 Intrinsic calculation error

The intrinsic error in the FESM technique is the difference between the simulated form error and the separated form error $SD\left(fe_{sep} - fe_{sim}\right)$ when no noise is used in the probe readings. In other words, this is the error in the separation when the probe reading errors are zero. Logically $SD\left(fe_{sep} - fe_{sim}\right)$ should be zero. Indeed it has been affirmed up to now that; if there is no error in the probe reading signals, there is no error in the separated form error. This is not strictly true. There is a residual error but it is very small. We will examine this residual error in this section.

Although every effort has been made to elucidate its origin, it remains unclear if the fact that $SD\left(fe_{sep} - fe_{sim}\right) \neq 0$ is due to a bug in the Matlab script used for the separation, a problem in the built-in Matlab routines used, finite length arithmetic, or intrinsic to the separation technique. It should be noted a similar saw tooth error, albeit not identical, also exists in a completely independent Labview vi.

In the previous sections we have looked at the effects of probe separation angles while holding the form error and spindle motion constant. In this section and the next we will relax this constraint.

Logic would suggest that varying form error or spindle motion should lead to equivalent results. Indeed, simulations were made that confirm this interchangeability. Therefore for simplicity only variable form error is considered bearing in mind that the results are fully applicable to spindle error and to a combination of both variable spindle motion and form error. For the tests in this section and the next, spindle motions are actually set to zero without loss of generality.

Two different simulations are performed in this section. The aim of these simulations is to examine the respective effects of probe angle separation, and form error (or spindle motion) upon this intrinsic separation error. For each type of simulation, 50 random samples of probe separation angle (φ_1, φ_2) pairs in Figure 4.16 are selected for which $k > m$, and in theory where the separation is possible. Then for each angle pair, 50 simulations are performed where three probe reading signals are constructed using different baseline form error signals. The mean absolute deviation of $\left(fe_{sep} - fe_{sim} \right)$ for the 360 samples (i.e. 0 degrees to 359 degrees in 1 degree steps) is calculated and finally, box plots are plotted for the 50 randomly selected probe separation angle (φ_1, φ_2) pairs.

Figure 4.20 shows the results of these simulations. First, graph a) gives an example of the differences between the simulated form error and the separated form error $\left(fe_{sep} - fe_{sim} \right)$ for one 360 sample data set. One remarks the regular saw tooth functional form. This saw tooth appearance is characteristic of the intrinsic error regardless of the probe separation angles φ_1 and φ_2, or the underlying form error. Values always oscillate between $\pm\left(fe_{sep} - fe_{sim} \right)$. For this reason the mean of the absolute deviation values of the 360 data sample $\left(fe_{sep} - fe_{sim} \right)$ are used for the construction of the box plots of graphs b) of this figure.

Normal probability plots and box plots are used extensively in this thesis. They are excellent ways to visualize statistical data. This type of 'exploratory' data approach is discussed in [94-96] for example.

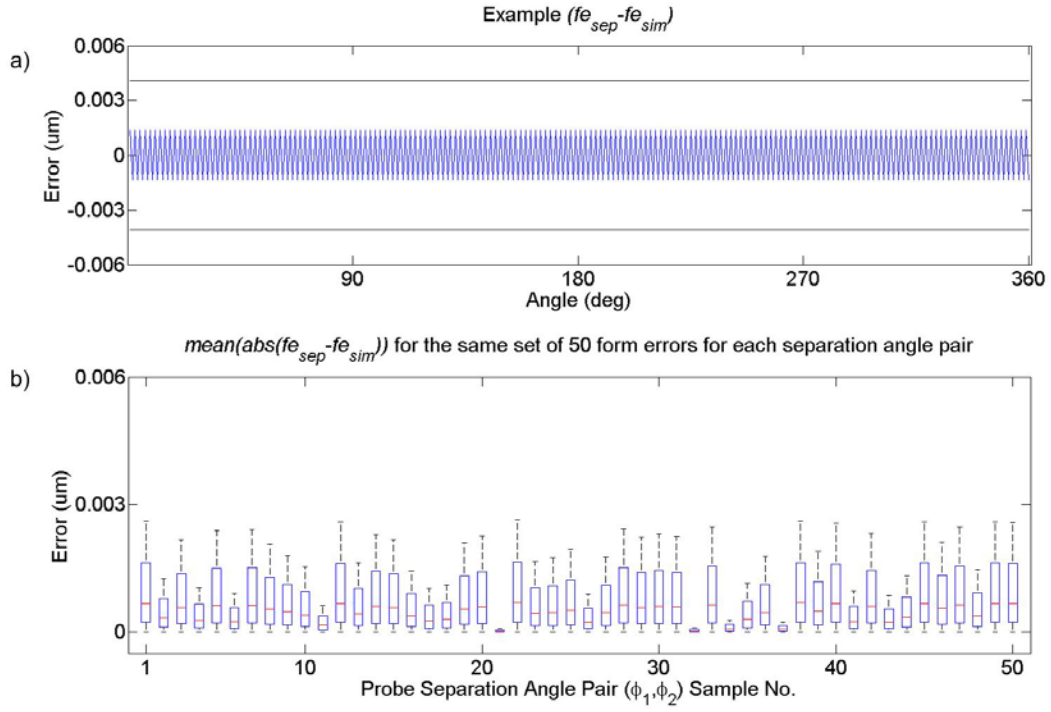

Figure 4.20 Graph a) shows an example of the intrinsic error saw tooth function. Graph b) shows box plots of $\text{mean}\left(\text{abs}\left(fe_{sep} - fe_{sim}\right)\right)$ for 50 simulations of underlying form error for the 50 randomly selected sample (φ_1, φ_2) probe separation angle pairs. The probe reading errors are zero. The same set of 50 form errors are used for each of the 50 probe separation angle pairs.

Each box of graph b) of Figure 4.20 is constructed using the same set of 50 different underlying form errors. This is to say that for each of the 50 probe separation angle pairs (φ_1, φ_2), the same set of 50 different form errors were used. We can conclude from these graphs that for the intrinsic error, the magnitude of $mean\left(abs\left(fe_{sep} - fe_{sim}\right)\right)$ is apparently dependent as evidenced by the variability of the box plots on the given set of probe separation angles and the underlying form error.

Nevertheless, we must place this intrinsic error in perspective. It represents (much) less than 1 part in 10000 of the range of the simulated form error. Furthermore, it is always roughly the same order of magnitude regardless of the size or the harmonic content of the form error or the probe separation angle pair (φ_1, φ_2). If, for example, the form error magnitude is increased

by a factor 10, the intrinsic separation error remains the same. It would represent (much) less than 1 part in 100000 of the range of the form error.

4.2.4.6 Generality of the approach

Over the previous sections we have established that there is an apparent dependence of the results of the FESM technique that is a function of the probe separation angle (i.e. $SD\left(fe_{sep} - fe_{sim}\right) = f\left(\varphi_1, \varphi_2\right)$) and contingent upon noisy probe reading signals. However until now, apart from the last section dealing with the intrinsic error of this technique, we have kept the form error for the simulations constant while varying the probe separation angles and introducing normally distributed random errors into the probe readings. In the previous section, we have seen that the intrinsic separation error is apparently influenced by both the probe separation angle and by the underlying form error. However this effect is small.

One can legitimately ask if the results issued from simulations in sections 4.2.4.3 and 4.2.4.4 are valid for different underlying form errors and/or spindle motions? Is the bias error in the separated form error predominantly a function of the probe separation angle or is it also influenced by the underlying form and spindle motion errors?

These questions can be answered by performing the simulations of the previous section concerning the intrinsic error and this time injecting, random normally distributed probe reading errors into a large number of different simulated underlying form errors for a given probe separation angle. This time however, the results will be expressed in $SD\left(fe_{sep} - fe_{sim}\right)$ as with sections 4.2.4.3 and 4.2.4.4.

Once again, because these simulations are time consuming, a random selection of 50 samples from the results shown in the right hand graph of Figure 4.16 is used for this study. Two different simulations are performed. First, for each of the 50 probe separation angle pairs $\left(\varphi_1, \varphi_2\right)$, the same set of 50 different form errors were used. Second, a random set of $50 \times 50 = 2500$ different form errors were used in the separation. The results of these studies are shown in Figure 4.21.

For comparative purposes, the same separations angle pairs as those used to generate the graphs in Figure 4.20 were used for graph b) of Figure 4.21. Each simulation for both graphs a) and b) used a different set of random probe reading errors. Many simulations have been made with different data sets which produce comparable to the results of this figure.

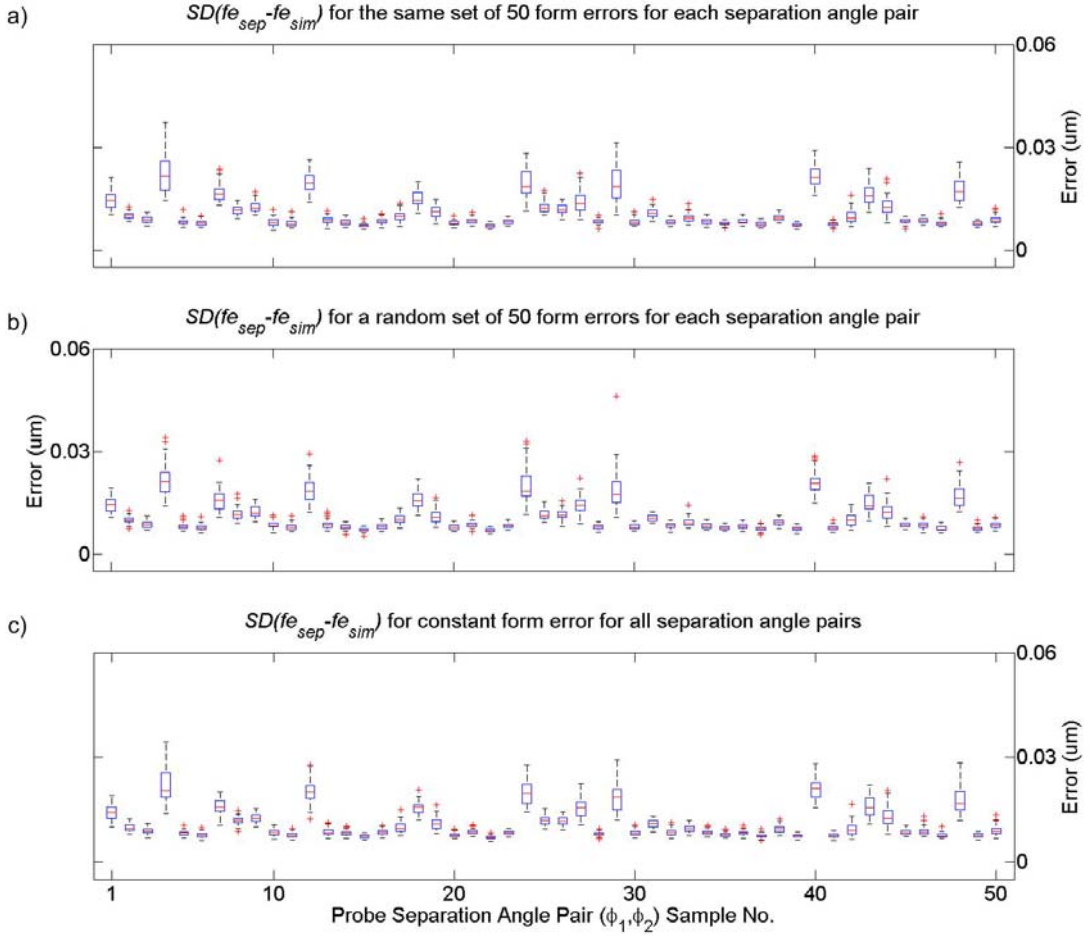

Figure 4.21 Dependence of $SD\left(fe_{sep} - fe_{sim}\right)$ on the probe separation angle (i.e. simulation sample number) φ_1 and φ_2 and the underlying form error. For comparison, graph a) uses the same form errors as those used in graph b) of Figure 4.20. Graph b) uses a random selection of different form errors for all of the simulations. Graph c) uses the same underlying form error for all simulations and probe separation angle pairs. All three graphs employ noisy probe reading signals.

The first thing we remark is the difference between Figure 4.21 graph a) and Figure 4.20 graph b). These two graphs use the same set of 50 different underlying form errors for each of the 50 probe separation angle pairs $\left(\varphi_1,\varphi_2\right)$. The only difference between them is the introduction of noisy probe reading signals. However, the results of the separations as manifested in $SD\left(fe_{sep} - fe_{sim}\right)$ of graph a) Figure 4.21 are an order of magnitude larger than

those of the intrinsic error. Furthermore, there is a great deal more variation as a function of probe separation angle.

Concentrating now on Figure 4.21, three different simulations are presented. The first in graph a) uses the same set of 50 underlying form errors for each of the probe separation angles (φ_1, φ_2). Graph b) uses a different underlying form error for every single simulation. Finally graph c) uses a single form error for all of the simulations. The three graphs are very similar. In fact, if the same sets of probe reading errors are used for each of the simulations, the medians and ranges of the box plots are identical.

This similitude indicates that the underlying form error has a small to negligible influence on $SD\left(fe_{sep} - fe_{sim}\right)$. The error in the FESM technique observed in this and other sections is principally dependent upon the probe separation angle φ_1 and φ_2. The variation in $SD\left(fe_{sep} - fe_{sim}\right)$ for a given separation angle pair is dependent upon the probe reading errors. In principle all things being equal, the larger the probe separation error effect, the more influence the probe reading errors will exert and the greater the variation in the value of $SD\left(fe_{sep} - fe_{sim}\right)$. The important implications of this on the HCC uncertainty will be discussed in section 6.6.

4.2.4.7 Summary of harmonic suppression in the FESM technique

We have spent some time on the clarification of the notion of harmonic suppression in the FESM problem. Briefly, because the transfer functions for A_k and B_k in equation (4.18) becomes undefined when $\alpha_j = \beta_j = 0$ at values $j = k \pm 1$, the success of this technique depends directly upon the value of k with respect to the value of m, the number of harmonics required in the reconstruction of the form error. In principle, if $k > m$, the separation is possible. Otherwise it is not.

However, we have also seen that this relationship is complex and that even when $k > m$ there can be considerable systematic harmonic error content in the separated form error and spindle motion. It has been shown through simulation that the intersections of resonance lines in the resonance diagram, which are strictly speaking points in the mathematical sense;

translate to peaks with a certain spread on a continuum when the phenomena is studied using simulated probe reading data polluted with error. When error free data is used, there is (practically) no error in the separation. In the presence of noisy data, the magnitude of the error in the form error – spindle motion technique is dependent upon the probe separation angles φ_1 and φ_2.

One can imagine moving across the resonance diagram horizontally (φ_1 variable and φ_2 fixed), or vertically (φ_2 variable and φ_1 fixed), encountering peaks and valleys whose frequency and magnitude are directly related to the angles between the capacitive probes. The magnitude of the error in the separated form error and consequently its uncertainty in the broader sense of its application to the qualification of the HCC is no longer strictly dependent on the value of k but rather the proximity to peaks on this continuum. We will look more closely at this with real data in the next chapter.

The main consequence of what we have seen in section 4.2.4 is that the uncertainty associated with this technique is highly non-linear. This must be considered when preparing the uncertainty statement of chapter 6.

4.3 Homogeneous transformation matrices

Homogeneous transformation matrices (HTM) are a useful tool for coordinate transformations and rotations that will be used in section 5.5. They are borrowed from, among others, the photogrammetry, and particularly the 'computer vision' community where they are extremely useful and used extensively. A good introduction to these and other transformations is given in [97]. Their particularity is that they use homogeneous coordinates. In mathematics, homogeneous coordinates, allow affine transformations[23][98] to be easily represented by a matrix.

[23] An affine transformation is any transformation that preserves colinearity (i.e. all points lying on a line initially still lie on a line after transformation) and ratios of distances (e.g., the midpoint of a line segment remains the midpoint after transformation). In this sense, affine indicates a special class of projective transformations that do not move any objects from the affine space to the plane at infinity or conversely. An affine transformation is also called an affinity.

Geometric contraction, expansion, dilation, reflection, rotation, shear, similarity transformations, spiral similarities, and translation are all affine transformations, as are their combinations. In general, an affine transformation is a composition of rotations, translations, dilations, and shears.

Their utility here is in that transformations involving translations and rotations are accomplished by simple matrix multiplication. The HTM can be defined to represent the coordinate transformation of a local coordinate system $(X,Y,Z)_L$ to a reference coordinate $(X,Y,Z)_R$. The following HTMs are defined to represent the three coordinate translations T_x, T_y and T_z by an amount t along; and the three coordinate rotations R_x R_y and R_z by an amount θ about the X_R, Y_R and Z_R axes respectively. These matrices are given by (4.28).

$$T_x(t)=\begin{bmatrix}1&0&0&t\\0&1&0&0\\0&0&1&0\\0&0&0&1\end{bmatrix}\quad T_y(t)=\begin{bmatrix}1&0&0&0\\0&1&0&t\\0&0&1&0\\0&0&0&1\end{bmatrix}\quad T_z(t)=\begin{bmatrix}1&0&0&0\\0&1&0&0\\0&0&1&t\\0&0&0&1\end{bmatrix}$$

$$R_x(\phi)=\begin{bmatrix}1&0&0&0\\0&\cos\phi&-\sin\phi&0\\0&\sin\phi&\cos\phi&0\\0&0&0&1\end{bmatrix}$$

$$R_y(\phi)=\begin{bmatrix}\cos\phi&0&\sin\phi&0\\0&1&0&0\\-\sin\phi&0&\cos\phi&0\\0&0&0&1\end{bmatrix}$$

$$R_z(\phi)=\begin{bmatrix}\cos\phi&-\sin\phi&0&0\\\sin\phi&\cos\phi&0&0\\0&0&1&0\\0&0&0&1\end{bmatrix} \tag{4.28}$$

Thus a series of translations and rotations; for example ($T_x(t_1), T_y(t_2), R_x(\theta_1), R_x(\theta_1)$, $R_y(\theta_2), R_z(\theta_3)$), is given by multiplying their respective matrices together as shown in (4.29) below.

$$\begin{bmatrix}x\\y\\z\\1\end{bmatrix}_R = T_x(t_1)\times T_y(t_2)\times R_x(\theta_1)\times R_y(\theta_2)\times R_z(\theta_3)\times\begin{bmatrix}x\\y\\z\\1\end{bmatrix}_L \tag{4.29}$$

5 Experimental evaluation and validation of the HCC

This chapter is concerned with the experimental work carried out to evaluate and develop a compensation model for the horizontal circle comparator (HCC) standard. It builds on the instrumentation and techniques presented in the previous chapter. As data or process modelling is an integral part of this evaluation, the chapter starts with a discussion of techniques and assumptions used. Capacitive probes are used extensively in the evaluation procedure and a full section is devoted to their calibration. Similarly the form error, spindle motions error separation technique is an essential technique in the characterisation of the HCC and a section is devoted to its implementation.

The HCC can be broken down into two component parts; the linked encoders configuration (LEC), and the rest of the instrument and its environment. Discussions concerning the assessment of each of these two parts are made through the small angle and full circle evaluations respectively.

This chapter outlines techniques used for the evaluation of the HCC. It deliberately stops short of their uncertainty evaluation. This is the subject of chapter 6.

5.1 Modelling

One of the stated aims of this thesis is to provide a horizontal angle standard that can be used to calibrate high precision spherical measuring system (SMS) instruments. This standard itself requires calibration by instruments that can provide a traceable uncertainty. The purpose of this calibration is to provide a model that can be consistently employed to correct the intrinsic HCC errors and ultimately provide a more reliable standard. This section will provide essential background for this process model.

Process modelling is the concise description of the total variation in one quantity y , by partitioning it into a deterministic component given by a mathematical function of one or more other quantities x_1, x_2, $\cdots$ and a random component that follows a particular probability distribution. This relationship is represented by:

$$y = f(\vec{x};\vec{\beta}) + \varepsilon \tag{5.1}$$

Here y is the response or dependent variable; $f\left(\vec{x};\vec{\beta}\right)$ is a mathematical function composed of two parts; the predictor or independent variables $\vec{x} \equiv x_1, x_2, x_3 \cdots$, and the parameters $\vec{\beta} \equiv \beta_1, \beta_2, \beta_3 \cdots$; and ε , the random errors. The predictor variables are measured at the same time as the response variable. The inclusion of random errors in the model makes the relationship between the response variable and the predictor variables a statistical rather than deterministic one. The functional relationship between the response and predictors holds only on average, not for each measured data point. [96]

For most of the work presented in this thesis, there is no easily defined deterministic underlying physical process or law such as the one relating the refractivity of air to atmospheric parameters temperature, pressure and humidity (also CO_2 and other gas content) (section 3.7.3). Although there are clear deterministic relationships (equation (5.1)), they are generally very complex and defy a logical parametric representation. Hence the mathematical model is typically arbitrary.

One approach to this type of problem is to use what is referred to as functional data analysis (FDA). FDA approaches discrete data with the principle that it can be represented by a smooth function which has been polluted by noise or uncertainty in the measurement process. These smooth functional observations are represented by basis functions. Polynomials, splines, wavelets and Fourier series are examples of basis functions. [99, 100]

Smoothing splines are used extensively in this work to determine the underlying deterministic part of a given process. The Fourier series is also used. Both of these basis functions present the same ambiguity with regard to what is the best representation of an underlying process with regard to bias and variance. This is discussed over the next paragraphs.

The smoothing spline used in this work[24] to determine a smooth functional representation of data minimises (5.2).

[24] The smoothing spline used in this thesis is the one provided by the Matlab function csaps.

$$p\sum_{i=1}^{n}\left|y_i - f\left(x_i\right)\right|^2 + \left(1-p\right)\int\left|D^2 f\left(t\right)\right|^2 dt \tag{5.2}$$

Here, $\left|y_i - f\left(x_i\right)\right|^2$ and $\left|D^2 f\left(t\right)\right|^2$ stands for the sum of the squares of all the entries of x, n is the number of entries of x, and the integral is over the smallest interval containing all the entries of x, and p is the smoothing parameter. $D^2 f$ denotes the second derivative of the function f.[101] When $p=1$ (5.2) returns an interpolating function that passes through all of the points. When $p=0$ it returns the best fit line through the data. This is a classical representation of a spline basis method that avoids the knot selection problem by using the maximal set of knots. (e.g. [102] p. 127) Minimising (5.2) leads to infinitely many solutions: any function passing through, or arbitrarily close to the training points $\left(x_i, y_i\right)$ is a solution. Any particular solution chosen might be a poor predictor at test points different from the training points. We distinguish here between the points used to determine the mathematical model, the training points; and the points used to qualify the model, the test points.

`pp = csaps(x,y)` returns the `ppform` of a cubic smoothing spline f to the given data `x,y` with the value of f at the data site `x(j)` approximating the data value `y(:,j)`, `for j=1:length(x)`. The values may be scalars, vectors, matrices, even ND-arrays. Data points with the same site are replaced by their (weighted) average, with its weight the sum of the corresponding weights.

This smoothing spline f minimizes

$$p\sum_{j=1}^{n} w(j)\left|y(:,j) - f\left(x(j)\right)\right|^2 + \left(1-p\right)\int \lambda(t)\left|D^2 f\left(t\right)\right|^2 dt$$

Here, $\left|z^2\right|$ stands for the sum of the squares of all the entries of z, n is the number of entries of `x`, and the integral is over the smallest interval containing all the entries of `x`. The default value for the weight vector `w` in the *error measure* is `ones(size(x))`. The default value for the piecewise constant weight function λ in the *roughness measure* is the constant function 1. Further, $D^2 f$ denotes the second derivative of the function f. The default value for the *smoothing parameter*, `p`, is chosen in dependence on the given data sites `x.` ⋯

`csaps(x,y,p)` lets you supply the smoothing parameter. The smoothing parameter determines the relative weight you would like to place on the contradictory demands of having f be smooth vs having f be close to the data. For `p=0`, f is the least-squares straight line fit to the data, while, at the other extreme, i.e., for `p=1`, f is the variational, or 'natural' cubic spline interpolant. As `p` moves from 0 to 1, the smoothing spline changes from one extreme to the other. The interesting range for `p` is often near $1/\left(1+h^3/0.6\right)$, with h the average spacing of the data sites, and it is in this range that the default value for `p` is chosen. For uniformly spaced data, one would expect a close following of the data for $p = 1/\left(1+h^3/60\right)$ and some satisfactory smoothing for $p = 1/\left(1+h^3/0.6\right)$. ⋯

One important question regarding smoothing data with basis functions in general and smoothing splines in particular is – what degree of smoothing is appropriate? 'On the one hand we wish to ensure that the estimated curve gives a good fit to the data, for example in terms of the residual sum of squares $\left|y_i - f\left(x_i\right)\right|^2$ in (5.2) . On the other hand, we do not wish the fit to be too good if this results in a curve that is excessively wiggly or locally variable. These competing aims can be seen, in some sense, as corresponding to the two elements of the basic principle of statistics.' ([99] p 58) This is to say, there must be balance between inherent bias and statistical variability, as can be expressed in the so-called Bias2Variance trade-off (see equation (5.3) below).

This is a complex question and a number of different criteria can be employed from the most subjective of 'when it looks right' to methods involving a variety of more or less sophisticated statistical approaches. For a discussion of some of these methods refer to [99] and [102], for example. The method employed here is generally a combination of 'when it looks right' and when the standard deviation of the residuals is close to what one might expect with the measurements being used.

A good example of this approach is shown in Figure 5.16 on page 143. The *S* shape in the normal probability plot indicates that the distribution has long tails. This is typical of a distribution with high kurtosis[25]. Kurtosis is a measure of the "peakedness" of the probability distribution. Positive kurtosis manifests itself as a more "peaked" distribution with an excess of values centred about the mean and longer tails. It is an indication that more of the variance is due to infrequent extreme deviations. A normal probability distribution has a kurtosis of 0 see footnote 25). Conversely, a distribution with negative kurtosis has a smaller peak around the mean with a lower probability than a normally distributed variable of both values near the

---

[25] Kurtosis is the variance-normalised 4th central moment. It is given by $\frac{\mu_4}{\sigma^4}$ where μ_4 is the fourth moment about the mean and σ^2 is the variance. The kth central moment is given by $\mu_k = E\left[\left(X - E\left(X\right)\right)^k\right] = \int_{-\infty}^{+\infty}\left(x-\mu\right)^k f\left(x\right)dx$ where E is the expectation operator. Kurtosis is more generally defined as $\frac{\mu_4}{\sigma^4} - 3$ to bring its value to zero for a normal distribution.

mean and extreme values. The normal probability plot of this type of distribution is an inverted s shape.

The example of Figure 5.16 has a kurtosis of 17.45. Changing the smoothing parameter p in (5.2) so the distribution of the residuals are normally distributed causes the smoothing function to approach an interpolating function passing very close to, or through all of the points. Intuitively this is not representative of the underlying process. Different smoothing models for the top graph of Figure 5.16 are examined later in this section and in Figure 5.2.

The Bias^2 Variance trade off is discussed extensively in [102] where (5.3) is given.

$$\text{Error} = \text{Irreducible Error} + \text{Bias}^2 + \text{Variance} \tag{5.3}$$

This equation assumes $y = f(\vec{x};\vec{\beta}) + \varepsilon$ (equation (5.1)), where the expectation $E(\varepsilon) = 0$ (i.e. zero mean) and $Var(\varepsilon) = \sigma_\varepsilon^2$ (i.e. a constant variance). In this equation, the Irreducible Error σ_ε^2 is the error inherent in the manner in which the data was gathered. It is for example the uncertainty in the measurement of a capacitive probe. The Bias^2 is the model bias. This is how well the model represents the data. The Variance is the model variance and represents how much the model 'wiggles' around. Model Bias^2 and Variance are mutually competing factors.

Very often we will develop a model to make some prediction concerning the underlying process that generates the data. If all of the data are used to create the model, we can come arbitrarily close to the measured points. However this will not necessarily be very representative of the actual process or of new points measured of it. This trade off is illustrated in Figure 5.1. Generally as the model complexity is increased, the Variance tends to increase and the Bias^2 tends to decrease (i.e. the model wiggles around more and the difference between the model and the measured points decreases). We would like to optimise the representation of the process in such a way so as to minimise the prediction error. On the left hand side of Figure 5.1 when $p = 0$ in equation (5.2) the data are represented by a best fit line. Under these conditions, there is low Variance and high Bias^2. On the other hand, when $p = 1$, the model is an interpolating function and there is high Variance and low Bias^2.

Somewhere between the two, the model will provide a good, or optimal representation of the underlying process and of new data. The challenge is to try and find this compromise.

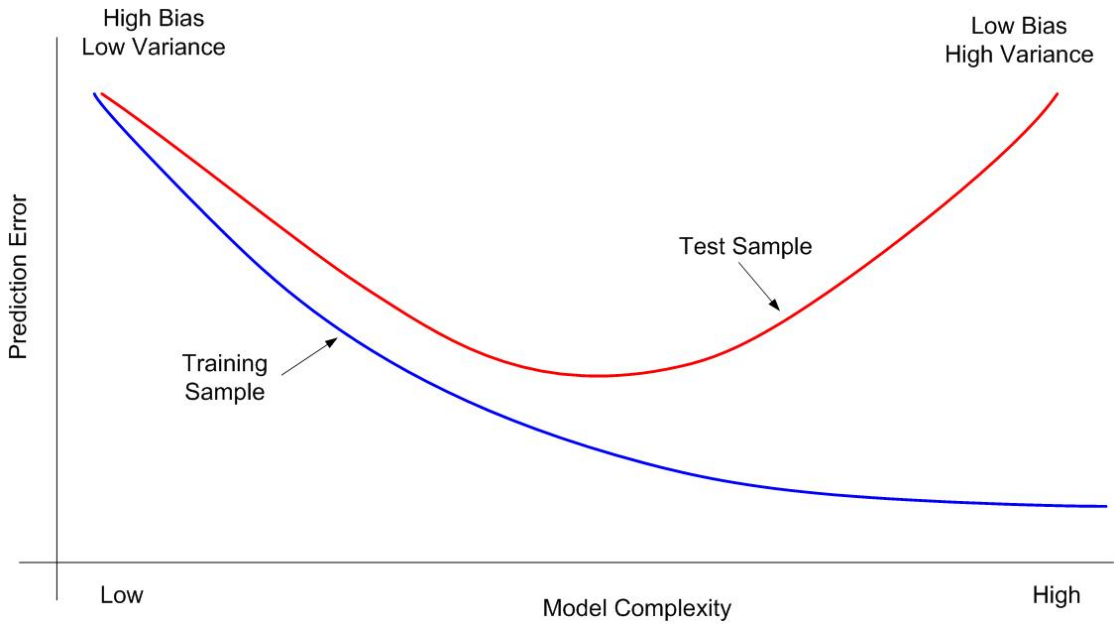

Figure 5.1 Illustration of the Bias^2 Variance trade off. The training sample may represent the measured data arbitrarily well. However, it may not be very representative of the underlying process or of a new series of measured data. There is some optimal point where the Bias^2 variance trade off will minimize the prediction error. This graph, reproduced by the author, comes from p.38 of [102].

The problem is that to rigorously find this compromise requires considerable effort and computation. Furthermore, the optimal model may be only very slightly better than a host of adjacent models. There is also the possibility that the optimal model will somehow appear flawed to the person building it. We will examine this in the next paragraph.

Once again taking our example of Figure 5.16, the chosen smoothing parameter is 0.001. As it turns out this p value is actually very close to the optimal one. Now clearly there are an infinite number of possible values for p . In many cases, pragmatism wins over pedantries and precision and one simply chooses 'when it looks right'. However, pedantics aside, one can easily evaluate the uncertainty of the model chosen. Thus even though we may not choose the optimal model (i.e. the low point of the Test Sample curve in Figure 5.1), we can always assess its uncertainty. Indeed it is generally some measure of this uncertainty that is used to choose an optimal model.

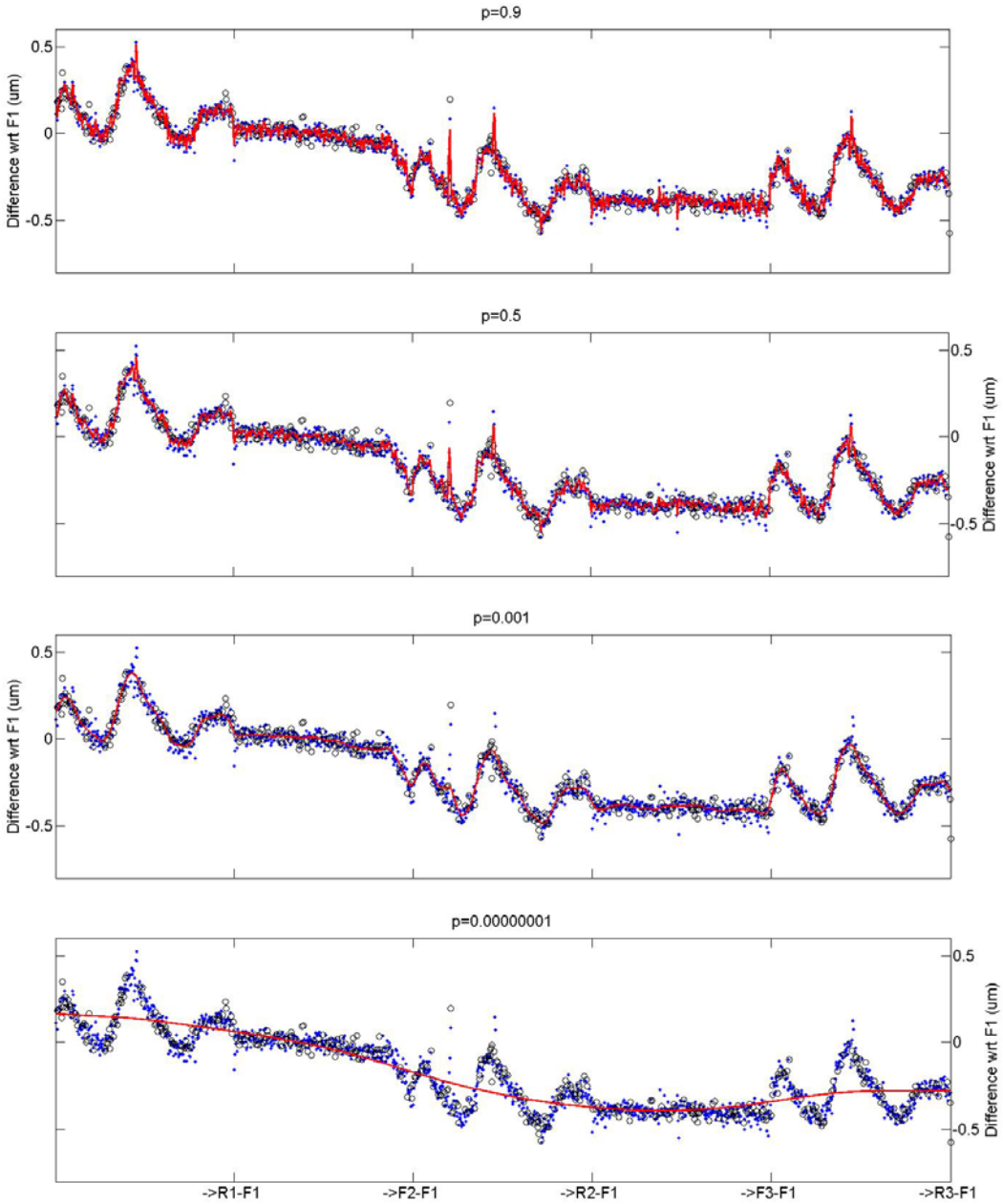

Figure 5.2 For different smoothing models for the data presented in Figure 5.16. From the top to the bottom graphs there is progressively more smoothing in the model (i.e. p=0.9 to p=0.00000001). This is also the passage from a high Bias^2, low Variance to a low Bias^2, high Variance model.

This approach discussed above is demonstrated in Figure 5.2 and Figure 5.3. The data set consists of 1805 points. Five hundred points were selected as a test sample and the remainder used to train the models. Several different smoothing models with p values ranging from 0.00000001 to 0.9 were employed. Four of these models are shown in Figure 5.2. This procedure was repeated 20 times and the mean value of variance of the residuals of the training and test data sets with respect to the smoothing models calculated. The results are shown in Figure 5.3

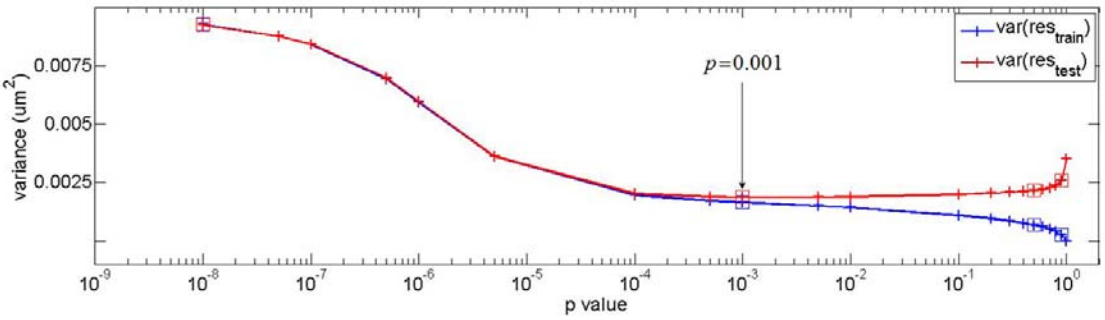

Figure 5.3 This Bias^2 Variance trade off is derived from data discussed in Bias^2 Variance trade off and Figure 5.2 above. As the p value increases (i.e. more smoothing) from left to right, the variance of the training and test samples decreases. However at $p = 0.0001$, the variance of the test set levels off and later begins to increase. The variance of the training data set decreases continuously as the model approaches an interpolating function.

It is clear from Figure 5.3 that the choice of the optimal model is not very easy. One can say that good smoothing models can be chosen over the range $p = 0.0004$ to $p = 0.001$. However, intuitively, one feels that the third graph of Figure 5.2 (i.e. $p = 0.001$) is a good representation of the underlying process. The actual minimum of this the test variance curve is near $p \simeq 0.002$. Indeed the form of the model at this p value is indistinguishable from the chosen value of $p = 0.001$.

The selection of an optimal model is difficult. Although statistical insights may be helpful, ultimately, the model relies heavily upon the common sense of the individual actually constructing it to represent the underlying deterministic process. The human mind and eye is highly developed in this task.

5.2 Evaluation of the Linked Encoder Configuration (LEC)

5.2.1 General remarks

The linked encoder configuration (LEC) was introduced in section 3.4.3. It is composed of two Heidenhain RON 905 angles encoders linked through a continuously rotating shaft. One encoder is fixed to the base of the HCC while the other rotates with the HCC plateau and the spherical measuring system (SMS) instruments; the robotic total station (RTS) or laser tracker (LT) mounted on it. The aim of this section is show how one may go about evaluating this instrument so as to ultimately provide an uncertainty statement related to it.

There are two facets to this evaluation. The first is the internal coherency of the LEC. This relates to the form and behaviour of its measurement signal. In particular, we are interested in the assumptions made in section 3.4.3.4. Recall that, first, we consider the LEC residual errors are smooth and continuous. Secondly, we consider that even if the function $\alpha_{RON1} - \alpha_{RON2}$ does not repeat itself after one full rotation, the error at zero will be the same after every revolution (i.e. $(\alpha_{RON1} - \alpha_{RON2})_0 - (\alpha_{RON1} - \alpha_{RON2})_{i\times 2\pi} \cong 0$ for all i under consideration). In other words the signal is non-divergent.

Secondly, we are interested in the coherence of the LEC measurement with regard to a known standard. By necessity, this evaluation is further divided into two categories; the small angle and the full circle evaluation. The small angle refers to displacements not greater then ±300 arc-seconds. The full circle evaluation is over the 360 degree reading capacity of the instrument. For angle displacements greater than approximately one degree, the other plateau motions (i.e. tilts about the x and y axes and the translation movements along the x, y and z axes) begin to influence measurements made by the instruments evaluating the LEC. To avoid these influences altogether we examine very small angle displacements.

The second category of evaluative measurements is over 360 degrees. It is not exclusively related to the LEC but rather to the HCC as a whole. To discuss this evaluation, plateau tilt and translational movements must be considered. This is introduced in section 5.4 and specifically done in section 5.5.

5.2.2 LEC data

The LEC data is collected from a National Instruments NI-PCI-6115 A/D card providing 12 bit resolution on 4 simultaneously sampled channels at a maximum of 10 Mega-samples/s. Data are typically sampled at 500 kilo-samples /second. With a standard revolution speed of 20º per second a full revolution takes 18 seconds. Thus 9 Mega-samples are used for the mean value (equation (3.2)) of the phase angle used to determine an angle displacement. Figure 5.4 shows a data sample record over three revolutions of the LEC. By necessity the sampling has

been reduced by a factor of ten for this example. The form of the curve is complex. At its base are the 36000 sinusoidal oscillations associated with the encoder gratings. However there are other identifiable long term trends.

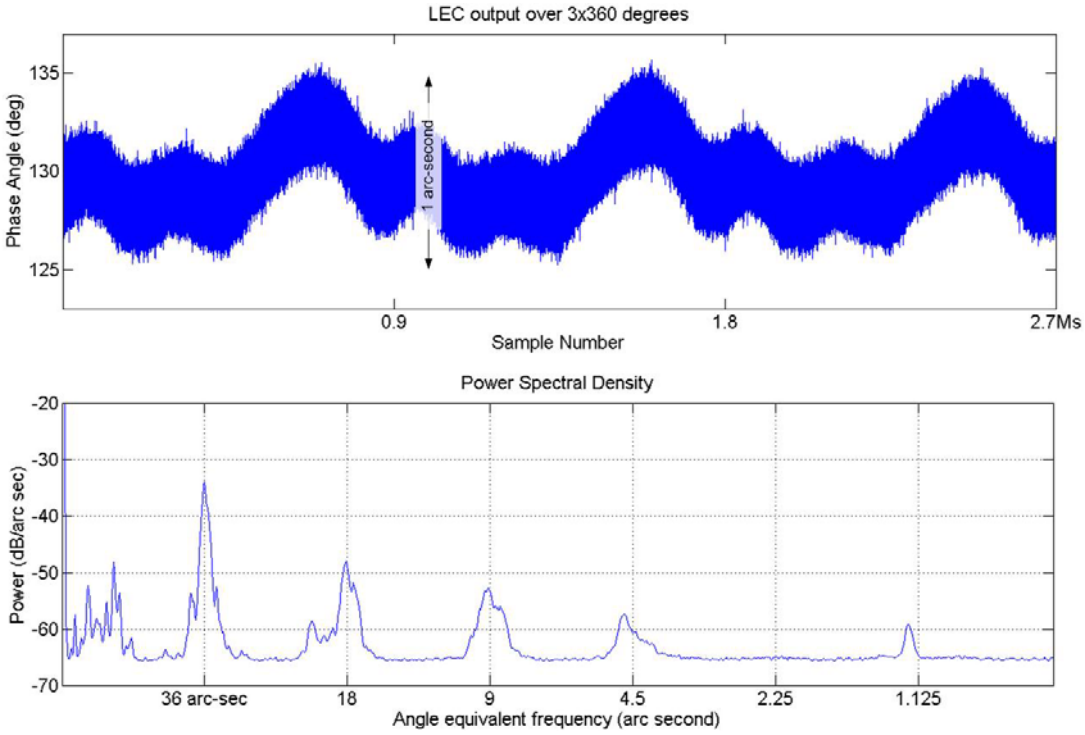

Figure 5.4 The top graph shows real RON905 differences ($\alpha_{RON1} - \alpha_{RON2}$) over three full turns (1080 degrees) of the LEC RV120CC. Note the sampling rate here is 50 Ksamples per second rather than the regular sampling rate of 500 Ksamples per second. Recall that 360 degrees of phase angle is equivalent to 36 arc-seconds of rotation, thus peak to peak $\alpha_{RON1} - \alpha_{RON2}$ is in the order of 1 arc-second. The lower graph shows the spectral content of the LEC $\alpha_{RON1} - \alpha_{RON2}$ signal in dB per arc second of equivalent frequency. Recall the nominal LEC rotation speed in 20º per second. There are notable peaks at 36 arc-seconds and its harmonics 18, 9 etc… arc-seconds.

Before continuing, it is important to spend some time understanding this graph and others like it. On the abscissa (x axis) is the number of samples. This is closely related, but not strictly identical to rotation angle of the LEC RV120 CC (i.e. 0.9 Mega-samples for this example is not precisely 360 degrees). The ordinate (y axis) is $\alpha_{RON1} - \alpha_{RON2}$. This value, which varies between 0 and 360 degrees, is proportional to a rotational displacement of the HCC plateau within one RON 905 encoder grating of 36 arc-seconds. For example a y value (phase angle in degrees) of 129.2245 degrees is related to a plateau rotational angle of $(129.2245/360)\times 36$ or 12.922 arc seconds.

The lower graph of Figure 5.4 shows the spectral content of the LEC signal. There are notable peaks at 36 arc-seconds and its harmonics 18, 9 etc… arc-seconds. Above 36 arc-seconds there are peaks at 98, 196 and 394 arc-seconds. These are close to multiples of 3 of the 36 arc-second grating signal (i.e. $108 = 3 \times 36$, $216 = 6 \times 36$ and $432 = 12 \times 36$). There is one notable non-harmonic type peak at 20.75 arc-seconds.

5.2.3 Signal assumptions

In section 3.4.3.4, we postulated that the LEC signal could be represented by a Fourier series. The advantage of the Fourier representation is that the sum of the sine and cosine terms is zero over 360 degrees. Using this representation we know that the LEC angle can be represented by its mean (DC) value. This section examines how well the assumptions regarding smoothness, continuity and non-divergence apply to the LEC data. Finally we must also look at how well we can determine where multiples of 2π radians fall and the influence of an error in estimating the data set composing a 360 degree data set.

5.2.4 Smoothness and continuity

To represent the LEC data in a tractable mathematical manner, we assume that it can be represented by a Fourier series which has been polluted by noise due to uncertainty in the measurement process. Implicit to this approach is that data are smooth and continuous. Figure 5.5 shows LEC data gathered over 6 gratings of 36 arc seconds each. At a speed of 20 degrees per second and sampling rate of 500 kSamples/second, each grating is sampled close to 250 times. This sample represents only one part in 18000 (i.e. $(6 \text{ gratings})/(3 \times 36000 \text{ gratings})$) of the LEC signal shown in Figure 5.4. Nonetheless, it may be considered representative of the LEC signal as a whole.

An order 20 Fourier basis[26] is used to produce the smooth curve that is considered to represent this signal. Problems and criteria related to the model selection; in this case an order 20 Fourier series, are discussed in section 5.1. As expected, there is significant noise around the smooth signal, and residuals with respect to it are shown in the bottom of Figure 5.5. A

[26] $a_0 + a_1 \cos(xw) + b_1 \sin(xw) + \cdots + a_{20} \cos(20xw) + b_{20} \sin(20xw)$ where $w = 2\pi/(\max(x) - \min(x))$

normal probability plot of these residuals is shown in the bottom right hand graph of this figure. These residuals appear normally distributed with a standard deviation of 0.043 arc-seconds.

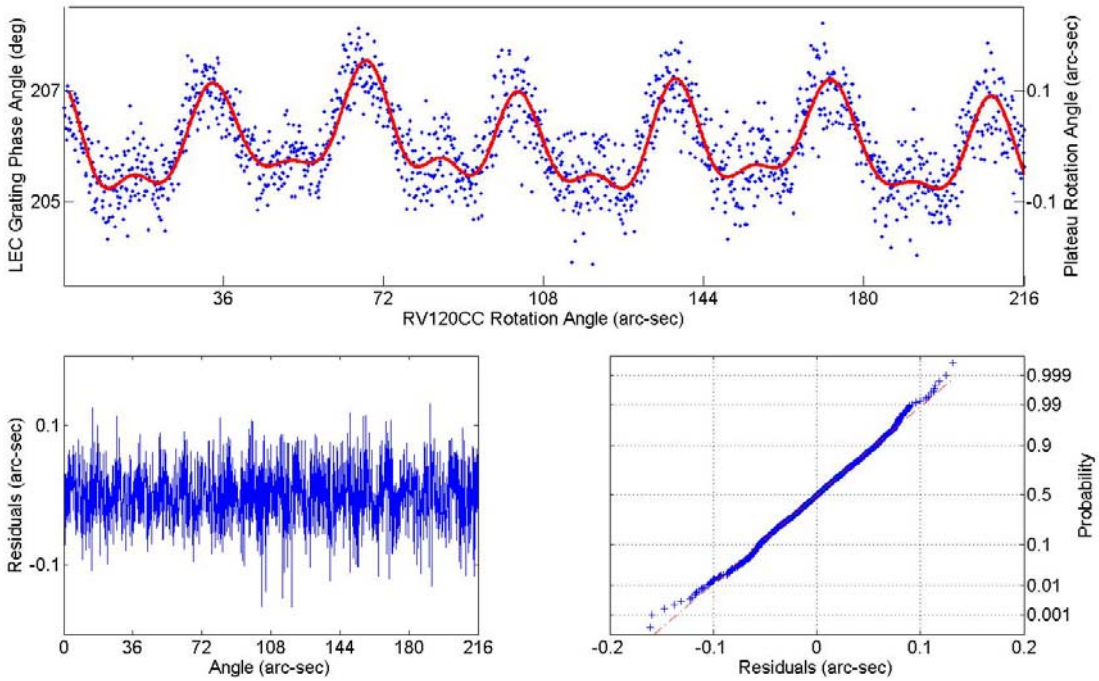

Figure 5.5 The top graph shows LEC data sampled over 6 gratings at 500 kSamples/s. The LEC has a revolution speed of 20 degrees per second so one grating of 36 arc seconds has 250 samples (i.e. $0.01° \times (500 \text{ kSample/sec}) / (20 \text{ °/sec})$). A smooth Fourier series basis function (order 20) is passed through the data. The bottom left hand graph shows residuals with respect to this curve and the bottom right hand graph is a normal probability plot of these residuals.

The aim of this exercise is to evaluate the smoothness of the LEC signal. Is it smooth? It is impossible to prove one way or another that this signal is. However, recall that the manufacturers claimed uncertainty in a RON 905 reading is 0.4 arc-seconds. With two RON 905s used in the LEC, the base expected uncertainty in the LEC measurement would be 0.566 arc-seconds (i.e. $\sqrt{2 \times 0.4^2}$). This uncertainty applies to the full 360 degree circle. The uncertainty in the smooth signal is over an order of magnitude smaller than this. Thus it is reasonable to assume the Gaussian distributed noise about the smooth signal can be attributed to the measurement uncertainty in the RON 905 itself. The conclusion is that the LEC error curve is smooth and that the Fourier series can be employed as a reasonable representation of it.

5.2.5 Non-divergence

The second assumption for the LEC data is that it is non-divergent. In other words the values at the LEC zero position, and multiples of it (i.e. $i \times 360$ degrees for $i = 1 \cdots n$ where n is the number of full revolutions of the RV120 CC), assuming there has been no induced plateau movement, are equal. Without loss of generality, we can assume these values (i.e. $i \times 360$) are equal to 0. We will see later that this is not strictly the case for all n due a number of environmental factors. However, before continuing, we must investigate a highly repeatable bias error due to a modulation of the LEC signal as a function of n. This is shown in Figure 5.6.

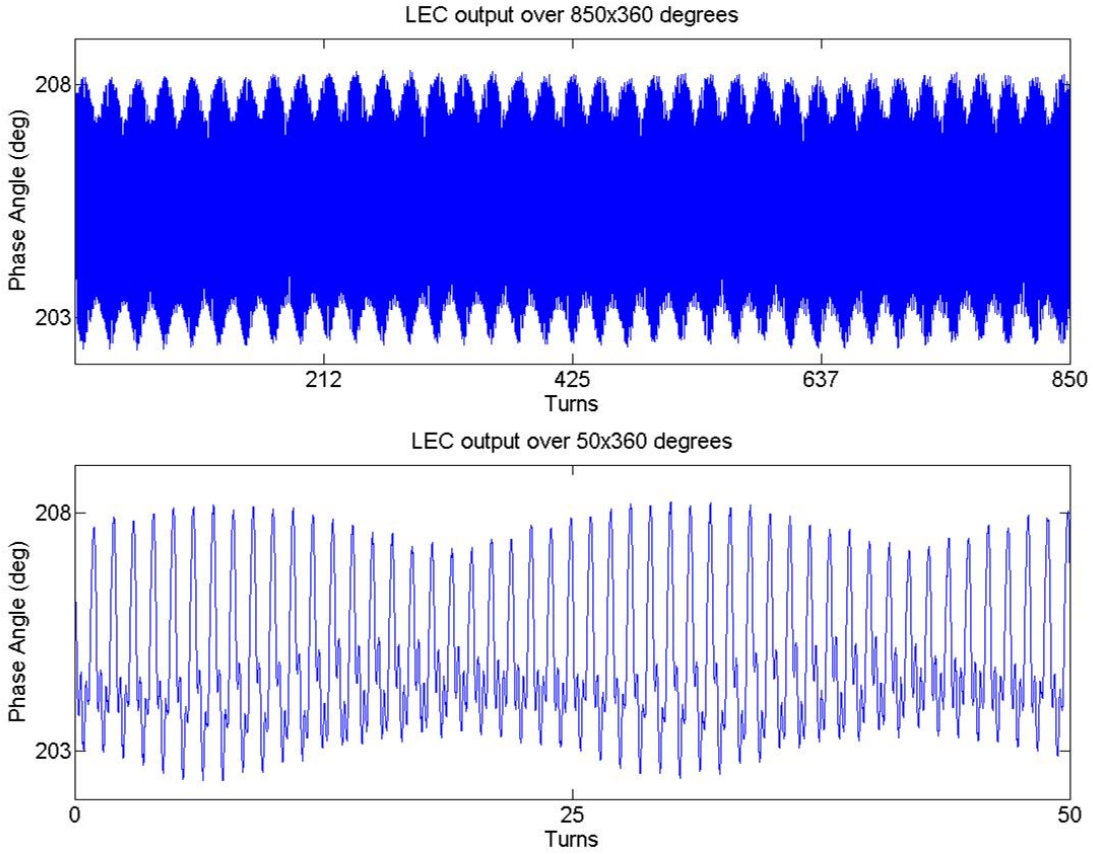

Figure 5.6 LEC data gathered over 850 revolutions. Each revolution consists of 180 mean values of 50 kSamples. The top graph therefore has 153000 points. The bottom graph is a zoom over 50 LEC revolutions. We see the characteristic oscillation over one LEC revolution shown in Figure 5.4. However we also see a clear amplitude modulation with a period in the order of 25 LEC revolutions.

Figure 5.6 shows successive mean values of 50 kSample data sets sampled at the standard 500 kSamples per second and a LEC revolution speed of 20 degrees per second. The top graph shows data for 850 LEC revolutions. Each revolution consists of 180 points. Thus there

are 153000 points in the top graph (i.e. 850 revolutions × 180 50 kS mean values). The bottom graph shows a zoom over 50 LEC revolutions. First we see the characteristic oscillation over one LEC revolution shown in Figure 5.4. Imposed on this, we also see a clear amplitude modulation with a period in the order of 25 LEC revolutions. This modulation is highly repeatable and is always observed, even after a plateau movement.

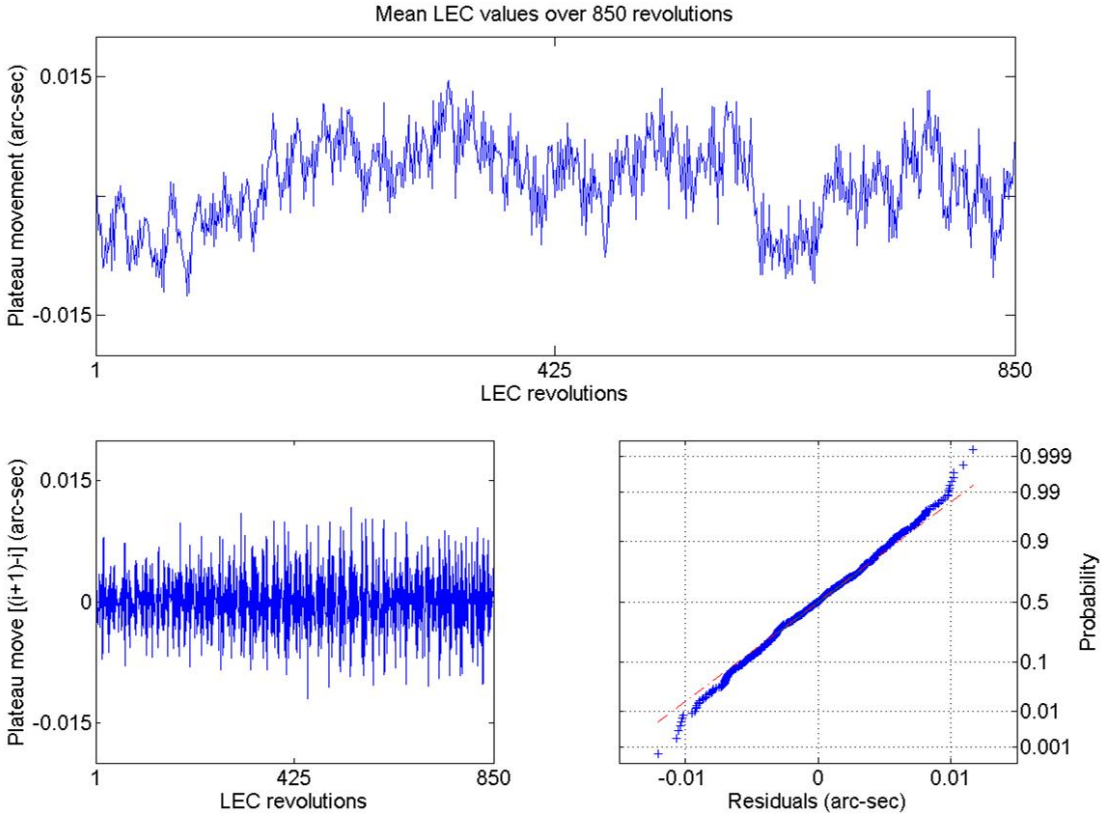

Figure 5.7 The top graph shows mean values of the LEC over one revolution for 850 revolutions. These two graphs give the impression the mean values follow a random walk process and are hence not deterministic. The bottom left hand graph shows the difference between successive mean LEC values. The bottom right hand graph shows a normal probability plot of these difference values. This graph shows a Gaussian distribution which supports a random walk hypothesis for the meaned LEC data.

Given its regularity it could potentially be modelled. However, the mean value of the 9 MSamples over one LEC revolution eliminates its influence. This is illustrated in Figure 5.7 where the mean value of successive LEC revolutions appears to be a random walk process; at least over the 850 revolutions or equivalently 4 hours and 15 minutes of observations. This indicates that under static conditions the LEC mean value does not appear to be influenced by (a) deterministic driving force(s). The standard deviation of these mean values over the observation period (i.e. top graph of Figure 5.7) is 0.005 arc-seconds. Although we have established that the modulation in the LEC values can be ignored, it is nonetheless interesting

to look this process more closely. To understand the nature of this signal modulation, we must first look at it differently. Placing the 180 data points for each of LEC rotations one after another results in a surface shown in Figure 5.8. The LEC error function is developed along the x (Sample Number) axis. It is worth noting that this axis also represents the LEC revolution and may be viewed as running from 2 degrees (sample number 1) to 360 degrees (sample number 180). The 850 revolutions are displayed one after another along the y (LEC revolution number) axis.

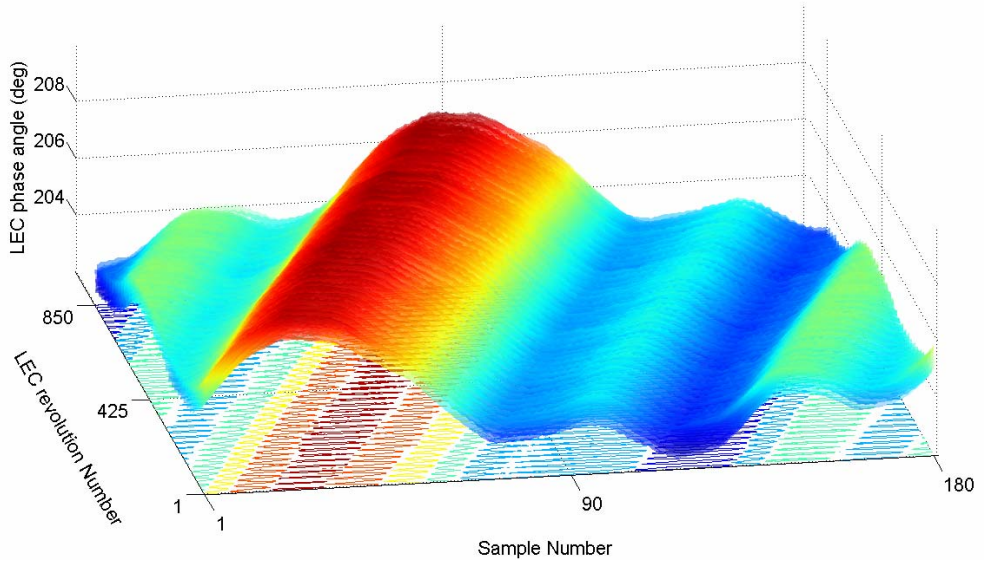

Figure 5.8 Folding the signal shown in Figure 5.6 so that we look at each LEC rotation one after another shows that the error curve appears to move to the right as a function of LEC revolution number or time. Superimposed on this rightward motion is a second oscillation. It is this second oscillation that appears as a modulation in Figure 5.6.

It is immediately clear from Figure 5.6 that the error curve appears to move to the right, with elements disappearing on the right hand side and reappearing to the left as a function of increasing LEC revolution number, or time. We also see superposed on, and synchronised with this rightward motion, the modulation shown in the top graph of Figure 5.4 and the bottom graph of Figure 5.6. This is perhaps more clearly seen with the contour plot under the surface.

In fact, because the LEC is in continual rotation, it acts like a spinning top or gyroscope and indeed, has similar characteristics to one. In particular, as with a spinning top or gyroscope, the LEC undergoes precession (rightward or clockwise motion with clock wise LEC rotation)

and nutation (the modulation signal seen in Figure 5.5). These motions which appear to explain the modulation seen in Figure 5.4 and Figure 5.6 will now be investigated.

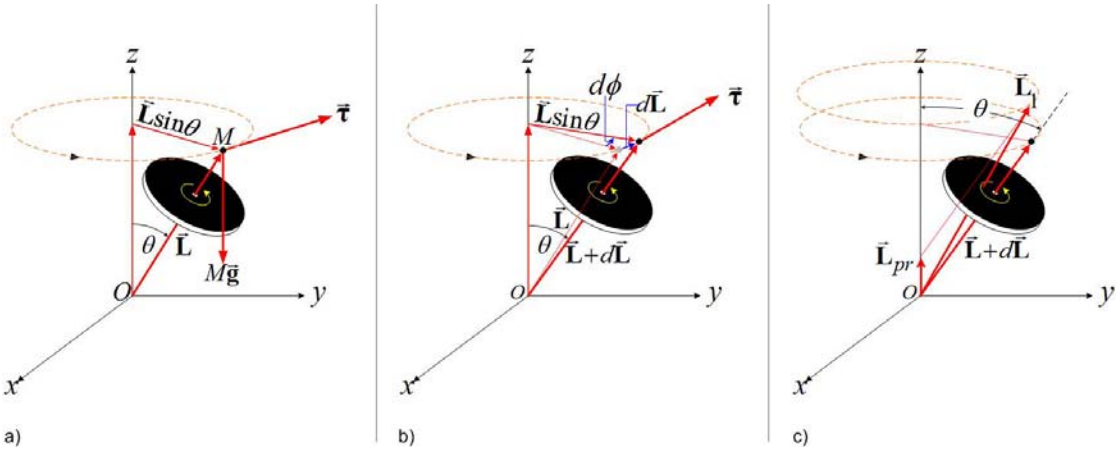

Figure 5.9 A spinning top precesses about the vertical axis z. The force $M\vec{\mathbf{g}}$ of the top due to gravity exerts a torque $\vec{\boldsymbol{\tau}}$ about the origin O. The torque is perpendicular to the angular momentum vector $\vec{\mathbf{L}}$. The torque b) changes the direction of the angular momentum vector $\vec{\mathbf{L}} + d\vec{\mathbf{L}}$ causing precession. However, the there are actually two components to the total angular momentum $\vec{\mathbf{L}} + d\vec{\mathbf{L}}$ and $\vec{\mathbf{L}}_{pr}$ due to the precession and the resultant vector $\vec{\mathbf{L}}_{total}$ does not generally lie in the symmetry axis of the spinning top. The difference between the ideal situation and the actual situation results in an oscillation called nutation of the top back and forth about the precsssional circle c).

Conceptually, the behaviour shown in Figure 5.4, Figure 5.6 and Figure 5.8 can be described by the addition of two motions; fast nutation about the vector $\vec{\mathbf{L}}_1$ (see Figure 5.9c) due to the deviation of $\vec{\mathbf{L}}_1$ from the axis of symmetry (angular momentum vector $\vec{\mathbf{L}}$), and simultaneous torque induced slow precession of this vector about the vertical z axis.

Combined precession and nutation is a complex phenomenon requiring relatively involved mathematics (see for example [103]) to describe fully. A simple approach without a full treatment of nutation is given in [104]. An interesting approach with a useful Java simulation is provided by [105]. The approach used below is based on the derivation given in [106].

The effect of precession and nutation is often described by the path of the curve projected by the body symmetry axis on a unit sphere in the fixed system. Using the notation and argument of [106] (p. 135), the general case of the precessional angular velocity is described by $\dot{\psi} = \dfrac{\gamma - Nu}{1-u^2}$ where γ and N are constants related to the moments of inertia and momentum of the spinning top, gyroscope or in our case, the LEC system, θ is the inclination of the

spinning axis with respect to the vertical z axis (see Figure 5.9 and Figure 5.10) and $u = \cos\theta$. If θ is held constant then the spin axis will generate a cone about the z axis of the fixed system due to precession. For a spinning top, θ is bounded on the sphere between two circles $u_1 = \cos\theta_1$ and $u_2 = \cos\theta_2$. The general case of precession above describes three different types of curve depending upon the initial conditions imposed upon the system (Figure 5.10).

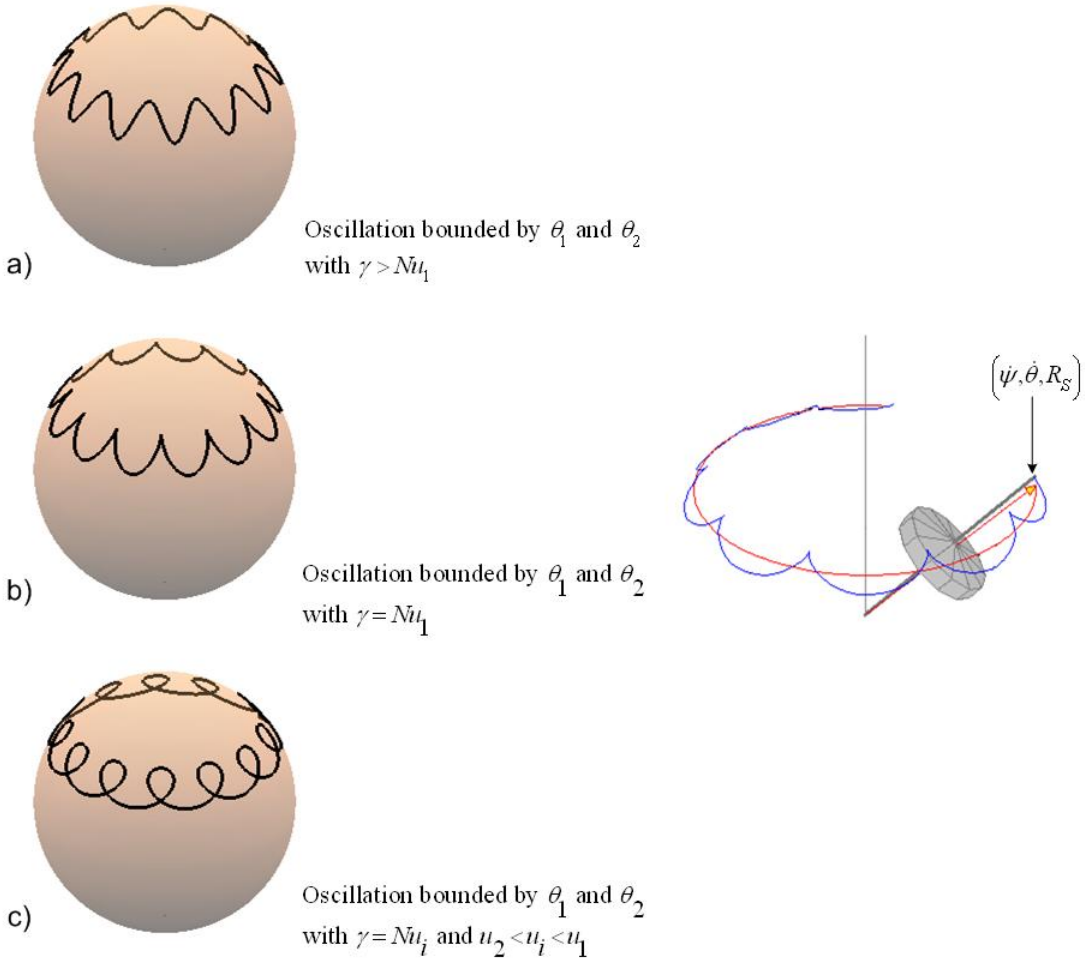

Figure 5.10 Three cases describing the precessional motion of a spinning top or gyroscope. The first case a) results when there is an initial angular velocity in the direction of the precession. Case c) results when there is an initial angular velocity in the direction opposite to the direction of precession. The most common case, and indeed the case of the LEC b) results from initial conditions $\theta = \theta_1$ and $\dot{\psi} = 0 = \dot{\theta}$.

The most common motion type is cusp like. It corresponds to the usual method of starting the top, and indeed, the method whereby the LEC is started. First the top is set to spinning around its axis, and then it is given an initial tilt and finally released. It immediately begins to fall due to the force of gravity. As the symmetry axis falls, its velocity increases and increases

over that of the regular precession which in turn makes the axis begin to move up. In this way the top oscillates back and forth. With a normal top, this 'nodding', or nutational motion damps due to friction. However, in the case of the LEC, there is a constant rotation and so the nutational motion (oscillation) is not damped.

The other two possible types of precessional motion are; a sinusoidal oscillation describing the motion when there is an initial angular velocity in the direction of the precession, or a looping motion if there is an initial angular velocity opposite to the direction of precession.[103, 106]. Precession for the LEC is the most common cusp form shown in (b of Figure 5.10 and given by (5.4). [106] In (5.4), N (as above) and β are constants of the system, and $\dot{\psi}$ and $\dot{\theta}$ are the angular velocities of precession and nutation respectively.

$$
\begin{aligned}
&\dot{\psi} = \frac{N\left(\cos\theta_0 - \cos\theta\right)}{\sin^2\theta} \\
&\dot{\theta}^2 = \left(\cos\theta_0 - \cos\theta\right)\left[\beta - \frac{N^2}{\sin^2\theta}\left(\cos\theta_0 - \cos\theta\right)\right] \\
&\text{and is bounded by} \\
&\left(\theta_0 = \theta_1\right) > \theta > \theta_2 \\
&\text{with} \\
&\cos\theta_2 = \frac{N^2}{2\beta} - \sqrt{1 - \frac{N^2}{\beta}\cos\theta_0 + \left(\frac{N^2}{2\beta}\right)^2}
\end{aligned}
\qquad (5.4)
$$

It is not clear how these equations relate to or are representative of the LEC motion. Nevertheless, having identified the motion source, we can make some estimates of precession and nutation (Figure 5.11) from the observed data. For the following we will use the maximum value of each revolution of the LEC shown in the graphs of Figure 5.6 and surface of Figure 5.8.

The first step in the precession estimate is to determine the sample number of the maximum value recorded in each LEC revolution. This is then plotted against the revolution number. Recall there are 850 LEC revolutions in Figure 5.6 and Figure 5.8. The plot is shown in graph a) of Figure 5.11. Passing a best fit line through this plot provides an estimate of the number precession degrees per LEC turn (0.1506 degrees/LECturn).

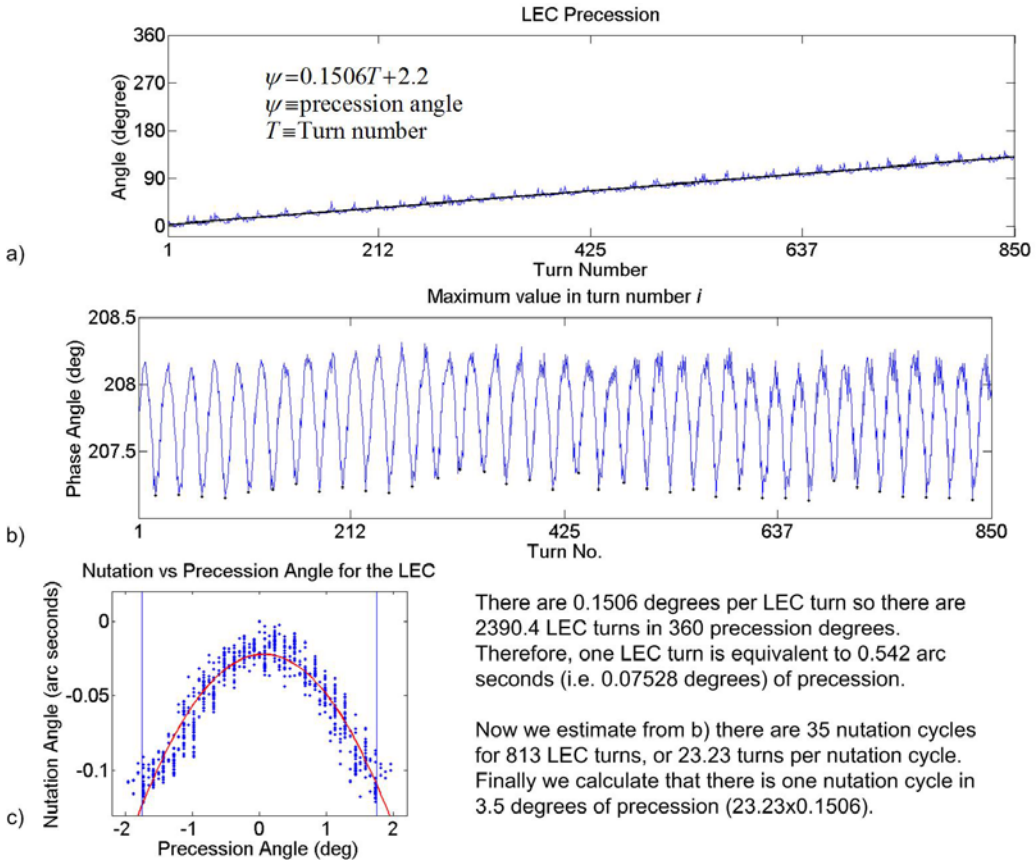

Figure 5.11 The top graph a) shows the sample number index of the maximum value in a given revolution in Figure 5.8 as a function of the revolution number. This provides an indication of the rate of precession which is estimated to be 0.1506 precession degrees per LEC turn. Now recuperating the phase angle corresponding to the maximum value index (once again from Figure 5.8) and plotting against LEC turn revolution provides graph in b). This resembles (an inverted version) the cusp form of Figure 5.10. Plotting each cycle of b) one on another and centring gives c). From these graphs we can estimate the nutation cycle to be 3.5 degrees (or ±1.75 degrees shown by the vertical lines in c) of precession cycle. This cycle is confirmed by the best fit 2nd degree polynomial (solid line in c) and the magnitude of the nutation is estimated to be $2\times(\pm 0.09)$ arc seconds.

For the nutation, we start by taking the maximum phase angle[27] (i.e. the ordinate or y value of Figure 5.6 and Figure 5.8) associated with a LEC revolution and plotting against LEC revolution number. This produces graph b) of Figure 5.11. There is a clear resemblance to the cusp like motion of Figure 5.10 graph b). That this presumed nutation motion of the LEC is inverted with respect to Figure 5.10 is not problematic because the equivalence between Figure 5.10, equation (5.4) and Figure 5.8 is not clear. Indeed, taking the minimum phase angle value gives an upward orientated cusp. In any event, we can really only correlate these phenomena at a qualitative level.

[27] This is simply the phase angle value associated with the sample number of Figure 5.11 b).

From graph b) we remark there are 35 nutation cycles for 813 LEC turns. This corresponds to $813/35 = 23.23$ LEC revolutions per nutation cycle. Using the results determined above for the precession, we can then calculate that there is one nutation cycle in 3.5 degrees of precession (i.e. 23.23 LEC revolutions $\times$ 0.1506 Precession degrees/LEC revolution).

Now, superposing all of the cycles delimited by the points at the cusp of the oscillations of Figure 5.11 b) on one another, and centring gives the graph in Figure 5.11 c). We may now estimate the magnitude of the LEC nutation using a 2nd degree polynomial through these data. The frequency of nutation was calculated to be 3.5 degrees of precession cycle. This corresponds to the distance between the two vertical lines (i.e. ±1.75 degrees) in Figure 5.11 c). Using the mean intersection of the polynomial with the two vertical lines, and the polynomial maximum, one can estimate the apparent nutation effect magnitude to be 0.09 arc-seconds. Note that in graph c) the ordinate axis is in arc-seconds whereas the ordinate axis of graph b) is in phase angle degrees. This was discussed in 5.3.1. Recall that 1 degree of LEC phase angle corresponds to 0.1 arc-second of real angle. Finally, because the signal is symmetric, we should multiply the apparent nutation effect by two resulting in a magnitude of ±0.09 arc-seconds.

This section was started with the aim of showing that the LEC signal is non-divergent. It has terminated with the identification of a modulation of the signal that appears to be a precession/nutation phenomenon resulting from the constant rotation of the LEC. However, because of the symmetry of the signal, it has no influence on the mean value determined over one revolution of the LEC. Therefore, one may state the LEC signal is non-divergent and that its mean value can be used in the determination of the HCC plateau rotation. Finally, we can assign a baseline uncertainty for the LEC at 0.005 arc-seconds determined from the top graph of Figure 5.7.

5.3 Form error spindle motion separation

5.3.1 General remarks

As we shall see in the section 5.5, the spindle motion which gives rise to tilts about the x and y axes and the translation movements along the x, y and z axes of the plateau (e

in Figure 3.5) is of critical importance in the full circle evaluation of the HCC. Thus the FESM is an essential technique. It was introduced in section 4.2. Here we will discuss its implementation. The simplest way to do this is to go through an example from the data collection, preparation and preliminary correction, through to the calculation of the form error and spindle motion.

5.3.2 Data gathering procedure

The procedure used to determine the plateau spindle motion is dictated by the fact the plateau can be rotated a maximum of 370 degrees in one direction. The procedure described in this section is triggered manually. For the analysis made here, this 'manual' procedure provides flexibility. However, identical data are gathered automatically during every instrument calibration made on the HCC.

A cycle consists of waiting at zero, rotating the plateau in the forward direction through 360 degrees, waiting, and rotating it back in the reverse (opposite) direction to zero. The plateau is rotated at a velocity of 5 degrees per second. Several forward – reverse cycles are performed. The example considered in this section consists of three cycles taken over a period of 8 minutes and 42 seconds and consisting of 5212 points. On average data are sampled at 0.5 degree intervals.

The wait periods are denominated Fn for a wait before a forward movement and Rn for a wait before a reverse movement. The wait period Fn takes place at 0 degrees while the wait period Rn takes place at 360 degrees. It is understood that 0 and 360 degrees is one and the same position. However, as we shall see, there is a difference between the two. In this example $n = 1 \cdots 4$ for the forward and $n = 1 \cdots 3$ for the reverse cases. The reason there are four forward cases is because the test ends after three full cycles. Thus there is a waiting period after the third reverse movement before a hypothetical forth forward movement. The data is shown in Figure 5.12.

Although the procedure could be easily automated, and indeed has been, this version is flexible and particularly convenient for the determination of plateau motion and the proper

functioning of the capacitive probes at the start of each calibration. Nevertheless, it is worth noting that the plateau motion is systematic and highly repeatable over time.

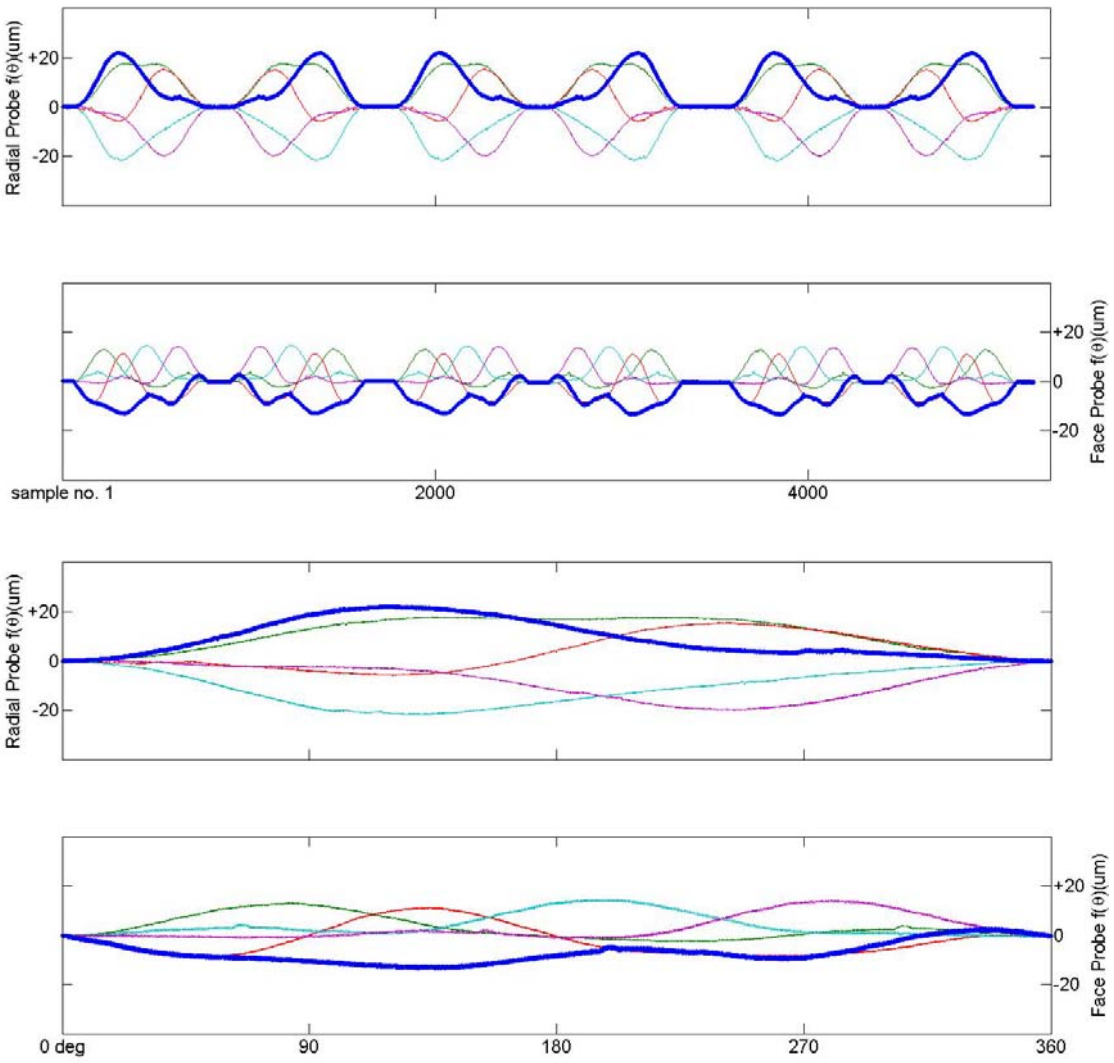

Figure 5.12 Probe data for the radial form error spindle motion separation (top graph) and face error spindle motion separation (2nd graph from top). This data represents three cycles of movements. The forward and reverse movements as well as the wait periods, which are flat and zero valued, can be clearly seen. The same data is shown as a function of angle for the radial probes (2nd graph from bottom) and face probes (bottom graph). The heavy line is the radial and face probe number 1.

Data are sampled continuously and simultaneously from 10 probes. Five each are installed in the radial and face error configurations. The orientations of the radial probes in this example (Figure 5.12) are (0, 46.705, 123.205, 191.799, 278.894) degrees. The orientations of the face probes are (0, 107.002, 158.279, 226.339, 314.873). It should be noted that the radial and face probes are not in the same system. The transformation into a common system is discussed in section 5.5.8. The capacitive probe data are sampled with a high degree of

fidelity in frequency from the A/D card installed on a PC. However, because the application program is running on a different computer than the sampling program, and because of the nature of the distributed computing system, the probe data are actually sampled less regularly by the application program. One data set (i.e. 10 values) is sampled on average every 102 msec. This sampling has a standard deviation of 22 msec and a range of 9 msec to 802 msec. Once again, the timing for this application could very easily be improved; however it is not essential and serves to illustrate how the common problem of synchronisation is dealt with. In summary, these data represent a redundant irregularly sampled set. This can be seen clearly in Figure 5.13 which presents a zoom of the graphs shown in Figure 5.12.

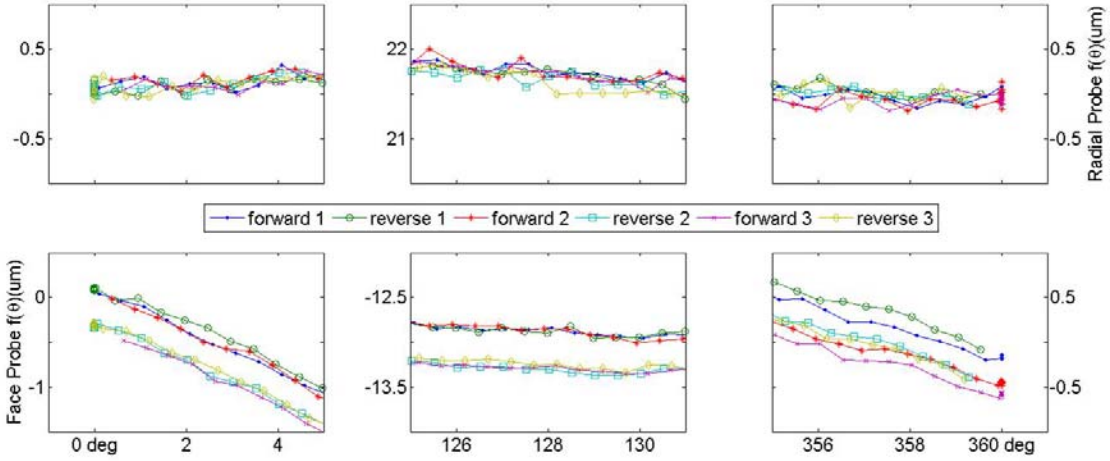

Figure 5.13 Zoom on the data taken from probe number 1 (bottom graphs) of Figure 5.12 for the radial and face form error spindle motion separation. The top graphs show data for three consecutive forward and reverse movements of radial probe 1 between 0 and 5 degrees (left), 125 and 131 degrees (middle), and 355 and 360 degrees (right). Data collected during the wait periods is shown by a large number of clumped points in the left and right hand graphs. The same is shown for the face error probe number 1 in the bottom three graphs. These graphs also highlight the irregularity in the sampling of the data set.

5.3.3 Closure

The probe data have the constraint that they must close (i.e. be equal) upon themselves at 360 degrees. Figure 5.13 shows a zoom of the acquisition sequence of Figure 5.12 at the beginning (0 to 5 degrees), the middle (125 to 131) and the end (355 to 360) for radial (top graph) and face (bottom graph) probe number 1. It is clear, at least for the face probe data, that this constraint is not respected.

For the radial probe number 1, the six data series (i.e. 3 forward and 3 reverse) appear 'intertwined' following the same paths. This is not the case with the face error probe shown in the bottom graphs where there is an evolution in the distance measured by the probe during the second forward movement (red curve with the * symbol in Figure 5.13). This is confirmed in Figure 5.14 where box plots showing the statistics for the wait periods before the forward movements at 0 degrees ($F1 \cdots F4$), and before the reverse movements ($R1 \cdots R3$) at 360 degrees, are given.

This evolution is in the order of 0.4 µm. Close inspection of the curve does not show a sudden change suggesting that it may be due some slow change induced by temperature change or settlement over the course of the latter half of the movement. This will be confirmed in the next section. In this case, because the movement is seen on all of the probes (refer to Table 5.1), it is certainly linked to their common support table. This closure error can be easily corrected. However before doing so, another linked phenomenon shown in Figure 5.13 and more clearly in Figure 5.14 must be discussed.

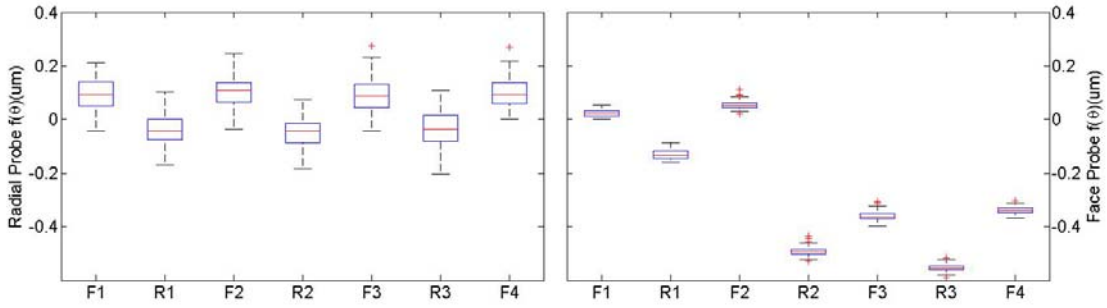

Figure 5.14 Box plots showing the statistics[28] for the wait periods before the forward movements at 0 degrees ($F1 \cdots F4$), where $F4$ is at the end of the test; and before the reverse movements ($R1 \cdots R3$) at 360 degrees shown in Figure 5.13. The left hand graph shows statistics for radial probe 1, while the right hand graph shows statistics for face probe 1.

[28] The box includes values between the lower quartile and upper quartile values. The red line represents the median value. Whiskers extend to the most extreme values within 1.5 times the inter-quartile range from the ends of the box. Outliers are data with values beyond the ends of the whiskers and are displayed with a red + sign

Table 5.1 Oscillations between probe readings at 0 and 360 degrees (i.e. the same nominal positions) during the waiting periods before forward and reverse movements.

	Radial Probe No.					*Face Probe No.*				
	1	*2*	*3*	*4*	*5*	*1*	*2*	*3*	*4*	*5*
R1-F1	-0.14	-0.04	0.11	0.13	-0.06	-0.15	-0.04	0.06	0.08	-0.04
F2-R1	0.15	0.05	-0.10	-0.13	0.08	0.19	0.07	-0.04	-0.10	0.08
R2-F2	-0.15	-0.06	0.10	0.14	-0.09	***-0.55***	***-0.29***	***-0.19***	***-0.43***	***-0.54***
F3-R2	0.13	0.05	-0.11	-0.14	0.06	0.13	0.02	-0.09	-0.10	0.03
R3-F3	-0.12	-0.02	0.10	0.10	-0.09	-0.19	-0.07	0.05	0.04	-0.06
F4-R3	0.13	0.03	-0.10	-0.11	0.08	0.21	0.07	-0.06	0.00	0.11

The first thing to remark in Figure 5.14 is that the data spread for the radial probe (i.e. the box size) is larger then the face probe. This is normal and is linked to the measurement range of the two probe sets. The radial probes have a measurement range of 0.5 mm while the face probes have a range of 0.25 mm. The second point to remark is that there is indeed a change in the median values between the wait before the second forward and second reverse movements of the face probe. This confirms the closure error discussed above. However, on top of this, one can remark there is an oscillation in the order of 0.15 µm of the median values measured at 0 and 360 degrees (see also Table 5.1). This applies to both the radial and face probes.

In principle these measurement points are at the same position. These repeatable oscillations are seen on all of the probe sets (Table 5.1). They could potentially be due to sub one undulation per revolution (UPR) asynchronous motion. In [107] (p 65) it is stated : ‘a rolling element spindle will typically have a’ (bearing) ‘cage rotation component near this frequency’ (i.e. 0.5 UPR). However, it is impossible to resolve to below 1 UPR with the HCC so this hypothesis can not be confirmed. Another speculation is that it could correlate with direction and hence with a backlash-like shift in the centre of mass associated with the platform drive system.

We choose here to correct these different closure errors. This is accomplished by constructing a straight line between the median (or mean) values of the probes in their waiting positions (see Figure 5.14) and determining correction values for the intermediate probe readings at their designated angle positions from this straight line. This of course assumes that the probe evolution is a linear function of angle. An alternative to this assumption is discussed in the next section 5.3.4. Applying this method gives the results shown in Figure 5.15. One sees there is considerable improvement with respect to Figure 5.13 in the face probe results. There is no perceptible change in the radial probe results.

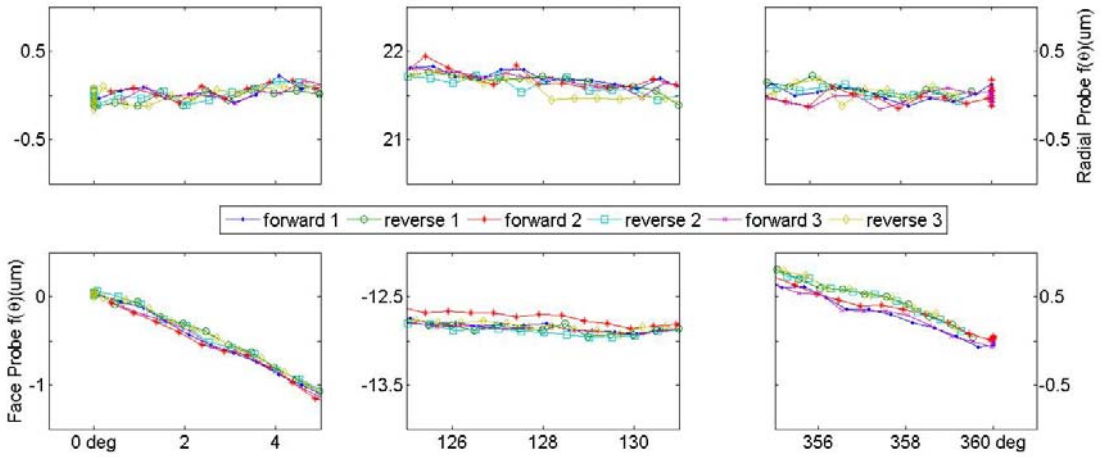

Figure 5.15 Application of the linear closure correction for radial and face probe number 1. These graphs are to be compared to those in Figure 5.13

5.3.4 Data evolution over time

For most purposes, the linear correction discussed in the previous paragraph is sufficient. Nevertheless, a second technique is discussed which demonstrates the use of interpolation and of a smoothing spline. It also permits a finer look at what is happening over the course of the experiment. This technique permits a correction which takes into account a non-linear temporal evolution of the probes. Typically this non-linear evolution is due to environmental factors such as the temperature changes over the experimental period.

The procedure adopted here consists first of interpolating values for the probe readings at regular angle intervals (e.g. every degree $0\cdots360$ for a total of 361 values). This is accomplished by a simple linear interpolation using the two closest measurements on either side of the integer degree. This is done for each forward and reverse movement. When all of

the data sets have been normalized to integer degrees, the first forward motion is subtracted from each subsequent data set (i.e. $R1-F1$, $F2-F1,\cdots$, $R3-F1$). Doing this we implicitly assume that successive probe measurements at the same angle should be equal. If they are not, the difference should reflect any evolution. These successive data difference sets are plotted one after another. This gives the points in the top graph of Figure 5.16.

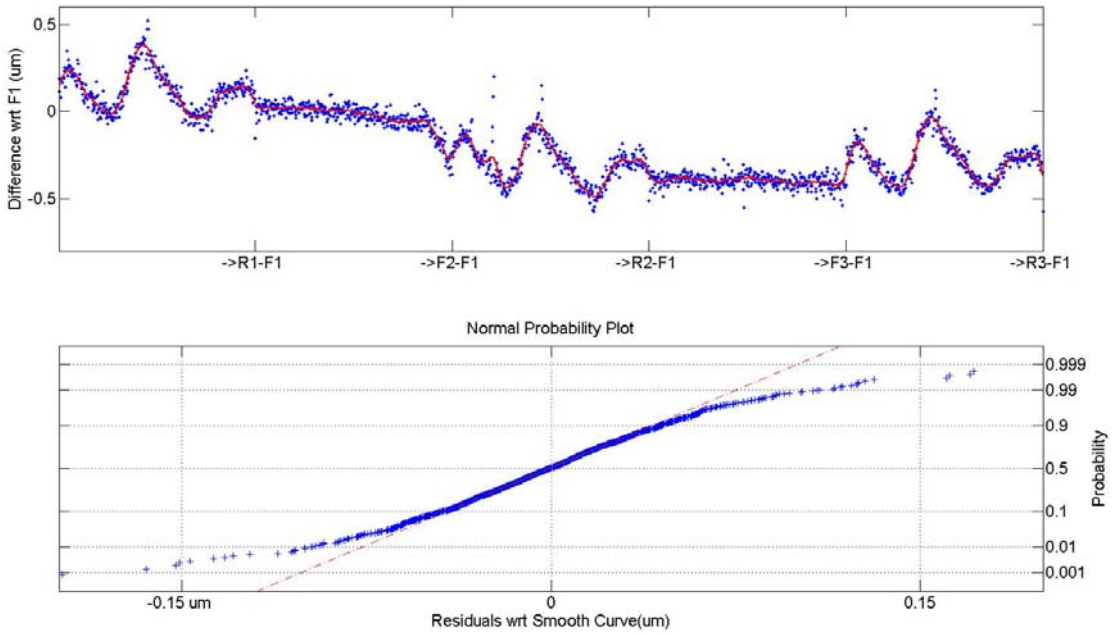

Figure 5.16 Example of the use of a smoothing spline to examine the evolution of the face probe 1 over the duration of the experiment period. The top graph shows the data and a smoothing spline. The bottom graph shows a normal probability plot of the residuals with respect to the smooth function.

The linear interpolation to integer degree values is performed using the built in Matlab interp1 function. Note that data sampling at 0.5 degrees justifies the use of this interpolation interval. We are down sampling in an approximate 2:1 ratio. Differences (i.e. $\rightarrow R1-F1$, $\rightarrow F2-F1,\cdots$, $\rightarrow R3-F1$) where $\rightarrow R1-F1$ represents the difference data for the 361 points of the first reverse sequence minus the same 361 points of first forward sequence) are then calculated for the five difference data sets. One may then use a smoothing spline (e.g. Matlab csaps), to construct an appropriate non parametric function through the data set. The suitability of the spline in this context is discussed in section 5.1. It actually uses this specific data example. The results are shown in Figure 5.16.

We remark in the top graph of Figure 5.16 that the differences between forward movements (i.e. $\rightarrow F2-F1$ and $\rightarrow F3-F1$) are basically linear. This linearity supports the straight line method employed in the correction of the closure error discussed in the previous section. There is, however, a more rapid downward evolution just before $\rightarrow F2-F1$ during the second forward movement. This is clearly where a good part of the evolution discussed in the previous section and shown in Figure 5.14 takes place.

The differences between the reverse motions and the first forward motion (i.e. $\rightarrow R1-F1$, $\rightarrow R2-F1$ and $\rightarrow R3-F1$), on the other hand, are not linear. There are clear systematic effects consisting of a modulation with three peaks. This is shown more clearly in Figure 5.17. Not surprisingly, it appears that the plateau motion is at least partially dependent on its direction of rotation. Thus, for the highest precision work and to avoid introducing a bias into the results, a correction must be applied if the forward and reverse data sets are used together.

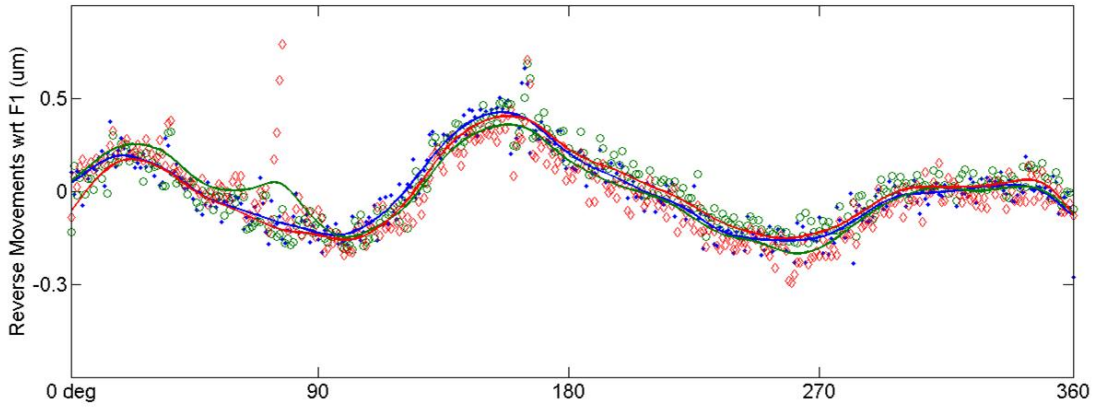

Figure 5.17 Zoom of the three sections $\rightarrow R1-F1$, $\rightarrow R2-F1$ and $\rightarrow R3-F1$ of Figure 5.16 with respect to their mean values.

However, as Figure 5.17 underlines once again, the selection of the model is not completely obvious. All three models appear to represent their section of data quite well; and, although all three models resemble each other closely, they are not identical. This is a combination of the classical problem of training, and testing data models discussed in section 5.1, as well as the underlying uncertainty of the data.

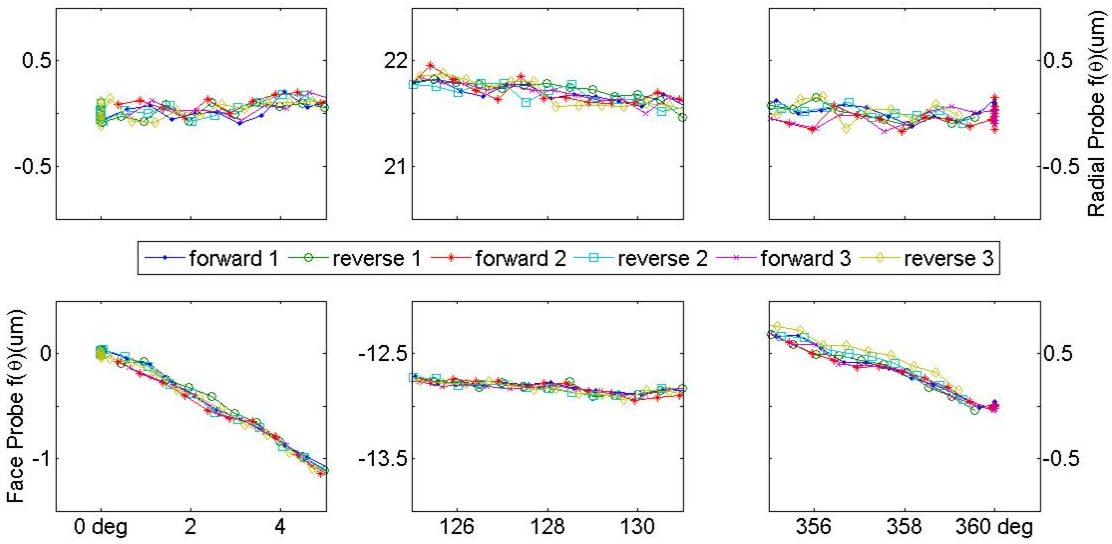

Figure 5.18 The final probe readings corrected for the non-linear evolution and the systematic closure error. This graph is to be compared with the original non-corrected data in Figure 5.13 and the linear closure correction in Figure 5.15.

The application of the non-linear correction to radial and face probe 1 data consists of subtracting the smooth curve of Figure 5.16 from the measured data of Figure 5.12. This gives the results in shown in Figure 5.18. There is slight improvement for the radial probe data, but their intrinsic uncertainty still results in spread in the data. There is, however, a remarkable improvement in the face probe data after the application of first the close correction of the last section and the non-linear correction of this one.

The final step in the preparation is to average the data that has been corrected for the closure and non-linear evolution errors. The data averaging done by passing a smoothing spline through the six superposed corrected forward and reverse data sets.

5.3.5 Data shifting

In section 4.2.3.1 equation (4.19) the problem of shifting the form error $fe(\theta)$ by the angle φ_1 (i.e. establishing $fe(\theta-\varphi_1)$) was evoked in the calculation of $y(\theta)$. The way in which this shift is accomplished is discussed in this section.

Generally form error measurements are at one degree intervals. However, it is extremely unlikely that the shift angle φ_1 is an integer multiple of this sampling interval. Therefore some form of interpolation is required. The form error signal $fe(\theta)$ issued from the form error –

spindle motion separation discussed in section 4.2.3 is smooth. Therefore a spline interpolation is used. Specifically, an array of angles at every degree starting with φ_1 is constructed (i.e. $A_{\text{interp}} = [\varphi_i, \varphi_i + 1, \cdots, \varphi_i + 360]$). Then values for these typically non-integer angles are interpolated[29] using a spline routine over the arrays of augmented integer angles A_{integer} and form error values $FE(\theta)$:

$$A_{\text{integer}} = [-360, -359, \cdots, 0, 1, \cdots 360, 361, \cdots, 719]$$
$$FE(\theta) = [fe(\theta), fe(\theta), fe(\theta)]$$

For example if $\varphi_1 = 21.15$ degrees. Then the form error must be interpolated to $[21.15,\ 22.15, \cdots,\ 379.15,\ 380.15]$ degrees from the data existing at $[21.0,\ 22.0, \cdots,\ 380,\ 381]$ degrees.

5.3.6 Form error – spindle motion separation

Of course the point of the previous sections has been to provide the cleanest data possible to the FESM algorithm. It is this separation that will now be investigated. Using the data discussed in the previous section we can perform the multi-probe error separation techniques discussed in section 4.2.3. Recall that we require a minimum of three probes to separate the radial form error from the spindle motion and a minimum of four probes to separate the plateau wobble and z motions from the face form error. In both cases, five measurements have been made permitting redundancy in the determinations.

There are 10 combinations of three probes, 5 combinations of four probes and one combination of five probes. This gives 16 radial determinations and 6 face determinations of the form error and spindle motion. The final results with these combinations are given in Figure 5.19. The overall standard deviations of the separations are given in Table 5.2. In fact although the different combinations (i.e. combinations of three probes and combinations of four probes) were studied separately, the results between them are homogeneous. Therefore

[29] The Matlab interp1.m routine or the equivalent Labview NI_Gmath.lvlib:Interpolate 1D.vi is used for this operation.

they are treated all together. The standard deviations of Table 5.2 indicate that these separations have an overall uncertainty in the order of 0.1 µm.

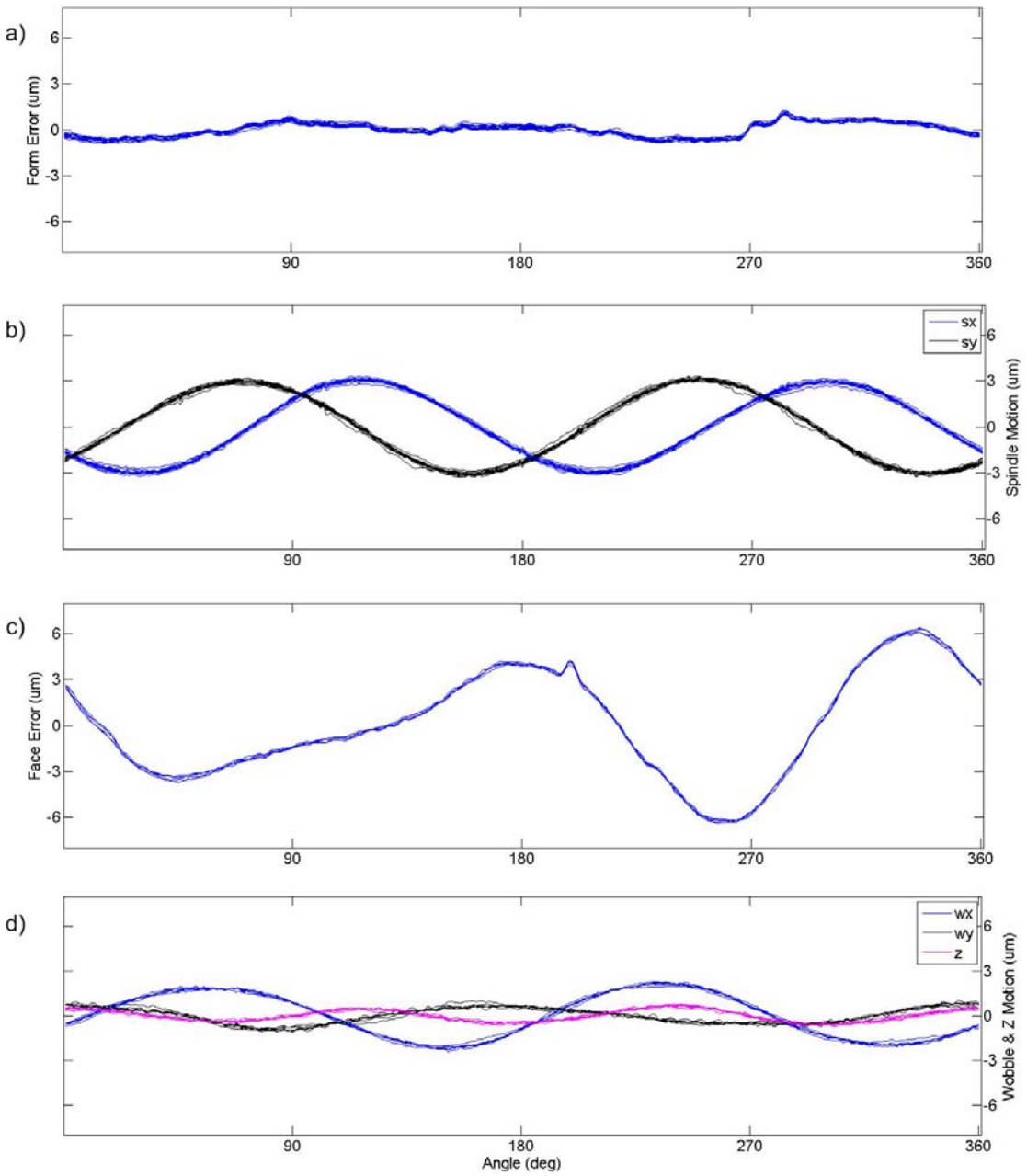

Figure 5.19 Final results of the radial FESM (graphs a and b) and face error wobble and z motion error separations (graphs c and d).

Table 5.2 Standard deviations of the elements of the radial form error – spindle motion separation and the face error motion separation. All standard deviation values are given in µm.

	Radial error separation			*Face error separation*			
	$fe(\theta)$	$sx(\theta)$	$sy(\theta)$	$fe(\theta)$	$wx(\theta)$	$wy(\theta)$	$sz(\theta)$
Standard deviation	0.094	0.098	0.102	0.092	0.086	0.090	0.066

5.4 HCC small angle evaluation

5.4.1 Background and experimental setup

By necessity, the numerical evaluation of the LEC is divided into two categories; the small angle and the full circle evaluation. The small angle refers to displacements not greater than ±300 arc-seconds. For angle displacements greater than approximately one degree, the other plateau motions (i.e. tilts about the x and y axes and the translation movements along the x, y and z axes) begin to influence measurements made by the instruments evaluating the LEC. To avoid these influences altogether we examine very small angle displacements. For an idea of the magnitude of HCC spindle motions, the standard deviation and peak to peak values of the motions shown in Figure 5.19 are less than 0.08 μm/degree and 0.2 μm/degree respectively in all cases[30].

A second reason to make small angle evaluations is that capacitive probes can be used. Given the experimental set up shown in Figure 5.20, and the uncertainty in capacitive probe readings (0.16 μm for a period up to 24 hours – refer to section 6.4.2 and Table 6.6 specifically), we can expect to potentially resolve down to 0.16 μrad or 0.031 arc seconds of angle motion. This is considerably better than any other instrument presently available at the ESRF.

To this end an experiment was made on the LEC, using a Möller-Wedel ELCOMAT 3000 autocollimator measuring to a 12 sided polygon mirror, and four capacitive probes measuring to a 1 m long bar installed on the HCC plateau. A number of temperature sensors were also employed. The experimental setup is shown in Figure 5.20

[30] Referring ahead to the discussion of the HCC collimation error CE_{HCC} at the end of this chapter, these spindle motions translate to peak to peak motions of less than ±0.1 arc seconds per degree intervals in all cases. Thus the maximum error expected in the 'small angle' evaluation over the range of HCC displacements of ±300 arc seconds due to HCC collimation error influences is considerably less than 0.1 arc seconds. Assuming quasi- linearity over one degree, this error will be in the order of $0.1 \times (300/3600) \cong 0.008$ arc seconds.

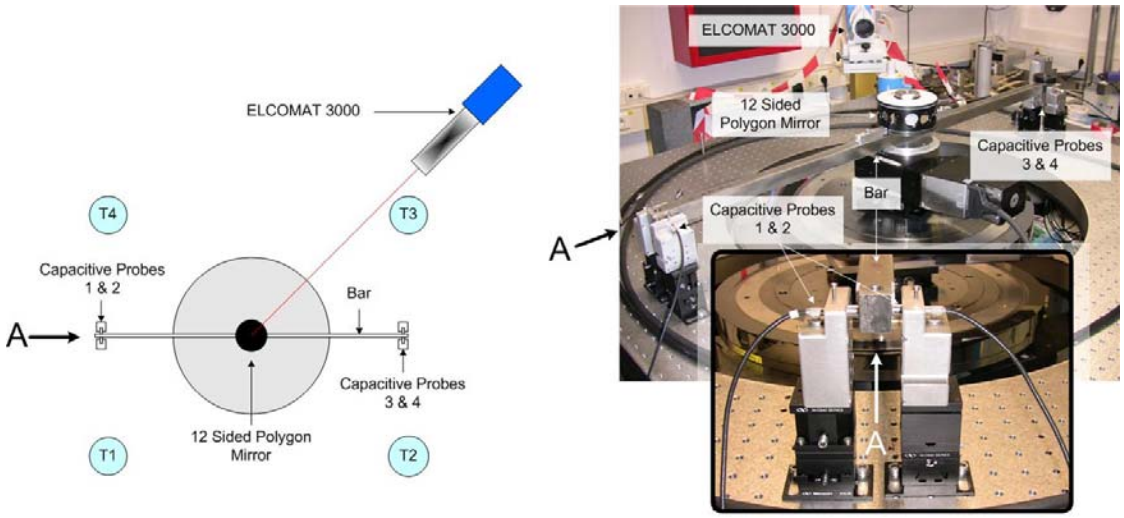

Figure 5.20 The small angle experimental setup. On the left hand side is a schematic while on the right hand side are two photos. The cut A is along the bar at the position of capacitive probes number 1 and 2. The bar was moved in small displacements of up to ±150 arc seconds or ±365µm at the capacitive probe positions (i.e. ~0.5 m from the centre). Angle displacements were also measured by the ELCOMAT 3000 to a 12 side polygon mirror. Positions of the temperature sensors are denoted by T1 ⋯ T4 in the drawing to the left. A fifth temperature sensor which is not shown was installed in the LEC encasement.

5.4.2 Experimental results

The experiment consisted of randomly moving the plateau in steps so that it was never more than ±150 arc seconds from its original position. The position of the plateau is shown in graph c) of Figure 5.21. The actual movements that were made are simply the differences between adjacent values in this graph. The top left hand graph shows the raw temperature over the study period. The readings from the four thermocouples shown in Figure 5.21 are clustered around 21 ºC while readings from a fifth thermocouple installed on the shaft linking the two RON 905 encoders (d in Figure 3.5) are clustered around 26.5 ºC. Filtered temperature differences (i.e. Matlab filter command[31]) with respect to the first reading in the test series are shown in graph b).

It is clear from this graph that there is considerable temperature variation at the LEC. One could speculate that this variation is due to its continuous rotation. However, there may be another, more banal reason for these temperature variations. The manner in which the cable connected to the RON 905 encoder is installed in the RV350 plateau causes it to 'rub'

[31] Temperature values in Figure 5.21 are the derived using a running average filter whose window size is 15 minutes. The running average filter uses the Matlab filter command $\text{filter}(\text{ones}(1, \text{ws}) / \text{ws}, \text{data})$ where ws is the sample length of 15 minutes of temperature data

unpredictably against the continually rotating shaft of the LEC (see c in Figure 3.5). At the time these tests were made, this was not known. As we shall see, this can be accounted and indeed corrected for. However this is not the most elegant solution and the manner in which this cable is managed is the subject of a foreseen amelioration to the system.

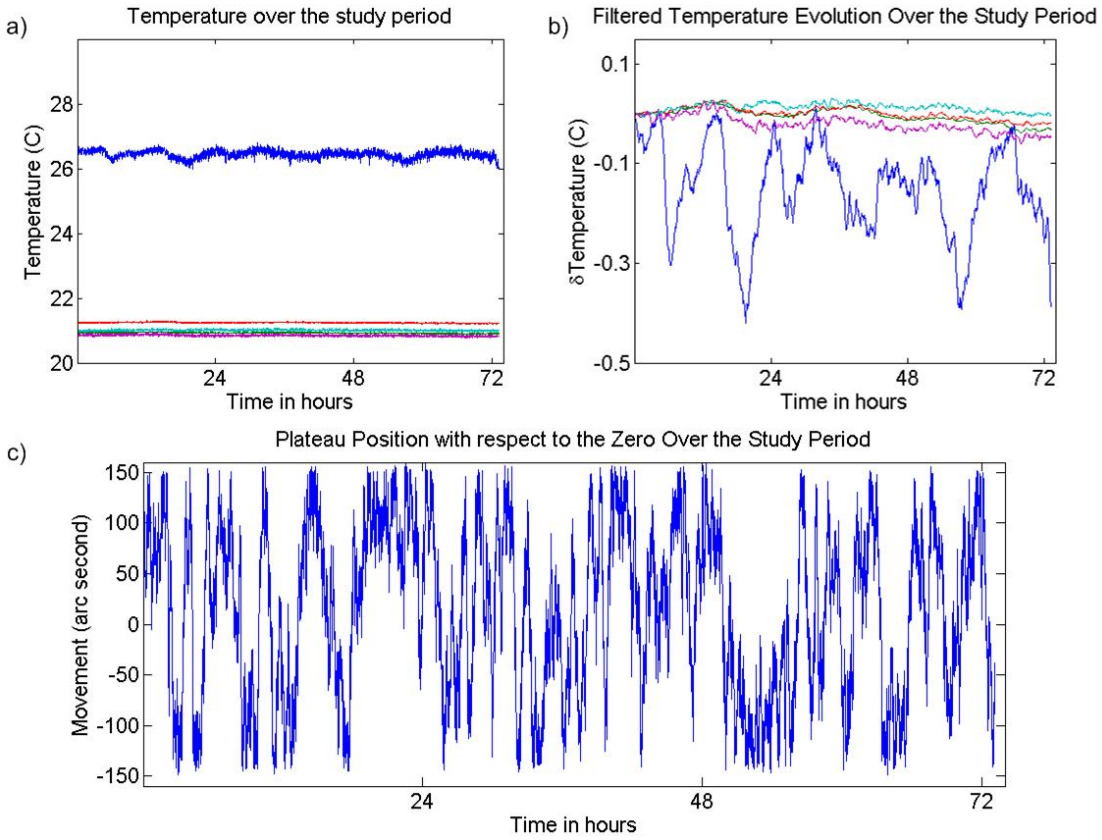

Figure 5.21 Experimental conditions for the small angle tests. Graph a) shows the raw temperature. Graph b) shows the filtered temperature evolution. The blue line (i.e. largest displacements) is the temperature on the continuously rotating shaft of the LEC. Graph c) shows the plateau position over the experiment.

At first glance one is temped to correlate the LEC temperature variation graph b) with plateau position in graph c). Indeed this was done, as well as a correlation between the first differences (i.e. $T_{i+1} - T_i$ and $P_{i+1} - P_i$ where T and P represent the filtered temperature evolution and the position respectively and $P_{i+1} - P_i$ is the plateau movement), and a cross correlation between the temperature and position and their first differences. In all cases, there is no correlation whatsoever. Thus, although there is significant temperature variation, it is not correlated with either the magnitude or the direction of the plateau movement.

Figure 5.22 shows the results of measurements made using 10964 small angle displacements over a period of just over 72 hours. The top graph a) shows the differences between angles measured by the ELCOMAT 3000 and the LEC (blue line) and the capacitive probes and the LEC (green line). These differences are moderately correlated (graphs b of this figure; $R = 0.4$ to 0.5) with the changes in temperature of the continually rotating LEC shaft temperature (blue line in graph b of Figure 5.21). Applying these temperature models give the results of graph c) of this figure.

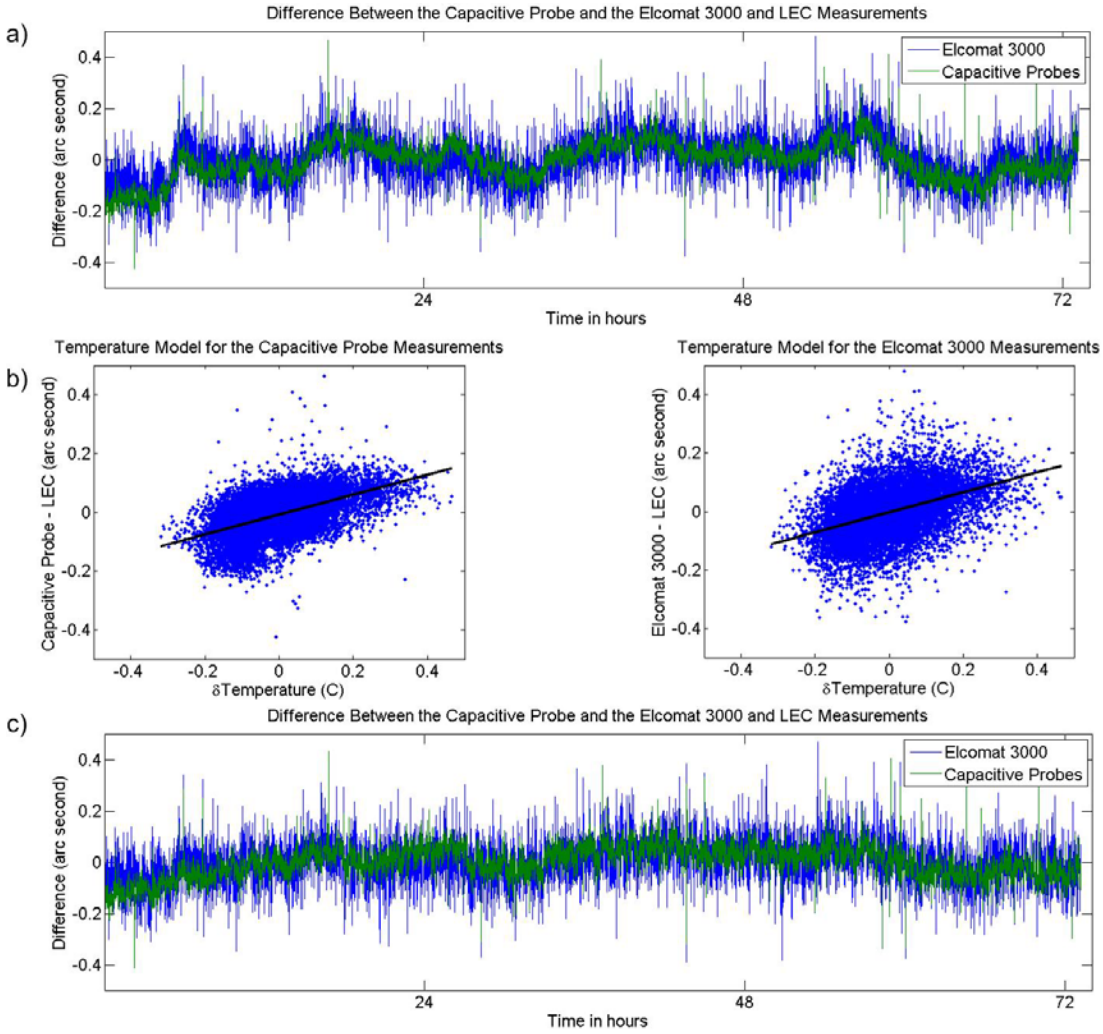

Figure 5.22 Experimental results of the small angle tests. The top graph a) shows the differences between measured angles for the ELCOMAT 3000 and the LEC (blue) and the capacitive probes and the LEC (green). The middle graphs show the temperature models for the capacitive probes and the ELCOMAT 3000 versus the LEC shaft temperature (graph b) of Figure 5.21. The bottom graph shows the temperature modelled differences between angles for the ELCOMAT 3000 and the LEC (blue) and the capacitive probes and the LEC (green).

The overall standard deviations for the full period of the test for graphs a) and c) of Figure 5.22 are summarized in Table 5.3. We remark a number of things. First, the capacitive probes

are in better agreement with the LEC than the ELCOMAT 3000. This is not surprising. After all, the manufacturer's stated uncertainty for the ELCOMAT 3000 is 0.2 arc seconds. Secondly, there is a modest improvement in the standard deviations of approximately 0.01 arc seconds using the temperature correction for both the capacitive probes and the ELCOMAT 3000.

Table 5.3 Overall standard deviations of the uncorrected and temperature corrected differences between; the capacitive probes measuring to the 1 m long bar, and the ELCOMAT 3000; and the angles determined by the LEC.

	Capacitive probes		*ELCOMAT 3000*	
	Uncorrected	*Temperature corrected*	*Uncorrected*	*Temperature corrected*
Difference standard deviation (arc sec)	0.074	0.063	0.090	0.081

The results of Table 5.3 apply to the full data set lasting approximately 72 hours. However, we are interested the LEC behaviour over shorter time periods. The majority of calibrations using the HCC are conducted in a period of 4 hours or less. For example the average time of a measurement for a calibration of every degree of an instrument (i.e. $0\cdots360$ degrees in steps of 1 degree) is 20 seconds. Therefore the total time is in the order of two hours. In four hours one can calibrate intervals of 30 arc minutes. This and the uncertainty of the LEC are thoroughly investigated in section 6.5.

5.4.3 Applicability to the full system

Small angle tests described above have been made at several angles and found to be independent of HCC plateau rotation position. In other words, the small angle uncertainties are independent of the plateau position. However, one may legitimately question the applicability of results of tests made over relatively small angles to the full circle or 360 degrees.

There is no instrument available in the author's toolbox that has an uncertainty inferior to 0.2 arc seconds and that can be used to measure continuously over 360 degrees and make a direct comparison with the LEC angle determination. However, it is the opinion of the author

that these results are applicable to any plateau angle movement regardless of its magnitude. The reasoning behind this affirmation is in the manner in which the LEC determines the magnitude of a rotation angle. The way this is done (refer to section 3.4.3) is in principle fully independent of the angular movement made. However we will have very strong evidence to the veracity of this assertion in the next section. In the meantime we shall state the LEC has an uncertainty ($k = 1$) for any angle displacement over a period of up to 72 hours of better than 0.07 arc seconds. This will be slightly improved upon in section 6.5 where a temporal uncertainty model is developed using the data discussed in this section.

Finally we note that the LEC uncertainty may be considerably better than this. At present it is limited by the capacitive probe system that is being used to calibrate the LEC. If the precision of this system was improved, or another more precise system employed, the small angle LEC uncertainty would almost certainly be improved.

5.5 HCC full circle evaluation

5.5.1 General

Because the tilts about the x and y axes and the translation movements along the x, y and z axes movements of the plateau have an important influence on any instrumentation being used to evaluate the HCC (e.g. autocollimator, capacitive probe, laser tracker etc…); its evaluation is divided into two parts. In the previous section we evaluated the HCC over small angles which are in principle not influenced by the plateau parasitic movements. This section is dedicated to the assessment of the HCC over its full measurement range.

In the previous section we were able to make a direct comparison between the results issued from the LEC and the capacitive probe measurements to a one metre long bar. In this section we are obliged to approach the problem in a more oblique manner. First we will show what the problem is; the way in which it was originally discovered. We will discuss different methods conceived to go about measuring it. Then we will show how the HCC plateau motions and their influences on other methods of measure can be evaluated using the FESM techniques carefully developed earlier in this and the last chapters. Finally we will show how this method can be used indirectly to evaluate the full circle of the HCC.

One point must be emphasized. We would like to establish a method whereby any angle can be evaluated. This precludes one of the most widely used techniques for this type of evaluation; namely the autocollimator and polygon mirror. This is because this instrumentation can only measure to well defined discrete angles; notably 30 degrees angle displacements in the case of the polygon mirror used here. As we shall see, this method may not be fully appropriate for the HCC because, contrary to common understanding, it can be influenced by small parasitic motions other than those about the primary axis of rotation. Nevertheless, it is used to help establish a baseline model for the HCC error.

5.5.2 The HCC full circle evaluation – the apparent LEC error

The first attempt at the full circle evaluation employed the ELCOMAT 3000 and a 12 sided polygon mirror. This produced results shown in Figure 5.23. It was disconcerting to find that the LEC had an apparent error over the full circle of ±0.76 arc seconds. Assuming there was no error in the ELCOMAT 3000 and polygon mirror pair; it is generally accepted that eccentricity motions due to mounting errors of the polygon mirrors have virtually no effect on the auto-collimation results.

The question of how small these eccentricity errors should be is alluded to in a paper [108] concerning the EUROMET project 371 - Angle calibration on precision polygons. In this paper (page 416) the authors state that the centring of the polygon mirror on the rotation table for this comparison was about ±30 um. In another document [68] (page 323) states; “We normally mount artefacts with less than 0.2 mm run out, and consequently eccentricity errors are expected to be below 0.012".”

Spindle motion and eccentricity errors due to the mounting of the main plateau on the Micro-Controle/Newport RV350 rotation table are approximately ±3 um and ±9 um respectively. Therefore the overall polygon centring errors are expected to be considerably less than the ±30um cited in the first article and certainly much smaller that those cited in the second. Consequently when the harmonic three signal was observed (Figure 5.23) by the ELCOMAT 3000 to the polygon mirror, the suspicion was that the error was associated with the LEC. This suspicion was further fuelled by the fact that this same harmonic three signal

was observed in the first calibration results issued from HCC for the Leica TDA5005 RTS. It was considered as being implausible that this instrument had such large angle errors; particularly in light of the confirmatory evidence of the autocollimator results of Figure 5.23 and particularly the experience using this instrument at the ESRF.

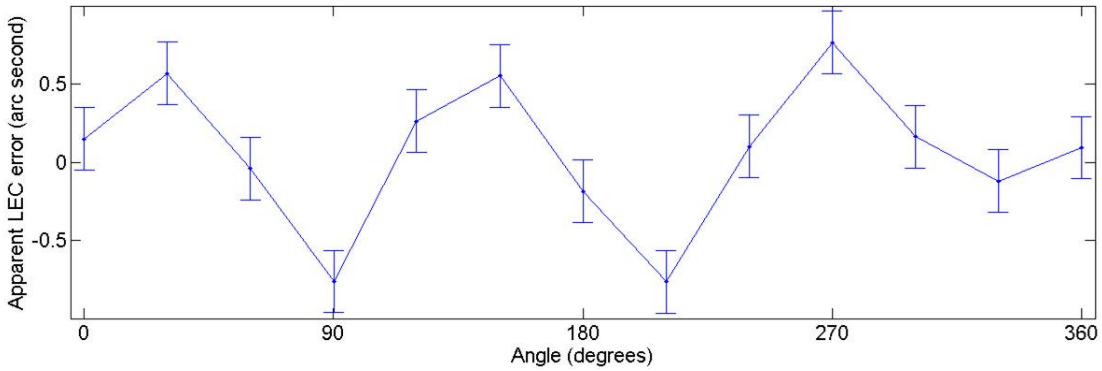

Figure 5.23 Apparent error of the LEC as observed by the ELCOMAT 3000. The error bars give the manufacturer's uncertainty of 0.2 arc seconds.

These results led to the investment of considerable effort in the quest to find a means by which the LEC could be calibrated with an appropriate uncertainty. Several techniques were investigated. The primary imperatives of this investigation were to find a method whereby any angle on the circle could be investigated with the best precision possible; preferably below 0.1 arc second.

Although the autocollimator is a useful and almost universally accepted tool for this type of work, its main draw back is that it is constrained to measure predefined discrete angles. Nevertheless, this did not prevent a moderately successful attempt using it to evaluate a larger number of discrete angles. A complex technique employing three interferometers mounted on rotation stages following three reflectors mounted on a rotation stage itself mounted eccentrically on the plateau was also tested. The idea here was to maintain the interferometer reflectors constantly pointing in the same direction in a configuration specifically designed to prevent losing the interferometer beam. An experiment employing two laser trackers measuring to reflectors mounted on the bar used in the evaluation of the LEC outlined in section 5.4 were used with (partial) success to reproduce a detailed map of the apparent LEC error shown in Figure 5.23. Finally the RTS calibration provides excellent confirmatory

evidence of the existence of this error. These techniques will be discussed briefly over the next four sections.

5.5.3 ELCOMAT 3000 HCC full circle evaluation – five degree intervals

The aim of this experiment was to evaluate the HCC at finer angle intervals than the standard 30 degree interval allowed with the 12 side polygon mirror. A similar technique is employed at SLAC [40] (see also section 2.4.1).

The technique involves measuring each of the polygon mirrors in turn after rotating the HCC through the nominal angle (i.e. a multiple of 30 degrees). The measured LEC angle is then subtracted from each of the angles issued from these 13 (i.e. 12+1 with the closure on mirror number 1 at 360 degrees) autocollimator – polygon mirror measurements. Typically one set of forward and one set of reverse measurements are made so the HCC plateau is returned to its nominal zero position.

The plateau is then rotated through five degrees and the polygon mirror rotated back through five degrees so that it is once again pointing at the autocollimator. The procedure is then repeated. The 13th closure measurement is not always possible because the HCC is limited to 370 degrees of angle movement. Naturally this gives a series of curves similar to those of Figure 5.23. For this test 15 series of measurements were made over a two day period at 2.5 degree intervals.

The premise that is taken is that the apparent LEC error function is smooth and continuous. Consequently, all of these separate data sets should lie on the same functional curve. It is assumed also this curve can be represented by a Fourier series. The procedure used to align the fifteen series of points is to first calculate their median values (med_i). The median of the 15 median values is then calculated (Med). The differences between each of the data series median values and the median of median values (i.e. $dm_i = med_i - Med$) is calculated and all of the series are translated onto one other by subtracting dm_i . Finally a 6th order Fourier series is passed through the transformed discrete points. Figure 5.24 graph a) shows the raw data for

the 15 data series. Graph b) shows the transformed data and the 6^{th} order Fourier series model. The standard deviation of the model residuals is 0.11 arc seconds.

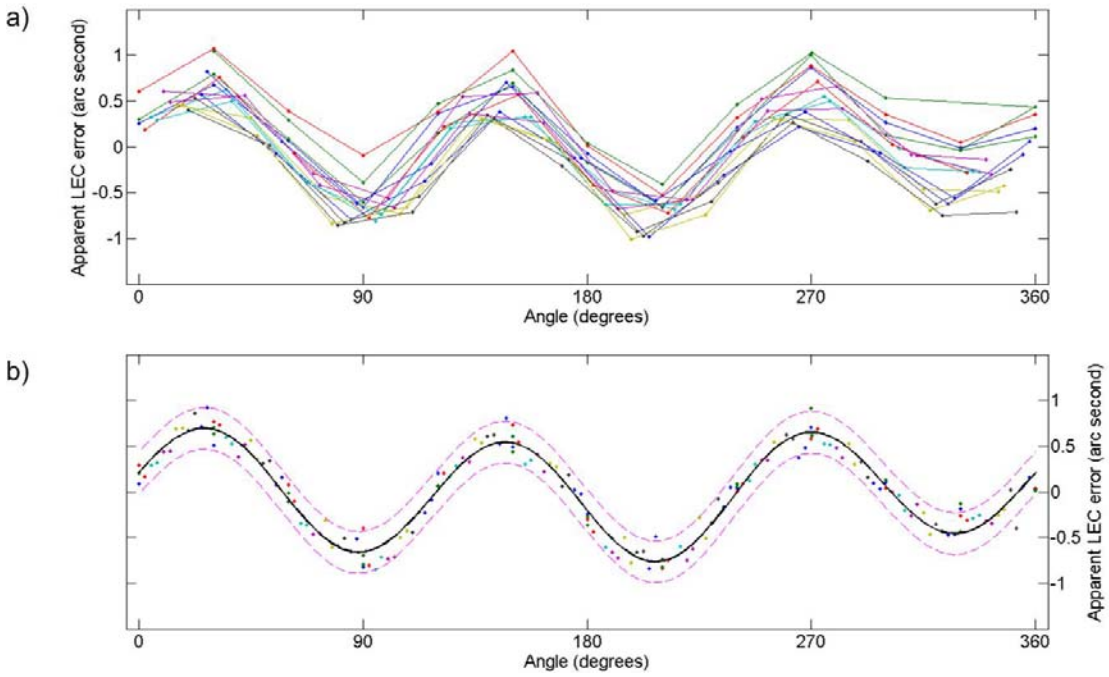

Figure 5.24 ELCOMAT 3000 observations and construction of the apparent LEC error using a 6^{th} degree Fourier series. Dashed magenta lines show the 95% prediction intervals for the Fourier curve. The model standard deviation is 0.11 arc-seconds.

5.5.4 Trilateration HCC full circle evaluation experiment

The main idea behind the angle verification by trilateration is to rotate the HCC plateau, constantly measuring distances ($d_{(1\cdots3)\,i}$ in Figure 5.25) to a reflector installation from three exterior servo-interferometer stations. When the HCC is rotated to a given angle (β_i in Figure 5.25), the coordinates, or rather the differences in coordinates from the start position, can be determined by trilateration. Because the reflectors are offset by 200 mm from the HCC plateau centre of rotation, rotation angles can be determined from these reflector coordinates and compared to the measured LEC angles.

This requires that: first the servo-interferometers continuously follow one prism and secondly that the reflectors always point more or less toward their respective interferometer. Clearly these conditions impose servo-controlling the interferometers and the reflectors so that they remain pointed at each other. Figure 5.25 shows the general setup for this experiment.

The first requirement that the servo-interferometers follow one prism all at all times was satisfied by mounting the interferometer on a Newport –MicroControle URS75PP rotation

table. These interferometer stations are marked by $IS_{1\cdots3}$ in Figure 5.25. Originally it was intended to use a single laser source to feed all three interferometers. However, due to the constraint requiring an optical path that maintains the polarisation of the laser light, it was very difficult to do this and in the end, each interferometer was supplied by a separate laser source. The second condition requiring the reflector to never lose the beam can be met if the reflector has a large enough opening (reflection) angle ($\alpha_{(1\cdots3)\,i}$). It was determined for the test configuration the maximum allowable opening angles were ±13.6°. Extensive tests revealed that this opening angle could be accommodated by both the AGILENT 10767A reflector and the Leica ½ inch CCR (corner cube reflector) – instrumentation available at the ESRF.

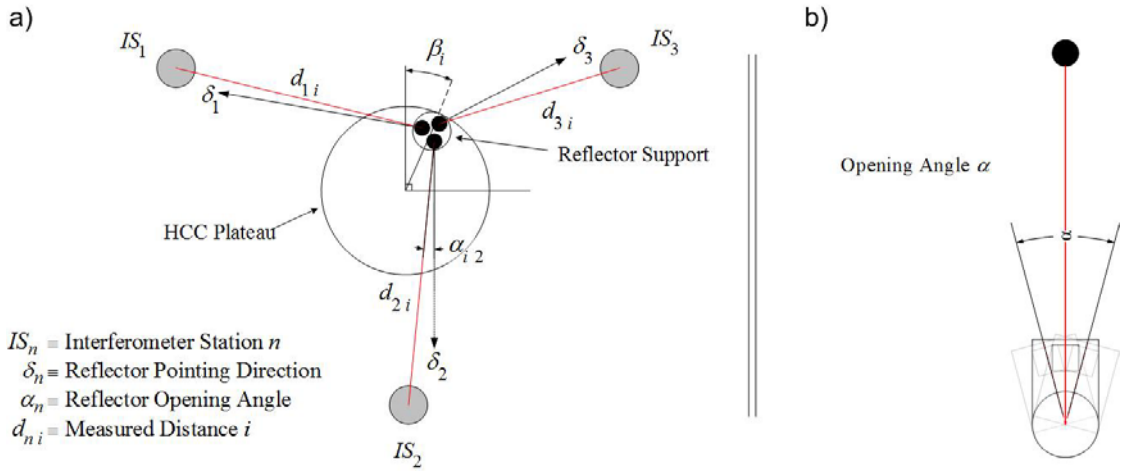

Figure 5.25 The trilateration test setup is show in drawing a). Three interferometer stations were setup at approximately 800 mm from the centre of the HCC plateau separated by roughly 120 degrees. Three reflectors were installed on a support which rotated about the HCC centre of rotation. The reflector normal directions δ_n do not change with the HCC rotation angle β_i, however, the reflector opening angles $\alpha_{i\,n}$ vary as a function of the HCC plateau position (drawing b). These opening angles varied by approximately ±13.6 degrees.

Although several experiments were conducted successfully (see for example Figure 5.26), results were disappointing. For this technique to work with an uncertainty in the determination of the angle β_i of $U(\beta) = 0.1$ arc seconds, the uncertainty in the coordinate error ellipses in the direction perpendicular to the direction of the angle β_i must be in the order of 0.1 µm. This tolerance is determined by the simple geometry (i.e. $D \times U(\beta) = 0.2\text{m} \times 0.5\mu\text{rad}$) where D is the distance from the HCC centre of rotation to centre of the three reflectors.

Unfortunately, this level of precision was simply too ambitious. Concurrently, the ESRF Alignment group acquired a high precision Leica LTD laser tracker which permitted another more successful test discussed in the next section. Nevertheless, it is not ruled out that this type of test will be tried again in the future using different instrumentation; for example laser trackers and high precision RTSs.

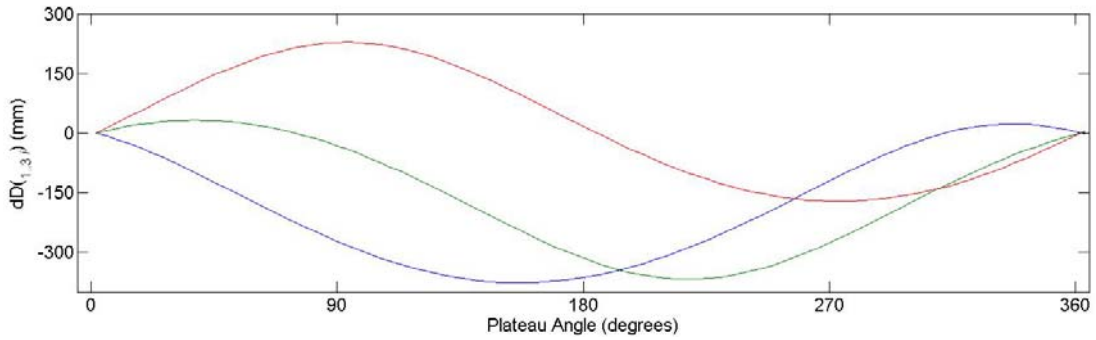

Figure 5.26 Distances measured from the three trilateration stations to their respective reflectors mounted on the HCC as the plateau is rotated through 360 degrees.

5.5.5 Laser tracker HCC full circle evaluation experiment

An experiment was made using two laser trackers measuring to two spherically mounted retro reflectors (SMRs) installed on the ends of a one metre long bar. The bar was itself mounted on a Micro-Controle Newport RV120PP rotation table, installed on the HCC. The setup for this experiment is shown in Figure 5.27. The idea behind this experiment was to use the relatively long lever arm between the centre of the HCC and the SMR, and the optimal alignment of the laser tracker (LT) interferometer along the rotation of the HCC. This permits the comparison of the angle displacements calculated using the interferometric distances and those measured by the LEC. Numerous tests made while preparing the trilateration experiments discussed in the previous section, determined that there was negligible error overhead on the measured distance when rotating the SMR. This is particularly true given the maximum SMR opening angle α in this configuration for $\beta = \pm 15$ degrees (refer to Figure 5.27) of less than 1 degree.

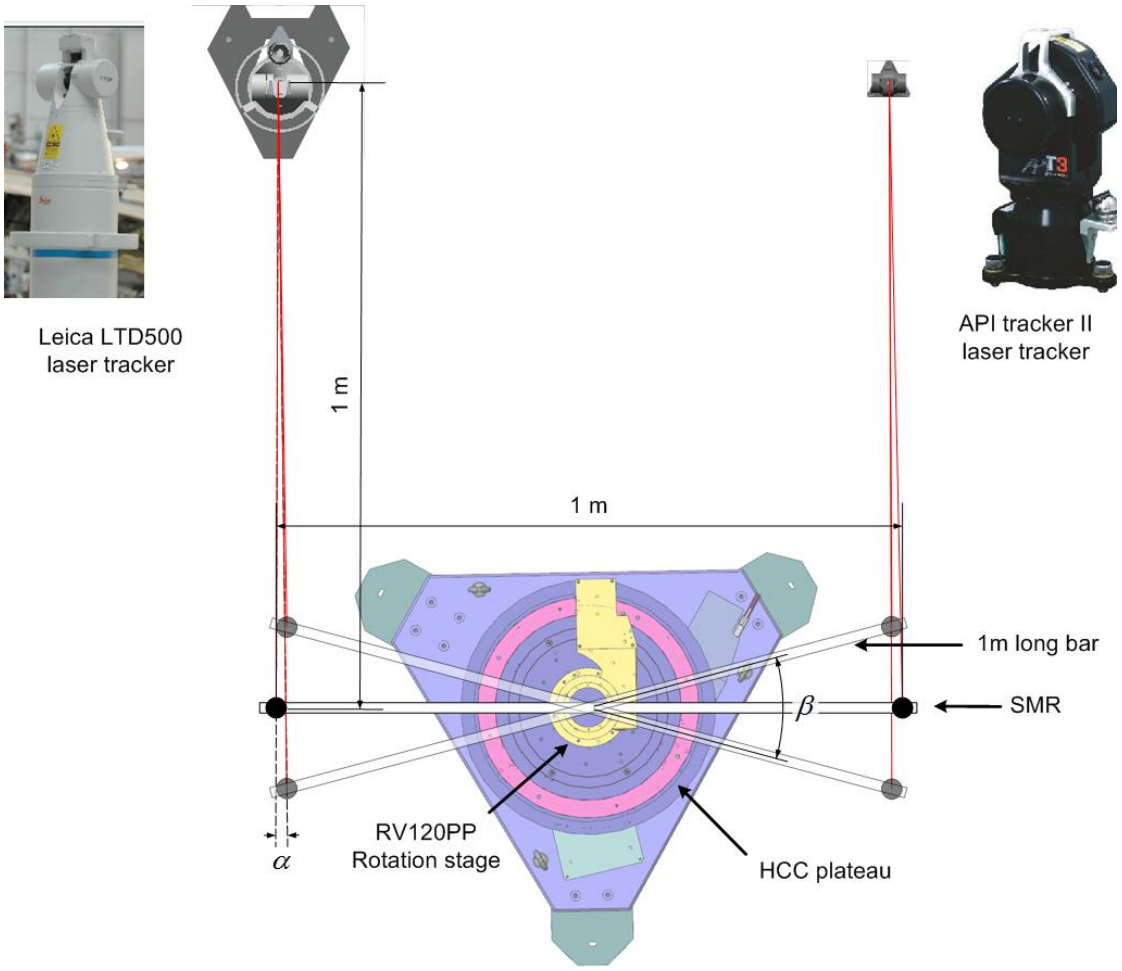

Figure 5.27 Laser tracker HCC verification setup.

First the SMR was positioned at a maximum position $\beta = 15$ and $\alpha \simeq 0.5$ degrees using the Micro-Controle Newport RV120PP. The HCC plateau was then moved in steps of 1 degree to the opposite maximum $\beta = -15$ and $\alpha \simeq -0.5$ degrees. The bar assembly and SMRs were then rotated back to their original maximum position $\beta = 15$ and $\alpha \simeq 0.5$ degrees using RV120PP rotation stage and the HCC rotation repeated. This back and forth motion was made 12 times (i.e. 12×30 degrees) to examine the full HCC circle.

The results of this test are shown in Figure 5.28. Their calculation is quite involved. First because the centres of rotation of the HCC and the RV120PP are not coincident, it requires the calculation of the offset of the RV120PP centre to the HCC centre of rotation for each 30 degree segment to reduce the angle data into the same system as the LEC. In parallel to the laser tracker measurements, the ELCOMAT 3000 measured precisely the ~30 degree angle moved for each segment. The distance to this centre (i.e. the radius of the centre of circle over which the segment was measured) was calculated with the precise ELCOMAT 3000 angle in

conjunction with the measured interferometric 30 degree segment distance (i.e. β) traversed by the HCC plateau.

Then because each 30 degree segment is in principle independent, they must all be smoothly stitched together. Each segment is appended to the one preceding it to form a coherent (non-closed) error curve. It does this by passing a best fit cubic polynomial through the segment data set. The difference between the modelled last point of the preceding series and the modelled first point of the following series is calculated and applied to smooth the jumps between consecutive series. These translations are then applied to the data in each consecutive series.

In this form, the full 360 degree data set is not closed upon itself. The closure is accomplished by passing a straight line between the first (i.e. HCC plateau position 0 degrees) and last point (i.e. HCC plateau position 360 degrees) and redressing the data set in a linear manner. This is identical to the procedure employed with the probe data in section 5.3.3. Finally because the RV120PP centre is offset from the HCC centre of rotation, there remain first and second harmonic elements in the data set which are removed to produce the graph of Figure 5.28.

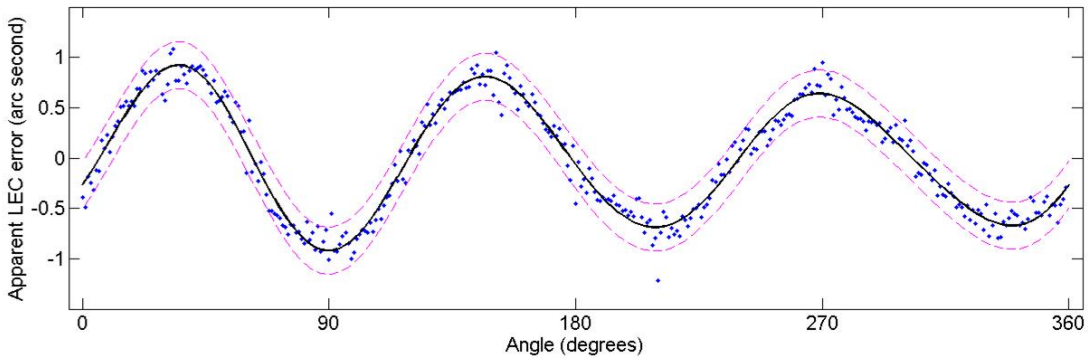

Figure 5.28 Leica LTD500 laser tracker LEC verification results using the experimental setup shown in Figure 5.27. The residual standard deviation with respect to the modelled curve is 0.12 arc seconds.

Originally it was intended to use the results of the API laser tracker in combination with those measured by the Leica LTD500. This would double the lever arm used in the angle calculation to one metre. Unfortunately, this instrument did not produce results quite as clean as those shown in Figure 5.28 and this combined effort was abandoned. Nevertheless, it is the

author's intention to eventually repeat these experiments with two LTD500 type laser trackers. The standard deviation of the residuals of the angle determinations using this technique with respect to the 6th degree modelled Fourier series curve is 0.12 arc seconds.

5.5.6 Robotic total station calibration

The characteristic harmonic three curve was observed in the data issued from the calibration of a RTS. In fact chronologically, this was first time this curve was actually observed. At the time it was considered extremely unlikely that this error was intrinsic to the RTS, and so it was taken to be a bias error of the LEC system. This was the impetus leading to the experiments discussed in the previous sections. These observations (Figure 5.29) are not as tightly grouped as those of the previous section or the ELCOMAT 3000. However, they do confirm the presence and approximate magnitude of this phenomenon.

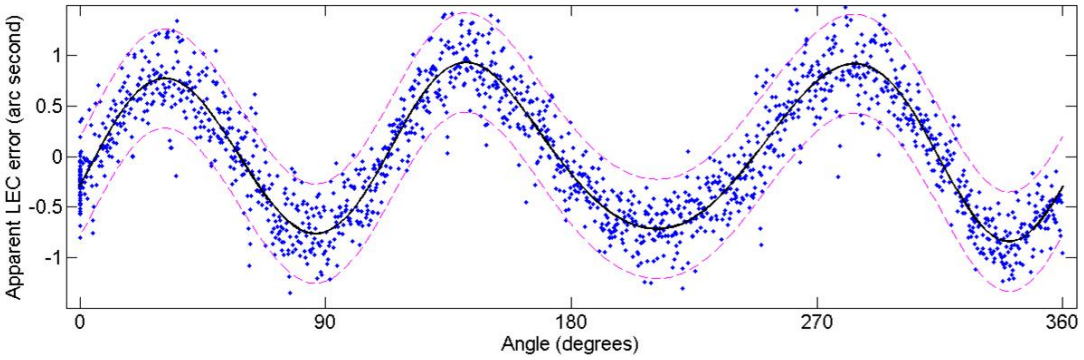

Figure 5.29 The apparent LEC harmonic 3 error seen in the calibration curve of a RTS (TDA5005).

The standard deviation of the residuals with respect to the 6th degree Fourier series model is 0.25 arc seconds. This is well within the manufacturers stated uncertainty of 0.5 arc seconds for this instrument (a Leica TDA5005). Note that this calibration curve certainly contains other harmonic errors that are intrinsic to the instrument. In fact, the error phenomenon is slightly more complex with the RTS. This will be discussed thoroughly in section 6.8.1. For this reason, the graph in Figure 5.29 is not immediately comparable to Figure 5.24 and Figure 5.28. Nevertheless it certainly provides confirmatory evidence to the existence of the harmonic three error.

5.5.7 HCC full circle evaluation experiments summary

We have spent considerable time here showing the so-called apparent LEC harmonic three error curve. We have confirmed quantitatively and qualitatively by three totally independent experimental setups the form and approximate magnitude of the error. Figure 5.30 shows a summary of the three different tests and the 95% confidence intervals for the experimentally determined model curves.

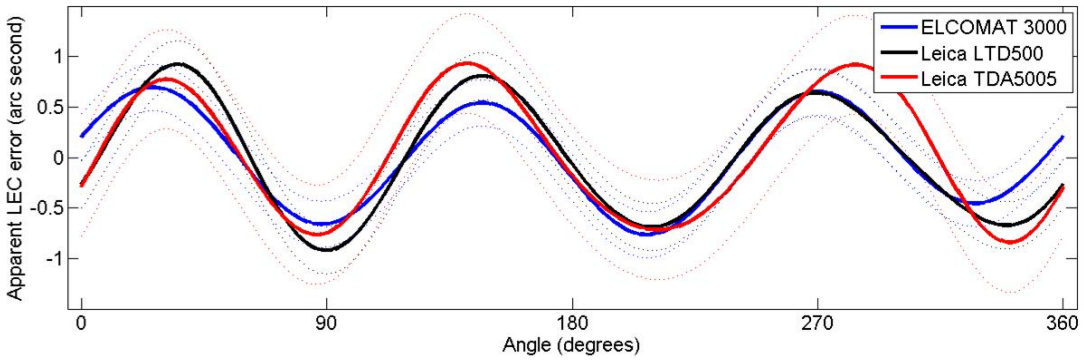

Figure 5.30 Summary of the 6th degree Fourier curves of the apparent LEC harmonic 3 error curve.

Although we have characterised this curve, we still do not know what exactly it is. At the start of this section it was assumed to be an intrinsic part of the LEC system. This conclusion was mainly based on the assumptions made concerning the autocollimator measurements to a polygon mirror on a rotation table. All three experimental results appear to confirm this hypothesis. However, the error is not in the LEC system. It is due to the parasitic motions of the HCC plateau as it is rotated through 360 degrees. We will now look at this phenomenon in detail.

5.5.8 Parasitic HCC motions and their influences

Recall that when we make a measurement with an autocollimator to a mirror, we are measuring relative movements of the normal vector of the mirror with respect to the line of sight of the autocollimator (see Figure 4.3). What was assumed in section 5.5.3 was that this normal vector is not influenced, or at least influenced to a negligible level, by plateau movements other than about the main rotation axis. This possibility appears not to have been considered in previous literature.

This is true under a relatively liberal set of conditions. Indeed, the centre of the polygon mirror may be offset from the centre of the plateau rotation without having an influence on the orientation of the mirror normal vector in the plane of rotation. In other words, if we consider a perfect polygon mirror and autocollimator (i.e. perfect mirrors whose normal vectors are separated by 30 degrees and an error free autocollimator), and the polygon mirror centre is offset by a value ε from the plateau centre of rotation; when the plateau is rotated by precisely 30 degrees, the autocollimator will not detect a change in the mirror normal angle. If however, the centre of rotation of the plateau is not stable, and changes as a function of the rotation angle, such as is the case of the HCC plateau with the $sx(\theta)$ and $sy(\theta)$ movements shown in graph b) of Figure 5.19; then the orientation of the mirror normal vector will change. It is these changes that give rise to the harmonic three curves shown in Figure 5.24 and Figure 5.27 through Figure 5.30.

We will show this by using the spindle motion errors determined in section 5.3 and applying them through the use of homogenous transformation matrices (HTM) discussed in section 4.3 to the polygon mirror normal vector and constructing an HCC error curve. More generally, this method can be applied to determine the collimation error[6][32] of an instrument or even a virtual instrument installed on the plateau. It may be employed to determine the so-called apparent LEC error discussed in the previous section. We will refer to this as the HCC collimation CE_{HCC} error henceforth.

[32] "The adjustment of the line of sight of a telescope, etc. Line of collimation: the line of sight or optical axis. Error of collimation: the amount by which the line of sight deviates from its position of accurate adjustment."

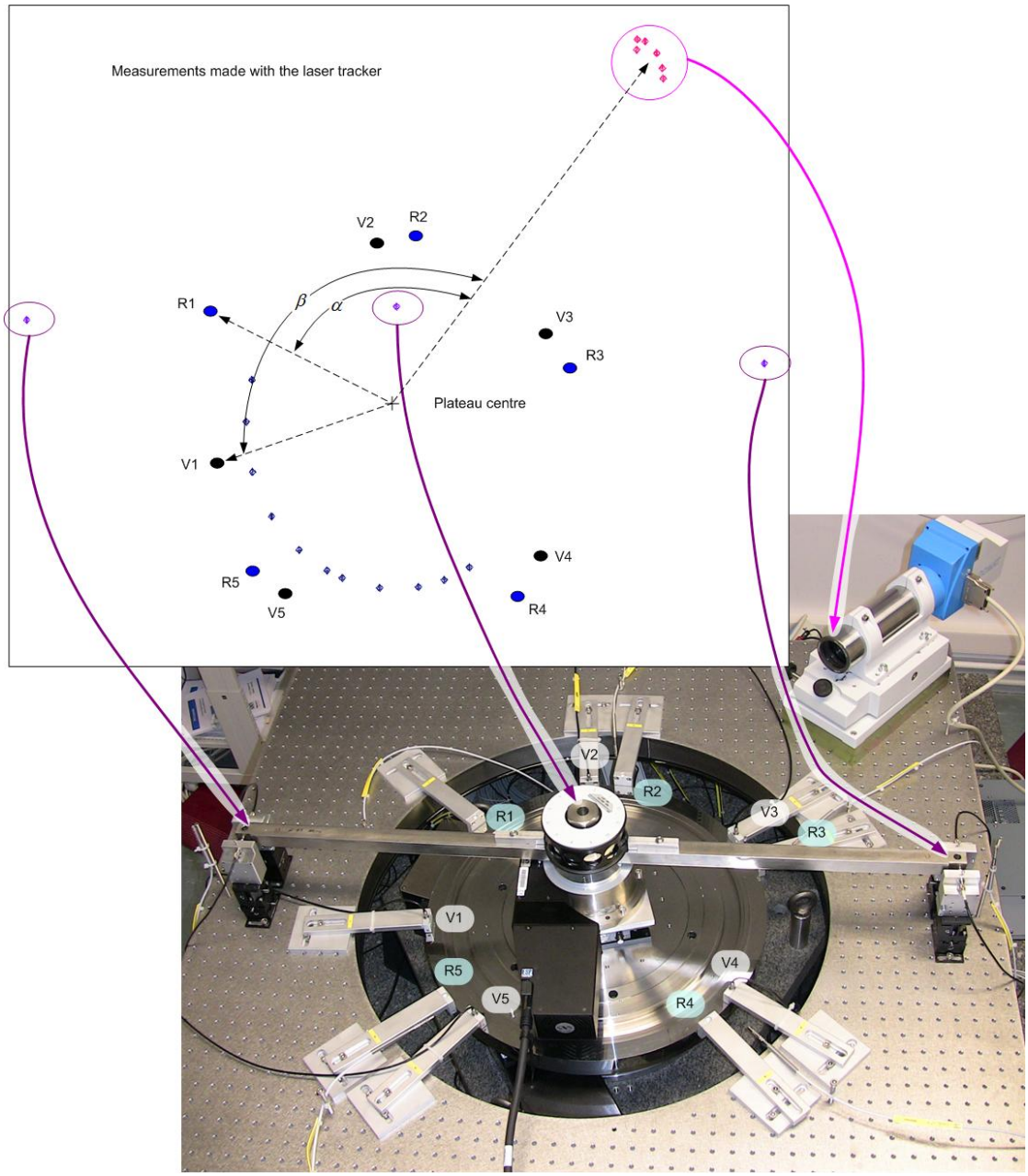

Figure 5.31 Measurements are made to determine the positions of the radial $(\mathrm{R1}\cdots\mathrm{R5})$ and vertical $(\mathrm{V1}\cdots\mathrm{V5})$ capacitive probes in relation to the autocollimator- polygon mirror to calculate the orientations of each of the systems with respect to one another.

However, before the HTM transformations can be applied and the HCC collimation error curve constructed the spindle motions must be transformed into the same coordinate system. Because of the experimental setup (refer to Figure 5.31), the radial spindle motions $sx(\theta)$, $sy(\theta)$, the vertical spindle motions $wx(\theta)$ and $wy(\theta)$, and the polygon mirror are in three independent systems with their x axes rotated in arbitrarily directions with respect to one another. This is illustrated in Figure 5.31. The vertical spindle motion $sz(\theta)$ being at the

origin (i.e. plateau centre) of the three systems does not require transformation. Values for the HCC plateau spindle motions; $sx(\theta)$, $sy(\theta)$, $sz(\theta)$, $wx(\theta)$ and $wy(\theta)$ are derived from the mean values of the curves given in graphs b) and d) of Figure 5.19.

The angles; α for the angle between the radial spindle motion x axes and the polygon mirror x axes; and β for the angle between the vertical spindle motion x axes and the polygon mirror x axes can be measured. This is done by measuring points in the different systems. The top part of Figure 5.31 is an extract of the measurement plan showing schematically points that are measured using a laser tracker. After a certain amount of 3D manipulation and construction of reference objects using these measured points[33], one can determine the orientations (i.e. α and β) of the axes of the three coordinate systems (i.e. radial $(\mathrm{R1}\cdots\mathrm{R5})$ and vertical $(\mathrm{V1}\cdots\mathrm{V5})$ capacitive probes and autocollimator - polygon mirror) with respect to one another. The spindle motions are then transformed (rotated) into a system common to the polygon mirror system.

This transformation (rotation) requires the application of equations derived from equations (4.10) and (4.20) with the form errors removed (i.e. separated) and appropriate values for the rotations for $sx(\theta)$, $sy(\theta)$ (i.e. α), and $wx(\theta)$ and $wy(\theta)$ (i.e. β) onto the polygon mirror system. The polygon mirror system x axis is taken to be the direction from the autocollimator to the polygon mirror. This system lies in the plane parallel to the HCC plateau surface. The rotated radial and vertical motions used in the determination of the collimation error, $sx_{new}(\theta)$, $sy_{new}(\theta)$, $wx_{new}(\theta)$ and $wy_{new}(\theta)$; are given by (5.5).

$$
\begin{aligned}
sx_{new}(\theta) &= sx(\theta)\cos(\alpha) + sy(\theta)\sin(\alpha) \\
sy_{new}(\theta) &= sx(\theta)\cos\left(\alpha + \pi/2\right) + sy(\theta)\sin\left(\alpha + \pi/2\right) \\
wx_{new}(\theta) &= z(\theta) + w_x(\theta)\cos(\beta) + w_y(\theta)\sin(\beta) \\
wy_{new}(\theta) &= z(\theta) + w_x(\theta)\cos\left(\beta + \pi/2\right) + w_y(\theta)\sin\left(\beta + \pi/2\right)
\end{aligned}
\tag{5.5}
$$

[33] The data acquisition and manipulation is performed with the graphical metrology software package Spatial Analyzer.

To construct the HCC collimation curves using the transformed spindle motions, first we establish three points that define the polygon mirror. These mirror points are in a Cartesian frame that can be oriented arbitrarily about the vertical z-axis. Note that although a polygon mirror is discussed here, this method is applied in the same way to determine the HCC collimation error regardless of the instrument used. The points are in a plane and given by $a=(r,0,z_m)$, $b=(r,ya,0)$ and $c=(r,0,za)$. The distance from the nominal HCC centre of rotation to the mirror face is given by $r=0.050$ m, and the height of the mirror centre $z_m=0.190$ m. The two points with arbitrary values $ya=1$ and $za=1+z_m$ are auxiliary points used to define the mirror plane. We define the mirror normal vector as $\vec{n}=\vec{b}\times\vec{c}$ [34] where $\times$ represents the vector cross product.

The procedure consists of transforming, using the HTM, the three points by appropriate values (i.e. $t_1=sx_{new}(\theta)$, $t_2=sy_{new}(\theta)$, $t_3=sz_{new}(\theta)$ in $T_x(t)$, $T_y(t)$, $T_z(t)$; and $\phi_1=\left[wx_{new}(\theta)-sz(\theta)\right]/D_p$, $\phi_2=\left[wy_{new}(\theta)-sz(\theta)\right]/D_p$, $\phi_3=\theta$ in $R_x(\phi_1)$, $R_y(\phi_2)$, $R_z(\phi)$) in equations (4.28) and (4.29)). D_p is the radial distance from the HCC plateau centre to the position of the face capacitive probes. It is nominally 0.24 m.

Performing the above HTM transformations to determine the polygon mirror normal and plotting the difference between it and the nominal mirror normal results in the solid line in the graph a) of Figure 5.32. The coloured points in this graph are the differences between the LEC and ELCOMAT 3000 readings shown in Figure 5.24. In a similar manner, one can calculate the HCC collimation error CE_{HCC} of the Leica LTD500 laser tracker versus LEC angles shown in Figure 5.28. In this case we are considering a type of virtual collimation error. The results for this comparison are shown in the bottom graph of Figure 5.32. The determination of the collimation error to apply with the RTS shown in Figure 5.29 is slightly more complex and will be treated in section 6.8.1.

[34] This provides an empirical approximation, not a true mathematical representation of the error function.

The standard deviation of the residuals between the ELCOMAT 3000 and polygon mirror collimations error and those determined by the capacitive probes is 0.13 arc seconds. This is remarkably close to the residual standard deviation 0.11 arc-seconds given by the Fourier series model in section 5.5.3. The standard deviation of residual errors for the LTD laser tracker comparison is 0.23 arc seconds.

It is clear from these results that the difference between the angles measured by the LEC and the ELCOMAT and polygon mirror, and the LTD laser tracker measurements to a SMR mounted on a bar on the HCC plateau can be explained by the parasitic spindle motions of the HCC. Given the intrinsic uncertainty of the instruments used and the methods employed, the results of Figure 5.32 are remarkably consistent.

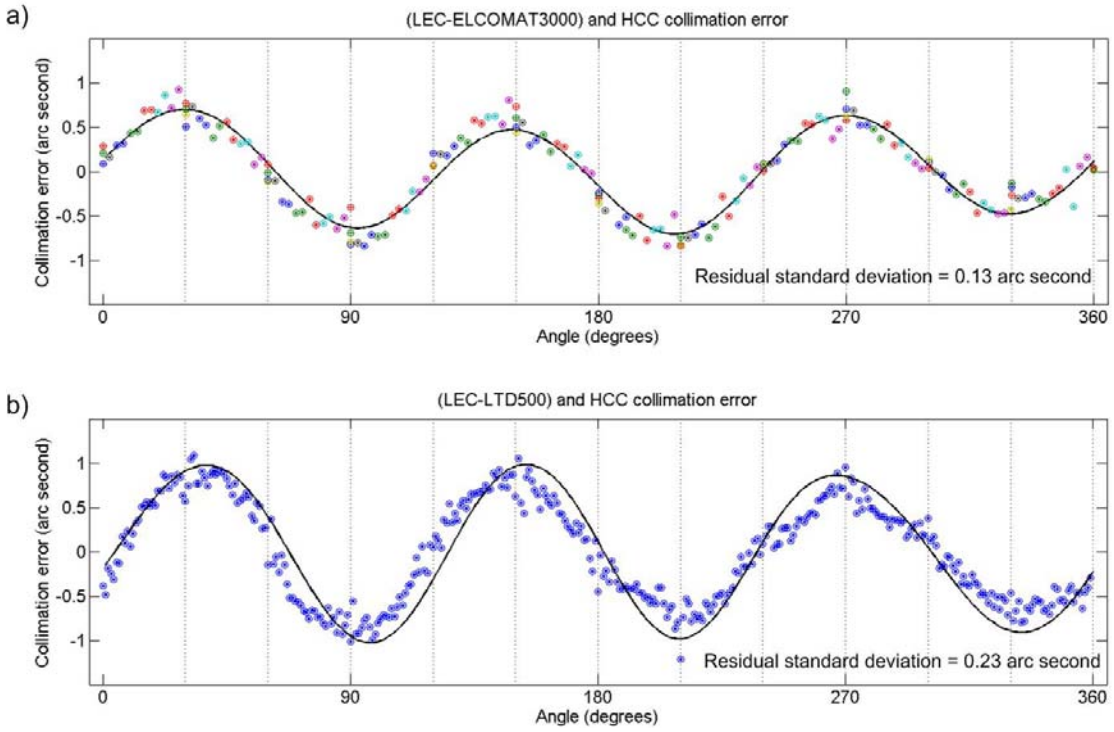

Figure 5.32 Graph a) shows the comparison between HCC collimation error determined by the ELCOMAT 3000 polygon mirror the same determined by the capacitive probe method Graph b) shows the comparison LTD laser tracker and capacitive probe methods for thee determination of the collimation error.

Recall that the manufacturers stated uncertainty for the ELCOMAT 3000 is ± 0.1 arc-second over any 20 arc-second range and ± 0.25 arc-second over the total instrument range. Furthermore the polygon mirror uncertainty given in its calibration certificate is 0.3 arc seconds. The nominal LTD laser tracker uncertainty for a coordinate given by the

manufacturer is ± 10 ppm (μm/m). This translates to a HCC angle resolution of $(10\mu m/m \times 1m)/0.5m \cong 4$arc seconds . Every effort has been made to circumvent this instrument limitation; apparently with a considerable degree of success, by optimising the use of its interferometer.

The manner in which the different sections of the Laser tracker curve are 'stitched' together is evident in the bottom graph of Figure 5.32. The 30 degree segments are highlighted by the dotted vertical lines. A small change in the slope of a segment can change the overall appearance of the curve. Constraints also apply to the manner in which the ELCOMAT 3000 curve was constructed.

These results have been discussed to show the viability of the application of the capacitive probes to the determination of the HCC collimation error. There is no instrument in the author's toolbox capable of measuring angle displacements to the required level of precision. As we shall see in the next chapter, the expanded uncertainty in the collimation error determination using the capacitive probes is considerably better than 0.1 arc second.

The main reason the experiments outlined in sections 5.5.3 and 5.5.5 to 5.5.7 have been made is to demonstrate that the so-called HCC collimation error CE_{HCC} exists. None of these instruments or setups is able to provide an uncertainty in this error of better than 0.1 arc-seconds. Nevertheless, the uncertainties achieved are actually quite remarkable given the ways in which they were achieved. What has been accomplished is the unambiguous identification of the error source and a method and instrumentation; namely the FESM technique, homogeneous transformation matrices and capacitive probes; that can be potentially be used to quantify it with an uncertainty better than 0.1 arc second. This will be investigated in chapter 6. As a final remark on the HCC collimation error CE_{HCC} ; we note that probe readings are made systematically during every calibration. The reason this is done is that although the different spindle motions are very small, for the most precise work the small observed variations between different instruments must be taken into account.

6 Errors and Uncertainty Evaluation

This chapter reviews the different factors contributing to the uncertainty of the horizontal circle comparator (HCC), the linked encoders configuration (LEC), and the vertical circle comparator (VCC). It builds on the previous two chapters with the aim of providing a clear statement of the uncertainty of these standards for the calibration of horizontal and vertical angles issued from spherical measurement systems (SMSs). The chapter starts with a review of the background to the establishment of uncertainty as prescribed by the 'Guide to the expression of uncertainty in measurement' (GUM) and its supplement 1, 'Propagation of distributions using a Monte Carlo method' (GUM1) in the context of the HCC, LEC and VCC. Also background to the ISO/CEI 17025 'General Requirements for the Competence of Testing and Calibration Laboratories' standard is given. The remainder of the chapter is centred on the construction of uncertainty statements for the HCC and VCC, and each of the main techniques and instruments used to establish their uncertainties.

6.1 Background

Two of the central motivations of this thesis are; first provide two angle standards that can be combined with the existing ESRF distance meter calibration bench (DCB) to provide a whole SMS instrument calibration suite; and second guarantee that these standards can be accredited under the International Standard ISO/CEI 17025 'General Requirements for the Competence of Testing and Calibration Laboratories'. [28] ISO/CEI 17025 comprises two main parts. The first specifies the requirements for sound management, while the second the requirements for technical competence for the type of tests and/or calibrations the laboratory undertakes.

Calibration laboratories that comply with this international standard also operate in accordance with ISO 9001. Although the laboratory management system is extremely important, it will not be considered further in this thesis. For the remainder of this chapter we shall look at the technical requirements related to the traceability and uncertainty of the VCC and HCC.

The technical requirements of ISO/CEI 17025 concentrate on the reliability aspects of the laboratory and in particular the way in which calibrations and measurements made by the laboratory are traceable to the International System of Units (SI - Système international d'unités). In particular, ISO/CEI 17025 stipulates a calibration laboratory must establish traceability of its own measurement standards and measuring instruments to the SI by means of an unbroken chain of calibrations or comparisons linking them to relevant primary standards of the SI units of measurement.

Before continuing, it is appropriate to put the different agreements underpinning the SI system into perspective. The basis of the SI system of units is the Convention of the Metre (Convention du Mètre). The Convention of the Metre is a treaty that created the International Bureau of Weights and Measures (BIPM), an intergovernmental organization under the authority of the General Conference on Weights and Measures (CGPM) and the supervision of the International Committee for Weights and Measures (CIPM). The BIPM acts in matters of world metrology, particularly concerning the demand for measurement standards of ever increasing accuracy, range and diversity; and the need to demonstrate equivalence between national measurement standards.

The Convention was signed in Paris in 1875 by representatives of seventeen nations. As well as founding the BIPM and laying down the way in which the activities of the BIPM should be financed and managed, the Metre Convention established a permanent organizational structure for member governments to act in common accord on all matters relating to units of measurement. The Convention, modified slightly in 1921, remains the basis of international agreement on units of measurement. The BIPM now has fifty-one Member States, including all the major industrialized countries.

At a meeting held in Paris on 14 October 1999, the directors of the National Metrology Institutes (NMIs) of thirty-eight Member States of the BIPM and representatives of two international organizations signed a Mutual Recognition Arrangement (CIPM MRA) for national measurement standards and for calibration and measurement certificates issued by NMIs. The CIPM MRA has now been signed by the representatives of 74 institutes – from 45

Member States, 27 Associates of the CGPM, and 2 international organizations – and covers a further 123 institutes designated by the signatory bodies.

On the occasion of the 22nd CGPM national delegations unanimously endorsed a resolution dealing with the importance of mutual recognition of measurement standards, calibrations and tests. Resolution 6 asked the CIPM to draw up a declaration on the importance and application of its MRA for trade, commerce, and regulatory affairs. The Resolution also invited Member States of the Metre Convention to promote the CIPM MRA as a framework for the acceptance of calibration and measurement certificates from NMIs as well as from accredited laboratories which could demonstrate traceability of their measurements to the SI.

In preparing the declaration, the CIPM recognized that its MRA was complemented by similar Arrangements drawn up by the Organization of Legal Metrology (OIML) and the International Laboratory Accreditation Cooperation (ILAC). Indeed all three are interlinked and all support the equivalence and acceptability of SI-traceable measurements world-wide. The aim of this international measurement system is to provide users with measurement results which can be accepted everywhere without the need for further measurements. An important feature of this system is that its use can help reduce the effects of technical barriers to trade and can provide a secure base for scientific and other measurements throughout society. [109]

Through the MRA and a common statement between BIPM, OIML and ILAC, measurements made by different NMIs and accredited laboratories are recognized between signatories. A calibration certificate issued by a COFRAC accredited laboratory is recognized in the UK and a calibration certificate issued by a UKAS accredited laboratory is recognized in France. Figure 6.1 provides a diagram showing schematically the interaction between the different bodies in the accreditation chain.

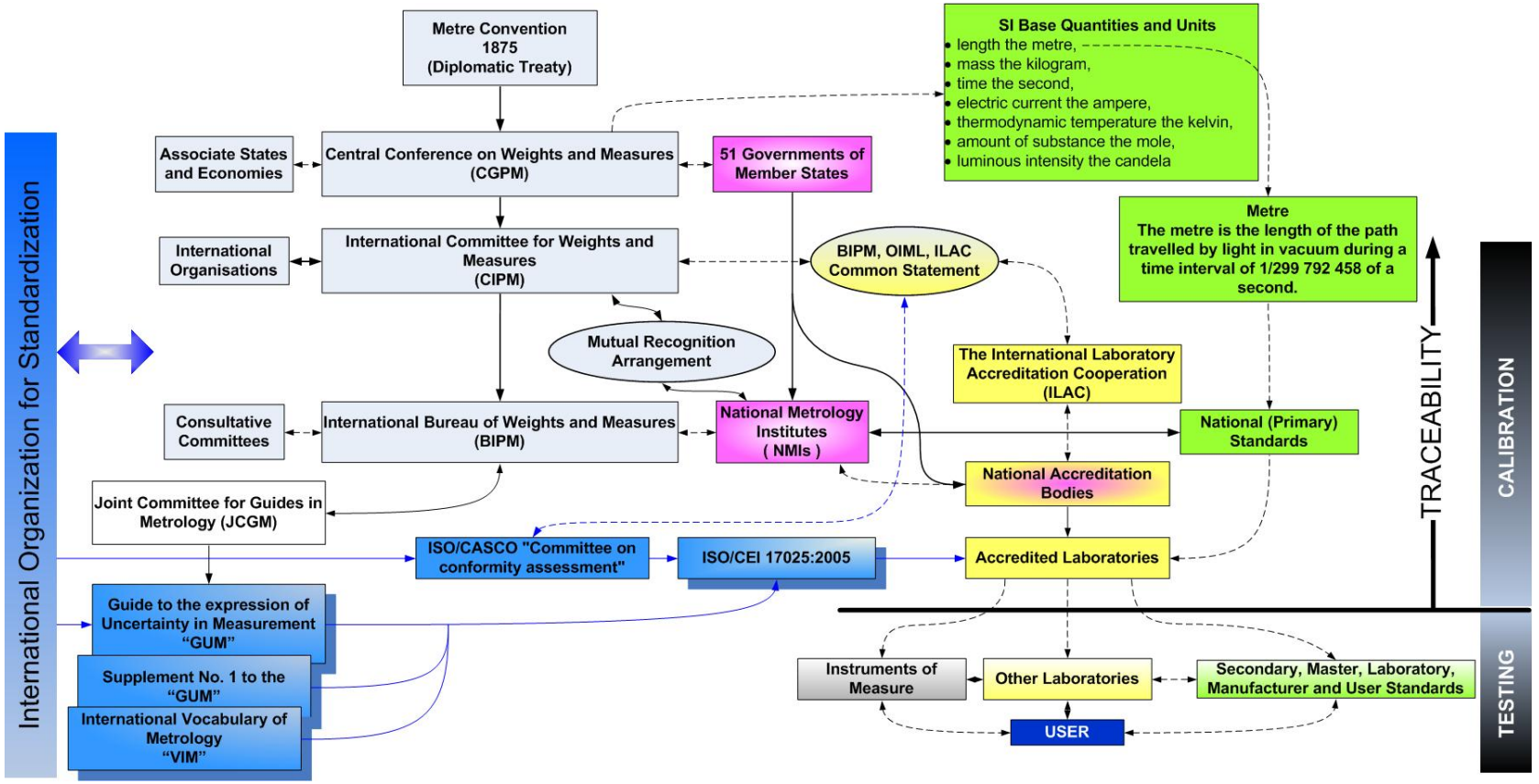

Figure 6.1 Schematic diagram showing the interaction between the different bodies in the accreditation chain. The main players at the national level are the national accreditation bodies (e.g. UKAS and COFRAC) and the national metrology institutes (e.g. NPL and LNE). Through the MRA and a common statement between BIPM, OIML and ILAC, measurements made by different NMIs and accredited laboratories are recognized between different signatories.

ISO/CEI 17025 stipulates a calibration laboratory must establish traceability of its own measurement standards and measuring instruments to the SI. The mechanics by which this is actually done is through the statement of uncertainty. Chapter 5.4.6 of ISO/CEI 17025 stipulates: "A calibration laboratory, or a testing laboratory performing its own calibrations, shall have and shall apply a procedure to estimate the uncertainty of measurement for all calibrations and types of calibrations." It specifically cites the GUM as a reference for the general rules used in evaluating and expressing uncertainty in measurement. [28] (pp14-15)

What is the GUM? The answer to this question is summed up in [110] which is itself largely inspired from the GUM Forward [111] : "The GUM provides general rules for evaluating and expressing uncertainty in measurement that are intended to be applicable to a wide range of measurements and for use within standardization, calibration, laboratory accreditation and measurement services. The basis of the GUM is Recommendation INC–1 (1980), 'Expression of experimental uncertainties' of the Working Group on the Statement of Uncertainties, convened in 1980 by the Bureau International des Poids et Mesures (BIPM) in response to a request by the Comité International des Poids et Mesures (CIPM). The CIPM approved the Recommendation in 1981, and reaffirmed it in 1986. The responsibility for developing a detailed guide based on the Working Group Recommendation was given to the Technical Advisory Group on Metrology (TAG4) of the International Organization for Standardization (ISO), in which six other international organizations were represented, namely, the BIPM, the International Electrotechnical Commission (IEC), the International Federation of Clinical Chemistry and Laboratory Medicine (IFCC), the International Union of Pure and Applied Chemistry (IUPAC), the International Union of Pure and Applied Physics (IUPAP) and the International Organization of Legal Metrology (OIML). The resulting document was published in 1993 and reprinted with minor corrections in 1995.

In 1997 a Joint Committee for Guides in Metrology (JCGM), chaired by the Director of the BIPM, was created by the seven international organizations that had originally prepared the GUM and the 'International Vocabulary of Basic and General Terms in Metrology' (VIM)

[5]. The JCGM assumed responsibility for these two documents from ISO TAG4. In 1998 a further organization joined these seven international organizations, namely, the International Laboratory Accreditation Cooperation (ILAC).

The JCGM has two Working Groups. Working Group 1, 'Expression of uncertainty in measurement', has the task of promoting the use of the GUM and preparing supplements for its broad application. Working Group 2, 'Working Group on International Vocabulary of Basic and General Terms in Metrology (VIM)', has the task of revising and promoting the use of the VIM."

The GUM is the currently accepted international consensus on the expression of uncertainty and comprises the techniques and methodology prescribed for use by the CIPM. The GUM [111], its Supplement Number 1 [112] and the VIM [27] constitute the main references used to establish the uncertainty of measurement in the rest of this chapter. Nevertheless, there are other very good comprehensive sources of information that can be used to this end[35]. [113-116]

6.2 Uncertainty in measurement as expressed by the GUM and GUM1

"The uncertainty of the result of a measurement reflects the lack of exact knowledge of the value of the measurand. The result of a measurement after correction for recognized systematic effects is still only an estimate of the value of the measurand because of the uncertainty arising from random effects and imperfect correction of the result for systematic effects." ([111] p. 7) Uncertainty of measurement defined in the GUM is a parameter associated with the result of a measurement that characterises the dispersion of values that could reasonably be attributed to the measurand. There are many possible sources of uncertainty in a measurement.

The GUM was originally published in 1993 and reprinted with minor corrections in 1995. It has been successful in providing a probabilistic based framework for uncertainty evaluation. The GUM adopts a pragmatic approach which is not overly-prescriptive. Notably the concept

[35] The advantage of these other references is that they are free of cost whereas until very recently the GUM, and VIM, as with all ISO standards were not. They may now, as well as GUM1, be downloaded from http://www.bipm.org/en/publications/guides/gum.html

of Type B (refer to section 6.2) evaluations of uncertainty provides certain flexibility. When justifiable, it subscribes to alternative methods to its recommended approach.

The GUM, and its underlying philosophy have been extensively adopted across metrology. The NMIs and industry have invested extensively in developing procedures that comply with it. For this reason, the body overseeing the development of the GUM, the JCGM is keen that the GUM remains unchanged in the foreseeable future and that any clarification and extensions are published as supplements. [117]

Nevertheless, the GUM has recognized weaknesses. Its standard approach is considered weak for nonlinear models or in situations in which the distribution for the value of the output quantity is asymmetrical or otherwise differs appreciably from normality. Some view the use of degrees of freedom as an unnecessary complication. The scope of the GUM is generally restricted to models with a single output quantity. [117]

With this in mind, it has been judged timely to supplement it with a number of documents. The publications planned by JCGM/WG1 comprise an introductory document, a document concerned with concepts and basic principles, three supplements to the GUM, and two documents concerned with the use of measurement uncertainty in the context of first conformance to specified requirements, and second the application of the method of least squares. The titles of these supplementary documents are: [112]

An introduction to the ‘Guide to the Expression of Uncertainty in Measurement’ and related documents,

Concepts and basic principles,

Supplement 1 to the GUM: Propagation of distributions using a Monte Carlo method (published 2008),

Supplement 2 to the GUM: Models with any number of output quantities.

Supplement 3 to the GUM: Modelling.

The role of measurement uncertainty in deciding conformance to specified requirements.

Applications of the least-squares method.

Only the Supplement 1 to the GUM: Propagation of distributions using a Monte Carlo method (GUM1 [112]), of the above mentioned documents is of interest to this work at the time of writing. This is because it has been published and is therefore (in principle[36]) recognized by ISO/CEI 17025. Other documents will be of interest, particularly Supplements 2 and 3, in the context of the HCC and VCC when they are published.

The GUM and GUM1 provide two different approaches to the problem of uncertainty evaluation. The principal difference is that although the GUM is rooted in probability theory, GUM1 uses the richer information available in the probability density functions (PDFs) [37] [96] for the values of the input quantities to a measurement model. In contrast , the GUM uses just the expectations and standard deviations of these PDFs to determine the PDF for the value of the output quantity. In other words, no approximations to the measurement model or about the PDF for the output value are made. The GUM1 approach can be used to validate the use of the GUM uncertainty framework in any particular instance. [118] We shall now briefly outline these two approaches before implementing them in the context of the VCC and HCC.

"The GUM provides a framework for assessing uncertainty based on the law of propagation of uncertainty and the characterization of the output quantity by a Gaussian distribution or a scaled and shifted *t*-distribution. Within that framework, the law of propagation of uncertainty provides a means for propagating uncertainties through the model. Specifically, it evaluates the standard uncertainty associated with an estimate of the output quantity, given;

the best estimates of the input quantities;

the standard uncertainties associated with these estimates, and, where appropriate,

degrees of freedom associated with these standard uncertainties, and

any non-zero covariances associated with pairs of these estimates.

[36] GUM1 is not formally mentioned in the ISO/CEI 17025 standard because it was published after the latter.

[37] For a continuous function, the probability density function is the probability that the variate has the value x. Because for a continuous probability function the probability of any specific value of x is zero, we can only attach actual probabilities to occurrences within a specified range of x values. Thus we express and plot distributions as probability density functions (crudely as probability per unit range) that are then integrated over small (or larger) ranges of x to give local estimates of likelihood.

Also within the framework, the PDF taken to characterize the output quantity is used to provide a coverage interval, for a stipulated coverage probability, for that quantity." (p. vii GUM1 [112])

A measurement comprises four elements; a value, a unity (when appropriate), a statement of uncertainty, and a coverage interval or expanded uncertainty. Both the GUM and GUM1 can provide an estimate of the output quantity (of a measurement/s), the standard uncertainty associated with this estimate and a coverage interval for that quantity corresponding to a specified coverage probability. The coverage interval is determined by multiplying the standard uncertainty by a coverage factor. Typically the coverage factor is 2; which when the Gaussian distribution applies, corresponds to a coverage interval having a level of confidence of approximately 95%.

Both the GUM and GUM1 are composed of two stages; the formulation and calculation. The formulation stage used in both approaches is unique to each application and requires the development of a model of measurement as a basis for the evaluation of uncertainty. This model can have any number of input quantities. Under the GUM and GUM1 uncertainty frameworks, this model produces a single output quantity referred to as the measurand.

Generally speaking, a measurand Y is not measured directly, but is determined from N other quantities through a functional relationship f ; $Y = f\left(X_1, \cdots, X_N\right)$. An estimate of the measurand Y denoted by y is obtained from this equation using estimates $x_1, \cdots, x_N$ of the N quantities $X_1, \cdots, X_N$. The output estimate y, which is the result of the measurement is given by $y = f\left(x_1, \cdots, x_N\right)$. The approaches of the GUM and GUM1 diverge at the calculation stage.

In fact there are (at least) three methods calculation. The analytical approach is the method of choice when it can be applied. It does not introduce any approximation. However, it is applicable in relatively simple cases only. It is not used in this work. The second approach is that outlined by the GUM uncertainty framework. This approach can be regarded as an approximate analytical method. The third approach, the Monte Carlo simulation method, is the one taken by GUM1. [118]

6.2.1 The GUM uncertainty evaluation approach

The GUM uncertainty framework is founded on probability theory where information regarding measured quantities is characterized by probability distributions. At the time of its writing, the evaluation of uncertainty for general (linear or non-linear) models was considered too complex to form its basis. For this reason, the GUM provided a simplified approach, the so-called GUM uncertainty framework. This framework linearizes the measurement model about the best available estimates of the input quantities. Rather than working with the distributions themselves, the approach uses summarizing parameters of the distributions, namely, expectations (means), and standard deviations. The expectations and standard deviations are propagated through the linearized model. A Gaussian distribution (or a scaled and shifted *t*-distribution) is then used to characterize the output quantity Y in order to obtain a coverage interval corresponding to a stipulated coverage probability. [110] The justification for the use of the Gaussian distribution is the invocation of the well know central limit theorem.

The uncertainty of measurement generally consists of several components which the GUM approach groups into two categories according to the method used to estimate their numerical values:

Type A: method of evaluation of uncertainty by the statistical analysis of series of observations,

Type B: method of evaluation of uncertainty by means other than the analysis of series of observations. [111]

Broadly speaking, a Type A determination of uncertainty will be made with a series of measurements of the measurand. An example we will come across later in this chapter is repeated measurements of LEC angle displacements determined by capacitive probes. Typically, Type B determinations of uncertainty will incorporate uncertainties determined by manufacturer's specifications, calibration certificates, recognized handbooks or simply experience with, or general knowledge of the behaviour of materials or instruments. An example of a Type B uncertainty used later is the calibration certificate issued by the

Laboratoire National d'Essais (LNE) for the frequency of the laser interferometer used in the calibration of capacitive probes.

Individual uncertainties whether they are Type A or Type B are combined together by applying the usual method for the combination of variances, the law of propagation of uncertainty; this is to say by the summing the squared variances. This combined uncertainty is then expressed in terms of an expanded uncertainty which is obtained by multiplying it by a coverage factor.

The steps for the uncertainty estimation following the GUM framework are (p.12 [112]) :

Obtain from the PDFs for the input quantities $\mathbf{X} = \left(X_1, \cdots, X_N\right)^T$ the expectations $\boldsymbol{x} = \left(x_1, \cdots, x_N\right)^T$ and the standard deviations (standard uncertainties) $\boldsymbol{u}\left(\boldsymbol{x}\right) = \left[u\left(x_1\right), \cdots, u\left(x_N\right)\right]^T$. Use instead the joint PDF for $\mathbf{X}$ if pairs of the X_i are not independent (in which case they have non-zero covariance);

Set the degrees of freedom (infinite or finite) associated with each $u\left(x_i\right)$;

For each pair i, j for which X_i and X_j are not independent, obtain from the joint PDF for X_i and X_j the covariance (mutual uncertainty) $u\left(x_i, x_j\right)$ associated with x_i and x_j;

Form the partial derivatives of first order of $f\left(\mathbf{X}\right)$ with respect to $\mathbf{X}$;

Calculate y, the model evaluated at $\mathbf{X}$ equal to $\boldsymbol{x}$;

Calculate the model sensitivity coefficients as the above partial derivatives evaluated at $\boldsymbol{x}$ (i.e. $\delta f / \delta x_i$);

Calculate the standard uncertainty $u_c\left(y\right)$ by combining $\boldsymbol{u}\left(\boldsymbol{x}\right)$ (i.e. $u_c^2\left(y\right) = \sum_{i=1}^{N} \left(\frac{\delta f}{\delta x_i} \right)^2 u^2\left(x_i\right)$), the $u\left(x_i, x_j\right)$ (i.e. $u_c^2\left(y\right) = \sum_{i=1}^{N} \sum_{i=1}^{N} \frac{\delta f}{\delta x_i} \frac{\delta f}{\delta x_j} u\left(x_i, x_j\right)$) and the model sensitivity coefficients;

Calculate ν_{eff}, the effective degrees of freedom associated with $u_c\left(y\right)$, using the Welch-Satterthwaite formula [GUM formula (G.2b)];

Calculate the expanded uncertainty U_p, and hence a coverage interval (for a stipulated coverage probability p) for Y, regarded as a random variable, by forming the appropriate multiple of $u(y)$ through taking the probability distribution of $(Y-y)/u(y)$ as a standard Gaussian distribution ($\nu_{eff}=\infty$) or *t*-distribution ($\nu_{eff}<\infty$).

There are no conditions for the valid application of the GUM uncertainty framework for linear models. However, there are conditions, outlined in the GUM1, to its validity when applied to non-linear models. (p. 13 [112]) This is considered one of its primary weaknesses that GUM1 aims to overcome with the more comprehensive Monte Carlo simulation approach.

6.2.2 The GUM supplement number 1 approach

"The Monte Carlo simulation method provides a general approach to obtain an approximate numerical representation **G**, say, of the distribution function $G_Y(\eta)$ for Y. The heart of the approach is repeated sampling from the PDFs for the X_i and the evaluation of the model in each case. Since $G_Y(\eta)$ encodes all the information known about Y, any property of Y such as expectation, variance and coverage intervals can be approximated using **G**. The quality of these calculated results improves as the number of times the PDFs are sampled increases.

Expectations and variances (and higher moments) can be determined directly from the set of model values obtained. The determination of coverage intervals requires these model values to be ordered. If y_r, for $r=1\cdots M$, represent M model values sampled independently from a probability distribution for Y, then the expectation $E(Y)$ and variance $V(Y)$ can be approximated using the y_r. In general, the moments of Y (including $E(Y)$ and $V(Y)$) are approximated by those of the sampled model values. Let M_{y_0} denote the number of y_r that are no greater than y_0, any prescribed number. The probability $\Pr(Y \le y_0)$ is approximated by M_{y_0}/M. In this way, the y_r provide a step function (histogram-like) approximation to the distribution function $G_Y(\eta)$. Each y_r is obtained by sampling at random from each of the

PDFs for the X_i and evaluating the model at the sampled values so obtained. **G** , the primary output from MCM, constitutes the y_r arranged in strictly increasing order." (GUM1 p14 [112])

The steps in the Monte Carlo simulation method are outlined as (p. 14 [112]) :

select the number M of Monte Carlo trials to be made;

generate M vectors, by sampling from the assigned PDFs, as realizations of the (set of N) input quantities X_i ;

for each such vector, form the corresponding model value of Y , yielding M model values;

sort these M model values into strictly increasing order, using the sorted model values to provide **G** ;

use **G** to form an estimate y of Y and the standard uncertainty $u_c(y)$ associated with y ;

use **G** to form an appropriate coverage interval for Y , for a stipulated coverage probability

6.3 VCC uncertainty

The VCC measurement procedure is discussed in detail in section 3.5. Recall measurements are made with the instrument being calibrated; robotic total station (RTS) or laser tracker (LT), to its reflector (i.e. spherically mounted retro-reflector or SMR) mounted on a servo-controlled carriage which runs up and down the VCC. Simultaneously, interferometer measurements are made to another reflector mounted on servo carriage. These interferometer measurements provide a traceable standard for comparison with the vertical angles measured by the instrument. The principle of the measurement is illustrated in Figure 6.2.

The functional model is given by equation (6.1). In the model, va' is the calibrated instrument angle. This is the measurand. The instrument being calibrated also measures distances d_0 and d_1 and the difference Δha between two horizontal angles measured to the SMR in position 0 and position 1 (Figure 6.2) at the same time as the vertical angle is measured. The difference between the horizontal angles Δha represents the inclination of the VC and instrument with respect to one another in the xz plane. It is always less than and often

very much less than 1 degree. D_I is the measured interferometer distance between the carriage in SMR position 0 and SMR position 1.

$$va' = \sin^{-1}\left(\frac{z_0 - \Delta z}{d}\right)$$

where

$$\begin{aligned}
&(x_0, y_0, z_0) = d\left(0, \cos(va_0), \sin(va_0)\right) \\
&\Delta x = d\cos(va)\sin(\Delta ha) \\
&\Delta y = y_0 - d\cos(va)\cos(\Delta ha) \\
&\Delta z = \sqrt{D_I^2 - \left(\Delta x^2 + \Delta y^2\right)}
\end{aligned} \tag{6.1}$$

One remarks immediately that the measurand appears on both the left hand (va') and right hand (va) sides of the functional model given by equation (6.1). Its use on the right hand side is unusual but will be justified in two ways. First its influence is very small (see the sensitivity coefficients of (6.2)). Even with an uncertainty in va in the order of 1000 arc seconds, its contribution in the functional model amounts to only 0.1 arc seconds. Secondly, because all parameters used in the calibration must be traceable, we will invoke before hand a simple model whereby the measurand va used on the right hand side of equation (6.1) will have an adequate and traceable uncertainty for the refinement of va' in the functional model used in (6.1). The simple model used for this purpose is $va = \sin^{-1}\left(\frac{z_0 - D_I}{d_1}\right)$. This will be discussed in section 6.3.2

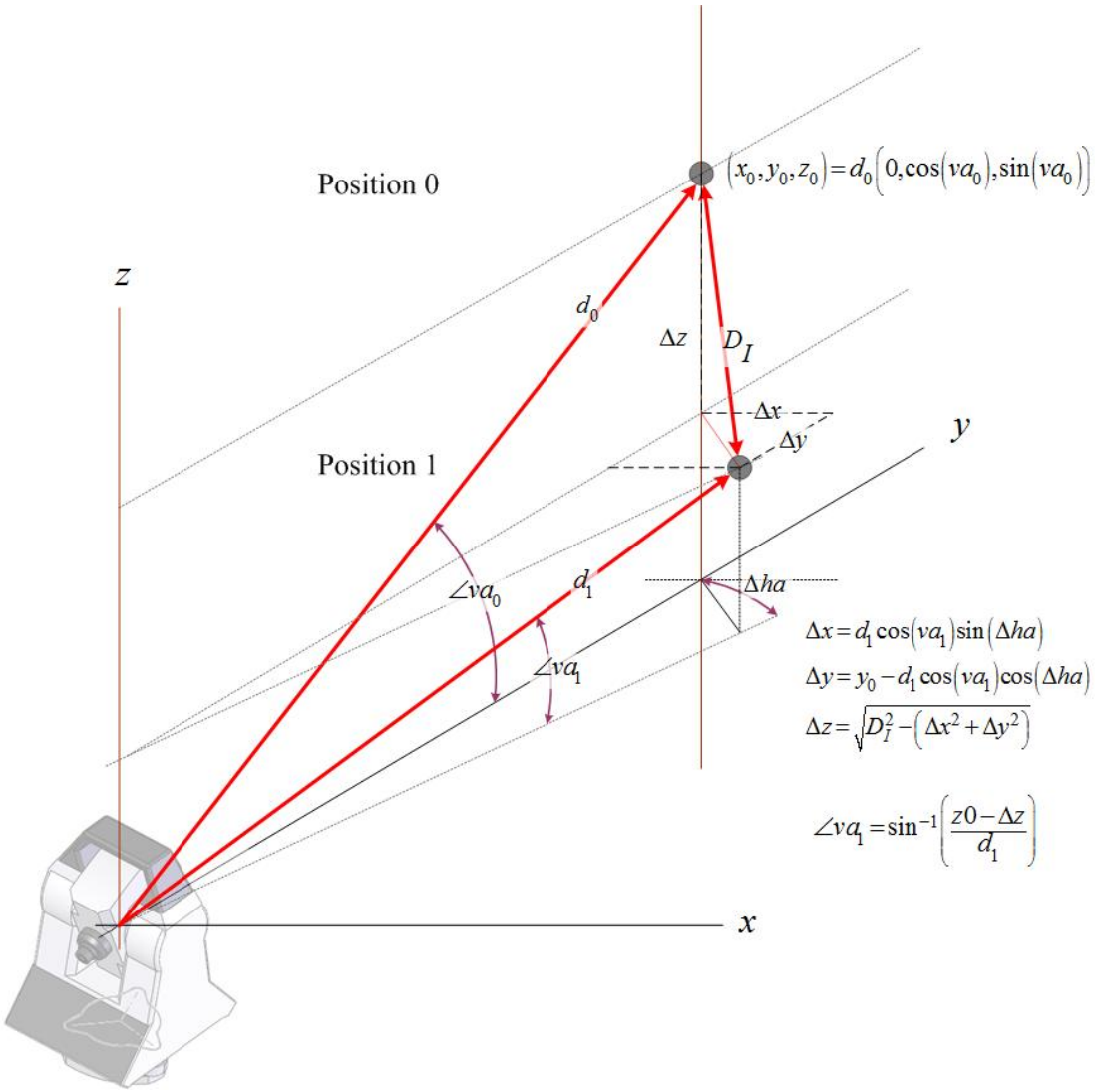

Figure 6.2 Measurement scheme of the VCC.

6.3.1 Uncertainty contributions

The uncertainty contributions to the VCC functional model are summarized in Table 6.1. In this table and the ones that follow, the heading *Quantity* refers to the input quantity or measurand, *PDF* refers to the probability density function assigned to it, μ is its nominal or mean value, and σ is its standard uncertainty. Unless otherwise stated, the coverage factor is $k = 1$. Insofar as the PDF is concerned, $N(\mu, \sigma^2)$ refers to a Gaussian distribution with expected value μ and standard deviation σ and $t_\nu(\mu, \sigma^2)$ refers to a shifted and scaled $t-$distribution with expected value μ, standard deviation σ and ν degrees of freedom. Each of these items is discussed separately in the following paragraphs. These uncertainties are used in the GUM uncertainty framework evaluations made in sections 6.3.2 below.

Table 6.1 Summary of the different uncertainty contributions to the VCC functional model given in equation (6.1) and Figure 6.2.

Ref	*Quantity*	*PDF*	μ	σ
$B_{VCC\ 1}$	Interferometer distance $U(D_I)$	$N(\mu,\sigma^2)$	D_I µm	10 µm
$B_{VCC\ 2.1}$	RTS distances $U(d_1)$ and $U(d_2)$	$N(\mu,\sigma^2)$	d µm	86 µm
$B_{VCC\ 2.2}$	LT distances $U(d_1)$ and $U(d_2)$	$N(\mu,\sigma^2)$	d µm	26 µm
$B_{VCC\ 3.1}$	RTS $U(\Delta ha)$	$N(\mu,\sigma^2)$	Δha arcsec	0.7 arcsec
$B_{VCC\ 3.2}$	LT $U(\Delta ha)$	$N(\mu,\sigma^2)$	Δha arcsec	2.8 arcsec
$B_{VCC\ 4.1}$	RTS $U(\Delta va)$	$N(\mu,\sigma^2)$	Δva arcsec	2.0 arcsec
$B_{VCC\ 4.2}$	LT $U(\Delta va)$	$N(\mu,\sigma^2)$	Δva arcsec	2.0 arcsec

6.3.1.1 Interferometer distance uncertainty $U(D_I)$

The uncertainty in the VCC interferometer distance D_I has several components. These components and the final interferometer distance uncertainty are summarized in Table 6.2. These uncertainties have been derived using the ESRF distance meter calibration bench (DCB) uncertainty calculation as a reference [119].

Table 6.2 Contributions to and summary of the VCC interferometer distance uncertainty.

Ref	*Quantity*	*PDF*	μ	σ
$B_{VCC\ 1A}$	calibration	$N(\mu,\sigma^2)$	0 µm	0.05 µm
$B_{VCC\ 1B}$	refraction correction	$N(\mu,\sigma^2)$	0 µm	0.88 µm
$B_{VCC\ 1C}$	cosine error	$N(\mu,\sigma^2)$	0 µm	0.21 µm
$B_{VCC\ 1D}$	carriage Abbe error	$N(\mu,\sigma^2)$	0 µm	0.08 µm
$B_{VCC\ 1E}$	VCC thermal movement	$N(\mu,\sigma^2)$	0 µm	5 µm
$B_{VCC\ 1}$	Interferometer distance $U(D_I)$	$N(\mu,\sigma^2)$	D_I µm	5.1 µm

BVCC 1A calibration: the uncertainty in Agilent 5519A laser interferometer is derived from its calibration certificate. This certificate gives an uncertainty of 15 fm for 633000000

fm, or 0.024 μm per m. The range of VCC measurement is 2.2 m. This uncertainty is taken as $2.2m \times 0.024\,\mu m/m$ or $0.05\mu m$.

BVCC 1B refraction correction: the following correction C to the measured interferometer distance due to atmospheric effects is provided by Agilent, the instrument manufacturer, and based on the Edlen model:

$$C = 10^6 - \frac{10^{12}}{N + 10^6}$$

with

$$N = 0.3836391P \times \left[\frac{1 + 10^{-6}P(0.817 - 0.0133T)}{1 + 0.0036610T}\right] - 3.033 \times 10^{-3} H\left[e^{0.057627T}\right]$$

Using the GUM approach, the sensitivity coefficients (i.e. partial derivatives) of this expression with respect to the atmospheric parameters: P pressure in Pascals, T temperature in degrees Celsius, and H in percentage relative humidity are given by:

$$\frac{\delta C}{\delta P} = 0.4118 \text{ Pa}^{-1}; \quad \frac{\delta C}{\delta T} = 1.0083 \text{ °C}^{-1}; \quad \frac{\delta C}{\delta H} = -0.0096 \text{ \%}^{-1}$$

Given uncertainties for these parameters of $U(P) = 0.5$ Pa, $U(T) = 0.3$ °C and $U(H) = 17$ % derived from the instrument calibration certificates, the combined uncertainty is expressed as:

$$U(C) = \sqrt{(0.4118 \times 0.5)^2 + (1.0083 \times 0.3)^2 + (-0.0096 \times 17)^2} = 0.40 \times 10^{-6} D_{\text{I}}$$

The range of VCC measurement is 2.2 m. Thus, the uncertainty in this correction is taken as $2.2m \times 0.4\,\mu m/m$ or $0.88\mu m$.

BVCC 1C cosine error: the laser is nominally aligned on its reflector at the two extreme carriage positions at either end of the VCC rail. However, the VCC carriage does not move in a perfectly straight line in space; there are deviations from its ideal axis in both directions. The measured VCC profile is shown in Figure 6.3. The standard deviation of the repeatability of five profiles each of R and Z is 9 μm and 2 μm respectively. These profile errors will provoke cosine errors in the interferometer distance (refer to section 4.1.1 for a discussion of the cosine error). The maximum cosine error combining the two profiles of Figure 6.3 is 0.21 μm.

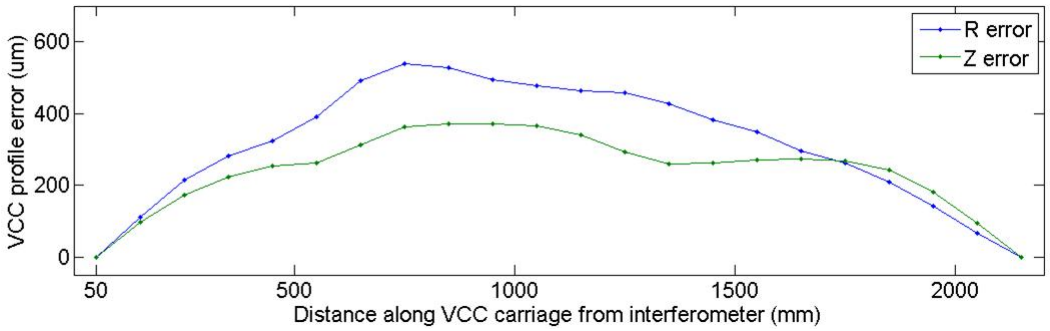

Figure 6.3 Measured VCC profile errors. In the vertical angle calibration configuration, the R error is in the direction perpendicular to the observation (the x direction in Figure 6.2) and the Z error is in the direction of the observation (the y direction in Figure 6.2).

BVCC 1D carriage Abbe error: as the carriage moves along the VCC, the two SMR reflectors, one each for the laser interferometer and for the instrument being calibrated must move in the direction of the VCC alignment axis. However, because of the variation of the bench profile, there is a rotation of one SMR with respect to the other. This results in an Abbe error. The is illustrated in Figure 6.4. The displacement of the instrument SMR is smaller than the measured interferometer distance of the carriage displacement. The maximum error du to this carriage motion is 0.08 µm.

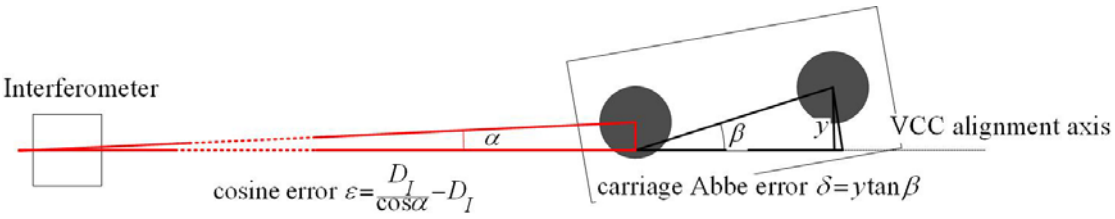

Figure 6.4 Schematic of the VCC cosine and carriage errors.

BVCC 1E VCC thermal induced movement: over the period of the vertical angle calibration which lasts less than 1 hour, temperature changes can induce elongation and/or contraction of the VCC rail and support structure. Maximum temperature variations are expected to be 0.1 degrees Celsius. Taking the thermal coefficient of expansion of aluminium as 23 µm/m/°C, these temperature changes will induce maximum movements of 5 µm.

6.3.1.2 RTS and LT distance uncertainties $U(d_1)$ and $U(d_2)$

The calibration technique employed by the VCC uses the distance meter incorporated into the instrument being calibrated. This requires that this distance meter is calibrated before hand

on the ESRF ISO/CEI 17025 accredited DCB. In this section the uncertainties for examples RTS and LT instruments are given.

Table 6.3 Summary of the RTS measured distance uncertainty and contributions to it.

Ref	*Quantity*	*PDF*	μ	σ
$B_{VCC\ 2.1A}$	calibration	$N(\mu,\sigma^2)$	d µm	85 µm
$B_{VCC\ 2.1B}$	refraction correction	$N(\mu,\sigma^2)$	0 µm	2.1 µm
$B_{VCC\ 2.1C}$	Movement RTS with respect to the VCC	$N(\mu,\sigma^2)$	0 µm	5 µm
$B_{VCC\ 2.1}$	RTS distances $U(d_1)$ and $U(d_2)$	$N(\mu,\sigma^2)$	d µm	85 µm

BVCC 2.1A RTS distance meter calibration uncertainty: the nominal distance meter uncertainty derived from its calibration certificate is 85 µm.

BVCC 2.1B RTS distance meter refraction correction: the following correction C to the measured distance due to atmospheric effects derived from the Barrel and Sears model is recommend by Leica, the instrument manufacturer:

$$C = 281.8 - \left[\frac{0.29065P}{1+\frac{T}{273.16}} - \frac{4.126\,10^{-4}\,H}{1+\frac{T}{273.16}} \times 10^{\frac{7.5T}{237.3+T}+0.7857} \right]$$

Using the GUM approach, the sensitivity coefficients of this expression with respect to the atmospheric parameters: P pressure in Pascals, T temperature in degrees Celsius, and H in percentage relative humidity are given by:

$$\frac{\delta C}{\delta P} = 0.2708 \text{ Pa}^{-1}; \quad \frac{\delta C}{\delta T} = 0.9390 \text{ °C}^{-1}; \quad \frac{\delta C}{\delta H} = 0.0090 \text{ \%}^{-1}$$

Given uncertainties for these parameters of $U(P) = 0.5$ Pa , $U(T) = 0.3$ °C and $U(H) = 17$ % derived from the instrument calibration certificates, the combined uncertainty is expressed as:

$$U(C) = \sqrt{(0.2708 \times 0.5)^2 + (0.9390 \times 0.3)^2 + (0.0090 \times 17)^2} = 0.35 \times 10^{-6} d$$

The maximum measured distance between the instrument and the VCC is 6 m. The uncertainty in this correction is taken as $6.0\text{m} \times 0.35\,\mu\text{m/m}$ or $2.1\mu\text{m}$. However, calculations

in section 6.7 indicate that the actual uncertainty, albeit for an IFM instrument, could be much smaller if the model developed in that section were to be exploited. For the time being it is not because it does not improve significantly the situation.

BVCC 2.1C movement on the RTS instrument with respect to the VCC: over the course of the calibration which lasts less than 1 hour, temperature changes can induce movements within the VCC laboratory. Studies made at the 50 m long ESRF DCB showed stability over a two hour period in the order of 10 μm. Similar movements in the VCC laboratory are estimated to be less than 5 μm.

Table 6.4 Summary of the LT measured distance uncertainty and contributions to it.

Ref	*Quantity*	*PDF*	μ	σ
$B_{VCC\ 2.2A}$	calibration	$N(\mu,\sigma^2)$	0 μm	25 μm
$B_{VCC\ 2.2B}$	refraction correction	$N(\mu,\sigma^2)$	0 μm	2.4 μm
$B_{VCC\ 2.2C}$	Movement LT with respect to the VCC	$N(\mu,\sigma^2)$	0 μm	5 μm
$B_{VCC\ 2.2}$	LT distances $U(d_1)$ and $U(d_2)$	$N(\mu,\sigma^2)$	d μm	26 μm

BVCC 2.2A LT distance meter calibration uncertainty: the nominal IFM uncertainty derived from its calibration certificate is 25 μm.

BVCC 2.2B LT distance meter refraction correction: the same uncertainty calculation employing the Edlen model discussed in section 6.3.1.1 paragraph BVCC 1B is used. The uncertainty in this correction is taken as $6.0\text{m} \times 0.4\mu\text{m/m}$ or 2.4 μm. Once again, with reference to the remarks under BVCC 2.1B above, the uncertainty could be much smaller if the model in section 6.7 were invoked.

$B_{VCC\ 2.2C}$ movement on the LT instrument with respect to the VCC: the same argument as paragraph $B_{VCC\ 2.1C}$ is used.

6.3.1.3 RTS and LT horizontal angle difference uncertainty $U(\Delta ha)$

The calibration technique employed by the VCC uses the simultaneously measured horizontal angles taken by the instrument being calibrated. For the time being the uncertainty of these angle differences are based on the manufacturers quoted angle precision. These

values conform to the author's experience. When the HCC has been accredited the uncertainty based on the calibration certificate will be used. The influence of this parameter is very small.

BVCC 3.1 RTS horizontal angle uncertainty: based on the manufacturers quoted horizontal angle precision of 0.5 arc seconds, this uncertainty is estimated to be $\sqrt{2 \times 0.5^2}$ which is 0.7 arc seconds. The factor two is used because two angles are measured.

BVCC 3.2 LT horizontal angle uncertainty: based on the manufacturers quoted horizontal angle precision of 2 arc seconds, this uncertainty is estimated to be $\sqrt{2 \times 2^2}$ which is 2.8 arc seconds.

6.3.1.4 RTS and LT vertical angle uncertainty $U(\Delta va)$

The calibration technique employed by the VCC uses the vertical angles measured by the instrument being calibrated. In order to provide a traceable value for these angles, a simple model $va = \sin^{-1}\left((z_0 - D_I)/d_1\right)$ is invoked. The uncertainty of these angles used in this model is based on the manufacturers quoted angle precisions. These values conform to the author's experience. It must be noted that the influence of this parameter is very small.

BVCC 4.1 RTS vertical angle uncertainty: will be less than 2 arc seconds (see section 6.3.2.2).

BVCC 4.2 LT horizontal angle uncertainty: will be less than 2 arc seconds (see section 6.3.2.2).

6.3.2 GUM uncertainty framework uncertainty evaluation

In this section the GUM uncertainty evaluation for the VCC is made. Under the GUM framework, there are two uncertainty sources referred to as Type A and Type B. "A Type A standard uncertainty is obtained from a probability density function derived from an observed frequency distribution, while Type B standard uncertainty is obtained from an assumed probability density function based on the degree of belief that an event will occur. Both approaches employ recognized interpretations of probability". (3.3.5 GUM [111])

First the uncertainty contributions from the Type B sources will be evaluated. This requires the development of a functional model. In this case, the functional model, referred to as the

full functional model, has the particularity the measurand is found on both sides of the model equation. This problem is approached by developing a simple functional model whereby a preliminary traceable uncertainty for the measurand is determined and reinserted back into the full functional model. The Type A uncertainties for a Leica TDA5005 RTS, a Leica AT901-MR LT and a API Tracker II+ LT are developed and their combined uncertainty statements are made.

6.3.2.1 Full functional model

In the GUM uncertainty framework each model input quantity X_i is summarized by its expectation and standard deviation. The expectation is taken as the best estimate x_i of X_i and the standard deviation as the standard uncertainty $u(x_i)$ associated with x_i. This information is propagated, using the law of propagation of uncertainty through a first-order Taylor series approximation to the model at x_i to provide an estimate y of the output quantity Y, and the standard uncertainty $u(y)$ associated with y.[112]

Values for the expectations and standard uncertainties are given in 6.3.1 and specifically in Table 6.1. The first order Taylor series approximation to the model is accomplished by performing partial differentiation with respect to each of the parameters. For the model described in equation (6.1) and Figure 6.2 this yields the sensitivity coefficients (6.2).

functional model:

$$va' = \sin^{-1}\left(\frac{z_0 - \Delta z}{d}\right)$$

sensitivity coefficients:

$$\frac{\delta va'}{\delta va} = \frac{\sin(va)\left(y_0 \cos(\Delta ha) - d\cos(va)\right)}{C_1}$$

$$\frac{\delta va'}{\delta \Delta ha} = \frac{y_0 \cos(va)\sin(\Delta ha)}{C_1}$$

$$\frac{\delta va'}{\delta D_I} = -\frac{1}{2dC_1}$$

$$\frac{\delta va'}{\delta d} = \frac{d\cos(va)\left(d\cos(va) - y_0\cos(\Delta ha)\right) - \Delta z\left(z0 - \Delta z\right)}{d^2 C_1}$$

where

$$\left(x_0, y_0, z_0\right) = d\left(0, \cos(va_0), \sin(va_0)\right)$$

$$\Delta x = d\cos(va)\sin(\Delta ha)$$

$$\Delta y = y_0 - d\cos(va)\cos(\Delta ha)$$

$$\Delta z = \sqrt{D_I^2 - \left(\Delta x^2 + \Delta y^2\right)}$$

$$C_1 = \Delta z\sqrt{\frac{1 - \left(z_0 - \Delta z\right)^2}{d^2}} \tag{6.2}$$

The uncertainty following the GUM is then given by (6.3)

$$\begin{aligned} U^2\left(va'\right)^2 = &\left(\frac{\delta va'}{\delta va}\right)^2 U\left(va_0\right)^2 + \left(\frac{\delta va'}{\delta d}\right)^2 U\left(d_0\right)^2 + \left(\frac{\delta va'}{\delta va}\right)^2 U\left(va_1\right)^2 \\ &\cdots + \left(\frac{\delta va'}{\delta d}\right)^2 U\left(d_1\right)^2 + \left(\frac{\delta va'}{\delta D_I}\right)^2 U\left(D_I\right)^2 + \left(\frac{\delta va'}{\delta \Delta ha}\right)^2 U\left(\Delta ha_1\right)^2 \end{aligned} \tag{6.3}$$

However because the vertical angle appears on both the right hand (as va) and left hand (as va') sides of this model, a so called simple model is first established to assign a traceable uncertainty to $U\left(va_0\right)$ and $U\left(va_1\right)$. The simple functional model is discussed next.

6.3.2.2 Simple functional model in the presence of bias error

The simple functional model for the VCC evaluation is given in given in equation (6.4). In this simple model, the vertical angle is no longer found on both sides of the equation. However, the model has two particularities. First the vertical angle uncertainty is expressed in terms of an angle difference (i.e. Δva) and second, a bias error in the measured interferometer measurement D_I as a results of VCC tilt with respect to the instruments (being calibrated) primary axis will be voluntarily left in the uncertainty calculation. For the first, because there

are two angle measurements involved, the uncertainty (expressed as variance in (6.4)) may be resolved by dividing the final uncertainty by two.

functional model:

$$\Delta va = va_0 - va_1 = \cos^{-1}\left(\frac{d_0^2 + d_1^2 - D_I^2}{2d_0 d_1}\right)$$

sensitivity coefficients:

$$\frac{\delta \Delta va}{\delta d_0} = \frac{d_1^2 - d_0^2 - D_I^2}{d_0^2 d_1 C_3}$$

$$\frac{\delta \Delta va}{\delta d_1} = \frac{d_0^2 - d_1^2 - D_I^2}{d_0 d_1^2 C_3}$$

$$\frac{\delta \Delta va}{\delta D_I} = \frac{2D_I}{d_0 d_1 C_3}$$

where

$$C_3 = \sqrt{4 - \left(\frac{d_0^2 + d_1^2 - D_I^2}{2d_0 d_1}\right)^2}$$

$$U^2(\Delta va)^2 = \left(\frac{\delta \Delta va}{\delta d_0}\right)^2 U(d)^2 + \left(\frac{\delta \Delta va}{\delta d_1}\right)^2 U(d)^2 + \left(\frac{\delta \Delta va}{\delta dD_I}\right)^2 U(D_I)^2$$

$$U^2(va) = \frac{\left(\frac{\delta \Delta va}{\delta d_0}\right)^2 U(d)^2 + \left(\frac{\delta \Delta va}{\delta d_1}\right)^2 U(d)^2 + \left(\frac{\delta \Delta va}{\delta dD_I}\right)^2 U(D_I)^2}{2} \qquad (6.4)$$

The second particularity is more difficult to work around. The GUM frame work specifically recommends that corrections be applied to measurement results for known significant systematic effects. (GUM 3.2.3 and 3.2.4) In the note of section 6.3.1 of the GUM, this point is enforced: "Occasionally one may find that a known correction for a systematic effect has not been applied to the reported result of a measurement, but instead an attempt is made to take the effect into account by enlarging the uncertainty assigned to the result. This should be avoided; only in very special circumstances should corrections for known significant systematic effects not be applied to the result of a measurement (see F 2.4.5 for a specific case and how to treat it). …" In appendix F.2.4.5, the proposed treatment is introduced with the following : "Although the Guide recommends that the corrections be applied to measurement results for known significant systematic effects, this may not always be feasible in such a situation because of the unacceptable expense that would be incurred in

calculating and applying an individual correction, and in calculating and using an individual uncertainty, for each value of $y(t)$. [111]

The inclusion of bias error in the uncertainty calculation has been discussed in the literature since shortly after the edition of the GUM. The first time it appears is in [120]. The authors of this paper point out that: "Uncorrected measurement bias may arise in situations where applying a correction for a known measurement bias would be costly, but increasing the measurement uncertainty to allow for the uncorrected bias would still result in an acceptable uncertainty statement. Initially, it might seem paradoxical to be aware of a measurement bias but fail to correct for it; however, such situations are rather common." They propose an extension to the GUM frame work that accommodates this common problem.

In [120], three approaches are evaluated:

$$\text{RSS}u_c \quad \text{method} \quad Y = y \pm U_{RSSu_c}$$
$$\text{where} \quad U_{RSSu_c} = k\sqrt{u_c^2 + \delta^2}$$

$$\text{RSS}U \quad \text{method} \quad Y = y \pm U_{RSSU}$$
$$\text{where} \quad U_{RSSU} = \sqrt{k^2 u_c^2 + \delta^2}$$

$$\text{SUM}U \quad \text{method} \quad Y = y \begin{cases} +U_+ \\ -U_- \end{cases}$$
$$\text{where} \quad U_+ = \begin{cases} ku_c - \delta & \text{if } ku_c - \delta > 0 \\ 0 & \text{if } ku_c - \delta \le 0 \end{cases}$$
$$\text{and} \quad U_- = \begin{cases} ku_c + \delta & \text{if } ku_c + \delta > 0 \\ 0 & \text{if } ku_c + \delta \le 0 \end{cases}$$

In these expressions u_c is the combined uncertainty, k the coverage factor, δ the bias, and U the expanded uncertainty. The SUMU method recommended by the authors proposes an uncertainty interval $y - U_- \le Y \le y + U_+$ be established. However, to avoid the confusing situation where the uncertainty can become negative using this interval, they stipulate that the uncertainty never be negative. However, this does not constrain the bias δ to being positive. For a full discussion of this technique please refer to the paper itself. This technique has its detractors [121] (recommends the RSSU method), however overall, particularly in the

literature related to the field of chemistry and chemical engineering, the authors (of [120]) choice of SUMU appears to be the preferred method to account for persistent systematic error in uncertainty calculation. [122-124]

Accepting that through economy there is no method available at present that may be used to correct for the systematic bias related to the effect of VCC tilt on the interferometer distance D_I, this error must somehow be integrated into the uncertainty calculation for the simple model. Also given that considerable effort has gone into determining the best approach to this problem with strong support in the literature for the SUMU method [120], it will be adopted in the analysis for the GUM uncertainty framework approach.

One final point concerning the bias error is that it is not constant. Its magnitude is dependent upon the proximity of the point to the origin on the VCC (refer to Figure 6.2). The actual bias in the interferometer distance is given by $D_I - \Delta z$ (refer to equation (6.2) for the definition of Δz). At the origin (i.e. $D_I = 0$) the bias is zero, and it is a maximum when $\max(D_I) \cong 2.1$ m for the VCC in its present configuration. The VCC can be aligned to within a maximum tilt error in the xz and yz planes (see Figure 6.2) with respect to the primary axis of the instrument being calibrated of 0.5 degrees in all cases. We shall illustrate the simple functional model uncertainty with an example.

$d_1 = d_2 = \sqrt{{d_H}^2 + \left(D_I/2\right)^2} = 5.599330$ m

unbiased interferometer distance $D_I = 2.1$ m

biased interferometer distance $D_{I\,b} = D_I \cos(\mathrm{T}) = 2.100170$ m

unbiased angle difference: $\Delta\mathrm{va} = \cos^{-1}\left(\dfrac{d_0^2 + d_1^2 - D_I^2}{2 d_0 d_1}\right) = 21.616462°$

biased angle difference: $\Delta\mathrm{va}_\mathrm{b} \cong \cos^{-1}\left(\dfrac{d_0^2 + d_1^2 - D_{I\,b}^2}{2 d_0 d_1}\right) = 21.618234°$

maximum angle bias $\delta_{\mathrm{va}} = \dfrac{6.4}{2} = 3.2$ arc seconds

(Note the factor 2 is used because there are two angles in Δva)

where:

$d_H = 5.5$ m

$\mathrm{T}_x = \mathrm{T}_y = 0.009$ radian $\simeq$ 0.5 degree

$sx = D_I \tan \mathrm{T}_x = 0.018901$ m

$sy = D_I \tan \mathrm{T}_y = 0.018901$ m

$s = \sqrt{{s_x}^2 + {s_y}^2} = 0.026729$ m

$\mathrm{T} = \tan^{-1}\left(s/D_I\right) = 0.012728$ radian

For the laser tracker

$$U(va) = \sqrt{\frac{\left(\dfrac{\delta\Delta va}{\delta d_0}\right)^2 U(d)^2 + \left(\dfrac{\delta\Delta va}{\delta d_1}\right)^2 U(d)^2 + \left(\dfrac{\delta\Delta va}{\delta d D_I}\right)^2 U(D_I)^2}{2}} \pm \delta_{\mathrm{va}}$$

$$= \left(\sqrt{\frac{2(-0.0682)^2 (0.000029)^2 + (0.1818)^2 (0.000010)^2}{2}}\right) \times \frac{180 \times 3600}{\pi} \pm 3.2 \text{ arc seconds}$$

$U_+ = k \times U(va) - 3.2 = 0.5 - 3.2 = -2.7 \Rightarrow U_+ = 0$ for $k = 1$

$U_- = k \times U(va) + 3.2 = 0.5 + 3.2 = 3.7$

Therfore the uncertainty $(k = 1)$ for the LT vertical angle is: $y \begin{cases} 0 \\ -3.7 \end{cases}$ arc seconds

For the robotic total station

$$U(va)=\sqrt{\frac{\left(\frac{\delta\Delta va}{\delta d_0}\right)^2 U(d)^2+\left(\frac{\delta\Delta va}{\delta d_1}\right)^2 U(d)^2+\left(\frac{\delta\Delta va}{\delta dD_I}\right)^2 U(D_I)^2}{2}}\pm\delta_{\text{va}}$$

$$=\left(\sqrt{\frac{2(-0.0682)^2(0.000086)^2+(0.1818)^2(0.000010)^2}{2}}\right)\times\frac{180\times3600}{\pi}\pm3.2 \text{ arc sec} \quad (6.5)$$

$$U_+=k\times U(va)-3.2=1.2-3.2=-2.0\Rightarrow U_+=0 \text{ for } k=1$$

$$U_-=k\times U(va)+3.2=1.2+3.2=4.4$$

Therfore the uncertainty $(k=1)$ for the RTS vertical angle is: $y\begin{cases}0\\-4.4\end{cases}$ arc seconds

Assuming a nominal horizontal distance d_H between the VCC and the instrument being calibrated of 5.5 m, and the maximum VCC tilt error of 0.5 degrees, and maximum unbiased interferometer distance D_I of 2.1 m symmetric about the instrument collimation axis (i.e. ±1.05 m); using values from Table 6.1 will give the uncertainty interval due to the inclusion of the VCC tilt bias developed in equation (6.5). The results of this analysis indicate that the vertical angle lies in an interval between $-4.4\le va\le 0$ arc seconds for the RTS. This result is satisfying because we know that the biased angle interval cannot be positive due to the physical configuration; the corrected interferometer distance Δz must be less than the measured interferometer distance D_I (i.e. $\Delta z\le D_I$) and hence the interval on which the vertical angle can be must also be negative.

It is assumed that VCC tilts can occur with equal probability at any angle between 0 degrees and ±0.5 degrees. This implies that a rectangular distribution describes the vertical angle uncertainty. The rectangular distribution has an expectation $E(X)=(a+b)/2$ and variance $V(X)=(b-a)^2/12$ where the distribution is defined over the interval $[a,b]$ with $a<b$.

For the vertical angle uncertainty developed with the given boundary conditions above, the RTS interval is $[-4.4,0]$ arc seconds and LT interval is $[-3.7,0]$ arc seconds. For this we can calculate expected values of -2.2 arc seconds and -1.9 arc seconds for the RTS and LT and variances of 1.6 arc seconds^2 and 1.4 arc seconds^2 respectively.

To complete the uncertainty calculation for the simple model, the Type A uncertainty must be calculated. For this, ten series of calibration measurements each were taken for a Leica TDA5005 RTS, the Leica AT901-MR LT and a API Tracker II+ LT. Results for these calibrations are indistinguishable from those shown in Figure 6.6. The standard deviations of the ten measurement series are 0.55 arc seconds, 0.31 arc seconds and 1.41 arc seconds respectively. The final uncertainty for the Leica TDA5005 is given by:

$$\begin{aligned} u(va) &= \sqrt{(\text{Type A})^2 + (\text{Type B})^2} \\ &= \sqrt{0.55^2 + 1.6} \\ &= 1.4 \text{ arc seconds} \end{aligned}$$

The final uncertainty for the Leica AT901-MR LT is given by:

$$\begin{aligned} u(va) &= \sqrt{(\text{Type A})^2 + (\text{Type B})^2} \\ &= \sqrt{0.31^2 + 1.4} \\ &= 1.2 \text{ arc seconds} \end{aligned}$$

The final uncertainty for the API Tracker II+ LT is given by:

$$\begin{aligned} u(va) &= \sqrt{(\text{Type A})^2 + (\text{Type B})^2} \\ &= \sqrt{1.4^2 + 1.4} \\ &= 1.8 \text{ arc seconds} \end{aligned}$$

These uncertainties will be used in the uncertainty calculation for the full functional model developed in section 6.3.2.1 discussed next.

6.3.2.3 VCC Type B uncertainty evaluation

Using uncertainty values from Table 6.1 and the above discussion, we are now in a position to derive the GUM framework Type B uncertainty for the VCC using equations (6.2) and (6.3). Once again, the actual Type B uncertainty is dependent upon the boundary conditions, most notably the distance between the instrument being calibrated and the VCC. An example calculation for the TDA5005 is given in equation (6.6). The sensitivity coefficients are given in equation (6.2). For this example the horizontal distance between the instrument being calculated and the VCC is taken to be 5.5 m; the corrected interferometer distance Δz is 0.5 m and the VCC tilts are 0.0115 degrees and 0.0917 degrees in the xz and yz planes respectively.

With these reasonable boundary conditions remark the relatively small contributions of sensitivity coefficients $\frac{\delta va'}{\delta va}$ and $\frac{\delta va'}{\delta ha}$ to the overall uncertainty. Their actual contributions to $U(va')$ are less that 0.001 arc seconds! For all sakes and purposes they may actually be ignored GUM 3.4.4 [111]. However, it is important to show this. It is also extremely important to show through the convoluted argument of section 6.3.2.2 that the instrument being calibrated can legitimately participate in its own calibration. This model is also used to show the limitations of the VCC calibration method discussed in section 3.5.3 and shown in Figure 3.13.

$$
\begin{aligned}
U^2(va') &= \left(\frac{\delta va'}{\delta va}\right)^2 U(va_0)^2 + \left(\frac{\delta va'}{\delta d}\right)^2 U(d_0)^2 + \left(\frac{\delta va'}{\delta va}\right)^2 U(va_1)^2 \\
&\quad \cdots + \left(\frac{\delta va'}{\delta d}\right)^2 U(d_1)^2 + \left(\frac{\delta va'}{\delta D_I}\right)^2 U(D_I)^2 + \left(\frac{\delta va'}{\delta \Delta ha}\right)^2 U(\Delta ha_1)^2 \\
\frac{\delta va'}{\delta va} &= -0.00010; \quad U(va_0) = U(va_1) = 2 \text{ arc seconds} = 9.7\times10^{-6} \text{ radian} \\
\frac{\delta va'}{\delta \Delta ha} &= 0.00014; \quad U(\Delta ha_1) = 2\times0.5 \text{ arc seconds} = 4.8\times10^{-6} \text{ radian} \\
\frac{\delta va'}{\delta D_I} &= -0.1282; \quad U(D_I) = 0.000005 \text{ m} \\
\frac{\delta va'}{\delta d} &= -0.0094; \quad U(d_0) = U(d_1) = 0.000085 \text{ m} \\
U^2(va') &= 2(-0.00010)^2\left(9.7\times10^{-6}\right)^2 + 2(-0.0094)^2(0.000085)^2 + \\
&\quad \cdots + (-0.1282)^2(0.000010)^2 + (0.00014)^2\left(4.8\times10^{-6}\right)^2 \\
U(va') &= 0.21 \text{ arc seconds at } k = 1
\end{aligned}
\tag{6.6}
$$

Using the same values for the LT, with the exception of $U(d) = 0.000026$ m, the Type B uncertainty is 0.14 arc seconds with this same example.

The actual uncertainty 'function' $U(va')$ is non-linear and dependent upon the position of the SMR with respect to the VCC zero position. Two examples for the worst case uncertainty scenarios (i.e. tilts of +1 degree in the xz and yz planes) for the RTS and LT are plotted in Figure 6.5. These graphs show that for all but the most degenerate conditions (i.e. less than ±0.02 m form the VCC zero position), the uncertainties for the RTS and LT are less than 0.6 arc seconds. For simplicity we shall take 0.6 arc seconds as the Type B uncertainty for

both the RTS and LT. Clearly, in many cases, particularly for the laser tracker, the uncertainty is much smaller than this.

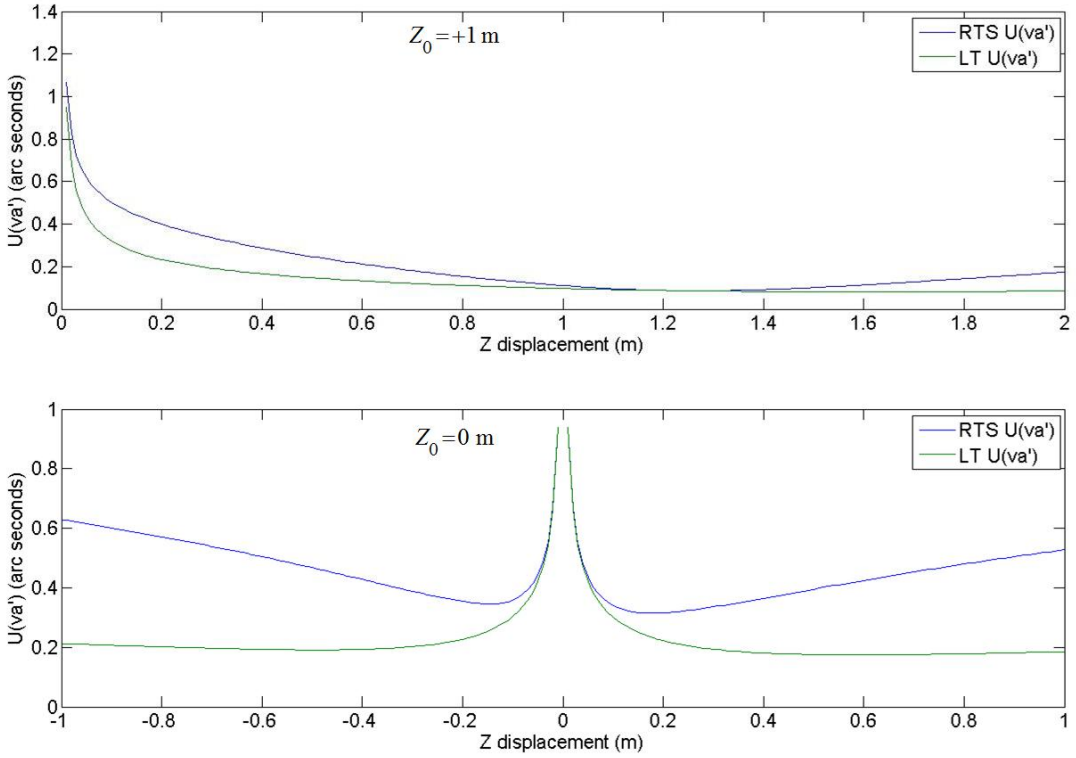

Figure 6.5 VCC Type B uncertainty $U(va')$ as a function of vertical displacement and VCC zero position. In the top graph the zero position is taken to be at the top of the VCC while with the bottom graph it is taken to be at the centre of the VCC. The asymmetry in the bottom (and top) graph is due to the direction of the tilts in the xz and yz planes.

6.3.2.4 VCC Type A uncertainty evaluation

Three sets of ten calibrations each for a Leica TDA5005 RTS, a Leica AT901-MR LT and API Tracker II+ LT are given in Figure 6.6. The standard uncertainties for these calibrations are 0.55 arc seconds, 0.31 arc seconds and 1.41 arc seconds respectively.

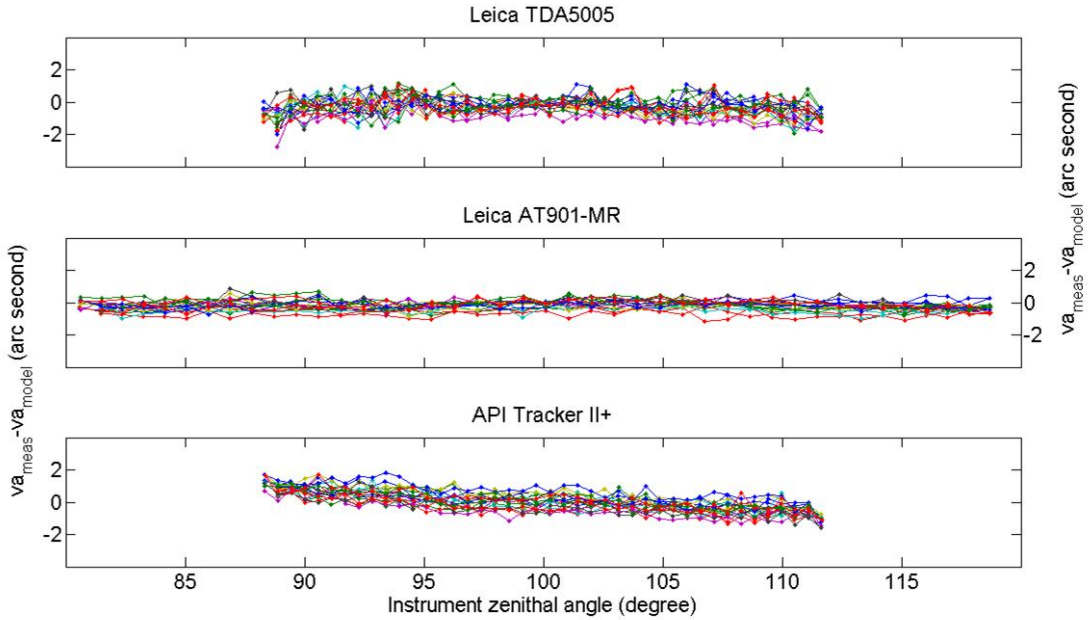

Figure 6.6 The results of ten calibrations each for a Leica TDA5005 RTS, a Leica AT901-MR LT and API Tracker II+ LT. The x axis is the instrument zenithal angle and the y axis gives the difference between the measured and modelled (equation (6.2)) vertical angle in arc seconds.

6.3.2.5 VCC full functional model final uncertainty

The final uncertainty for the Leica TDA5005 is given by:

$$\begin{aligned} u(va) &= \sqrt{(\text{Type A})^2 + (\text{Type B})^2} \\ &= \sqrt{0.55^2 + 0.60^2} \\ &= 0.8 \text{ arc seconds} \\ U &= 1.6 \text{ arc seconds } (k = 2) \end{aligned}$$

The final uncertainty for the Leica AT901-MR LT is given by:

$$\begin{aligned} u(va) &= \sqrt{(\text{Type A})^2 + (\text{Type B})^2} \\ &= \sqrt{0.31^2 + 0.6^2} \\ &= 0.7 \text{ arc seconds} \\ U &= 1.4 \text{ arc seconds } (k = 2) \end{aligned}$$

The final uncertainty for the API Tracker II+ LT is given by:

$$\begin{aligned} u(va) &= \sqrt{(\text{Type A})^2 + (\text{Type B})^2} \\ &= \sqrt{1.4^2 + 0.6^2} \\ &= 1.5 \text{ arc seconds} \\ U &= 3.0 \text{ arc seconds } (k = 2) \end{aligned}$$

It is understood that the uncertainties for the vertical angles of these instruments vary as a function of the position of the instrument SMR on the VCC, and that generally they are (much) better than the values quoted above (see section 6.3.2.3). This point must be developed if the VCC is accredited.

6.4 Capacitive probe uncertainty

6.4.1 Capacitive probe calibration

Capacitive probes are used extensively in the evaluation of the HCC. An important component in their uncertainty is linked to their calibration. The calibration procedure is discussed in section 4.1.4 where it is shown that from a purely theoretical point of view, the expected uncertainty for a calibration point is 13 nm.

Figure 6.7 shows the results of the calibration of a typical probe used in the different experiments discussed later in this chapter. The probe output is almost linear with displacement distance as shown in graphs a) and b) of Figure 6.7. Graph b) shows the residuals of 10 independent calibrations made with the same probe with respect to a best fit straight line. This gives an idea of the repeatability of the probe calibration. The repeatability and temporal stability of the calibration is further demonstrated by overlaying results of two calibrations of the same probe made at a two year interval (graph d).

Generally a polynomial is used to correct the non-linearity of the probe output. In graph c) the residuals with respect to a degree 5 polynomial using the data given in b) are shown. The uncertainty of this fit as given by the root mean squared error (RMSE) is 22 nm. This is reassuringly close to the theoretical value for the calibration (13 nm) estimated in section 4.1.4.

Figure 6.8 shows calibration results for 15 different capacitive probes used in the HCC validation experiments discussed later in this chapter. These results are the residuals after fitting a degree 5 polynomial. They are equivalent to those shown in graph c) of Figure 6.7. The residuals are normally distributed (b in Figure 6.8) with a standard deviation for the 15 degree 5 polynomials of 14 nm.

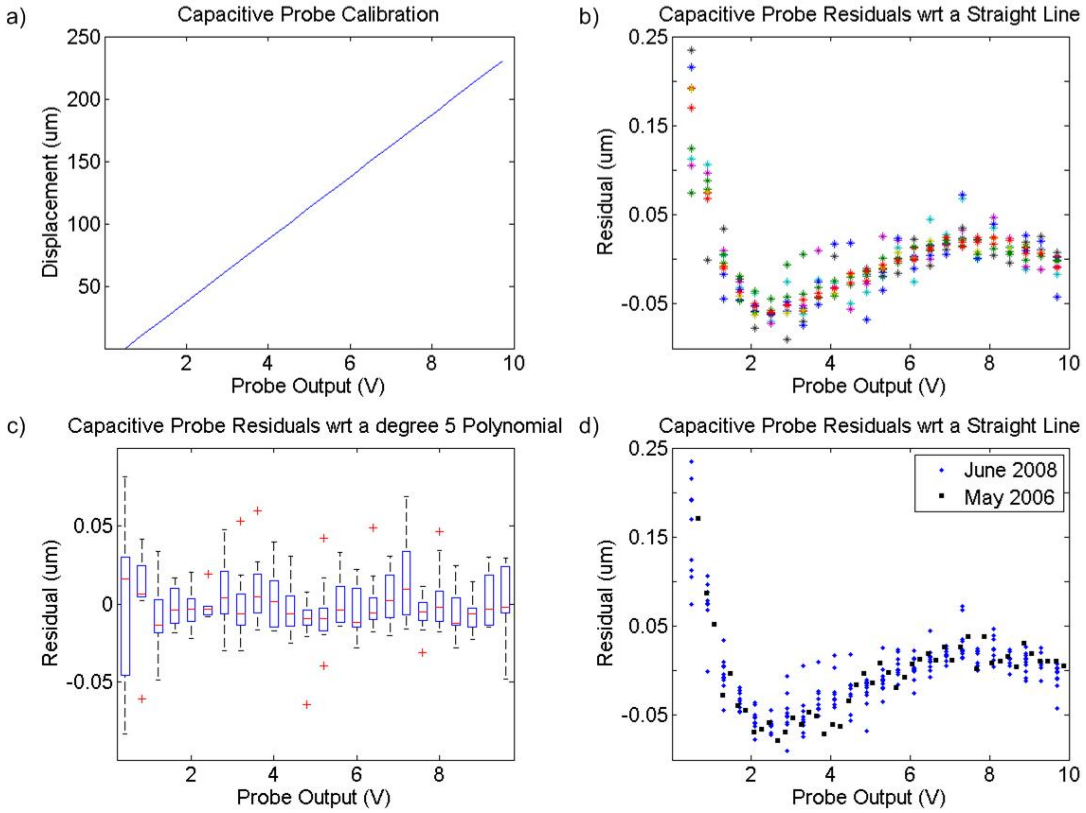

Figure 6.7 Capacitive probe calibration using the method discussed in section 4.1.4. The top left hand graph a) shows the displacement measured by the interferometer as a function of the probe output in Volts. The top right hand graph b) shows the residuals with respect to a best fit line through graph a). In graph b), 10 independent calibrations were made on the same capacitive probe. Graph c) shows box plots of the residuals of the 10 calibrations with respect to a degree 5 polynomial. Finally, to demonstrate its the long term stability, results of a calibration made on the same probe two years previously are superimposed on the results shown in b).

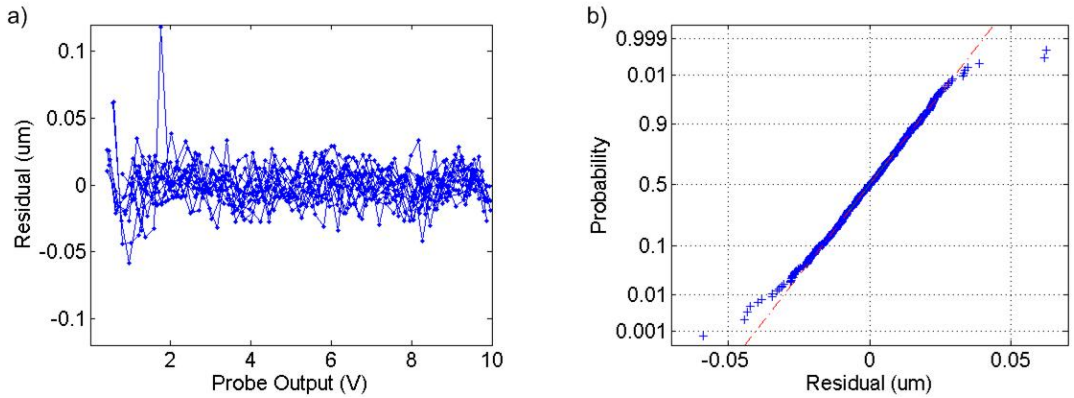

Figure 6.8 Calibration results of 15 capacitive probes used in the validation experiments of the HCC. Residuals after fitting a degree 5 polynomial to the calibration data are shown in graph a). Graph b) shows a normal probability plot of the residuals in a).

Figure 6.7 and Figure 6.8 show that the capacitive probes used here can be calibrated with an over all uncertainty of better than 30 nm. These results apply to a large number of probes

as well as the repeatability of the procedure and its temporal stability. The uncertainty in the probe calibration is summarized in Table 6.5.

Table 6.5 Summary of the capacitive probe calibration uncertainty where the final probe calibration uncertainty is the square root of the sum of squared contributing uncertainties.

Quantity	*PDF*	μ	σ
Intrinsic Uncertainty	$N\left(\mu,\sigma^2\right)$	0	0.013 μm
Calibration of probe	$N\left(\mu,\sigma^2\right)$	0	0.014 μm
Repeatability of calibration	$N\left(\mu,\sigma^2\right)$	0	0.022 μm
Final probe calibration uncertainty	$N\left(\mu,\sigma^2\right)$	0	0.029 μm

6.4.2 Temporal capacitive probe stability

Calibration of the capacitive probes is one way of characterising their uncertainty. However, calibration is performed under as close to ideal conditions as possible. Typically the probes are used in more rugged conditions and over relatively long periods. This section will examine their characteristic uncertainty under normal operating conditions.

Six capacitive probes were installed in conditions similar to those shown in Figure 5.20. Measurements were made over a period of 50 hours. The results of these measurements are shown in Figure 6.9.[38]

Theoretically there should be no change in the probe readings over time. However, there is movement. It is evident that this movement detected by the capacitive probe is dependent, at least to some extent, on temperature variation. This of course is quite natural and expected. It is simple to model this relationship in these experimental circumstances. However, under normal operating conditions probe readings are changing due to some induced movement such as the HCC rotation. Under these circumstances, it is generally impossible to separate the induced movement from that due to thermal (or other) effects, and hence deduce a

[38] Temperature values in Figure 6.9 are the derived using a running average filter whose window size is 15 minutes. The running average filter uses the Matlab filter command $\text{filter}(\text{ones}(1,\text{ws})/\text{ws},\text{data})$ where ws is the sample length of 15 minutes of temperature data.

temperature dependent correlative model. Therefore, this at least partially deterministic probe signal evolution must be assimilated into the probe uncertainty.

The probe uncertainty of Figure 6.9 is clearly time, or more precisely temperature dependent. To quantify this dependency, an empirical model representing the probe uncertainty is built using a type of Bootstrap approach [102, 125]. One step in the development of this model is outlined in Figure 6.10.

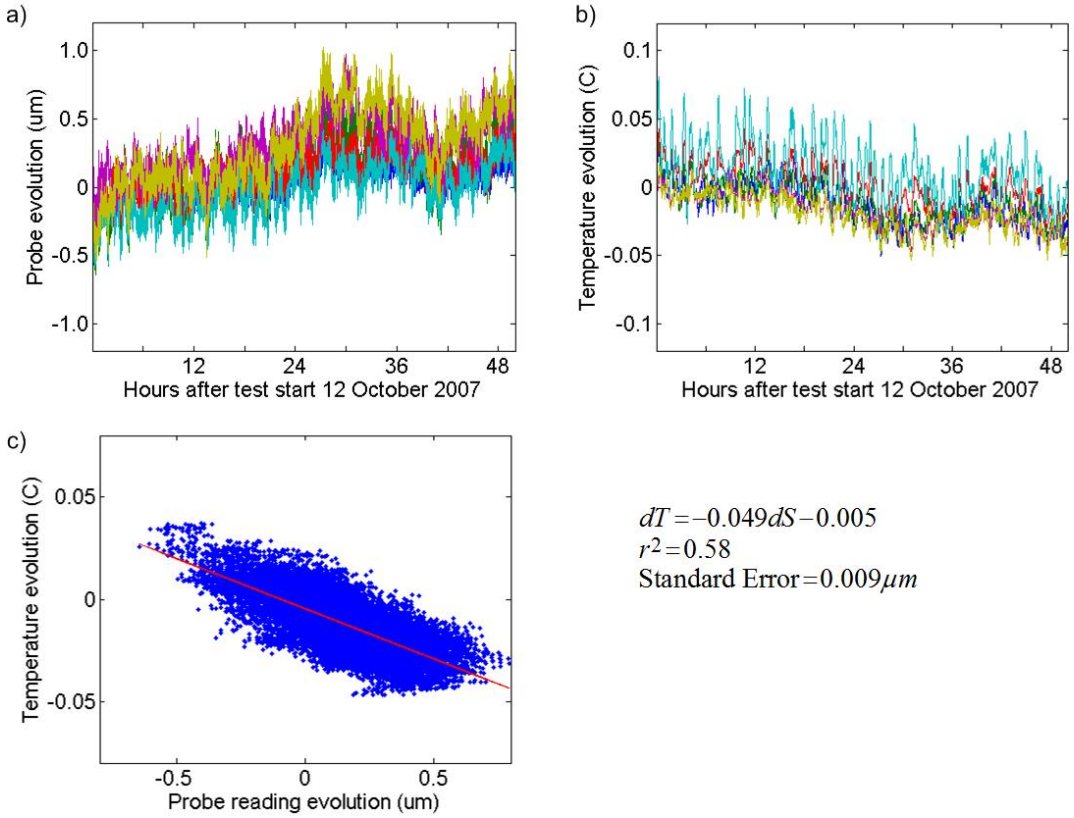

Figure 6.9 Graph a) shows the evolution of 6 capacitive probes over a 50 hour period starting on 12 October 2007. Graph b) shows the evolution of thermocouples installed adjacent to the probes. Graph c) shows the clear correlation between the capacitive probe evolution dS and the temperature evolution dT .

To build this temporal uncertainty model, contiguous sets for different time periods were sampled from the data shown in graph a) Figure 6.9. The sampling periods chosen were 5, 15, 30 minutes and 1, 2 4 8, 12 18 and 24 hours. For each probe, every possible combination of each of these time periods was sampled from the available data.

Data is taken at 10 second intervals so there are a total of $N_s = 17998$ samples in the 50 hour period. In general there are $N_s - n_p$ trials for a given time period t . Here n_p is the number of samples for a given period. For example, the 60 minute time period $n_s = 360$

samples (i.e. $6\,\text{samples}/\text{min} \times 60\,\text{min}$). Therefore there are a total of 17638 trials each composed of 360 contiguous samples for the 60 minute time period.

Figure 6.10 demonstrates how one of the 17638 trials for the 60 minute time period is evaluated. Graph a) shows the full data set for one of the 6 probes of Figure 6.9. a). Graph b) shows the corresponding temperature data. These temperature data are included to illustrate that there is a degree of correlation between temperature and overall drift but that it is not incorporated into the temporal model for reasons discussed previously. One example 60 minute trial sample, of a total of 17638 samples, extracted between the vertical lines of graphs a) and b) are shown in graphs c) and d) of this figure. Graph e) is a normal probability plot and graph f) a histogram of the probe data shown in graph c). These are perfectly equivalent representations of this data and illustrate that the data composing the trial is reasonably normally distributed. The standard deviation of this specific trial is 0.100 μm.

The mean standard deviation of the 17638 trials gives one point (in the grey ellipse) in graph g) of Figure 6.10. This graph shows the mean standard deviations for each of the 6 capacitive probes at 5, 15, 30 minutes and 1, 2 4 8, 12 18 and 24 hours. One of the data sets (shown by red crosses in circles) is different than the five others. This data set was excluded. However, it will be within the coverage interval of the uncertainty model developed next.

Each of the points in Figure 6.10 g) is a standard deviation. It, along with the mean value which is always zero here, fully describe the statistical properties of the temporal stability of a given probe for a given time period under the assumption of normally distributed data sets. The uncertainty model is completed by sampling simultaneously from the five probability distributions of the five probes for each of the time periods. The five distributions are actually concatenated to permit this sampling. For illustration, the distributions are overlaid on one another for each of the 10 time periods in Figure 6.11 a). The distribution shown by the red curve is determined from a random sampling with replacement (250000 samples) of the five concatenated probe distributions. The standard deviation these distributions are plotted in graph b) of this figure.

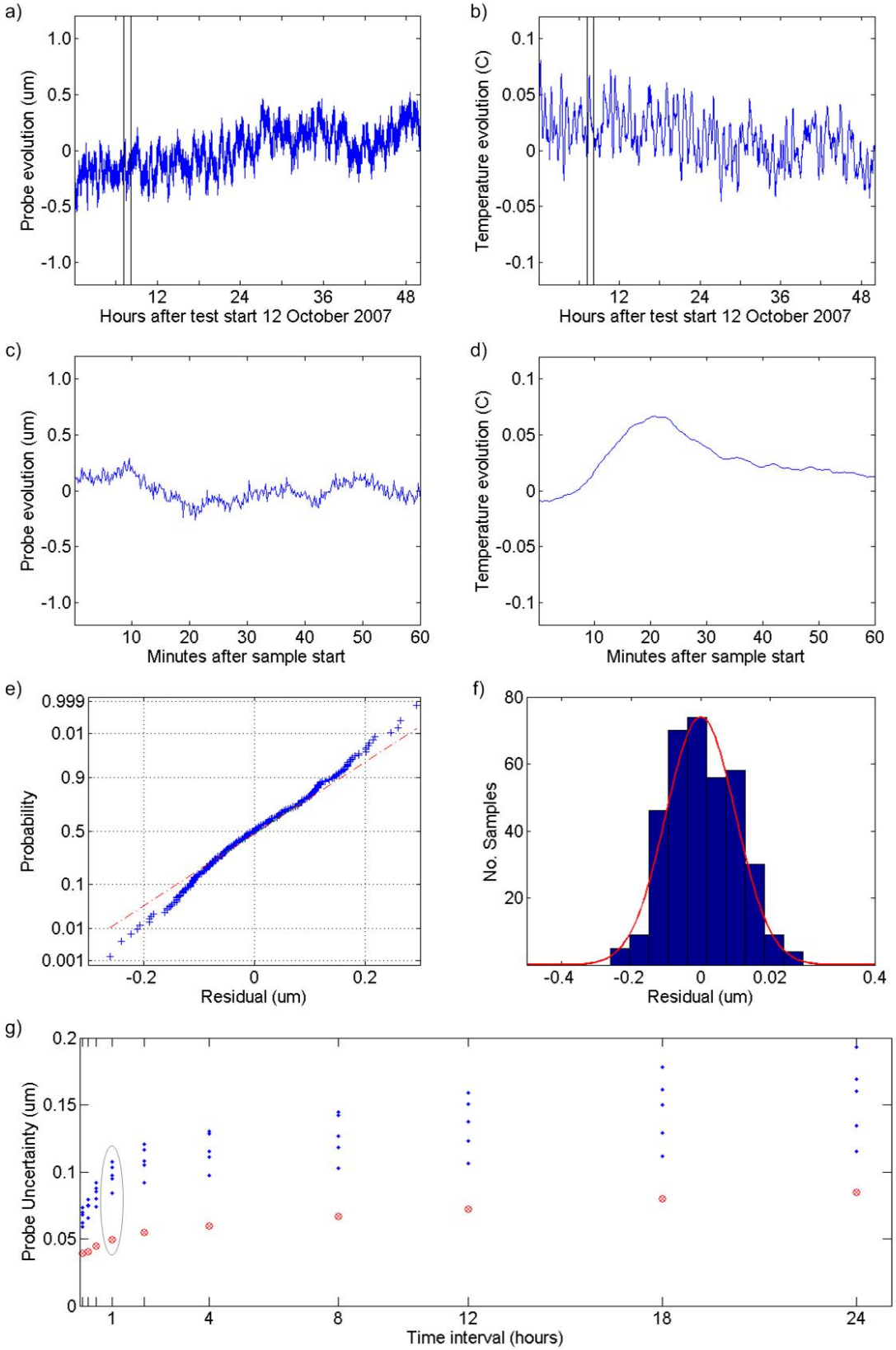

Figure 6.10 Development of the capacitive probe uncertainty model. Graphs a) and b) are the full probe and temperature data sets for one probe. Graphs c) and d) are examples of a 60 minute part of the two data sets. Graphs e) and f) show a normal probability plot and histogram for the probe data and graph g) shows the mean standard deviations for the six probes at 10 time intervals.

Finally, one may construct a non-parametric temporal uncertainty model for the capacitive probes under normal operating conditions of the HCC in its laboratory environment. This model is shown in graph b) of Figure 6.11.

From this model, and Table 6.6, one may conclude that a probe will have an uncertainty of 0.1 μm for periods up to and including one hour. Over this time limit, the uncertainty increases slowly to 0.16 μm for periods up to 24 hours. This type of model will be used again in section 6.5. The final capacitive probe uncertainty for the typical calibration period of 4 hours is given in Table 6.7.

Table 6.6 The temporal uncertainty summary for the capacitive probe data.

Quantity	*PDF*	μ	σ
Probe reading uncertainty (5 minutes)	$N(\mu,\sigma^2)$	0	0.067 μm
Probe reading uncertainty (10 minutes)	$N(\mu,\sigma^2)$	0	0.072 μm
Probe reading uncertainty (30 minutes)	$N(\mu,\sigma^2)$	0	0.084 μm
Probe reading uncertainty (1 hour)	$N(\mu,\sigma^2)$	0	0.098 μm
Probe reading uncertainty (2 hours)	$N(\mu,\sigma^2)$	0	0.109 μm
Probe reading uncertainty (4 hours)	$N(\mu,\sigma^2)$	0	0.117 μm
Probe reading uncertainty (8 hours)	$N(\mu,\sigma^2)$	0	0.128 μm
Probe reading uncertainty (12 hours)	$N(\mu,\sigma^2)$	0	0.137 μm
Probe reading uncertainty (18 hours)	$N(\mu,\sigma^2)$	0	0.148 μm
Probe reading uncertainty (24 hours)	$N(\mu,\sigma^2)$	0	0.157 μm

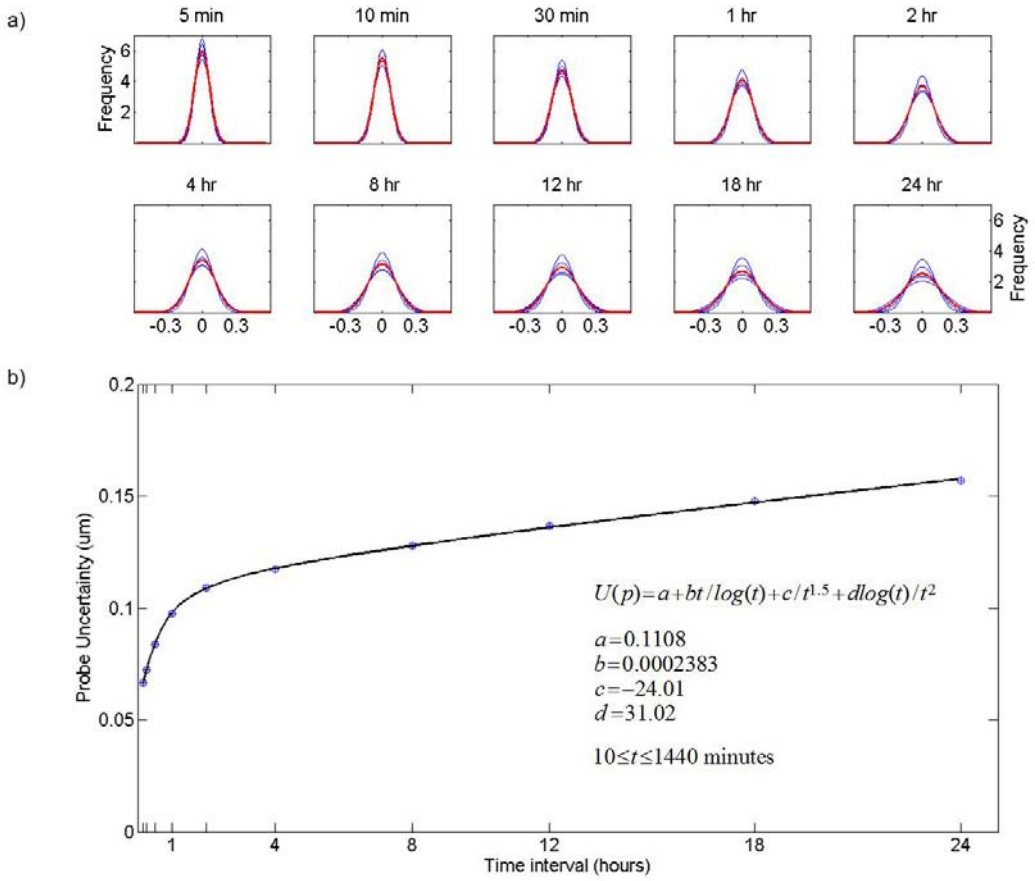

Figure 6.11 Final capacitive probe temporal uncertainty model. Graph a) shows the distributions for the 5 probe data sets at each of the selected time periods t. The bottom graph shows the standard deviations for 250000 samples from these data sets for each of the time periods considered.

Table 6.7 The uncertainty summary for the capacitive probe used with the HCC. The reference time period used is 4 hours. This corresponds to the maximum time required for a typical calibration.

Quantity	*PDF*	μ	σ
Probe reading uncertainty (4 hours)	$N(\mu,\sigma^2)$	0	0.117 µm
Final probe calibration uncertainty	$N(\mu,\sigma^2)$	0	0.029 µm
Final capacitive probe uncertainty	$N(\mu,\sigma^2)$	0	0.121 µm

6.5 LEC uncertainty

As with the capacitive probes, we can construct an uncertainty function for the validation of the LEC. This is done using a boot strap approach. The data discussed in section 5.4 and specifically in Figure 5.22 will be used for this model. Random samples of consecutive data over a given time period from each of the curves of Figure 5.22 graphs a) and c) are used. For

example, given that the mean time between movements is 23.9 seconds; one data set for the four hour period comprises 604 consecutive data points (i.e. $\text{No. pts} \approx (\sim 3600 \times 4)/23.9 = 603$). This sampling is with replacement. In other words a given contiguous data set can be sampled more than one time. The median value of the contiguous data set is subtracted from it. All data samples are concatenated one after the other. Sampling is done in such a way as to limit the number of concatenated data sets to a grand total number of points of approximately one million. We then calculate the standard deviation of this concatenated data set. Using the example 4 hour data set, the total number of points used to calculate the standard deviation is $1658 \times 604 = 1001432$. There are 1658 randomly sampled contiguous data sets. The standard deviation of the concatenated data sets for a given period is represented by one point in each of the graphs of Figure 6.12.

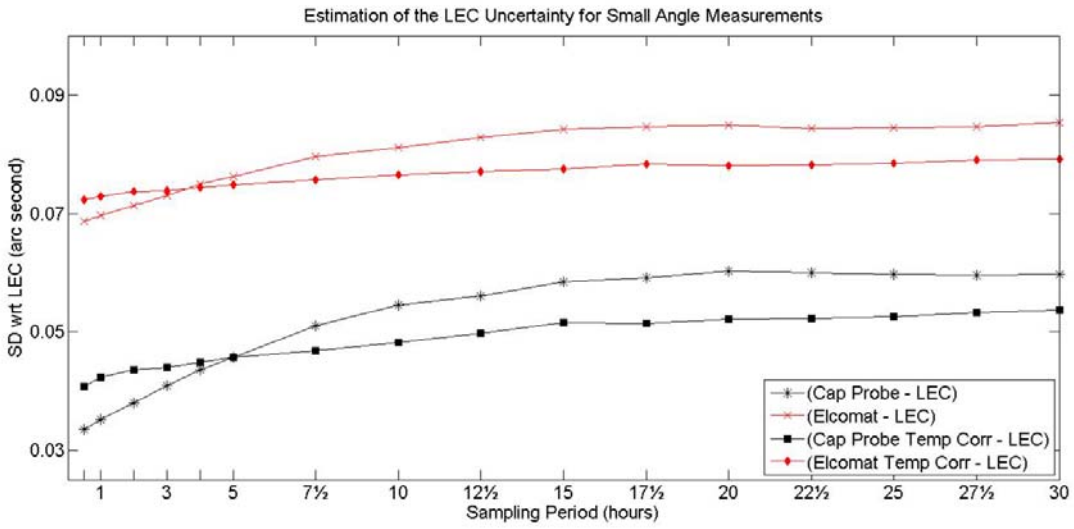

Figure 6.12 Summary of the standard deviations of difference between the capacitive probe and ELCOMAT 3000 angle measurements and the LEC angle measurements with and with out the temperature corrections model of Figure 5.22.

Figure 6.12 shows the temporal uncertainty of the difference between the capacitive probe measurements to a one metre long bar and the LEC angle readings; and the ELCOMAT 3000 angle observations and the LEC angle readings. The points given by the * and × symbols are uncorrected differences between the ELCOMAT 3000 and LEC and capacitive probe and LEC. The points given by the filled squares and circles employ the temperature correction model shown in Figure 5.22.

It is clear that the temperature model is not useful for time periods less than five hours; neither for the ELCOMAT 3000 or the capacitive probe measurements. Above this boundary the temperature correction models permit a considerable amelioration in the uncertainty of the difference with respect to the LEC angles.

The reason the temperature model is not particularly effective for time periods below 4 or 5 hours is because it behaves like a filter and has a smoothing effect that is inefficient over short time periods. For this reason, a combined uncertainty model that employs the best of both the uncorrected and the temperature corrected models is proposed for the capacitive probe LEC differences to establish a baseline uncertainty for the LEC. The results of the capacitive probe experiments are used exclusively here because they are considerably better than those of the ELCOMAT 3000. Furthermore, the capacitive probe measurements are traceable through the laser interferometer calibration, which has itself a calibration certificate delivered by the LNE. The model is given in Figure 6.13. It employs the uncorrected uncertainties up to a period of 5 hours and the temperature corrected uncertainties over this limit. Typical LEC expected uncertainties for different calibration periods and horizontal circle resolutions are given in Table 6.8.

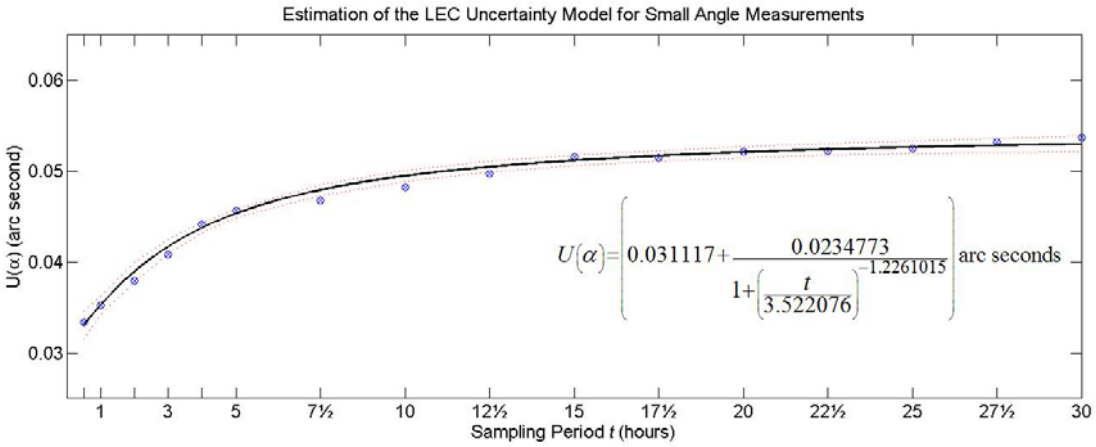

Figure 6.13 Final uncertainty model for the small angle LEC tests using the capacitive probes. The overall standard deviation of the points with respect to the modelled curve is 0.6×10^{-4} arc seconds.

Table 6.8 Expected LEC uncertainty for typical calibration periods and angle resolutions.

Quantity	*PDF*	μ *(arc sec)*	σ *(arc sec)*	*Number of calibration points*	*Calibration angle resolution*
LEC uncertainty (½ hr)	$N(\mu,\sigma^2)$	0	0.033	90	4º
LEC uncertainty (1 hr)	$N(\mu,\sigma^2)$	0	0.035	180	2º
LEC uncertainty (2 hrs)	$N(\mu,\sigma^2)$	0	0.039	360	1º
LEC uncertainty (4 hrs)	$N(\mu,\sigma^2)$	0	0.044	720	1/2°
LEC uncertainty (8 hrs)	$N(\mu,\sigma^2)$	0	0.043	1440	1/4°
LEC uncertainty (12 hrs)	$N(\mu,\sigma^2)$	0	0.050	2160	1/6°
LEC uncertainty (24 hrs)	$N(\mu,\sigma^2)$	0	0.052	4320	1/12°

6.6 Form error – spindle motion error uncertainty

In this section the FESM uncertainty is examined. These results impinge directly upon the determination of the HCC collimation error and the uncertainty of the horizontal angle calibration technique. The FESM technique was introduced in section 4.2. In that section considerable attention was paid to the harmonic suppression (excitation) problem which can have an important influence on the results of the separation. The data gathering and reduction was detailed in section 5.3 where it was explained that with the HCC, five probes are systematically used for each of the radial and face FESM procedures. This provides considerable redundancy. Ten combinations of three probes, five combinations of four probes, as well as the five probe combination can be used for the radial FESM case. Similarly, five combinations of four probes, as well as the five probe combination can be used for the face FESM case.

This section is divided into three parts. The first discusses an assumption in the FESM technique linked the geometry of the setup. This is followed by simulations of errors linked to the separation and the establishment of a PDF for this technique. Finally examples using real data are given.

6.6.1 Discussion of the geometric model approximation used in FESM

The multi-probe error separation techniques make several implicit assumptions. For example with the multi-probe radial error separation, all readings and motions are considered truly radial in the same co-ordinate system. All of the probe axes are assumed to intersect at the same point on the spindle axis of rotation and lie in the same plane thus 'seeing' the same virtual trace on the spindle target. There are similar alignment assumptions concerning the face error separation. All the probes measure along the same circle on the target face and that its circle is at the centre of the rotation axis. Similarly all probe axes have the same orientation as the axis of rotation. In practice it is unlikely any of these assumptions are correct.

The effects of these assumptions on the three probe radial FESM are examined in [126]. This paper derives an exact geometric model for the conventional three-probe method and shows that equation (4.10) given in section 4.2.3.1 is only a first order approximation to it. Therefore, the procedure of eliminating the x and y spindle motion contributions outlined by equations (4.11) and (4.12), does not in fact fully cancel them out. This of course will result in an error in the separation of the form error and the spindle motions using the procedure outlined in section 4.2.3.1.

The procedure used in [126] is to construct so called idealized spindle motions and form errors. These parameters are then input into the equations for the exact geometrical model (refer to [126] for the exact geometric model equations), and the true probe measurements can be derived. The probe measurements are then introduced into the separation algorithm (section 4.2.3.1) which produces the separated form error and spindle motions. These separated form errors and spindle motions can then be compared with the idealized values to determine the conversion error. Precautions are taken to eliminate sources of error and ensure the fidelity the of the separation process.

The main conclusion of this paper is to maintain the error due to the separation or conversion process (i.e. the difference between the separated and idealized form error and spindle motions), to less than 10%, the form error should be at least ten times smaller, and the probe mounting errors should be less than fifty times smaller than the size of the spindle

motion. These results are troubling. In section 5.3.6 it was shown that the HCC measured radial spindle motion is approximately ±3 μm. Translated to the HCC, the results of [126] suggest that form errors and probe alignment must be in the order of 0.3 μm and 0.06 μm respectively.

These conclusions do not conform well to results found in this work. However, both the simulation method used in this thesis to determine the effects of probe and alignment error, and perhaps more importantly, the ratio of the arbour radius to spindle motion r/e_r is fundamentally different to that discussed in [126]. The arbour radius used in [126] is 0.1 mm while the HCC plateau radius is 250 mm. The paper concentrates on arbour radius to spindle motion ratio r/e_r and form error to spindle motion ratio $\Delta r/e_r$ of 10 and 1 respectively. For the HCC, these ratios are 83000 and 3 which may be outside of the models range of applicability.

The results of the simulations below (section 6.6.2) show that indeed there are intrinsic errors in the separation. Intrinsic errors are the difference between the idealized form error input to and the form error resulting from the FESM algorithm (section 4.2.3.1). These errors have already been discussed in 4.2.4.5. Although they could very easily be due to the inexact model used, they are nonetheless two orders of magnitude smaller than the separated spindle error. This appears to be considerably smaller than the effects shown in [126] (i.e. 10%), at least as the author understands them.

6.6.2 Simulation to determine the FESM uncertainty

In this section, the influence of uncertainty in the probe readings and in the probe alignment on the FESM results are investigated using Monte Carlo simulation. This is a different way from [126] of looking at the influence of probe alignment and reading errors. The geometric errors due to the assumptions of the multi-probe FESM techniques dealt with in [126] are implicitly not considered in this treatment.

Probe reading errors are simulated by adding sample errors drawn from the PDF developed in section 6.4 and given in Table 6.7. The probe alignment errors are introduced as error ε_1 in

the probe separation angles $\varphi_1 \cdots \varphi_n$ For example in the radial separation, probe 2 (Figure 4.10) will see the trace drawn out by

$$m_2(\theta) = f(\theta - \varphi_1 + \varepsilon_1) + x(\theta)\cos(\varphi_1 + \varepsilon_1) + y(\theta)\sin(\varphi_1 + \varepsilon_1)$$

rather than that implicitly assigned in equation (4.10).

These errors have a complex effect on the separation results. If more than the minimum three probes are used for the radial separation, or four for the face separation, then each of the probes and the combinations of probes used in the separation will impact differently on the separation results.

In addition to the probe error and the separation angle uncertainty, there is the misalignment of the probes with respect to one another in the vertical plane for the radial error separation and in the horizontal plane for the face error separation. The effect of this misalignment is that none of the probes will see exactly the same trace. This misalignment effect cannot be investigated through simulation but is naturally incorporated into the real measured results discussed in the next section.

The probe misalignment and reading simulations use the radial FESM case. The mean values of the form errors and spindle motions shown in Figure 5.19 are taken as base values. Probe readings for the five probes at angles $(0, \varphi_1, \cdots, \varphi_4)$ are generated using these mean values and equations (4.10) and (4.20). Results are generated by making 500 simulations of the radial FESM developed in section 4.2.3. For each simulation errors are introduced into the probe readings and/or the probe separation angles φ_i. Note that although 500 simulations appears small at first, there are in fact 16×360 values in each one. This corresponds to the 10 three, 5 four and one five probe combinations and the 360 one degree samples around the circle. Thus for 500 simulations, there are nearly 2.9 million samples. It is assumed that all of these samples have the same underlying standard uncertainty. Finally, only results of the radial form error are actually presented here. However, the face form errors as well as the spindle motion results are fully comparable.

Errors for the probe readings were taken to have a standard uncertainty of 0.121 μm (see section 6.4). Probe separation angle is estimated to be 0.05 degrees. This represents a

misalignment uncertainty of the probes with respect to their nominal positions of ±0.1 mm at the 250 mm HCC radius. The results of one of 500 such simulations are shown in Figure 6.14.

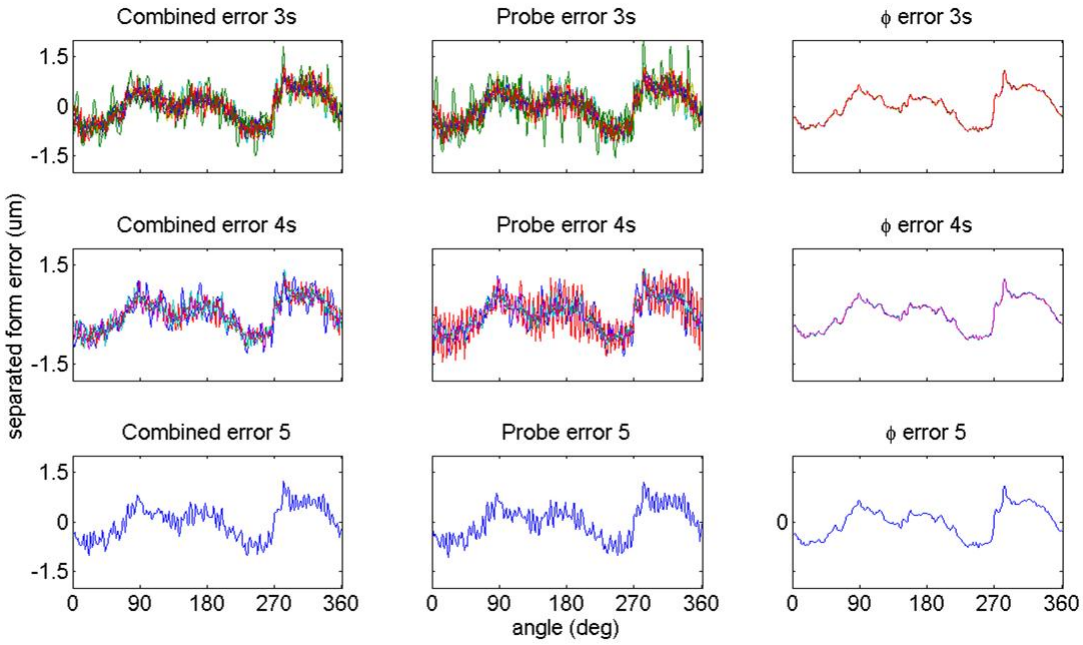

Figure 6.14 The effects of introducing error into the FESM process. On the top row, the effects (from left to right) of the combined probe reading and separation angle φ_i errors, probe errors alone and probe separation angle errors alone, on the separated form error from the 10 combinations of three probes in the radial separation. The second row gives the same results for the 5 combinations of 4 probes and the bottom row the results for the five probe combination. The reference form error (top graph in Figure 5.19) resembles closely that of the three right hand graphs.

This figure shows that under the uncertainty conditions described above, the probe reading errors dominate the results of the separation. These results are very similar to those developed in section 4.2.4 and it is presumed that the harmonic excitation developed in detail in this section is the principal underlying generator of the errors in the FESM techniques. This will be investigated next.

As we shall see in the next section, real results resemble closely the simulated ones shown in Figure 6.14. The values adopted for the final form errors and spindle motions of the HCC are the median values of all of the combinations of the separation results. For example, with the radial separation, this involves 16 determinations of the form error and spindle motions (i.e. 10 combinations of three probes, 5 combinations of four probes and one five probe determination). This approach is used because it employs the maximum redundancy of the data, and, although these different determinations are not fully independent, they do give

(sometimes very) different results. The median is also a more robust estimation of central tendency. Highly asymmetric extreme values can shift the mean but have little influence on the median. This is important given the sometimes large fluctuations of certain probe combinations.

Finally, the so-called intrinsic error in the separation has been investigated. Recall this is the separation error in the FESM without error being injected into either the probe readings or the probe separation angles φ_i. Theoretically this error should be zero. In section 4.2.4.5 and specifically in the top graph of Figure 4.20 it was found to have a highly characteristic saw tooth form. In the cases of the simulations studied here, the residual error no longer has this regular form. However, its magnitude remains comparatively small and extremely constant (0.002±0.00003 μm peak to peak) for the 16 cases inspected (i.e. 3 probe, 4 probe and 5 probe separation).

Table 6.9 Standard uncertainties in of the separation errors with respect to the different probe combinations in the radial FESM.

Error contribution	*Standard deviation with respect to the reference form error (μm)*			*Standard deviation of median values with respect to the reference form error (μm)*		
	Threes	*Fours*	*Five*	*Threes*	*Fours*	*All*
Probe error	0.191	0.180	0.216	0.088	0.122	0.084
φ error	0.006	0.005	0.010	0.003	0.004	0.003
Combined error	0.206	0.176	0.229	0.088	0.119	0.084

Results of the different combinations with respect to reference form error are given in Table 6.9. The standard deviations are given of the differences between the form errors determined using the different combinations of probes and the reference form error (i.e. the mean of the top graph of Figure 5.19) on the one hand (the three left hand columns); and the difference between the median values of the different probe combinations, and the reference form error on the other (the three right hand columns).

The three left hand columns of Table 6.9 give an estimate of the standard deviation of the separation error (i.e. separated form error – reference form error) associated with the radial

FESM for the different probe combinations and uncertainty conditions described above. The three right hand columns give an estimate of the standard deviations of the 'best estimate' of the form error derived from the median values of the different probe combinations. Three cases are examined; first where there is only probe error introduced into the probe reading (Probe error), second when there is only error introduced into the probe separations angle (φ error) and third, the comprehensive case when both errors are employed.

Once again it is clear that the probe errors dominate the separation results. Surprisingly, overall, the combinations of three probes appear to better determine the form error than the combinations of four probes and the combinations of five probes. The results in the three right hand columns suggest that using all of the 16 combinations is slightly better than using the median of the 10 three probe combinations. However, this is not the whole story. The PDFs differ (strongly) from Gaussian: although fairly symmetric, they have high kurtosis. Thus, standard deviation from the mean is not necessarily a good measure of spread.

Figure 6.15 shows the distributions of the residuals issued from the difference between the calculated (separated) form errors and the reference form error for the different combinations of probes discussed above. These graphs also show distribution fits for these data. The black curves are Gaussian distribution fits while the red curves are Student's *t*-distribution fits.

In all cases the Student's *t*-distribution better represents that data than the Gaussian distribution. This is because for all cases the residual distributions between the separated form error and the reference form error have very long tails. These tails are due to the punctual extreme values which are postulated here to be due to the harmonic effects intrinsic to the FESM techniques discussed at some length in section 4.2.4. Nevertheless, it is clear from Figure 6.15 that the effects of the tails diminish as the number of probes used in the separation increases. Actual values for these distributions are given in of Table 6.10.

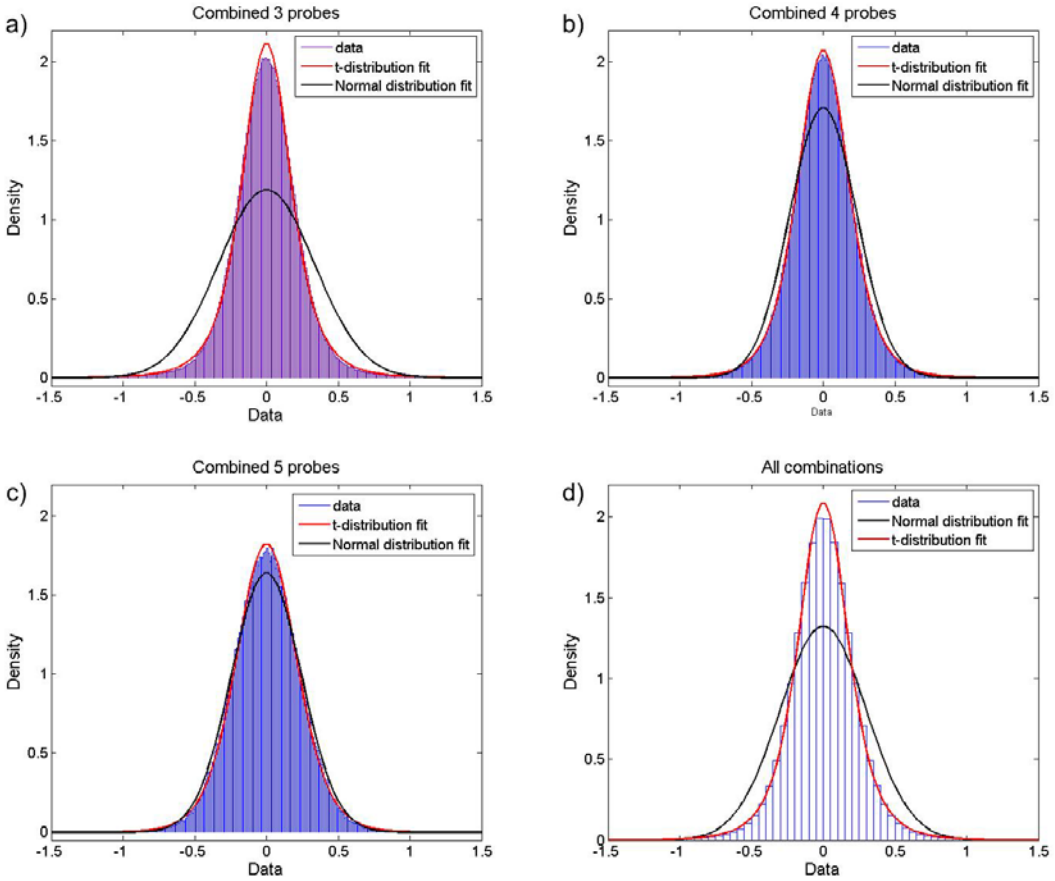

Figure 6.15 These histograms show the PDFs of the residuals of the form errors issued from the previous simulations with respect to the reference form error (i.e. the mean value of the form errors – top graph of Figure 5.19). Histogram a) is the PDF for the combinations of three probes differences; histogram b) the PDF for the combinations of four probes; histogram c) the five probe differences and histogram d) the combination of all combinations (i.e. the amalgamation of 3, 4 and 5 probes). The red curves show a Student's *t*-distribution fit[39] and the black curves show a Normal distribution fit to the data.

Fig 6.14 (and Table 6.10) emphasises that the Gaussian distributions do not express well the spread. Table 6.10 shows that standard deviation on the mean (which is based on a Gaussian model) overestimates the spread in these cases, at least for the purposes of uncertainty assessment according to the GUM.

[39] The fit is actually made using the Matlab routine t Location-Scale Distribution in the distribution fitting toolbox dfittool, which is part of the Statistic toolbox. The Statistic toolbox manual states "The *t* location-scale distribution has the density function

$$\frac{\Gamma\left(\frac{\nu+1}{2}\right)}{\sigma\sqrt{\nu\pi}\,\Gamma\left(\nu/2\right)}\left[\frac{\nu+\left(\frac{x-\mu}{\sigma}\right)^2}{\nu}\right]^{-\left(\frac{\nu+1}{2}\right)}$$

with location parameter μ, scale parameter $\sigma > 0$, and shape parameter $\nu > 0$. If x has a *t* location-scale distribution, with parameters μ, σ and ν then $\frac{x-\mu}{\sigma}$ has a Student's *t* distribution with ν degrees of freedom."

Table 6.10 Parameters for the Normal ($N\left(\mu,\sigma^2\right)$) and Student's *t* distribution $t_\nu\left(\mu,\sigma^2\right)$ (Matlab t Location-Scale distribution – see footnote 39 on page 219).

Quantity	*PDF*	μ *(μm)*	σ *(μm)*	ν *(dof)*
3 probe combinations	$N\left(\mu,\sigma^2\right)$	0	0.335	-
4 probe combinations	$N\left(\mu,\sigma^2\right)$	0	0.233	-
5 probes	$N\left(\mu,\sigma^2\right)$	0	0.243	-
Amalgamated 3, 4,and 5 probes	$N\left(\mu,\sigma^2\right)$	0	0.302	-
3 probe combinations	$t_\nu\left(\mu,\sigma^2\right)$	0	0.175	3.719
4 probe combinations	$t_\nu\left(\mu,\sigma^2\right)$	0	0.184	5.469
5 probes	$t_\nu\left(\mu,\sigma^2\right)$	0	0.212	8.795
Amalgamated 3, 4,and 5 probes	$t_\nu\left(\mu,\sigma^2\right)$	0	0.179	4.208

Figure 6.15 (and Table 6.10) emphasises that the Gaussian distributions do not express well the spread of these distributions, and in particular the spread of the combinations of three probes and the amalgamation of the 3, 4 and 5 probe cases. Table 6.10 shows that standard deviation on the mean (which is based on a Gaussian model) overestimates the spread in these cases, at least for the purposes of uncertainty assessment according to the GUM. Note that for the amalgamated case, the 10 three probe combinations provide a dominating weight factor and so this case resembles closely the three probe combinations one.

6.6.3 Form error – spindle motion separation real data and resonance effects

These FESM data were investigated using the techniques developed in section 4.2.4 and in particular using the vicinity graphs of φ_1 and φ_2 shown in Figure 4.19. The results of this study for one set of real radial probe error data are shown in Figure 6.16.

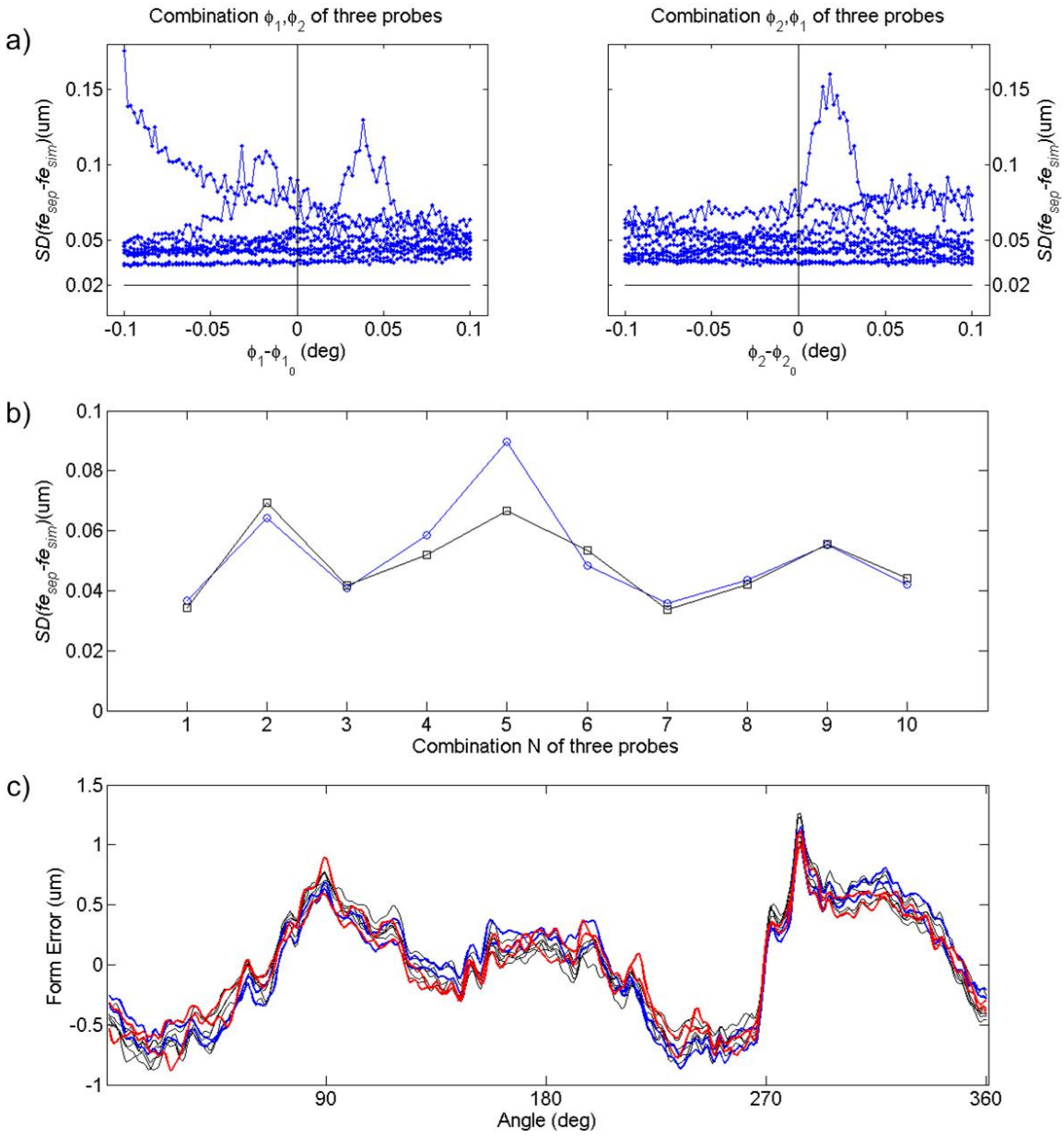

Figure 6.16 Results of the vicinity studies on real HCC plateau probe separation data based on the techniques developed in section 4.2.4. The top graphs are the equivalent of the vicinity graphs of φ_1 and φ_2 shown in Figure 4.19. However for the sake of space all 10 curves are superposed on one another. This is done by subtracting the nominal values for φ_1 and φ_2. The black horizontal lines in these graphs represent the standard deviation of the simulated probe reading errors used. The middle graph is a resume of these graphs showing the values for $SD\left(fe_{sep} - fe_{sim}\right)$ at the nominal angles φ_1 and φ_2. In the bottom graph, the two largest values of $SD\left(fe_{sep} - fe_{sim}\right)$ (i.e. index by 2 and 5 in the middle graph) are plotted in red while the two smallest values (1 and 7) are plotted in blue.

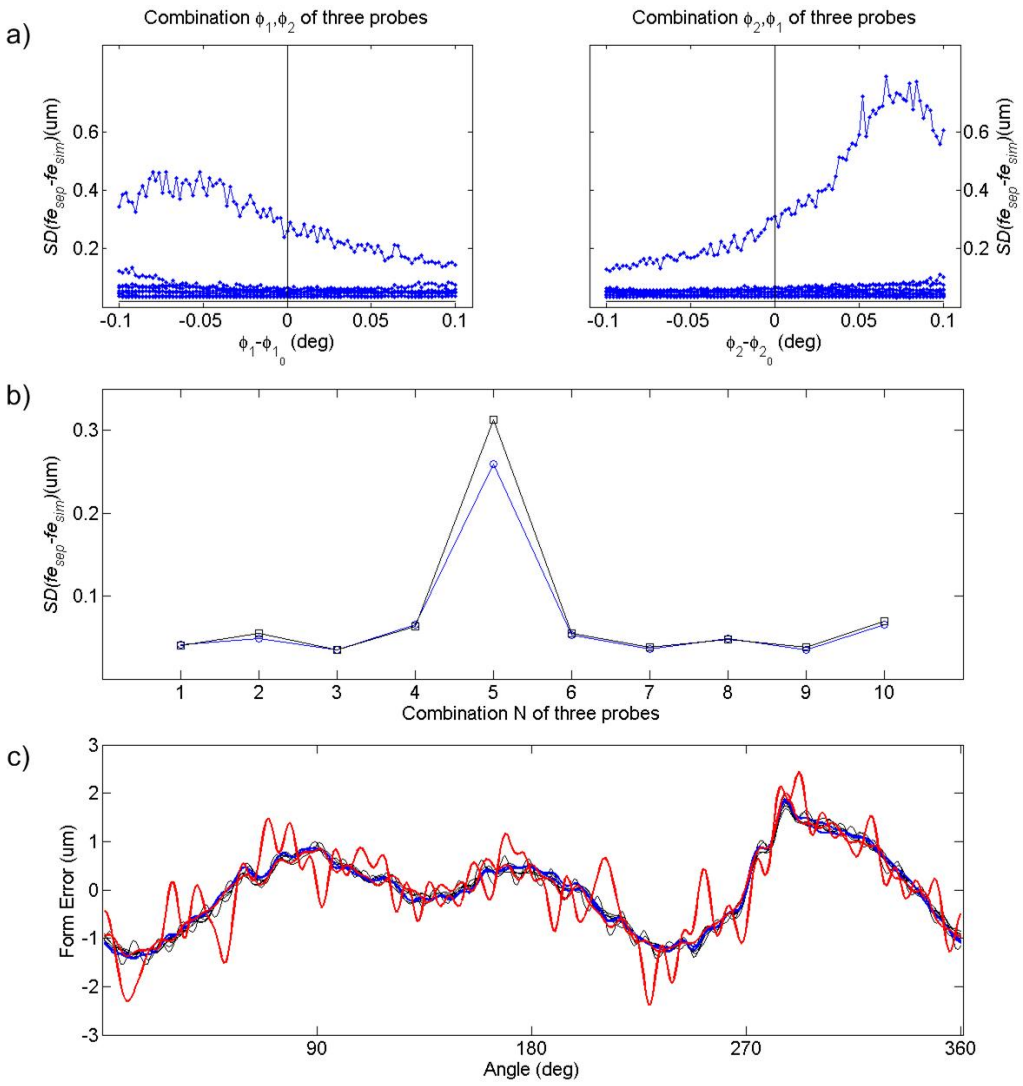

Figure 6.17 Vicinity graphs of real data once again. However, this time there are real resonant effects with the fifth combination of angles 0, $\varphi_1 = 119.843$ and $\varphi_2 = 279.900$. In this case there is a clear harmonic effect apparently due to the placement on the shoulder of a peak.

What is clear in the bottom graph of Figure 6.16 is that there is no resonance influence due to the values of φ_1 and φ_2 in this data. Neither of the 'worst case' nor the 'best case' data sets stand out as being different from each other; nor from the other six data sets for that matter. This is not surprising given the values of the probe separation angles (0.000, 46.705, 123.205, 191.799, 278.894 degrees); none of which have small k values. In the top graph, we see there are small peaks nearby. Indeed if the values of φ_1 and/or φ_2 are changed slightly, we see resonant effects in the separated form error.

A second case where the probe separation angles are (0.000, 56.200, 119.843, 189.594, 279.900 degrees) is given in Figure 6.17. In this case one probe angle combination (0, $\varphi_1 = 119.843$ and $\varphi_2 = 279.900$) results in strong harmonic excitation. Nevertheless, for this

combination of angles, $k \gg 180$, the cut-off frequency. The bottom graph (c) of this figure illustrates why the median values for the 16 form errors and spindle motions are preferred as output from this technique.

6.7 Laboratory refraction

The temperature regime of the angle calibration laboratory is highly regular. Recall form section 3.7.2, laboratory temporal and spatial temperature variations are in the order of ±0.1 Celsius and ±0.9 Celsius respectively. To evaluate an order of magnitude of the effects of refraction, a three dimensional grid 4m (length) by 4m (width) by 3m (height) of temperatures in the laboratory was measured. Pressure and humidity gradients are assumed to be zero.[40] Thermocouples were positioned at regular intervals within this volume. The aim of this experiment was to derive representative refraction corrections based on (3.11).

The main experiment consisted of moving a 'tree' equipped with 16 sensors to 23 positions (stations) based on a regular grid system around the laboratory. The 'tree' consisted of four sets of four 0.5 m long 'branches' set at 90 degree intervals and heights of 0.2 m, 1.0 m, 2.01 m and 2.98 m above the floor level. It was left in position at each of the 23 stations for periods ranging between 4 and 60 hours over the thirteen day study period.

Temperatures and their horizontal and vertical gradients are interpolated between thermocouples to representative lines of sight within the laboratory. Five lines of sight are shown on the right hand volumetric graph of Figure 6.18. The derived corrections for IFM distances and horizontal and vertical observed angles for nine lines of sight; the five shown in Figure 6.18 and four others to each of the corners of the volume cube, are given in Table 6.11. They indicate that the effect of refraction on both horizontal and vertical angles is very small. Distance errors in the order of 1 ppm, on the other hand, are significant.

[40] Although no formal attempt has been made to measure pressure and humidity gradients in the HCC – VCC laboratory, measurements were made at the ESRF distance meter calibration bench (DCB) in the cadre of the COFRAC accreditation. Within the calibration tolerance of the instruments used, no horizontal pressure or humidity gradients were detected over the 50 m bench. With these tests in mind, it is assumed that pressure and humidity gradients are small. Indeed employing the so-called barometric formula which relates change in pressure to change in altitude on the earth's surface indicates there is no perceptible change in pressure for the 2 to 3 m height difference encountered in the laboratory. As far as the humidity is concerned, one can assume constant mixing of the atmosphere and its constituents within the relatively small volume of the laboratory.

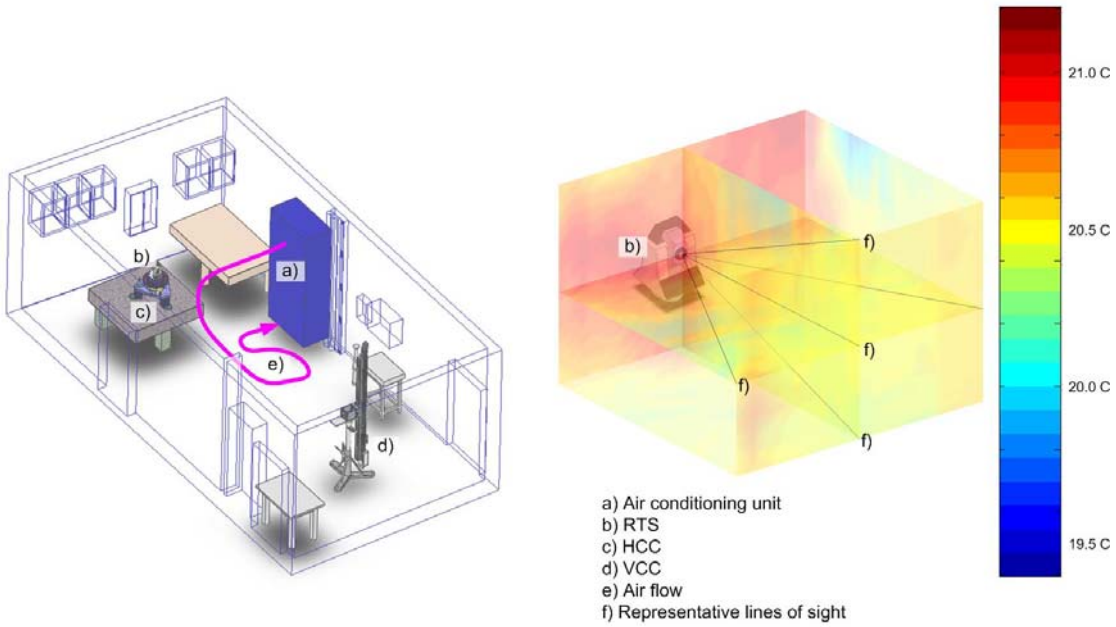

Figure 6.18 Temperature profile of the laboratory in which the HCC and VCC are installed. Spatial variations can reach ±0.9 Celsius, largely due to the air conditioning unit.

Table 6.11 Representative refraction corrections for IFM distances, horizontal and vertical angles through representative lines of sight with in the laboratory.

	IFM correction (ppm)	*IFM correction (μm)*	*Horizontal angle correction (arc-sec)*	*Vertical angle correction (arc-sec)*
	-0.90	-3.61	-0.03	-0.01
	-0.90	-3.59	-0.02	-0.01
	-0.89	-3.56	-0.02	0.00
	-0.98	-3.90	-0.03	0.01
	-0.91	-3.63	-0.03	0.01
	-0.85	-3.39	-0.02	0.01
	-0.94	-3.75	-0.02	0.03
	-0.88	-3.51	-0.03	0.01
	-0.85	-3.39	-0.02	0.02
Mean	-0.90	-3.60	-0.03	0.01
Standard deviation	0.04	0.16	0.01	0.01

6.8 HCC SMS horizontal angle calibration uncertainty evaluation

A schematic of the horizontal angle calibration process is shown in Figure 6.19 . It provides an overview and reminder of the calibration data gathering and analysis steps. The left hand part of this figure is discussed in section 3.4. The right hand side is discussed in chapter 5. This section is concerned with the uncertainty evaluation of the HCC. In the past four sections, the uncertainty of important component parts have been reviewed. These are, the capacitive probes used in the FESM techniques which establish the plateau motions and the HCC collimation error, the LEC angle standard, and the laboratory refraction effects. These results will be used in this section. However before progressing to the actual uncertainty calculation, we must investigate one last parameter regarding the HCC when it is used to calibrate the horizontal angles of SMS instruments. This is the HCC induced SMS instrument horizontal angle collimation error CE_{SMS} .

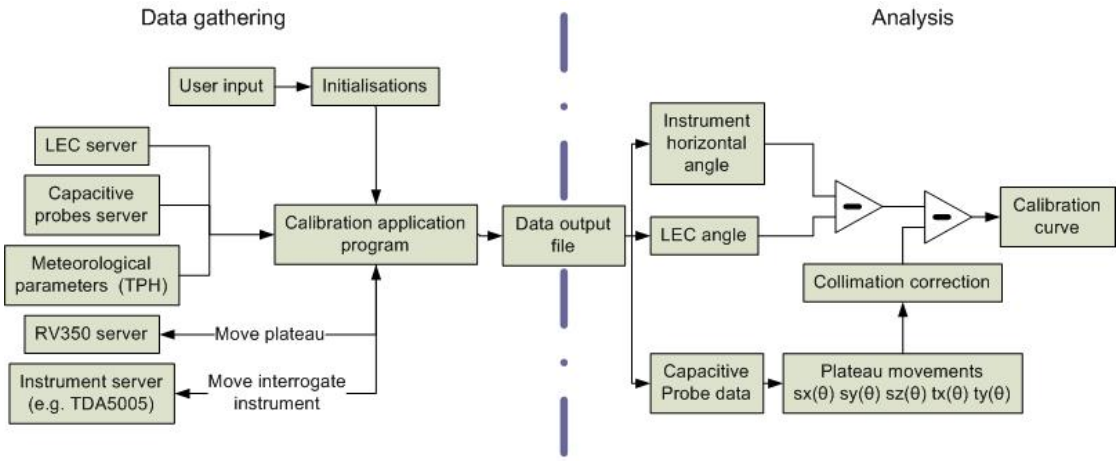

Figure 6.19 Overview of the horizontal angle calibration process.

6.8.1 HCC induced SMS instrument horizontal angle collimation error

Under normal operating conditions, all systematic errors are corrected within the limits of the instrument's precision and capabilities. This was discussed in section 3.1 and particularly with respect to angle errors in section 3.1.4. However, because the HCC causes the instrument being calibrated to rotate about its own axis, collimation axis errors (see section 3.1.4.1) are reintroduced into the instrument readings. These collimation axis errors will be referred to as SMS instrument horizontal angle collimation errors or CE_{SMS} . They are not to be confused with, and are in addition the HCC collimation error CE_{HCC} , discussed in 5.5.8.

The mechanics of horizontal angle collimation axis error is well known. It is nicely described in [15]. Referencing Figure 6.20 and quoting from this book (pp 127 and 128): "The influence (c) of the collimation axis error c on a direction observed in one telescope position when sighting to a point P at a vertical angle β (zenithal angle $\varsigma = \pi/2 - \beta$), can be derived with the aid of a semi sphere (Figure 6.20). Because of the error c, the collimation axis is not normal to the horizontal axis KK' and thus does not move within the plane CZC' when the telescope is tilted. It follows a conical path, which intersects the semi-sphere in a circle passing through D', P, Z' and D''. If $Z'S$ were normal to KK', the plane ZQC, normal to the horizontal axis would coincide with the plane ZPD. This is not the case because of c. Instead, ZPD is turned in respect to the normal section by the angle $CSD = (c)$, which is the influence of the collimation axis error c on the value for P to be read at the horizontal circle. To determine (c), one places a great arc $KPQK'$ through P, normal to ZQC. According to the orthogonal spherical triangle: $\sin c = \cos\beta \sin\gamma$ and, since c and γ are small: $c = \gamma \cos\beta$. Since $\gamma = DSC = (c)$, it is obtained as

$$(c) = \frac{c}{\cos\beta} \text{ or } (c) = \frac{c}{\cos\varsigma} \text{ where } \varsigma \text{ is the zenital angle}"$$

This equation shows that the influence of c is smallest on horizontal sights (i.e. when $\beta = 0$) and is equal to c. This is exactly the case with the HCC where all sights are very close to horizontal ($\ll \pm 1$ degree). As was mentioned in section 3.1.4.1, this error is normally eliminated by observing in face left and face right positions of the telescope. However, because the instrument is turning about the HCC primary axis, it is inherent to the HCC.

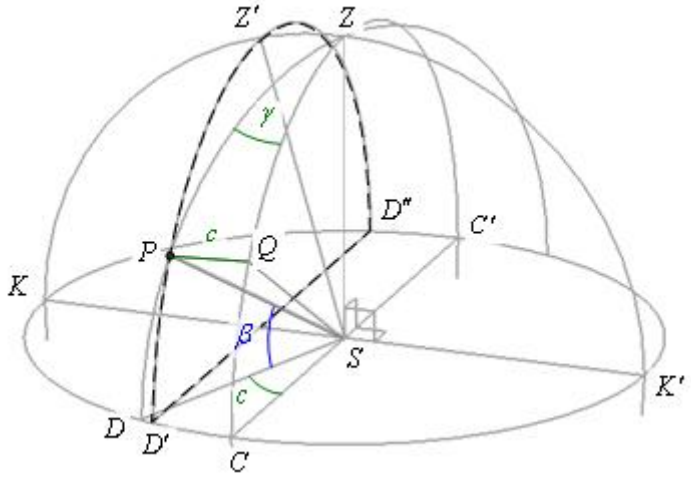

Figure 6.20 Influence of collimation axis error on horizontal angle observations made with SMS instruments (after figure 333 [15]).

This HCC induced horizontal collimation axis error is straightforward to calculate. The correction depends upon the rotation of the instrument due to HCC tilts in the direction perpendicular to the sighting axis. This will be referred to as movement along the x axis. The collimations axis points along the y axis. A point 50 mm below the HCC plateau is estimated to be the centre of rotation (inclination) about the HCC's x and y axes. The magnitude of the movement along the x axis at the instrument collimation axis height, with respect to the origin position $x_i - x_0$, is determined using the HCC spindle motions and the instrument collimation axis height H above the HCC centre of rotation about x and y axes, as input to the HTM routine (sections 4.3 and 5.5.8). The inclinations are typically very small (i.e. < 2.5 arc seconds see Figure 1.1) justifying the small angle approximation. HCC horizontal angle collimation axis error CE_{SMS} is then calculated using:

$$CE_{SMS} = c = \tan^{-1}\left(\left(x_i - x_0\right)/H\right) \cong \left(x_i - x_0\right)/H$$

The final correction of the instrument horizontal angle reading is determined by adding this error (i.e. the HCC induced horizontal collimation angle error) to the collimation error discussed in section 5.5.8.

$$CE_{total} = CE_{HCC} + CE_{SMS} \tag{6.7}$$

6.8.2 Example calibrations

The HCC SMS horizontal angle calibration uncertainty evaluation requires several calibrations of the same instrument to establish a Type A uncertainty for the classical GUM uncertainty framework. These calibrations are presented here.

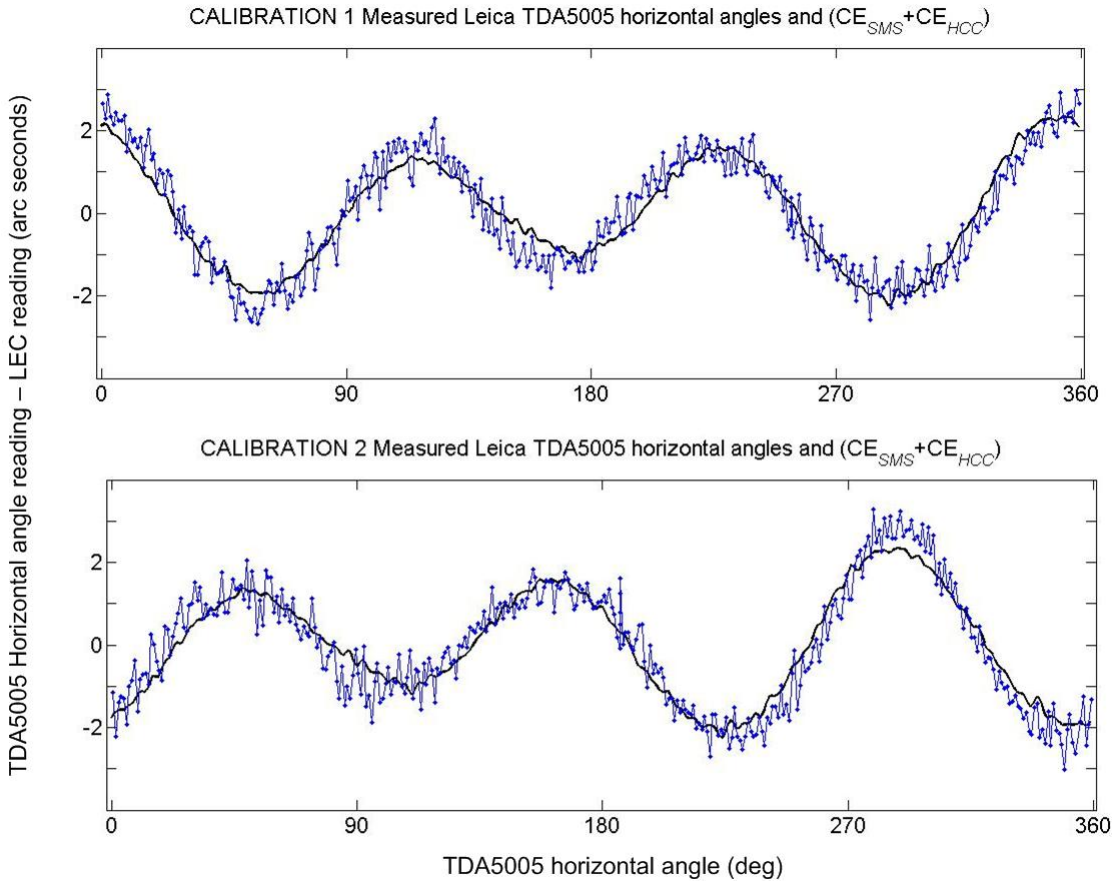

Figure 6.21 Two independent calibration curves with two different shim positions. The horizontal axis gives the TDA5005 horizontal angle position with respect to its zero position[41]. The black solid line gives the combined collimation error while the blue points give the difference between the TDA5005 horizontal angle readings and the LEC reading.

The instrument used for this work is a Leica TDA5005 serial number 438679. The calibration data set consists of 13 independent instrument calibrations. Each calibration consisted of making measurements in the following sequence:

$$\text{Series no. 1} \quad (0°, 1°, 5°, 9°, \cdots, 357°, 360°, 359°, 354°, \cdots, 7°, 3°, 0°)$$
$$\text{Series no. 2} \quad (0°, 2°, 6°, 10°, \cdots, 358°, 360°, 356°, 352°, \cdots, 4°, 2°, 0°)$$

Therefore the calibration visits every degree of the instrument in two series of 4 degrees steps between 0 and 360 degrees. Two example calibrations are shown in Figure 6.21.

[41] Note that the TDA5005 circle zero can be reset at any time. Therefore the zero position is arbitrary. This must be accommodated if a calibration curve is used to correct the instruments horizontal angle readings.

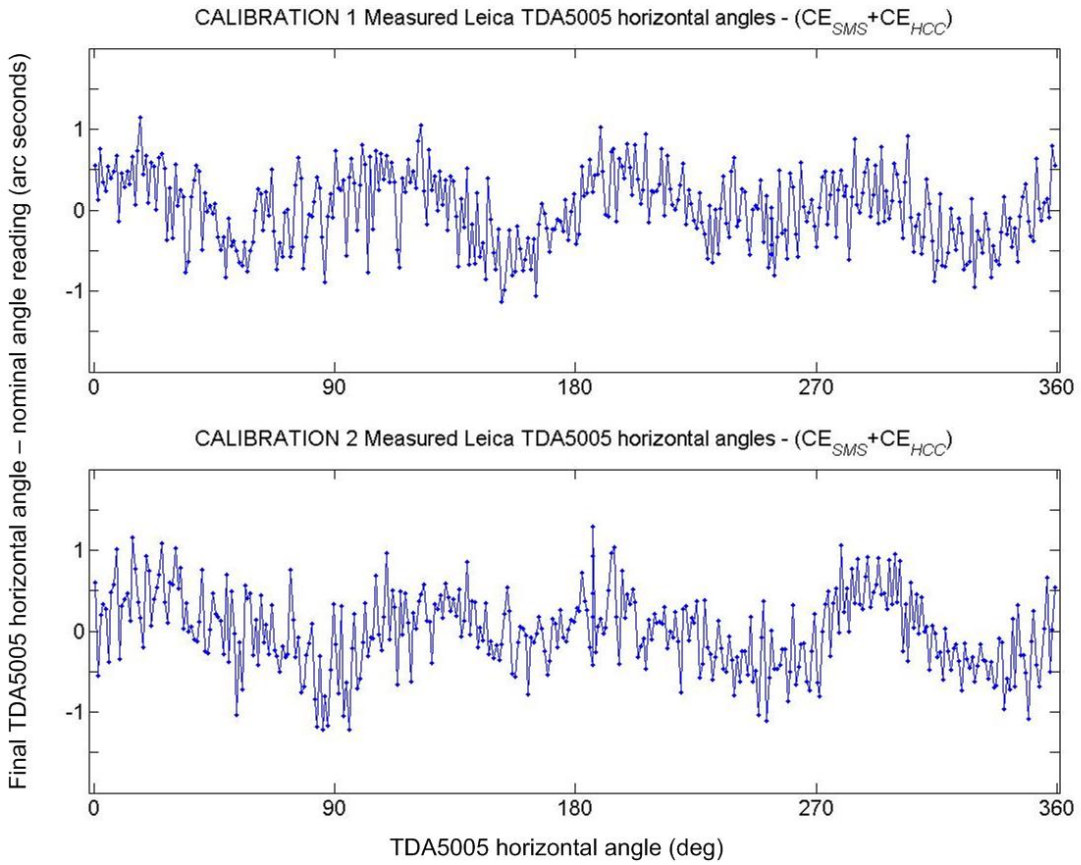

Figure 6.22 The residual errors of the TDA5005 horizontal angle readings minus the LEC readings minus the combined collimation error for the calibration example presented in Figure 6.21 above. These curves represent the final calibration corrections to be added to the nominal horizontal angle readings referenced to the instruments horizontal angle zero position.

The Leica TDA5005 is fixed to a tribrach. The tribrach has a threaded bore and is itself screwed onto the HCC adaptor support. The problem is that this will ensure that the tribrach is always (more or less) orientated in the same direction when installed on the HCC. To ensure the independence of the calibration results, a set of shims were made so that when the tribrach is screwed onto the HCC support, it assumes a different orientation with respect to the base orientation as a function of the shim thickness. This in turn ensures that a different part of the RTS instrument circle is oriented towards the SMR in the HCC zero position. Four shims with the base position ensure five different orientations each taken at least twice for the 13 calibrations. Two example calibration; one without a shim and one with a shim causing a phase shift of approximately 180 degrees, are shown in Figure 6.21. The final calibration curves are shown in Figure 6.22. These graphs represent the corrections to apply to the nominal horizontal angle readings.

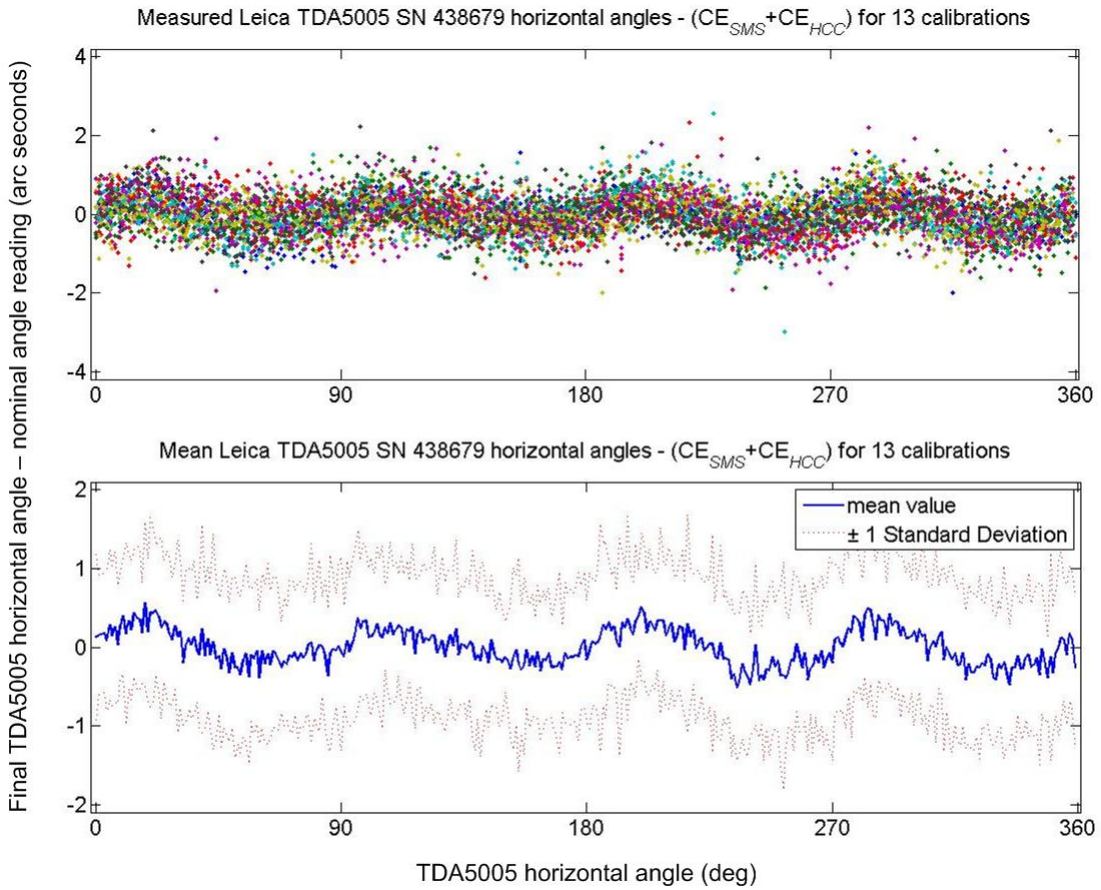

Figure 6.23 Resume of the 13 calibration curves made for the Leica TDA5005 serial number 438679. The top graph shows the residuals of al 13 calibrations the TDA5005 horizontal angle readings while the bottom graph shows the mean values and curves for the mean values ± one standard deviation.

The graphs in Figure 6.21 and Figure 6.22 show results for two of the 13 calibrations made. Figure 6.23 shows a summary of the curves for the 13 calibrations. The residuals in these graphs are the differences between the instrument horizontal angles and the horizontal angle issued from the HCC and corrected for the collimations errors CE_{HCC} and CE_{sms}. They are given by:

$$res_{ha\ i} = ha_{meas\ i} - \left(LEC_i + CE_{HCC} + CE_{SMS}\right)_i$$

The top graph shows the residuals of the instrument horizontal angle readings for each of the 13 calibrations. The bottom graph of this figure shows a summary of the curves in the form of the mean value and standard deviation for each degree between 0 and 359 degrees of nominal instrument horizontal angle reading. These summary statistics are used in the establishment the calibration uncertainty in the next section.

6.8.3 HCC uncertainty

The development of an explicit functional model for the HCC is not simple. For this reason, the determination of the uncertainty of the HCC calibration will use the GUM1 framework. (refer to section 6.2.2 and [112]) Nevertheless, there is a type of 'default' way in which to apply the classical GUM uncertainty framework to this type of calibration. This approach will be discussed first.

6.8.4 Classical GUM uncertainty framework approach

The functional model for classical GUM uncertainty calculation approach to the HCC following is given in (6.8).

$$\delta = ha_{\text{measured}} - ha_{\text{modelled}} \tag{6.8}$$

This is actually really no different that the normal approach except that no sensitivity coefficients (i.e. partial derivatives) are formed for the ha_{modelled} term. This approach still remains within the 'spirit' of the GUM. Section 4.1.2 of the GUM states: "The input quantities $X_1, X_2, \cdots$, upon which the output quantity Y depends may themselves be viewed as measurands and may themselves depend on other quantities, including corrections and correction factors for systematic effects, thereby leading to a complicated functional relationship f that may never be written down explicitly. Further f may be determined experimentally (see 5.1.4) or exist only as an algorithm that must be evaluated numerically. The function f as it appears in the Guide is to be interpreted in this broader context, in particular as that function which contains every quantity, including all corrections and correction factors, that can contribute a significant component of uncertainty to the measurement result." [111].

With this approach, the modelled values are subtracted directly from the measured values and a standard uncertainty determined, typically from repeated measures at the same point. This is a classical Type A uncertainty. All other contributions that can reasonably be included in the uncertainty calculation are then added (square root of the sum of squares contributions) as Type B uncertainties. A list of the contributions for the HCC is given in Table 6.12. These

contributions assume a calibration time inferior to 4 hours. The uncertainty calculation is completed by adding as root sum of squares the Type A and Type B contributions.

Table 6.12 Summary of the different uncertainty contributions to a HCC horizontal angle calibration. The time taken for the calibration is assumed to be inferior to 4 hours.

Ref	*Quantity*	*PDF*	μ	σ
$B_{HCC\ 1}$	LEC $U(LEC)$	$N(\mu,\sigma^2)$	LEC_{meas} arc sec	0.044 arc sec
$B_{HCC\ 2}$	Refraction $U(E_{refraction})$	$N(\mu,\sigma^2)$	$E_{refraction}$ arc sec	0.01 arc sec
$B_{HCC\ 3}$	HCC collimation correction $U(CE_{HCC})$	$N(\mu,\sigma^2)$	CE_{HCC} arc sec	0.012 arc sec
$B_{HCC\ 4}$	HCC induced horizontal angle collimation correction $U(CE_{SMS})$	$N(\mu,\sigma^2)$	CE_{SMS} arc sec	$\frac{0.046}{H}$ arc sec

The uncertainties in Table 6.12 are derived from: section 6.5 for the LEC uncertainty $U(LEC)$, section 6.7 for the refraction uncertainty $U(E_{refraction})$, and section 6.6 Table 6.9 for the collimation error uncertainties $U(CE_{HCC})$ and $U(CE_{SMS})$. The HCC induced horizontal angle collimation correction CE_{HCC} must be divided by the height H in m above the HCC centre of rotation about x and y axes. Note that the uncertainties used here for the spindle motion uncertainties are those given in Table 6.9 under the heading 'Standard deviation of median values with respect to the reference form error' and column heading 'All'. These are considered the most representative values for the spindle motion uncertainties.

The collimation error uncertainties are determined by simulation. Ten thousand determinations of the collimation errors are made by introducing random error into each of the spindle motions (i.e. $sx(\theta), sy(\theta), sz(\theta), wx(\theta)$ and $wy(\theta)$) and calculating the collimations errors CE_{SMS} and CE_{HCC}. Once again the number of simulations is limited by time and resources. However, these uncertainties represent the standard deviations of 10000×360 or 3600000 values once again all samples have the same standard uncertainty.

The standard deviation of the Type A determinations is derived from the results presented in Figure 6.23. The overall standard deviation with respect to the mean values determined at one degree intervals between 0 and 359 degrees is 0.47 arc seconds. The overall standard deviation of the residuals of Figure 6.23 (i.e. not subtracting the mean value) is 0.50 arc seconds. The manufacturers stated uncertainty for the horizontal angles for this instrument is 0.5 arc seconds.

From these results and the ones in Table 6.12, we are now in a position to calculate the GUM uncertainty for this type of calibration (6.9).

$$\begin{aligned} u_c &= \sqrt{\sum(\text{Type B})^2 + \sum(\text{Type A})^2} \\ &= \sqrt{0.04^2 + 0.01^2 + 0.01^2 + \left(\frac{0.05}{0.41}\right)^2 + 0.47^2} \\ &= 0.49 \text{ arc seconds} \end{aligned} \qquad (6.9)$$

$$\begin{aligned} U &= \pm 2u_c \\ &= \pm 0.98 \text{ arc seconds} \end{aligned}$$

The results of (6.9) shows that the main contribution is from the Type A uncertainty. This is quite typical. It indicates that there is very little systematic component in the residual errors issued from the instrument being calibrated. Nevertheless, the calibration curve resulting from the 13 calibrations (Figure 6.23) shows a very clear harmonic 4 signal that could be exploited to improve measurement results. This will be discussed in 6.9.

6.8.5 GUM supplement number 1 uncertainty framework approach

The GUM1 approach was discussed in some detail in section 6.2.2. Figure 6.24 shows schematically how it will be implemented here. Once again we shall use (6.8) as the functional model, but will use more representative PDFs for the simulations. When a calibration is made, in addition to the instrument horizontal angles, capacitive probe data for the FESM and ultimately the determination of the two collimation errors CE_{SMS} and CE_{HCC} is also collected. These data serve as the base values for the simulations.

There are five uncertainties to input to the GUM 1 model below. The instrument uncertainty is derived from the manufacturer's specification. For example with the Leica TDA5005 it is

0.5 arc seconds[42]. The LEC uncertainty, 0.044 arc seconds was derived in section 6.5. The probe separation angle uncertainty is once again taken to be 0.05 degrees. The probe reading uncertainty of 0.121 μm was derived in section 6.4. The refraction uncertainty of 0.01 arc seconds is derived from section 6.7. These five uncertainties have Gaussian PDFs.

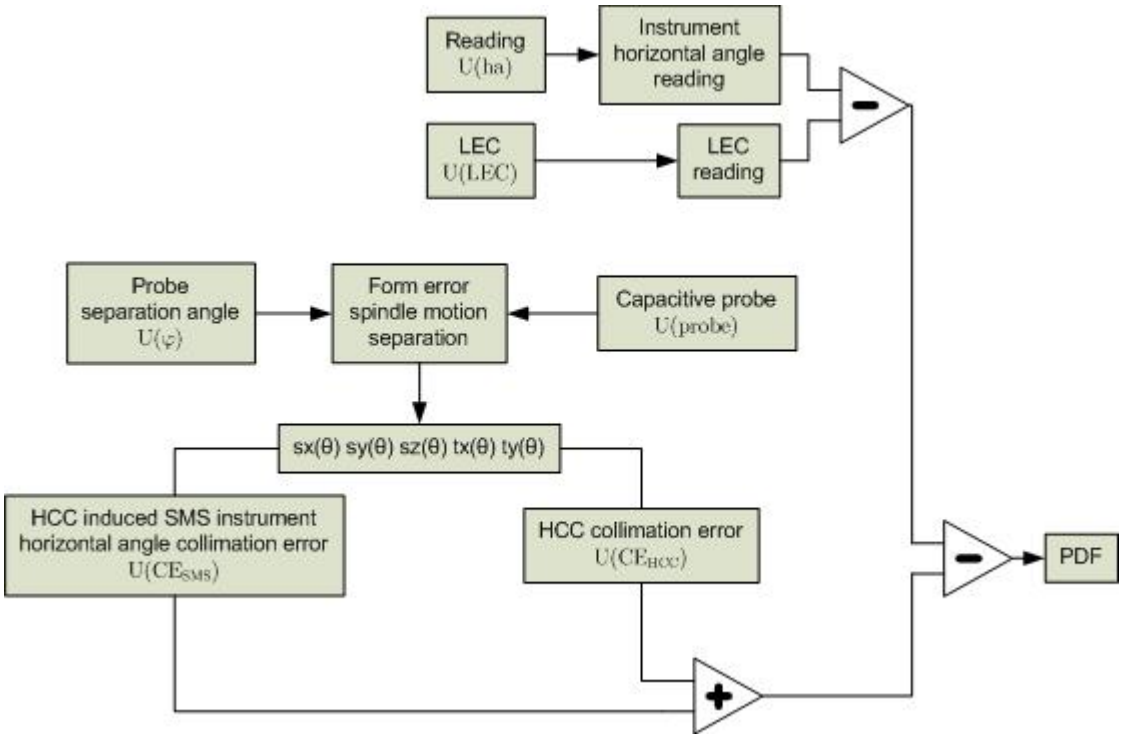

Figure 6.24 Schematic showing the different inputs to the GUM supplement number 1 approach to the uncertainty calculation.

The procedure is to sample a large number of times from each of these distributions, adding the error to the measured input data and calculating the output in the usual way. The GUM1 offers guidance on how to go about selecting the number of samples. Chapter 7.9 of this document outlines the procedure which involves carrying out an increasing number of Monte Carlo trials until the various results of interest have stabilized in a statistical sense. The procedure consists of repeating a preselected number of simulations, typically $M = 10000$, h times at which point a numerical result is deemed to have stabilized if twice the standard deviation associated with it is less than the numerical tolerance associated with the standard uncertainty $u_c(y)$ and the values y_{low} and y_{high} (see below). Typically the numerical

[42] Note that the Type A uncertainty derived in section 6.8.2 could just as easily be used. However, with the GUM1 framework this very time consuming step can potentially be side stepped. For this reason, the manufacturers quoted uncertainty is used. Later the results using this uncertainty will be compared with the classical GUM approach which uses the Type A uncertainty of 0.47 arc seconds derived in section 6.8.2 . Not surprisingly they are virtually identical.

tolerance is accepted to be 2 significant digits. In the case of the horizontal angle calibration, the tolerance is defined to be 0.01 arc seconds.

The GUM1 recommends constructing a coverage interval. Chapter 7.7 of this supplement outlines the procedure for the generation of this coverage interval. First the M model values are sorted into strictly increasing order. The recommended procedure is as follows. Define p as the coverage probability. The value 0.95 is often selected (i.e. 95%). Let $q = pM$, if pM is an integer. Otherwise, take q to be the integer part of $pM + 1/2$. Then $\left[y_{low}, y_{high} \right]$ is a $100p\%$ coverage interval for Y, where, for any $r = 1 \cdots M - q$, $y_{low} = y_r$ and $y_{high} = y_{r+q}$. The probabilistically symmetric $100p\%$ coverage interval is given by taking $r = \left(M - q \right)/2$, if $\left(M - q \right)/2$ is an integer, or the integer part of $\left(M - q + 1 \right)/2$, otherwise. The shortest $100p\%$ coverage interval is given by determining r^* such that, for $r = 1 \cdots M - q$, $y_{r^*+q} - y_{r^*} \le y_{r+q} - y_r$.[112] Computationally, one estimates the shortest $100p\%$ coverage interval by simply trying a sufficiently large number of values of r between 1 and $M - q$ and selecting the shortest interval. [127]. In practice this is only necessary if the PDF is asymmetric.

A large number (1500) of simulations were made. Recall that a calibration comprises 361 points at degree intervals between 0 and 360 degrees. Although each of these points has in principle and different value, they are assumed to have the same standard uncertainty. Under this reasonable assumption, a representative PDF for all of the samples can be constructed. It comprises a total of 1500×361 or 541500 samples.

Unfortunately, the adaptive Monte Carlo technique cannot be used here. The reason is that the mean value of the N simulations used at each step must be subtracted for each of the one degree calibration points. It was found that doing this for smaller groups of simulations; twenty for example, gave smaller overall standard uncertainties. Therefore, the mean of all of 1500 simulations must be used. Nevertheless, it was found using the adaptive Monte Carlo technique in a post processing way and subtracting the mean values of the 1500 simulations

that after approximately 250 simulations the uncertainty and the endpoints of the 95% coverage interval stabilize.

This is illustrated in Figure 6.25. The top graph, a) in this figure, illustrates the uncertainty of the calibration of the Leica TDA5005. It shows the values asymptotically approach a constant and fluctuations become smaller and smaller. For this calibration we take the standard uncertainty to be 0.52 arc seconds and the upper and lower end points of the 95% coverage interval are ±1.02 arc seconds. These results are to be compared directly with those of the classical GUM framework given in (6.9) (i.e. 0.49 arc seconds and 0.98 arc seconds respectively).

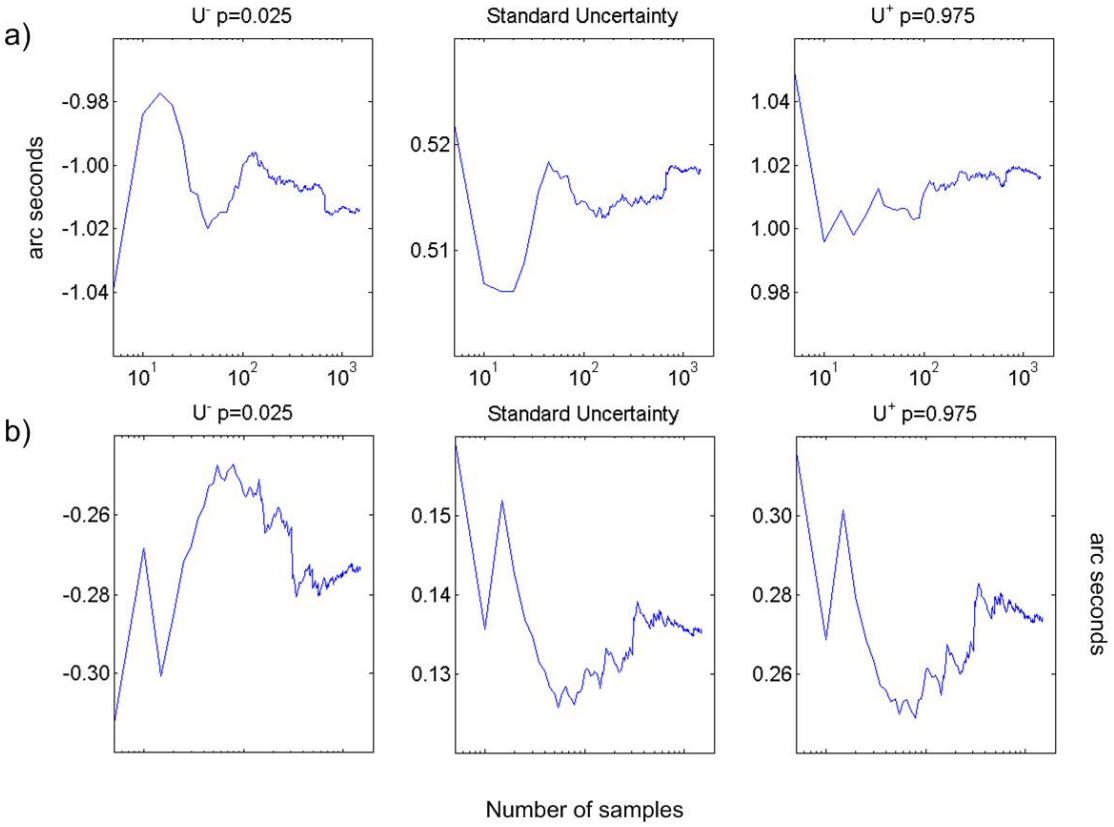

Figure 6.25 These graphs show the convergence of the lower and upper endpoints of the 95% coverage interval and the standard uncertainty for 1500 simulations following the GUM supplement number 1 framework. The top graphs a) show the results for simulations when error is introduced into the instrument readings while the bottom graph show the results when no error is introduced. This case (b) represents the uncertainty of the HCC in the calibration of horizontal angles.

The differences between the standard uncertainties and the 95% coverage interval can be explained by the difference in the uncertainties for the instrument in the two cases (i.e. 0.47 arc seconds for the classical GUM case and 0.5 arc seconds for the GUM1 approach). Indeed,

using 0.5 arc seconds for the classical GUM uncertainty gives identical results to the GUM1 approach. These results are dominated by the normally distributed instrument errors.

Graph a) of Figure 6.26 shows the PDF of the TDA 5005 calibration. It is clearly normally distributed. In graph b) the PDF of the calibration of a API Tracker II+. This normally distributed PDF has a standard uncertainty of 2.00 arc seconds. The manufacturers' quoted uncertainty is 2 arc seconds.

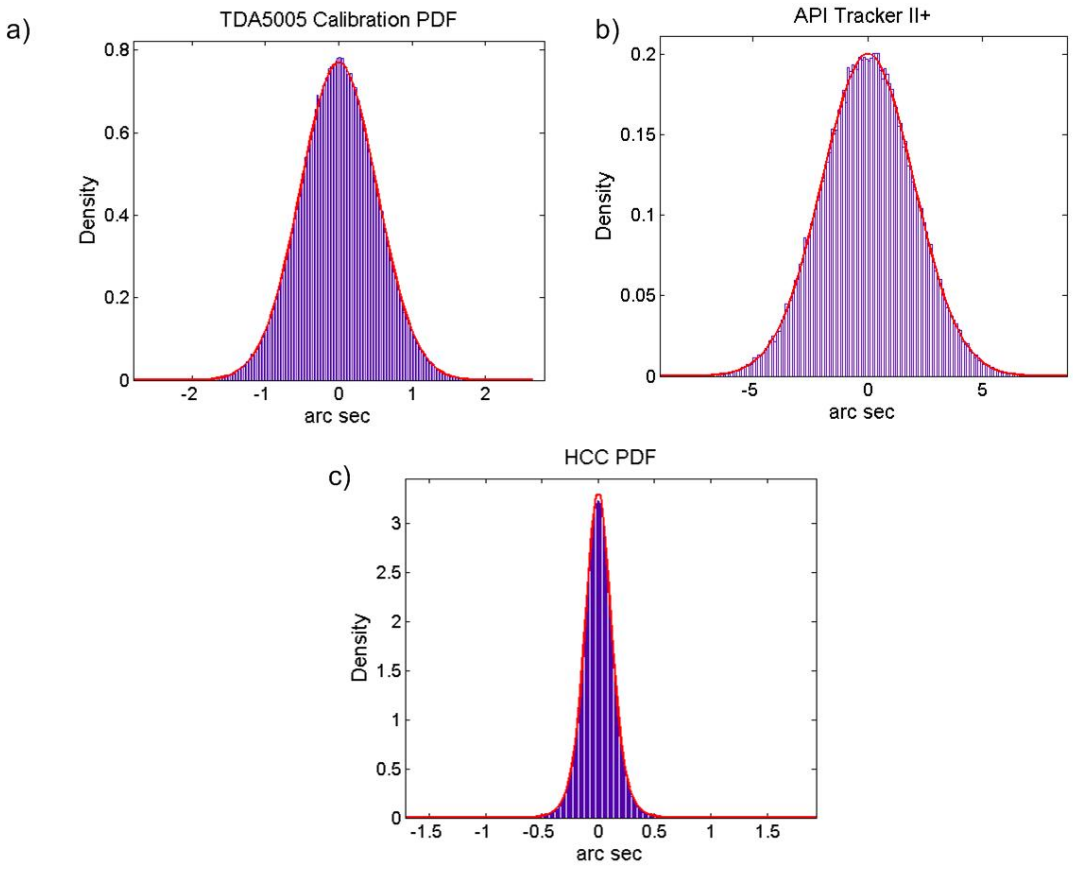

Figure 6.26 Probability density functions for the calibration of a TDA5005 (a), an API Tracker II+ laser tracker (b). The bottom graph c) shows the PDF for the HCC.

Finally, the bottom graph of Figure 6.26 shows the PDF for the HCC itself. This is produced by not injecting error into the simulations. This distribution is not normally distributed. It has a *t*-distribution (see footnote 39) with standard uncertainty of 0.12 arc seconds and 6.49 degrees of freedom. This *t*-distribution is due to the influence of the FESM discussed in section 6.6. However, the effect is too small to influence the overall calibration results as evidenced by the two calibration PDFs a) and b) of this figure. The expanded coverage interval (95% or $k = 2$) for the HCC derived from the PDF in c) of Figure 6.26 is:

$$U\left(HCC\right) = 0.27 \text{ arc seconds } k = 2 \tag{6.10}$$

The three histograms of Figure 6.26 illustrate a fundamental underlying concept inherent to uncertainty calculations. Even though the HCC has a very good uncertainty, and indeed suggestions will be made in the next chapter as to how to go about reducing it further, the uncertainty in the calibration of an instrument such as the TDA5005 is limited and will always be limited to the instruments intrinsic uncertainty.

6.9 Calibration curves and models

An ISO/CEI 17025 accredited calibration certificate gives the results of a calibration and an expanded uncertainty. This expanded uncertainty was developed both using the classical GUM and GUM1 approaches in the last section. Here we will look at the establishment of a calibration curve.

However, before continuing, it is important to note that at the time of writing, the inclusion of a calibration model in an ISO/CEI 17025 accredited calibration certificate is not permitted[43], at least in France. In fact, it is not stated anywhere within the standard that a calibration model is not allowed. The only point where the question of a model is addressed in a tertiary way in ISO/CEI 17025 is in section 5.10.4.2 which states "The calibration certificate shall relate only to quantities and the results of functional tests. …" [28] However, the GUM itself actually gives an example, albeit very simple ('H.3 Calibration of a thermometer' [111]), of a calibration model. Nonetheless, given the fact that at least two GUM supplements; Supplement 3 to the GUM: Modelling, and Applications of the least-squares method; are in preparation that specifically address the problem of modelling implicitly supports this point of view. French accreditation authorities (COFRAC) are reluctant to approve mathematical models without a solid base and grounding in the GUM. Calibration authorities in other countries may take a more liberal view to this.

[43] This is the experience of the author with the French accreditation body COFRAC interpretation of the ISO 17025 standard.

Nonetheless, one of the main objectives of this work is to establish a calibration model for the TDA5005, the main workhorse for all high precision survey work at the ESRF. To this end, a calibration model is established.

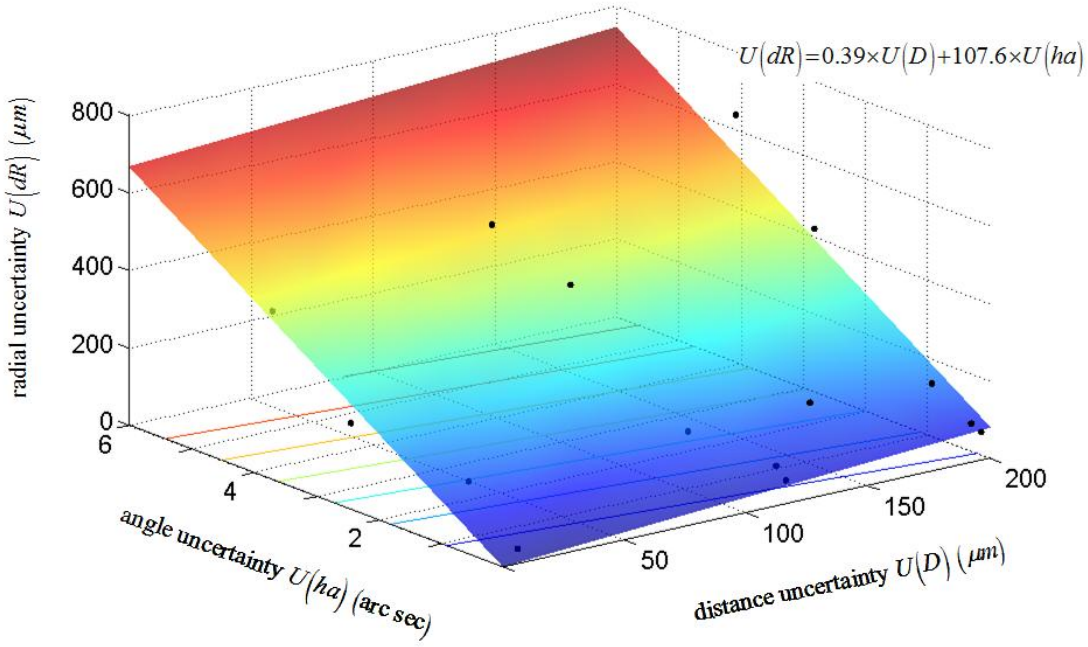

Figure 6.27 ESRF storage ring radial error surface as a function of distance meter and horizontal angle measurement uncertainty.

Before this however, it is instructive to understand what may be gained from using a calibration model. A study was made on the influence of distance and angle measurements on the ESRF survey network. [128] This study consisted of making a large number of simulations of the radial error issued from the least squares calculations of the ESRF storage ring survey network with different distance and angle measurement uncertainties. Ten simulations each were made for 15 different combinations of uncertainties. The results of this study are shown as black points on Figure 6.27. Fitting a plane to these points gives an uncertainty surface for the ESRF storage ring radial uncertainty as a function of distance and angle measurement uncertainty. Recall from the introductory section 1.2.2 and particularly Figure 1.1 and Figure 1.2 that the radial uncertainty (i.e. in the direction orthogonal to the travel of the electron beam) is the most sensitive to alignment errors. This error surface in Figure 6.27 indicates that an improvement of 0.1 arc seconds will yield an improvement in the radial uncertainty of 11 µm.

As often is the case, the model selection in not always obvious. Figure 6.28 gives a plausible calibration model for this instrument. The RMSE of the fit is 0.37 arc seconds. Applying the uncertainty model to this data, and considering that the present horizontal angle uncertainty is 0.5 arc seconds, we could reasonable expect an improvement in the order of 14 µm in the radial positional determination uncertainty of the ESRF storage ring. Thus given the present situation where the distance uncertainty is in the order of 100 µm, and the angle uncertainty about 0.5 arc seconds, the improvement would be approximately 15% passing from $U(dR) = 93\ \mu\text{m}$ to $U(dR) = 79\ \mu\text{m}$.

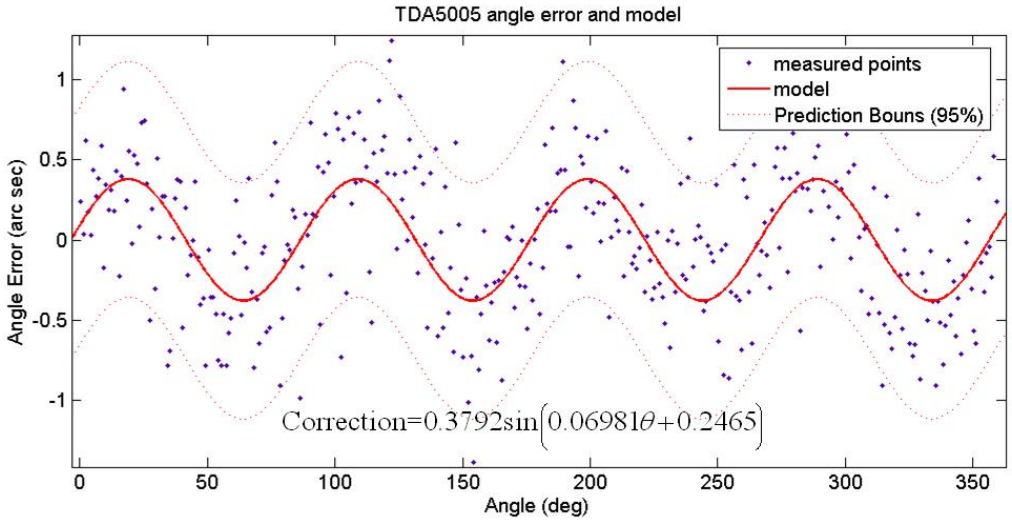

Figure 6.28 Calibration model for the TDA5005 RTS used in the main survey at the ESRF. The RMSE of the fit is 0.37 arc seconds.

Figure 6.29 shows a calibration model for the API Tracker II+ laser tracker. The RMSE of the fit is 1.07 arc seconds. This is an improvement of a factor two with respect to the manufacturers quoted uncertainty. Applying this model would afford a spectacular imprudent in the SR radial uncertainty by a factor of two to $U(dR) = 108\ \mu\text{m}$.

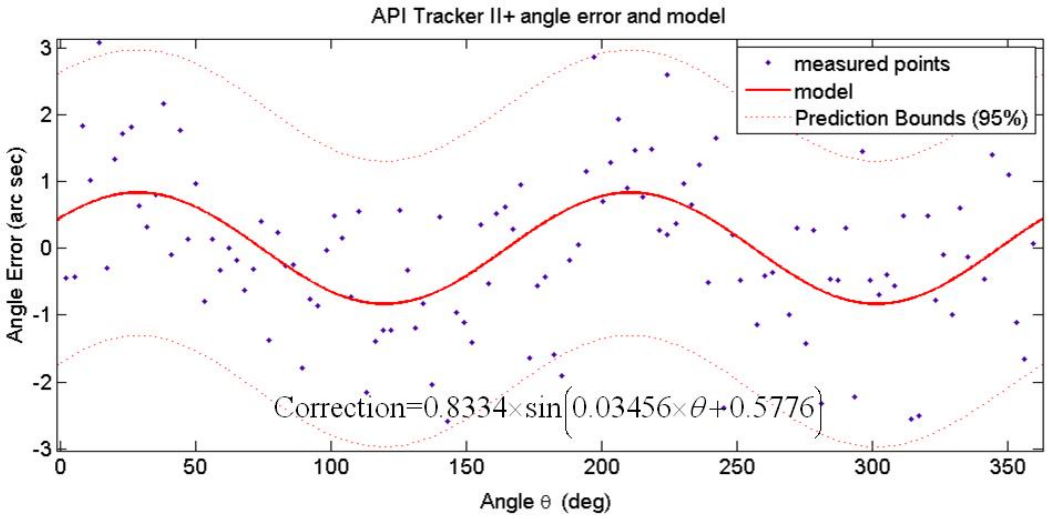

Figure 6.29 Calibration model for the API Tracker II+ LT. The RMSE of the fit is 1.07 arc seconds.

7 Summary, Conclusions and Outlook

In conclusion, this chapter provides a summary of the work done, describes what are believed to be the novel contributions and investigates means to improving the two standards developed in this thesis.

7.1 Summary

This thesis concerns two new standards developed at the ESRF to calibrate the vertical and horizontal angle readings issued from spherical measurement systems (SMSs). The main impetus for the development of these standards has been to provide assurance in, and ultimately improve, the quality of measurements made on the ESRF survey networks. Nevertheless, this work will also be relevant to ultra-precise metrology in broadly similar calibration facilities across many countries and applications.

The standards, the horizontal circle comparator (HCC) and the vertical circle comparator (VCC), in combination with the existing distance meter calibration bench (DCB) provide a full calibration suite for SMSs. Recall that SMSs are an important class of instruments used extensively in the field of large scale (volume) metrology. They comprise automated total stations (theodolites equipped with distance meters), referred to here as robotic total stations (RTSs); and laser trackers (LTs).

There are two key aims in this thesis. The first is to provide mathematical models, through calibration, of any instrument horizontal and vertical systematic angle reading errors. These models may then be used to compensate the systematic error and improve the instrument's overall performance. The second aim is to provide traceable standards and techniques that are fully compatible with the ISO/CEI 17025:2005 General Requirements for the Competence of Testing and Calibration Laboratories standard. For this reason of ISO/CEI 17025 standard compliance, special attention has been taken to ensure that the instruments and techniques used to quantify the uncertainties of these standards are traceable to the metre. This has been done specifically because the radian, the official SI unit for angle, is a dimensionless unit defined using the metre as $m \cdot m^{-1}$.

Both of the stated aims of the thesis have been achieved. In so far as the first is concerned, the ESRF survey network positional accuracy can only be improved with higher precision in the Leica TDA5005[44] horizontal angle readings. There are two reasons for this. The first is that the limit to improvement in distance meter uncertainty with this instrument has been attained through careful calibration on the DCB and the application of corrections employing a mathematical model developed from its calibration curve. More importantly, however, the influence of horizontal angle measurements in a long narrow network such as the ESRF storage ring (SR) dominate the attainable positional uncertainty in the direction orthogonal to the travel of the electron beam (dR). This is the direction of greatest interest for the ESRF accelerators. A simulation model developed for the uncertainty of this critical alignment factor $U(dR)$ as a function of distance meter uncertainty $U(d)$ and horizontal angle uncertainty $U(ha)$ estimates that for the ESRF SR survey network, an improvement of 10 μm requires either; an improvement in $U(d)$ of 26 μm, or an improvement in $U(ha)$ of 0.09 arc seconds.

It is for this reason, until now at least, that laser trackers have not been used in the ESRF SR survey network. Although they have impressive distance meter performance ($U(d) = 26$ μm)[45], the horizontal angles have manufacturers quoted uncertainty of 2 arc seconds (Refer to footnote 16). Thus even excluding the distance meter contribution altogether from the uncertainty estimation gives a $U(dR)$ of over 200 μm with the laser tracker. This can be compared to the present ESRF situation $U(dR) = 93$ μm.

Nevertheless, there is tremendous potential for improvement with the latest generation of LTs using corrections derived from the horizontal angle calibration on the HCC. The most recent LTs could rival the horizontal angle uncertainty of the best RTSs. Combined with their excellent distance meter uncertainty, decreasing price and increasing manoeuvrability; LTs could one day replace the RTSs used at the ESRF.

---

[44] Recall the Leica TDA5005 is the instrument used for all of the high precision survey work at the ESRF at the time of writing of this thesis.

[45] This uncertainty $(k = 1)$ has been determined on the ESRF DCB.

More importantly however, these studies have implications for metrology beyond the world of ESRF and accelerators. Aerospace and other manufacturing environments might not be quite as extreme in their current demands, but we can anticipate greater use of improved LTs and with the types of calibration developed here there may be economically significant opportunities for using long, thin networks to the advantages of factory efficiency (plant layout, lines of sight, etc.).

7.2 Novel contributions

Novel contributions of this work centre principally on the HCC. The HCC presented two main challenges. The first was how to measure very precisely an angle displacement. The second, which only became evident as the work progressed, was how to model and compensate the inherent errors of the HCC.

The best angle encoders available on the market have comparable precision to the SMS instruments used at the ESRF. Therefore, to provide a standard with a sufficiently small uncertainty, the linked encoders system (LEC) was developed. However, having developed the LEC, the development of a traceable means to quantify its uncertainty became necessary. The LEC was estimated to have an angle uncertainty of 0.044 arc seconds ($k = 1$) using high precision capacitive probes.

However, the more difficult problem was the understanding and qualification of the observed HCC harmonic errors. Ultimately, it was found that the combination of two categories of collimation error could account for the observed HCC error. These collimation errors are directly linked to the spindle motions of one of the main component parts of the HCC; the RV350 rotation table. The first of these collimation errors CE_{HCC} is inherent to the HCC. The second is due to the installation of the instrument being calibrated on the HCC.

The second CE_{SMS} was reasonably straight forward when the mechanism behind the first CE_{HCC} had been understood. However, understanding this mechanism was not simple, and made more difficult by the application of guidelines developed for autocollimators and polygon mirrors that were not fully appropriate to the HCC. There are subtle differences in the interaction of geometric effects between the classical autocollimator - polygon mirror

application and the HCC which led to confusing results. Applying a series of transformations based on the spindle motions of the HCC gave a clearer understanding of what was happening.

Because of the importance of the HCC spindle motions, a means to measure them had to be developed. Several different possibilities were considered. Finally it was decided the simplest way to measure them with the highest precision was to employ multi-probe radial and face form error – spindle motion separation (FESM) techniques. Although these techniques are not new, they gave surprising results when applied to the HCC. In particular, unexpected occasional but very large errors were encountered.

This led to a detailed investigation into error behaviour of these techniques. It was found that this behaviour, particularly in the presence of probe measurement errors, is significantly more complex than was previously considered in the literature. A more comprehensive investigation into the mechanism behind this behaviour could be a line of future research.

In summary novel and significant contributions comprise:

development of, especially, the HCC and LEC, based on extensions of a little-known concept;

new levels of rigour in the analysis of uncertainty estimation and to traceability at ESRF.

These main drivers then lead to:

identification and detailed analysis of a source and regime of influence of systematic error, related to spindle run-out, that is not very important in some other conventional optical angle calibration set-ups and so has been unwisely ignored in the literature;

extensions to modelling and understanding of multi-probe spindle error separation techniques.

finally, perhaps not a ‘novelty’ in quite the same sense but still significant; rigour of methodology that provides new case-study educative benefit to the ultra-precision metrology community.

7.3 Improvements and future work

The VCC and the HCC provide a reliable and robust means to explore the vertical and horizontal angle uncertainties of SMS instruments. The VCC expanded uncertainty (i.e. $k = 2$) for three representative instruments ranges between 1.4 arc seconds and 3.0 arc seconds. The HCC expanded uncertainty is 1.0 arc second for the Leica TDA5005 and 2.0 arc seconds for the API Tracker II+.

These uncertainties may appear large. However, the standard uncertainty of a calibration technique cannot be less than the standard uncertainty of the inherent error of the instrument being calibrated. Regardless of the approach used; GUM or GUM1, the intrinsic built-in instrument uncertainty enters into the calculations either as a Type A component or as part of the Monte Carlo simulation. If an instrument being calibrated has a highly systematic error component that the manufacturer includes in their tolerance specification, it is possible to have a standard uncertainty that is less than the quoted instrument uncertainty[46]. This is the case with the distance meters built into the RTS instruments. If however, the uncertainty of the instrument being calibrated is dominated by random error, it is not possible to have standard uncertainty that is less than its intrinsic uncertainty.

It is natural to desire the lowest possible uncertainty for a standard. Having achieved the present VCC and HCC uncertainties one may ask; how could these standards be improved? However, it may be more relevant to question what is the right uncertainty for the calibration of SMS instruments? The response to this question can be tempered by the extent to which one can invest in time, instrumentation, techniques and money to improve on the uncertainty of the standard.

Reasonably assuming Gaussian or near Gaussian PDFs, this question of improvement can be investigated using the law of propagation of uncertainty given in the GUM.

$$u = \sqrt{(\text{Type A})^2 + (\text{Type B})^2}$$

[46] Clearly this is also possible if the manufacturer is over conservative in their tolerance specification for the instrument.

In this equation, the Type A uncertainty components come from the repeated measurements of the instrument being calibrated (i.e. the analysis of a series of observations). They represent its intrinsic uncertainty. This of course assumes that the Type B uncertainty contribution is significantly smaller than the Type A contribution to the combined uncertainty. The Type B uncertainty components are those that come by means other than the analysis of a series of observations. In reality, the Type B uncertainty components, at least for the cases discussed in this thesis, are a function of the uncertainty of the standard (i.e. the HCC and the VCC) used to calibrate the instrument.

Thus the question becomes what is the most appropriate uncertainty (Type B) for the instruments being calibrated? In this thesis the TDA5005 Type A standard uncertainty was found to be 0.47 arc seconds[47]. The HCC Type B uncertainty component is estimated to be 0.13 arc seconds. The HCC uncertainty is supported by the GUM1 approach where its contribution was found to be 0.12 arc seconds. The difference between the two is explained by the long tails in the distribution due to the FESM technique used to determine the HCC collimation errors CE_{HCC} and CE_{SMS}.

With these results, and the law of propagation of uncertainty, one can estimate the influence of any improvements to the HCC. Taken in a different light, this investigation can be considered to be an indication of the quality of the standard for the task at hand. As a percentage of the total uncertainty, the contribution of the Type B uncertainty component is given by:

$$\text{Type B contribution} = \left[1 - \frac{\left(\text{Type A}\right)^2}{\left(\text{Type A}\right)^2 + \left(\left[X \right]_{X=\text{TypeB1}\cdots\text{TypeB}n} \right)^2} \right] \times 100\ \%$$

In this equation, the Type B uncertainty is varied over a range of values of interest. For example, one may examine the influence of Type B uncertainty between 0 and 0.13 arc seconds for the HCC.

Figure 7.1 shows the behaviour of this function for the uncertainties of the horizontal angles determined using the HCC for two instruments studied in this thesis. For the API Tracker II+

[47] The manufacturer's quoted uncertainty is 0.5 arc seconds.

laser tracker, there is clearly not very much to be gained by improving the HCC uncertainty. The HCC (Type B) contribution to the combined uncertainty represents considerably less than 1%. Any improvement would simply diminish an already nearly insignificant contribution to the combined uncertainty. For the Leica TDA5005, on the other hand, there could be interest in improvement. In both cases, the HCC as it stands can be considered as reasonably well adapted to the task of calibrating the horizontal angles issued from this class of instruments.

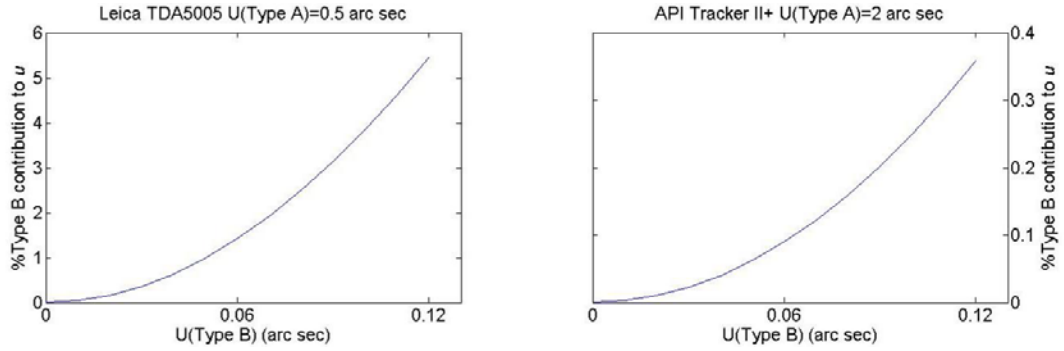

Figure 7.1 The percentage contribution of Type B uncertainty to the combined uncertainty in the horizontal angle calibration of the Leica TDA5005 (left hand side) and the API Tracker II+ (right hand side)

With the acknowledged imperfections (section 3.5.3) of the VCC, there is actually very little room for improvement with the given setup. Ignoring the negligible influence of the tilt on the VCC Type B uncertainty (i.e. $U(ha)$ and $U(va)$), the influence of the two main contributions, the VCC interferometer distance uncertainty $U(D_I)$, and the RTS and LT distance uncertainties $U(d)$, on the VCC combined uncertainty have a complex interplay. The instrument distance uncertainties $U(d)$ cannot be improved. They are already calibrated and corrected for using the DCB. The interferometer distance uncertainty $U(D_I)$ is estimated to be 5 μm. The main contribution to this uncertainty is due to thermal effects in the order of 0.1 degrees Celsius. Without changing the laboratory it is unlikely that this could be improved upon. Therefore to significantly improve the VCC would require considerable economic investment.

For the HCC, nearly all of the Type B uncertainty contribution comes from the instrument collimation error CE_{SMS}. The Type B contribution to the combined uncertainty determined by the classical GUM approach is 0.13 arc seconds. The contribution attributable to the

instrument collimation error CE_{SMS} is 0.12 arc seconds. Thus any decrease in the uncertainty of the instrument tilt measurement along the direction orthogonal to the instrument line of sight would improve the HCC uncertainty. This could be done by improving the uncertainty of the capacitive probes used to determine the spindle motion errors of the HCC, and in particular the three vertical components $wx(\theta)$, $wy(\theta)$ and $z(\theta)$. However, the main contribution to the capacitive probe uncertainty are influences external to the probe itself. In other words, a probe with a much higher resolution would have no influence on the overall results. As with the VCC improvement to the HCC uncertainty requires an improvement in the laboratory environmental, and specifically its thermal conditions.

Without a change in the laboratory environment, there is really not a great potential (and certainly no medium-term economic case) for further improvement to either the VCC or the HCC. Both standards are more than adequate for the task of calibrating and constructing a mathematical model to compensate systematic errors remaining in the horizontal and vertical angles issued from high precision robotic total stations and laser tracker instruments.

In conclusion, methods and instrumentation have been established that more than satisfy the needs of all but the most demanding applications, such as those at ESRF, for at least the next decade. In all cases they provide a level of calibration that now awaits better inherent performance for new generations of commercial instruments.

References

1. Estler, W.T., et al., *Large-scale metrology - An update.* CIRP Annals Manufacturing Technology 2002. **51**(2): p. 587-609.
2. IWAA, *Conference proceedings*. 1989 to 2008, www-conf.slac.stanford.edu/iwaa/.
3. ESRF. *European Synchrotron Radiation Facility*. 2008 [cited; Available from: www.esrf.eu.
4. Martin, D. and G. Gatta. *Calibration of Total Stations Instruments at the ESRF* in *XXIII FIG Congress in Munich, Germany, 8-13 October 2006* 2006. Munich: FIG.
5. Emain, G., *Analyse des relevés topographiques de l'ESRF*, in *Ecole Supérieure des Géomètres et Topographes*. 2006, Conservatoire National des Arts et Métiers: Le Mans. p. 74.
6. OED, *Oxford English Dictionary*, O.U. Press, Editor. 2008, Oxford University Press,.
7. Emerson, W.H., *A reply to "Definitions of the units radian, neper, bel and decibel" by I. M. Mills et al.* Metrologia, 2002. **39**(1): p. 105-109.
8. Boyer, C.B. and U.C. Merzbach, *A history of mathematics*. 2nd ed. 1991, New York ; Chichester: Wiley. xviii, 762.
9. Beckmann, P., *A history of pi (pi)*. 1989, New York: Dorset Press. 200.
10. Evans, J.C., et al., *Measurement of angle in engineering*. 3rd ed , ed. 1986, London: H.M.S.O : HMSO Publications Centre. vii, 48 , [8] of plates.
11. Alder, K., *The measure of all things : the seven-year odyssey that transformed the world*. 2002, London: Little Brown. xii, 466.
12. BIPM, *The International System of Units (SI)*. 2006, Comité International des Poids et Mesures
13. Emerson, W.H., *Differing angles on angle.* Metrologia, 2005. **42**(4): p. L23-L26.
14. Leleu, S., J.M. David, and G.P. Vailleau. *La Mesure des Angles au BNM-LNE - Cretion d'une Nouvelle Reference de Mesure Angulaire*. in *Congrès International de Métrologie 2005*. 2003. Toulon.
15. Deumlich, F., *Surveying Instruments*. 7th ed. 1982: Walter de Gruyter. 316.
16. Rueger, J., *Electronic Surveying Instruments: A Review of Principles, Problems and Procedures*. First ed, ed. U.o.N.S.W. School of Surveying and Spatial Information Systems. Vol. Monograph 18. 2003, Sydney: UNSW Sydney, Austrailia. 155.
17. Rueger, J.M., *Electronic Distance Measurement- An Introduction*. 4th ed. 1996: Springer.
18. Burnside, C.D., *Electromagnetic distance measurement*. 3rd ed ed. 1991, Oxford: BSP Professional. x, 278.
19. Agilent, *Agilent 10770A Angular Interferometer with Agilent 10771A Angular Reflector*, in *Laser and Optics User's Manual*, A. Technologies, Editor. 2002, Agilent Technologies.
20. Estler, W.T. and Y.H. Queen, *An Advanced Angle Metrology System.* CIRP Annals 1993. **41** (1): p. 573-576.
21. Probst, R., et al., *The new PTB angle comparator.* Measurement Science & Technology, 1998. **9**(7): p. 1059-1066.
22. Just, A., et al., *Calibration of high-resolution electronic autocollimators against an angle comparator.* Metrologia, 2003. **40**(5): p. 288-294.
23. Chetwynd, D.G., et al., *Applications of x-ray interferometer-generated Moire patterns.* Nanotechnology, 1998. **9**(2): p. 125-132.
24. Filatov, Y.V., D.P. Loukianov, and R. Probst, *Dynamic angle measurement by means of a ring laser.* Metrologia, 1997. **34**(4): p. 343-351.
25. Watanabe, T., H. Fujimoto, and T. Masuda, *Self-calibratable rotary encoder*, in *7th International Symposium on Measurement Technology and Intelligent Instruments*, X.J.W.D.J. Jiang, Editor. 2005. p. 240-245.
26. Probst, R., *Self-calibration of divided circles on the basis of a prime factor algorithm.* Measurement Science & Technology, 2008. **19**(1).

27. ISO, *ISO/CEI GUIDE 99:2007: International vocabulary of metrology — Basic and general concepts and associated terms (VIM)*. First edition ed. 2007: International Organization for Standardization.
28. ISO, *ISO/CEI 17025:2005 General Requirements for the Competence of Testing and Calibration Laboratories*. Second edition ed. 2005: International Organization for Standardization.
29. ISO, *ISO 17123-3:2001(E) Optics and optical instruments - Field procedures for testing geodetic and surveying instruments Part 3: Theodolites*. Vol. 17123. 2001, Geneva Switzerland: ISO.
30. ASME, *B89.4.19 - 2006 Performance Evaluation of Laser-Based Spherical Coordinate Measurement Systems*. 2006: American Society of Mechanical Engineers.
31. ISO, *ISO 9001: Quality management systems — Requirements*. Third edition ed. 2000: International Organization for Standardization.
32. Wendt, K.Z., R., *Development of Test and Calibration Procedures for Automated Theodolite Systems in Production Metrology Project No. 34511/1/0/195/91/9-BCR-D(39),* , ed. P.-T. Bundesanstalt. 1995: European Commission, Brüssel/Luxemburg.
33. Martin-Rabaud, A., *Intercomparaison des méthod de mesur dans le domaine de ls Métrologie Tridimensionnelle par Procédés Optiques (MTPO)*. XYZ Revue de l'Association Français de Topographie, 2004(98): p. 33-34.
34. Ingensand, H. *A new method of theodolite calibration*. in *Fédération Internationale des Géomètres - XIX congrès international*. 1990. Helsinki Finland.
35. Palmateer, J. *Uncertainty characterization for portable variable geometry coordinate measurement systems*. in *8ème Congrès international de Métrologie, 20-23 octobre 1997*. 1997. Besançon France.
36. Maurer, W., *Ein interferometrisched Verfahren zur Bestimmung von Strichverbesserungen an eingebauten Theodolitteilkreissn*, in *Faculty of Civil Engineering and Geodesy* 1982, Technische Universitaet Muenchen. p. 79.
37. Ingensand, H., *Theodolite angle calibration*, M. D., Editor. 2002, e-mail.
38. Lambalieu, P. and J.P. Senelaer. *Mise au Point d'une methode d'étalonnage de théodolites*. in *9ème Congrès international de Métrologie, 18-21 Octobre 1999*. 1999. Bordeaux France.
39. Bručas D., Giniotis V., and P. P., *Basic Construction of the Flat Angle Calibration Test Bench for Geodetic Instruments.* Geodesy and Cartography (Geodezija ir kartografija), 2006. **30**(3): p. 66-70.
40. Gassner G.L. and R.R. E. *Laser Tracker Test Facility at SLAC - Progress Report: SLAC-PUB-13129*. in *IWAA08, 2/11/2008—2/15/2008, KEK*. 2008. Tsukuba, Japan.
41. Sim, P.J., *Angle standards and their calibration*, in *Modern Techniques in Metrology* P.L. Hewitt, Editor. 1984, World Scientific: Singapore. p. 102-121.
42. ISO, *ISO 17123 Optics and optical instruments - Field procedures for testing geodetic and surveying instruments Parts 1 to 8*. 2001-2007, ISO: Geneva Switzerland.
43. University College London, N.P.L., Leica UK, *Best Practice for non-contacting CMMs : Project 2.3.1/2/3 – Large Scale Metrology, Ref. MPU 8/61.1 - 09 12 1999*, U.C. London, Editor. 2001.
44. Martin, D., *A Modern Calibration Bench: Calibrating Survey Instruments.* GIM International, 2007. **21**(8): p. 21-23.
45. Martin, D. *Some Reflections on the Validation and Analysis of HLS Data*. in *Eighth International Workshop on Accelerator Alignment*. 2004. CERN, Geneva Switzerland.
46. d'Oreye de Lantremange, N.F.C., *Inclinomètre à niveaux hydrostatiques de haute résolution en géophysique / High Resolution Water-Tube Tiltmeter in Geophysics*, in *Physics*. 2003, Université Catholique de Louvain. p. 338.
47. Palmer, E.W., *Goniometer with Continuously Rotating Gratings for Use as an Angle Standard.* Precision Engineering-Journal of the American Society for Precision Engineering, 1988. **10**(3): p. 147-152.

48. Leleu, S., *Contribution a l'Evaluation de Angles - Conception, Realisation et Validation dún Plateau Pivotant de Tres Haute Precision : Vers une Nouvelle Reference Angulaire Nationale*, in *Mecanique*. 2000, Ecale Nationale Supérieure d'Arts et Métiers: Metz. p. 233.
49. Ellin, A. *The accuracy of angle encoders*. Technical article from the Encoder Products Division 2004 [cited; Available from: www.renishaw.com.
50. Heidenhain. *Angle Encoders*. [WWW] [cited; Technical documentation pertaining to the RON 905 operation principle]. Available from: http://www.heidenhain.com/phaise2/angenc.html.
51. Ellin, A. and G. Dolsak, *The design and application of rotary encoders.* Sensor Review, 2008. **28**(2): p. 150-158.
52. Mancini, D., E. Cascone, and P. Schipani, *Galileo high-resolution encoder system*, in *Proc. SPIE Vol. 3112, Telescope Control Systems II*, H. Lewis, Editor. 1997, The International Society for Optical Engineering. p. 328-334.
53. Mayer, J.R.R., *High-Resolution of Rotary Encoder Analog Quadrature Signals.* Ieee Transactions on Instrumentation and Measurement, 1994. **43**(3): p. 494-498.
54. Martin, D. and D. Chetwynd. *High precision angle calibration of robotic total stations and laser trackers*. in *5th International Symposium on Instrumentation Science and Technology*. 2008. Shenyang, China.
55. Martin, D. *Instrumentation and Survey Networks at the ESRF*. in *Eighth International Workshop on Accelerator Alignment*. 2004. CERN, Geneva Switzerland.
56. Martin, D. *Calibration of Total Station Instruments at the European Synchrotron Radiation Facility*. in *3rd International Workshop on Traceability in Large-Scale Metrology*. November 14th - 15th, 2006 Braunschweig Germany.
57. Moritz, H., *Zur Reduktion eletronisch gemessener Strecken und beobachteter Winkel wegen Refraktion.* Osterreichische Zeitschrift fur Vermessungswesen, 1961.
58. Moritz, H., *Application of the conformal theory of refraction.* Zeitschrift fur Vermessungswesen, 1967. **25**(Proceedings of the International Symposium Figure of Earth and Refraction, Wein, 14-17 March): p. 323-333.
59. Huiser, A.M.J. and B.F. Gachter, *A Solution to Atmospherically Induced Problems in Very High-Accuracy Alignment and Leveling.* Journal of Physics D-Applied Physics, 1989. **22**(11): p. 1630-1638.
60. Böckem, B., *Development of a Dispersometer for the Implementation into High-Accuracy Direction Measurement Systems*, in *Institute of Geodesy and Photogrammetry, Geodetic Metrology and Engineering Geodesy*. 2001, Swiss Federal Institute of Technology Zurich: Zurich. p. 140.
61. Korpelainen, V. and A. Lassila, *Acoustic method for determination of the effective temperature and refractive index of air in accurate length interferometry.* Optical Engineering, 2004. **43**(10): p. 2400-2409.
62. Barrel, H. and J.E. Sears, *The Refraction and Dispersion of Air for the Visible Spectrum.* The Royal Society Philosphical Transactions Mathematical, Physical and Engineering Sciences, 1939. **238**.
63. Edlen, B., *The Refractive Index of Air.* Metrologia, 1966. **2**(2): p. 71-81.
64. Rueger, J.M., *Refractive Indices of Light, Infrared and Radio Waves in the Atmosphere*, in *International Association Of Geodesy Special Commission*. 1999.
65. Ciddor, P.E., *Refractive index of air: New equations for the visible and near infrared.* Applied Optics, 1996. **35**(9): p. 1566-1573.
66. Ciddor, P.E. and R.J. Hill, *Refractive index of air. 2. Group index.* Applied Optics, 1999. **38**(9): p. 1663-1667.
67. Jupp, D.L.B., *Calculating and Converting between Common Vapour Measures in Meteorological Data and Their Use in Support of Earth Observation Validation*, C.E.O. Centre and C.A. Research, Editors. 2003, CSIRO.
68. Stone, J.A., et al., *Uncertainties in small-angle measurement systems used to calibrate angle artifacts.* Journal of Research of the National Institute of Standards and Technology, 2004. **109**(3): p. 319-333.

69. Huang, S.M., et al., *Electronic Transducers for Industrial Measurement of Low Value Capacitances.* Journal of Physics E-Scientific Instruments, 1988. **21**(3): p. 242-250.
70. Jones, R.V. and J.C. Richards, *Design and Some Applications of Sensitive Capacitance Micrometers.* Journal of Physics E-Scientific Instruments, 1973. **6**(7): p. 589-600.
71. Heerens, W.C., *Application of Capacitance Techniques in Sensor Design.* Journal of Physics E-Scientific Instruments, 1986. **19**(11): p. 897-906.
72. Baxter, L.K. and IEEE Industrial Electronics Society., *Capacitive sensors : design and applications*. IEEE Press series on electronics technology. 1997, New York: IEEE Press. xiv, 302.
73. LIONPrecision (2006) *Capacitive Sensor Operation and Optimisation TechNote LT03-0020.* **Volume**,
74. Bruère, A. and C. Galaud, *Chaîne de mesure dimensionnelle capacitive à sortie linéaire.*, O.N.D.E.e.d.R.A. FR, Editor. 1988-12-09, Institut National de la Propriété Industrielle FR 2640373 A1.
75. Bissoli Nicolau, V., *Mesure de distance par capteur capacitif et électronique numérique*, in *Génie Electrique*. 2007, Institut National des Sciences Appliquées de Lyon: Lyon. p. 41.
76. PerkinElmer, *What is a Lock in Amplifier?: Technical Note TN 1000*. 2000, Perkin Elmer Instruments: Oak Ridge TN.
77. Smith, P.T., R.R. Vallance, and E.R. Marsh, *Correcting capacitive displacement measurements in metrology applications with cylindrical artifacts.* Precision Engineering-Journal of the International Societies for Precision Engineering and Nanotechnology, 2005. **29**(3): p. 324-335.
78. Evans, C.J., R.J. Hocken, and W.T. Estler, *Self Calibration: Reversal, Redundancy, Error Separation, and 'Absolute Testing.* Annals of the CIRP, 1996. **45**(2): p. 617-633.
79. Grejda, R.D., *Use and Calibration of Ultraprecision Axes of Rotation With Nanometer Level Metrology*, in *Mechanical Engineering*. 2002, The Pennsylvania State University. p. 135.
80. Chetwynd, D.G. and G.J. Siddall, *Improving the Accuracy of Roundness Measurement.* Journal of Physics E-Scientific Instruments, 1976. **9**(7): p. 537-544.
81. Whitehouse, D.J., *Some Theoretical Aspects of Error Separation Techniques in Surface Metrology.* Journal of Physics E-Scientific Instruments, 1976. **9**(7): p. 531-536.
82. Moore, D., *Design Considerations in Multiprobe Roundness Measurement.* Journal of Physics E-Scientific Instruments, 1989. **22**(6): p. 339-343.
83. Zhang, G.X. and R.K. Wang, *Four-point method of roundness and spindle error motion measurement.* CIRP, 1993. **42**(1): p. 593-596.
84. Zhang, G.X., et al., *A multipoint method for spindle error motion measurement.* CIRP, 1997. **46**(1): p. 441-445.
85. Grejda, R., E. Marsh, and R. Vallance, *Techniques for calibrating spindles with nanometer error motion.* Precision Engineering-Journal of the International Societies for Precision Engineering and Nanotechnology, 2005. **29**(1): p. 113-123.
86. Marsh, E., J. Couey, and R. Vallance, *Nanometer-level comparison of three spindle error motion separation techniques.* Journal of Manufacturing Science and Engineering-Transactions of the Asme, 2006. **128**(1): p. 180-187.
87. ISO, *ISO 230-7:2006 Geometric accuracy of Axes of Rotation*. First edition ed. 2006: International Organization for Standardization.
88. Evans, C.J., R.J. Hocken, and W.T. Estler, *Self Calibration: Reversal, Redundancy, Error Separation, and 'Absolute Testing'.* Annals of the CIRP, 1996. **45**(2): p. 617-633.
89. Zhang G.X. and Wang R.K., *Four-Point Method of Roundness and Spindle Error Motion Measurements.* CIRP, 1993. **42**(1): p. 593-596.
90. Zhang G.X., et al., *A Multi-Point Method for Spindle Error Motion Measurement.* CIRP, 1997. **42**(1): p. 441-445.

91. Grejda, R.D., *Use and Calibration of Ultraprecision Axes of Rotation With Nanometer Level Metrology*, in *Mechanical Engineering*. 2002, The Pennsylvania State University. p. 135.
92. Wikipedia, c. *Modulo operation* 2008 12 October 2008 09:24 UTC [cited 2008 20 October 2008 09:41 UTC]; Available from: http://en.wikipedia.org/w/index.php?title=Modulo_operation&oldid=244743169
93. Clapham, C., *The concise Oxford dictionary of mathematics*. 3rd ed. 2005, Oxford ; New York: Oxford University Press. 510 p.
94. Hoaglin, D.C., F. Mosteller, and J.W. Tukey, *Understanding robust and exploratory data analysis*. Wiley Classics Library ed. Wiley classics library. 2000, New York Chichester: John Wiley. xx, 447 p.
95. Cleveland and W.S., *Visualizing Data*. 1993: Hobart Press.
96. NIST, *NIST/SEMATECH e-Handbook of Statistical Methods*, N.I.o.S.a. Technology, Editor. 2008.
97. Hartley, R. and A. Zisserman, *Multiple view geometry in computer vision*. 2nd ed. 2003, Cambridge: Cambridge University Press. xvi, 654 p.
98. Weisstein and E. W. (2008) *Affine Transformation*. **Volume**,
99. Ramsay, J.O. and B.W. Silverman, *Functional data analysis*. Springer series in statistics. 1997, New York ; London: Springer. xiv, 310.
100. Ramsay, J.O. and B.W. Silverman, *Applied functional data analysis : methods and case studies*. Springer series in statistics. 2002, New York ; London: Springer. x, 190 p.
101. Matlab, *Spline Toolbox Users Guide*, I. The Mathworks, Editor. 2008, The Mathworks, Inc.
102. Hastie, T., R. Tibshirani, and J.H. Friedman, *The elements of statistical learning : data mining, inference, and prediction*. Springer series in statistics. 2001, New York: Springer. xvi, 533 p.
103. Marion, J.B., *Classical dynamics of particles and systems*. 2nd ed. 1970, New York, NY ; London: Academic Press. xvi, 573 p.
104. Resnick, R., et al., *Physics*. 5th ed. 2002, New York: Wiley.
105. Butikov, E., *Precession and nutation of a gyroscope.* European Journal of Physics, 2006. **27**(5): p. 1071-1081.
106. Thomson, W.T., *Introduction to space dynamics*. Dover books on engineering. 1986, New York: Dover. xiv, 317 p.
107. Marsh, E., *Precision Spindle Metrology*. 2008: DEStech Publications Inc.
108. Yandayan, T., S.A. Akgoz, and H. Haitjema, *A novel technique for calibration of polygon angles with non-integer subdivision of indexing table.* Precision Engineering-Journal of the International Societies for Precision Engineering and Nanotechnology, 2002. **26**(4): p. 412-424.
109. BIPM. *The Metre Convention* 2008 [cited 2008 November 2008]; Available from: http://www.bipm.org.
110. Bich, W., M.G. Cox, and P.M. Harris, *Evolution of the 'Guide to the Expression of Uncertainty in Measurement'.* Metrologia, 2006. **43**(4): p. S161-S166.
111. BIPM-IEC-IFCC-ISO-IUPAC-IUPAP-OIML, ed. *Guide to the Expression of Uncertainty in Measurement*. 1995, International Organization for Standardisation: Geneva.
112. JCGM, ed. *Evaluation of measurement data — Supplement 1 to the "Guide to the expression of uncertainty in measurement" — Propagation of distributions using a Monte Carlo method*. ed. J.C.f.G.i. Metrology. 2006, BIPM: Sèvres.
113. Cox, M.G. and P.M. Harris, *Software Support for Metrology Best Practice Guide No. 6 Uncertainty Evaluation*, NPL, Editor. 2006, National Physical Laboratory.
114. Taylor, B.N. and C.E. Kuyatt, *NIST Technical Note 1297 Guidelines for Evaluating and Expressing the Uncertainty of NIST Measurement Results*, NIST, Editor. 1994, National Institute of Standards and Technology, USA.
115. EAL_Taskforce, *EA-4/02 Expression of the Uncertainty of Measurement in Calibration*, EA, Editor. 1999, European co-operation for Accreditation.

116. *M3003 The Expression of Uncertainty and Confidence in Measurement*, UKAS, Editor. 2007, United Kingdom Accreditation Service: Feltham, Middlesex, UK.
117. Cox, M.G., A.B. Forbes, and P.M. Harris. *Bayesian estimation methods in metrology*. 2004: AIP.
118. Cox, M. and P. Harris, *An outline of supplement 1 to the guide to the expression of uncertainty in measurement on numerical methods for the propagation of distributions.* Measurement Techniques, 2005. **48**(4): p. 336-345.
119. ALGE, *D-AEMD-06 calcul incertitude edition 8*, ALGE, Editor. 2008, ESRF: Grenoble. p. 17.
120. Phillips, S.D., K.R. Eberhardt, and B. Parry, *Guidelines for expressing the uncertainty of measurement results containing uncorrected bias.* Journal of Research of the National Institute of Standards and Technology, 1997. **102**(5): p. 577-585.
121. Lira, I.H. and W. Woger, *Evaluation of the uncertainty associated with a measurement result not corrected for systematic effects.* Measurement Science & Technology, 1998. **9**(6): p. 1010-1011.
122. Synek, V., *Attempts to include uncorrected bias in the measurement uncertainty.* Talanta, 2005. **65**(4): p. 829-837.
123. Maroto, A., et al., *Effect of non-significant proportional bias in the final measurement uncertainty.* Analyst, 2003. **128**(4): p. 373-378.
124. O'Donnell, G.E. and D.B. Hibbert, *Treatment of bias in estimating measurement uncertainty.* Analyst, 2005. **130**(5): p. 721-729.
125. Efron, B. and R.J. Tibshirani, *An introduction to the bootstrap*. Monographs on statistics and applied probability. 1993, New York ; London: Chapman & Hall. xvi, 436 p.
126. Tu, J.F., B. Bossmanns, and S.C.C. Hung, *Modeling and error analysis for assessing spindle radial error motions.* Precision Engineering-Journal of the International Societies for Precision Engineering and Nanotechnology, 1997. **21**(2-3): p. 90-101.
127. Cox, M.G. and P.M. Harris, *Software Specifications for Uncertainty Evaluation*, in *NPL Report DEM-ES-010 (CMSC 40/04 revised)*, NPL, Editor. 2006, National Physical Laboratory.
128. Martin, D. *Instrumentation and Calibration at the ESRF*. in *Seventh International Workshop on Accelerator Alignment*. 2002. SPRING-8, Japan.